DEFORMATION STUDIES ON Fe 3.5 wt % Si SINGLE CRYSTALS BY X-RAY TOPOGRAPHY

by

Michael Dudley

A thesis submitted to the Department of Engineering Science, University of Warwick, in accordance with the requirements for the degree of Doctor of Philosophy.

September 1982

CONTENTS

ABSTRACT

For many years the Plastic Deformation of bcc metal crystals has formed the subject of numerous investigations comprising a wide range of experimental techniques. One of the more recent and novel of these techniques is Synchrotron White Radiation Topography. This is well suited for examination of relatively large areas of comparatively thick crystals, without the need for undesirably long exposure times (as encountered, for example, in conventional topography), typical values being of the order of seconds, making dynamic, in situ experiments feasible.

In this study, Synchrotron White Radiation Topography was used to make in situ, dynamic observation of the evolution of slip bands in single crystals of Fe 3.5 wt % Si (of rectangular cross-section) with two different surface orientations under uniaxial tensile stress in the [011] direction. Both types of crystal were oriented for double slip, in one the primary Burgers vectors lying in the crystal surface, and in the other the primary Burgers vectors lying at an angle of 35° 16' with the surface. Slip morphology in particular, was found to be a sensitive function of surface orientation.

The studies reported in this thesis form a continuation of the work reported in Miltat and Bowen ([32]), and demonstrate the usefulness of the technique in studies of this nature. Important information on the early stages of deformation and the progress of slip was obtained.

In Chapter 1 a brief review of the type of work that has already been conducted on bcc metals is presented, with particular reference to Iron and its alloys with Silicon.

Chapter 2 presents a description of the apparatus used throughout the work, including a detailed description of synchrotron X-ray sources, and the sophisticated direct imaging equipment essential for dynamic experiments.

The basic experimental approach adopted is outlined in Chapter 3.

Chapters 4 and 5 comprise a brief review of contrast theory in X-ray topography, and how this theory can be applied to interpret topographs.

Experimental results are presented in Chapter 6, and these results are discussed in detail in Chapter 7.

A brief description of the effect of stress on the magnetic domain configurations in the specimens is given in Appendix I.

Details of a calculation conducted with J. Miltat ([225]) on the projective geometries of white beam topographs are presented in Appendix II.

Results of detailed calculation of integrated intensities expected on the topographs are given in Appendix III.

ILLUSTRATIONS

TABLES

REFERENCES

CHAPTER 1

[1] J.W. Christian; Proceedings of 2nd Int. Conf. on strength of Metals and Alloys; Asilomar ASM pp29 (1970).

[2] P.B. Hirsch; Trans. Jap. Inst. Metals. Supp 9 (1968).

[3] R.A. Foxall, M.S. Duesbery and P.B. Hirsch, Can. J. Phys. 45 607 (1967).

[4] G. Taylor and J.W. Christian Phil. Mag 15 893 (1967).

[5] J.R. Low and A.M. Turkalo, Acta Met 10 215 (1962).

[6] E. Furubayashi, Trans. Jap. Inst. Metals Supp 9 939 (1968).

[7] E. Furubayashi, Journ. of Phys. Soc. Jap. 27 130 (1969).

[8] S. Takeuchi, E. Furubayashi and T. Taoka, Acta Met. 15 1179 (1967).

[9] D.K. Bowen, J.W. Christian and G. Taylor, Can. J. Phys. 45 903 (1967).

[10] D. Vesely, Phys. Stat. Sol. 29 675 (1968).

[11] A. Luft and L. Kaun, Phys. Stat. Sol. 37 781 (1970).

[12] M.S. Duesbery and R.A. Foxall, Phil. Mag. 20 719 (1969).

[13] C.J. Bolton and G. Taylor, Phil. Mag. 26 1359 (1972).

[14] A.J. Garratt-Read and G. Taylor, Phil. Mag. 33 577 (1976).

[15] J. Nakagawa and M. Meshii, Phil. Mag. A44 1165 (1981).

[16] L. Kaun, A. Luft, J. Richter and D. Schulze, Phys. Stat. Sol. 26 485 (1968).

[17] R.G. Garlick and H.B. Probst, Trans AIME 230 1120 (1964).

[18] F. Louchet, L. Kubin and D. Vesely; Proc. 4th Int. Conf. on Strength of Metals and Alloys; Nancy, France Vol. 1 171 (1976).

[19] V. Novak, K.Z. Saleeb, S. Kadeckova and B. Sestak, Czech.J. Phys. B26 (1976).

[20] A.S. Keh and Y. Nakada, Trans. Jap. Inst. Metals Supp. 9 876 (1968).

[21] J. Diehl and R. Berner, Z. Metallkde 51 522 (1960).

[22] R. Zeyfang, O. Buck and A. Seeger, Phys. Stat. Sol.(b) 61 551 (1974).

[23] V. Novak and B. Sestak; Proc. 4th Int. Conf. on Strength of Metals and Alloys; Nancy (1976).

[24] N. Zarubova and B. Sestak, Phys. Stat. Sol.(a) 30 365, 479 (1975).

[25] L. Granas and B. Aronsson, Scr. Met. 2 541 (1968).

[26] D.F. Stein and J.R. Low Jr., J. Appl. Phys. 31 362 (1960)

[27] D.K. Bowen, D. Phil. Thesis, Oxford University (1966).

[28] V. Novak, B. Sestak and S. Kadeckova; Proc. 5th Int. Conf. on Strength of Metals and Alloys, Aachen (1979) Eds. P. Haasen, V. Gerald, and G. Kostory, Pergammon Press, Oxford Vol. 1 pp133.

[29] N. Zarubova and S. Kadeckova, Czech. J. Phys. B22 215 (1972).

[30] B. Sestak and V. Novak, Phys. Stat. Sol.(a) 23 703 (1974).

[31] B. Sestak and Z. Arnold, Phys. Stat. Sol.(a) 23 155 (1974).

[32] J. Miltat and D.K. Bowen, J. de Physique 40 389 (1979).

[33] JCM Li and C.D. Needham, J. Appl. Phys. 31 1318 (1960).

[34] P. Haasen, pp27 Physical Metallurgy, CUP Cambridge (1978).

[35] S. Libovicky; Electron Microscopy of Pure Iron Alloys, Proc. of Symp. on High Purity Materials in Science and Technology, Dresden (1980).

[36] T. Yamashita and Y. Nakada, Trans. Jap. Inst. Metals Supp. 9 465 (1968).

[37] K.F. Hale and M. Henderson-Brown; Proc. Roy. Soc. A310 479 (1969).

[38] A. Gemperle, M. Rozsival and B. Sestak, Gech. J. Phys. B12 555 (1962).

[39] F. Louchet, L. Kubin and D. Vesely, Phil. Mag. A39 433 (1979).

[40] F. Louchet, These D'Etat, L'Universite Paul Sabatier de Toulouse (1976).

[41] F.J. Humphreys and J.W. Martin, Phil. Mag. 16 927 (1967).

[42] P.B. Hirsch and F.J. Humphreys; Proc. Roy. Soc. A318 45, 73 (1970).

[43] P.B. Hirsch and P.J. Humphreys; Proc. 2nd Int. Conf. on Strength of Metals and Alloys, Asilomar ASM (1970).

[44] E. Orowan, Discussion, Symp. on Internal stresses in metals and alloys (Inst. of Metals; London) 451 (1948).

[45] P.B. Hirsch, J. Inst. Metals 86 7 (1957).

[46] F. Kroupa, Phil. Mag. 7 783 (1962).

[47] P.B. Hirsch, Phil. Mag. 7 67 (1962).

[48] G. Saada and J. Washburn, J. Phys. Soc. Japan, Suppl. 1 18 43 (1963).

[49] J.C. Crosskreutz and M.B. McNeil, Phil. Mag. 16 401 (1967).

[50] S. Mader, Z. Physik 149 73 (1957).

[51] S. Mader, A. Seeger and Ch. Seitz, J. Appl. Phys. 34 3368 (1963).

[52] B. Sestak and S. Libovicky. The Relation Between the Structure and Mechanical Properties of Metals, Teddington (1963).

[53] B. Sestak and S. Libovicky, Acta Metal, 11 1190 (1963).

[54] B. Sestak and S. Libovicky, Czech. J. Phys. B13 266 (1963).

[55] G.I. Taylor; Proc. Roy. Soc A118 1 (1928).

[56] W.A. Spitzig and A.S. Keh, Met. Trans. 1 2751, 3325 (1970).

[57] F.L. Vogel Jr. and R.M. Brick, J. Metals 5 700 (1953).

[58] R.P. Steijn and R.M. Brick, Trans ASM 46 1406 (1954).

[59] D.F. Stein and J.R. Low, Acta Met. 14 1183 (1966).

[60] A.S. Keh and Y. Nakada, Can. J. Phys. 45 1101 (1967).

[61] T.E. Mitchell, Phil. Mag. 17 1169 (1968).

[62] M.S. Duesbery, Phil. Mag. 19 501 (1969).

[63] S. Argon and S.R. Maloof, Acta Met. 14 1449 (1966).

[64] S. Ikeda, J. Phys. Soc. Japan 27 1564 (1969).

[65] T. Takeuchi, Jap. J. Appl. Phys. 8 320 (1969).

[66] T. Takeuchi, J. Phys. Soc. Japan 26 354 (1969).

[67] B. Sestak and N. Zarubova, Phys. Stat. Sol. 10 239 (1965).

[68] F. Kroupa and V. Vitek, Can. J. Physics 45 945 (1967).

[69] B. Sestak, N. Zarubova and V. Sladek, Can. J. Phys. 45 1031 (1967).

[70] S.V. Afanasev and B.V. Molotilov, Fig. Metallov i Metallovedervie 27 111 (1969).

[71] J.W. Christian, Comments on Solid State Physics 1 19 (1968).

[72] F. Kroupa and V. Vitek, Phys. Stat. Sol. 36 K143 (1969).

[73] D. Vesely, Phys. Stat. Sol. 29 685 (1968).

[74] D. Vesely; Proc. 3rd Int. Conf. on HVEM, Oxford (1973).

[75] D. Vesely, Scripta Met. 6 753 (1972).

[76] W.G. Johnston and J.J. Gilman, J. Appl. Phys. 31 632 (1960).

[77] J.S. Koehler, Phys. Rev. 86 52 (1952).

[78] J.R. Low Jr. and R.W. Guard, Acta Met. 7 171 (1959).

[79] R.A. Foxall and C.D. Statham, Acta Met. 18 1147 (1970).

[80] P.B. Hirsch, (oral communication); 5th Int. Congress of Crystallography (1960).

[81] F. Kroupa, Phys. Stat. Sol 3 K, 391 (1963).

[82] B. Escaig, J. de Phys. 27 C3, 205 (1966).

[83] B. Escaig, J. de Phys. 28 171 (1967).

[84] B. Escaig, Phys. Stat. Sol. 28 463 (1968).

[85] M.S. Duesbery, P.B. Hirsch, 'Dislocation Dynamics', Ed. A.R. Donenfeld, G.T. Hahn, A.L. Bement, R.I. Jaffe - McGraw Hill p57 (1968).

[86] J. Friedel, Internal Stresses and Fatigue in Metals (eds. G.M. Rassweiler and W.L. Grube) Elsevier Publishing Co., Amsterdam-London-New York, p239, Princetown (1949).

[87] L.P. Kubin, Rev. Deform. Behav. Mater. 1 244 (1977).

[88] B. Sestak and J. Blahovec, Phys. Stat. Sol. 40 599 (1970).

[89] C.D. Statham, D. Vesely and J.W. Christian, Acta Metal 18 1243 (1970).

[90] R. Conte, P. Groh, B. Escaig, Phys. Stat. Sol. 28 475 (1968).

[91] B. Escaig, These, Fac. des Sciences d'Orsay (1968).

[92] V. Vitek, Phil. Mag. 18 773 (1968).

[93] V. Vitek, Phil. Mag. 21 1275 (1970).

[94] Z.S. Basinski, M.S. Duesbery and R. Taylor, Phil. Mag. 21 1201 (1970).

[95] M.S. Duesbery, V. Vitek and D.K. Bowen; Proc. Roy. Soc. A332 85 (1973).

[96] J.W. Christian and V. Vitek, Rep. Prog. Phys. 33 307 (1970).

[97] D.A. Smith and K.M. Bowkett, Phil. Mag. 18 1219 (1968).

[98] D.A. Smith and J. Gallot, Metal Sci. Journal 3 79 (1969).

[99] J.T. Lynch, G.K.L. Cranstoun, D.A. Smith and G.D.W. Smith, Nature 223 637 (1969).

[100] D.A. Smith and V. Vitek, unpublished work.

[101] R. Chang, Phil. Mag. 16 1021 (1967).

[102] R. Bullough and R.C. Perrin, Dislocation Dynamics, Batelle Colloquium (Eds. A.R. Rosenfield, G.T. Hahn, A.L. Bement and R.I. Jaffee) p175, New York; McGraw-Hill (1968).

[103] H. Suzuki, Dislocation Dynamics, Battelle Colloquium (Eds. A.R. Rosenfield, G.T. Hahn, A.L. Bement and R.I. Jaffee) p679, New York; McGraw-Hill (1968).

[104] P.C. Gehlen, G. Hahn and A.R. Rosenfield, Fundamental Aspects of Dislocation Theory, p305 Washington; US National Bureau of Standards (1969).

[105] P.C. Gehlen, J. Appl. Phys. 41 5165 (1970).

[106] V. Vitek, R.C. Perrin and D.K. Bowen, Phil. Mag 21 1049 (1970).

[107] L.L. Boyer and J.R. Hardy, Phil. Mag. 24 647 (1971).

[108] C. Wuthrich, Phil. Mag. 35 325 (1977).

[109] Z.S. Basinski, M.S. Duesbery and R. Taylor, Can. J. Phys. 49 2160 (1971).

[110] V. Vitek, Cryst. Latt. Defects 5 1 (1974).

[111] V. Vitek, Proc. Roy. Soc. A352 109 (1976).

[112] Z.S. Basinski, M.S. Duesbery and R. Taylor, Interatomic Potentials and Simulation of Lattice Defects, Battelle Colloquium (Eds. P.C. Gehlen, J.R. Beeher Jr. and R.I. Jaffee) p537, New York and London; Plenum Press (1971).

[113] P.C. Gehlen, Interatomic Potentials and Simulation of Lattice Defects, Battelle Colloquium (Eds. P.C. Gehlen, J.R. Beeler Jr., and R.I. Jaffee) p475 New York and London; Plenum Press (1971).

[114] B. Escaig, Scripta Metal 5 199 (1971).

[115] A. Seeger and B. Sestak, Scripta Metall 5 875 (1971).

[116] H. Suzuki, A Theory of Solid Solution Hardening in bcc Alloys, Nach. Akad. Wiss. Gottingen. Math. Phys. K12 No. 6 1 (1971).

[117] L. Kubin and F. Louchet, Phil. Mag. 38 205 (1978).

[118] A. Sato and M. Meshii, Acta Met. 21 753 (1973).

[119] L. Kubin and F. Louchet, Acta Met. 27 337 (1979).

[120] A. Seeger, Phys. Stat. Sol. 55 (No.2) 457 (1979).

[121] W. Frank and B. Sestak, Scripta Met. 4 451 (1970).

[122] A.H. Cottrell, Dislocations and Plastic Flow in Crystals, Oxford (1953),

[123] J. Friedel, Dislocations, Pergammon Press (1964).

[124] F. Seitz, Adv. Phys. 1 43 (1952).

[125] F. Seitz, Phys. Rev. 88 722 (1952).

[126] D. Kuehlman-Wilsdorf, Phil. Mag. 3 125 (1958).

[127] R. Grilhe, Acta Met. 11 56 (1962).

[128] D.A. Jones and J.W. Mitchell, Phil. Mag. 3 1, 334 (1958).

[129] D.J. Barber, K.B. Harvey and J.W. Mitchell, Phil. Mag. 2 704 (1957).

[130] A.S. Parasnis and J.W. Mitchell, Phil. Mag 4 171 (1959).

[131] J.T. Bartlett and J.W. Mitchell, Phil. Mag. 3 334 (1958).

[132] A. Fourdeux and A. Berghezan, Compt. Rend. 252 1462 (1961).

[133] J.S. Lally and P.B. Partridge; Proc. 5th Int. Conf. on Electron Microscopy, Philadelphia 1 5112 (1962).

[134] J.E. Bailey, Acta Met. 11 267 (1963).

[135] R.S. Barnes and D.J. Mazez, Acta Met. 11 281 (1963).

[136] J.J. Gilman, Acta Met. 7 608 (1959).

[137] J.J. Gilman, J. Appl. Phys. 30 1584 (1959).

[138] D.M. Marsh, Phil. Mag. 5 1197 (1960).

[139] D.K. Bowen and M. Dudley, to be published.

[140] D.K. Bowen and J. Miltat, J. Phys. E: Scientific Instruments 9 868 (1976).

[141] Synchrotron Radiation Techniques and Applications, Topics in Current Physics, Vol. 10, ed. C. Kunz, Springer-Verlag Berlin, Heidelberg, New York (1979).

[142] U. Bonse, Characterization of Crystal Growth Defects by X-ray Methods, p298 eds. B.K. Tanner and D.K. Bowen, Plenum (1980).

[143] M. Sauvage and J.F. Petroff, Synchrotron Radiation Research, p607 ed. H. Winick and S. Doniach, Plenum press (New York and London) (1980).

[144] J. Schwinger, Phys. Rev., 75 798 (1949).

[145] J. Schwinger, Phys. Rev. 75 1912 (1949).

[146] D.H. Tomboulian and P.L. Hartman, Phys. Rev. 102 1423 (1956).

[147] J.D. Jackson, Classical Electrodynamics, John Wiley, New York, London, Sydney, Toronto, p76 (1975).

[148] J. Miltat, Characterization of Crystal Growth Defects by X-ray Methods, p401, eds. B.K. Tanner and D.K. Bowen, Plenum (1980).

[149] M. Hart, Characterization of Crystal Growth Defects by X-ray Methods, p216, eds. B.K. Tanner and D.K. Bowen, Plenum (1980).

[150] T. Tuomi, K. Naukkarinen and P. Rabe, Phys. Stat. Sol. (a) 25 93 (1974).

[151] M. Hart, J. Appl. Cryst. 8 436 (1975).

[152] J.F. Petroff and M. Sauvage, J. Cryst. Growth 43 628 (1978).

[153] J. Chikawa and I. Fujimoto, Appl. Phys. Lett. 13 No. 11 387 (1968).

[154] G.A. Rozgonyi, S.E. Haszko and J.L. Statile, Appl. Phys. Lett. 16 No. 11 443 (1970).

[155] J. Chikawa, I. Fujimoto and Takao Abe, Appl. Phys. Lett. 21 No. 6 295 (1972).

[156] J. Chikawa, J. Cryst. Growth 24/25, 61 (1968).

[157] W. Hartmann, G. Markewitz, V. Rettenmaier and H.J. Queisser, Appl. Phys. Lett. 27 No. 5 308 (1975).

[158] A.R. Lang in Diffraction and Imaging Techniques in Materials Science, Volume II; Imaging and Diffraction Techniques, Second Revised Edition (ed. S. Amelinckx, R. Gevers and J. Van Landuyt) North Holland publishing Company, Amsterdam-New York-Oxford p623 (1978).

[159] D.K. Bowen and C.R. Hall, Microscopy of Materials, Macmillan (1970).

[160] M. Sauvage, Characterization of Crystal Growth Defects by X-ray Methods, p433 eds. B.K. Tanner and D.K. Bowen, Plenum (1980).

[161] J. Bradler, Private communication.

[162] R.W. James, The Optical Principles of the Diffraction of X-rays, G. Bell and Sons, London (1950).

[163] B.W. Batterman and H. Cole, Rev. Mod. Phys. 36 No. 3 681 (1964).

[164] N. Kato, Acta Cryst. 13 349 (1960).

[165] N. Kato, J. Phys. Soc. Jap. 18 1785 (1963).

[166] N. Kato, J. Phys. Soc. Jap. 19 67 and 171 (1964).

[167] N. Kato, 'X-ray Diffraction', Ed. L. Azaroff, McGraw-Hill, New York (1974).

[168] N. Kato, The Characterization of Crystal Growth Defects by X-ray Methods, p264, Ed. B.K. Tanner and D.K. Bowen, Plenum (1980).

[169] N. Kato, Acta Cryst. 14 526 and 627 (1961).

[170] Y. Ando and N. Kato, J. Appl. Cryst. 3 74 (1970).

[171] A. Authier and F. Balibar, Acta Cryst. A26 647 (1970).

[172] G. Borrmann, Z. Physik 42 157 (1941).

[173] G. Borrmann, Z. Physik 127 2971 (1950).

[174] A. Authier, 'Advances in X-ray Analysis', Vol 10, Ed. J.B. Newkirk and G.R. Mallett, p10, Plenum Press, New York (1967).

[175] D. Taupin, Acta Cryst. 23 25 (1967).

[176] Y. Epelboin, These, Universite de Paris, CNRS AO 9961 (1974).

[177] M. Schlenker, These, D'etat Universite de Grenoble (1970).

[178] M. Polcarova and A.R. Lang, Proc. Roy. Soc. A285 297 (1965).

[179] M. Hart, PhD Thesis, University of Bristol (1963).

[180] M. Hart and A.R. Lang, Acta Cryst. A16 102 (1963).

[181] A. Authier and M. Sauvage, J. de Physique 27 C3-137 (1966).

[182] N. Kato, K. Usami and T. Katagawa, 'Advances in X-ray Analysis', Vol. 10, Eds. J.B. Newkirk and G.R. Mallet p46, Plenum Press, New York (1967).

[183] J.I. Chikawa, J. Appl. Phys. 36 3496 (1965).

[184] J. Miltat and D.K. Bowen, J. Appl. Cryst. 8 657 (1975).

[185] J. Miltat, These D'Etat, Universite de Paris-Sud (1976).

[186] M. Kleman and J. Miltat, Proc. Int. Summer School on X-ray Dynamical Theory and Topography, B13 Limoges (1975).

[187] G. Rieder, Abhandl. Braunshweig Wiss. Ges. 11 20 (1959).

[188] F. Kroupa and I. Vagera, Czech J. Phys. B19 1204 (1969).

[189] M. Polcarova and A.R. Lang, Bull. Soc. Fr. Mineral. Crist. 91 645 (1968).

[190] M. Polcarova and J. Kaczer, Phys. Stat. Sol. 21 635 (1967).

[191] M. Polcarova and A.R. Lang, Phys. Stat. Sol (a) 4 491 (1971).

[192] M. Polcarova, Z. Naturforsch. 28a 639 (1973).

[193] M. Schlenker, P. Brissonneau and J.P. Perrier, Bull. Soc. Fr. Mineral. Crist. 91 653 (1968).

[194] M. Polcarova and J. Gemperlova, Phys. St. Sol. 32 769 (1969).

[195] J. Miltat, The characterization of Crystal Growth Defects by X-ray Methods, p576, Ed. B.K. Tanner and D.K. Bowen, Plenum (1980).

[196] J. Miltat and M. Kleman, Phil. Mag. 28 1015 (1973).

[197] L.J. Dijkstra and V.M. Martius, Rev. Mod. Phys. 25 146 (1953).

[198] E.S. Meieran and I.A. Blech, J. Appl. Phys. 36 3162 (1965).

[199] D.K. Bowen and J.W. Christian, Phil. Mag. 12 369 (1965).

[200] E.I. Salkovitz and J.S. Koehler, Acta Met. 1 568 (1953).

[201] R.F. Miller, Trans. A.I.M.E. 111 135 (1934).

[202] C. Crussard, Rev. Met. 42 286, 321 (1945).

[203] C. Crussard, Bull. Mineral. 68 174 (1945).

[204] J. Washburn and E.R. Parker, J. Met. 4 1076 (1952).

[205] J.B. Hess and C.S. Barrett, Trans A.I.M.E. 185 599 (1940).

[206] E. Orowan, Nature 149 643 (1942).

[207] C.S. Barrett, Imperfections in Nearly Perfect Crystals, Wiley N.Y. (1952).

[208] R.W.K. Honeycombe, J. Inst. Metals 80 45, 49 (1951).

[209] R. Maddin and N.K. Chen, Progr. Met. Physics, 5 53 (1956).

[210] R. Maddin and N.K. Chen, J. Met. 6 280 (1954).

[211] F.D. Rosi, Acta Met. 4 26 (1956).

[212] V.R. Regel, H. Berez and G.V. Kova, Sov. Phys. Cryst. 4 718 (1960).

[213] K. Kuehlman-Wilsdorf, Phil. Mag. 3 125 (1958).

[214] R.J. Stokes, Trans. A.I.M.E. 244 1227 (1962).

[215] B.K. Tanner, X-ray Diffraction Topography, p75, Pergamon Press (1976).

[216] J. Di Persio, These D'Etat, Universite de Lille (1980).

[217] S. Chikazumi, Physics of Magnetism, J. Wiley (1964).

[218] M. Labrune, These D'Etat, Orsay (1979).

[219] J. Miltat, Private Communication.

[220] M. Labrune, M. Kleman, J. Appl. Phys. 45 2716 (1974).

[221] M. Schlenker and M. Kleman, J. Physique, C1 32 256 (1971).

[222] A. Authier, Phys. Stat. Sol. 27 77 (1968).

[223] L. Landau and E. Lifschitz, Men of Physics Vol. I, Pergamon N.Y. (1965).

[224] M. Labrune, Private communication.

[225] J. Miltat and M. Dudley, J. Appl. Cryst. 13 555 (1980).

[226] A. Guinier and J. Tennevin, Acta Cryst. 2 133 (1949).

[227] International Tables for X-ray Crystallography Vols. III and IV, Kynoch Press, Birmingham (1968).

[228] D.T. Cromer, Acta Cryst. 18 17 (1965).

[229] A. Authier, Proc. of Int. Summer School on X-ray Dynamical Theory and Topography (A1-A2), Limoges France, (1975).

[230] J. Miltat in Proceedings of the Workshop on Imaging Processes and Coherence in Physics, Les Houches, Springer-Verlag, Berlin, March (1979).

[231] C.M. Dozier, D.B. Brown, L.S. Birsks, P.B. Lyons, R.F. Benjamin, J. Appl. Phys. 47 3732 (1976).

ACKNOWLEDGEMENTS

I would like to express my gratitude to my supervisors Dr. D.K. Bowen and Dr. J. Miltat for providing help, guidance and inspiration throughout the course of this work. I would also like to thank all workers at the Laboratoire de Minéralogie-Cristallographie, at Paris University, for providing an atmosphere conducive to good work.

I am grateful to Dr. N. Zarubova (Prague), Dr. M. Sauvage (Paris), Professor B. Sestak (Prague), Dr. S. Davies (Warwick) and Dr. E. Manghi (Paris) for helpful discussions.

I wish to thank Mr. C. Lovatt and Mr. A. Jeanne-Michaud for help with photography and Mr. C. Bidmead and Mr. Y. Bernard for technical assistance. I would also like to express my appreciation of the hard work and patience of Miss L.J. Laws in typing and helping to prepare this thesis.

I also wish to thank Professor A. Authier for welcoming me to his laboratory in Paris and Professor J. Douce for welcoming me to his laboratory in Warwick.

I am indebted to my family and friends for their encouragement throughout the past three-and-a-half years.

Finally, thanks are given to the Science and Engineering Research Council, and the French Government for the award of research grants which made this investigation possible.

PREFACE

Dynamic experiments are essential in studies of the early stages of deformation of single crystals. X-ray topography is a technique which is especially useful in assessing bulk defect structures in single crystals, and if used in conjunction with a synchrotron source, the short exposures in the high intensity beam make dynamic in situ experiments feasible.

This thesis aims to outline a methodology of how best to exploit the technique of White Beam Synchrotron Radiation Topography for such dynamic deformation studies. Design of experiment is discussed in detail, as well as how to extract the maximum amount of information from the data obtained.

Single crystals of Fe 3.5 wt % Si were deformed in situ in the white X-ray beam emitted from the synchrotron source at DCI, LURE, Orsay, France. Specimens of two different surface orientations were tested in order to investigate the influence of surface orientation of sheet specimens on the type of slip that ensued under tensile deformation.

The usefulness of the technique in assessing the sites where slip nucleates will be investigated in detail as well as how slip propagates from these sites. It is hoped to be able to classify the room temperature deformation of Fe 3.5 wt % Si within the general framework of the deformation of iron silicon alloys at various temperatures.

This work will form a continuation of the work reported by Miltat and Bowen ([32]).

In addition to White Beam Synchrotron Radiation Topography, conventional X-ray Topographic techniques will be used as well as optical microscopy and dislocation etch pitting.

The image obtained in X-ray Topography is an unmagnified projection of the crystal. Enlargement must therefore be achieved photographically. As is the convention, topographs are presented as they appear on the X-ray plate. Thus internegatives must be made and subsequently enlarged to a positive point. Thus darkening on the print corresponds to increased X-ray intensity (unless indicated otherwise).

CHAPTER 1

Literature Review

1.1 INTRODUCTION

Studies of the plastic behaviour of bcc metals have provoked much discussion based on the effects of dislocation mobility. In general, the relative mobilities of edge and screw dislocations and the frequency of cross slip are recognized to be important factors in glide deformation of bcc single crystals (for review see [1]).

The plastic properties of bcc metals are found to be very temperature dependent. Generally, two temperature regimes exist (ignoring creep effects at very high temperature, when diffusion becomes possible), separated by a transition range over which striking changes in behaviour occur. At moderately high temperature ($T > (0.1 \rightarrow 0.15)Tm$) and low strain rates, single crystals of bcc metals exhibit three stage hardening, and can develop dislocation structures similar to those found for example in Copper (see [2], [3]). In the early stages of deformation at these temperatures there is usually no unique slip system, even for crystals with ideal slip orientation. Dislocations of all four Burgers vectors have been detected in the microstrain or stage O region ([3], [4]) and only after some strain does slip on a single system, which is characteristic of stage I become established.

At lower temperatures the deformation behaviour of bcc metals is strikingly different from that of Fcc

metals, and is characterized by a quasi parabolic stress-strain curve with no clearly distinguishable stages, and by the development of a structure of long screw dislocations accompanied by loop debris ([4], [5], [6], [7], [8], [9]). At these lower temperatures the initiation of macroscopic plastic flow is less well defined and dislocations of different Burgers vectors continue to contribute to deformation up to quite high strains ([10], [11]).

Whilst the author does not wish to enter into a detailed description of the behaviour of all bcc metals it is felt useful to distinguish here between Group Va and VIa elements. The former (Nb, V, Ta) generally exhibit simpler hardening behaviour with fewer Burgers vectors activated after a short initial region, but they also show anomalous $(0\bar{1}1)$ slip behaviour at low temperatures ([12], [3], [9], [13], [14], [15]). The latter (Mo, W) often show a very extended stage 0 with many slip systems active; ([16], [17]). Anomalous slip analogous to that observed in Nb and V has not been observed in these metals. The behavioural characteristics of Iron and its alloys with Silicon appear to fall in between these two extremes (for example cross slip is easier in Mo than Nb, Fe being intermediate [18]).

It is intended to restrict this chapter to a study of the plastic deformation behaviour of Iron and its

alloys with Silicon, as it is these materials which are of most interest to the author.

1.2 Stress Strain Curves

1.2.1 Pure Iron

Work hardening curves of single crystals of Iron have been investigated at various temperatures by Novak and coworkers ([19]) see Fig. 1).

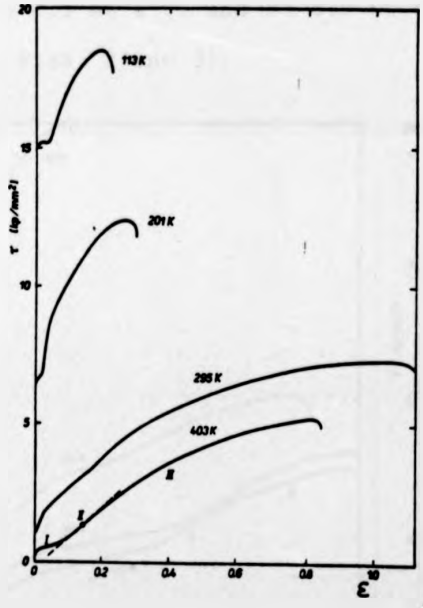

Fig. 1 Shear stress - shear strain curves of Iron single crystals oriented for single slip, measured in tension at various temperatures (after [19])

Two clearly defined temperature regimes of deformation become apparent (ignoring creep effects at very elevated temperatures). The upper regime, which shall be called the High Temperature Regime, is characterized by a Three Stage Hardening curve, similar to those characteristic of Fcc metals, except that stage II degenerates into an inflexion point, and a larger part of the shear stress-shear strain curve belongs to stage III.

The lower regime, which shall be called the Low Temperature Regime, is characterized by a quasi parabolic shear stress-shear strain curve.

1.2.2 Alloys of Silicon in Iron

A study of the effect of alloying on work hardening in Iron Silicon crystals of low silicon content has also been made by Novak and coworkers [19]. Single crystals of Fe 0.5 wt % Si and Fe 0.9 wt % Si were studied (see Figs. 2 and 3).

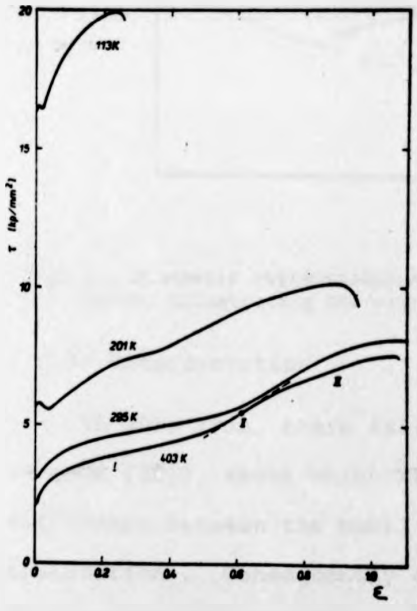

Fig. 2 As in Fig. 1, but for single crystals of Fe -0.5 wt % Si ([19])

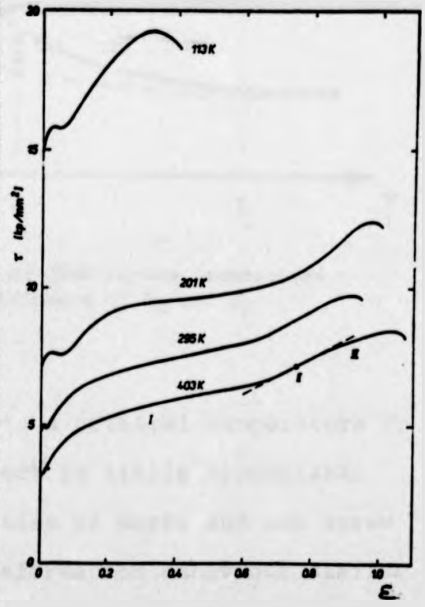

Fig. 3 As in Fig. 1, but for single crystals of Fe 0.9 wt % Si ([19])

General trends were noted, for example, that with increasing silicon content (a) the transition between the high temperature deformation regimes (characterized

by Three Stage Hardening curves) and the low temperature regime is shifted to lower temperatures, (b) Stage I hardening is enhanced, and (c) the flow stress level increases.

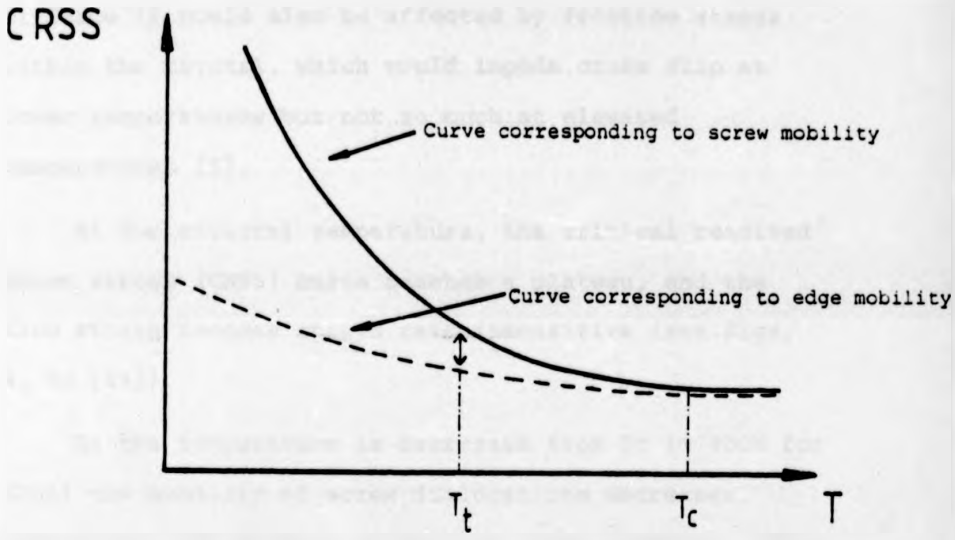

Fig. 4 Schematic representation of CRSS versus temperature curve, illustrating the significance of T_t and T_c

1.2.3 Interpretation

In pure Iron, there exists a critical temperature Tc (≈ 400K [20]), above which there is little appreciable difference between the mobilities of screw and non screw dislocations. Consequently deformation behaviour similar to that found in Fcc metals is expected, with characteristic Three Stage Hardening curves (for example [21], [22]). In Stage I, one would expect the formation of isolated clusters of primary edge dipoles (see section 1.4 for a detailed study of dislocation configurations). The degeneration of Stage II into a point of inflexion

can be considered from the point of view that in bcc metals (as opposed to Fcc) it is easier from the start of deformation for extensive cross slip to occur (i.e. no long Stage II is necessary). This degeneration of Stage II could also be affected by friction stress within the crystal, which would impede cross slip at lower temperatures but not so much at elevated temperatures [9].

At the critical temperature, the critical resolved shear stress (CRSS) curve reaches a plateau, and the flow stress becomes strain rate insensitive (see Figs. 4, 5a [19]).

As the temperature is decreased from Tc ($\sim$ 400K for Iron) the mobility of screw dislocations decreases appreciably whilst that of the non screw does not. This effect will be considered in more detail in section 1.7.

Below a certain temperature known as the transition temperature T_t, the difference in mobility (see Schematic diagram Fig. 4) between screw and non screw dislocations becomes so large that it becomes easier for slip to occur via the motion of secondary edge dislocations than by the motion of primary screw dislocations, since the flow stress increases so much. Although movement of both edge and screw dislocations is needed for loops to expand, it is the screw mobility which controls the flow stress. Below T_t, the stress strain curves are parabolic in shape (see Fig. 1).

Multiple slip systems have been observed in many bcc metals at low temperature ([10],[11]).

Addition of Silicon to Iron produces solution hardening. The CRSS measured at room temperature increases from 10 MPa for Iron to 150 MPa for Fe 3 wt % Si ([23], [24]).

Results obtained by Novak ([19]) on the dependence of the CRSS on temperature and on silicon content are presented in Figures 5(a) and.(b).

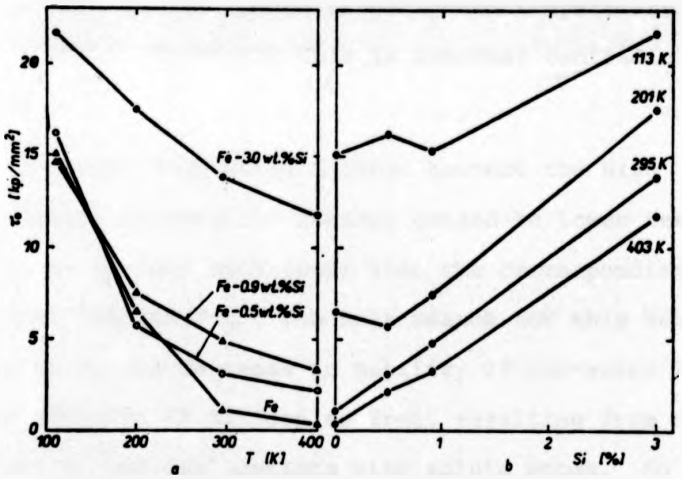

Fig. 5 The CRSS for Fe, Fe 0.5 wt % Si, Fe 0.9 wt % Si and Fe 3 wt % Si as a function of (a) Temperature and (b) Silicon content ([19],[24])

It can be seen that the plateau region of the CRSS versus Temperature curve is displaced to higher temperatures as silicon content increases. This corresponds to an increase of Tc with silicon content, quoted values being Tc Iron ∿ 400K [20], Tc Fe 3 wt % Si ∿ 550K [25]. The length of stage I and the flow stress increment over

this stage also increase with increasing silicon content.

However, investigations of alloys ranging from 0 to 3% silicon show that alloys deform according to the high temperature regime (i.e. exhibit Three Stage Hardening Curves), at temperatures substantially lower than their Critical Temperatures (which are indicated by the position of the onset of the plateau region on the CRSS versus Temperature curves). Single crystals of Fe 3 wt % Si (Tc $\sim$ 550K) deformed in the high temperature regime even at the lowest investigated temperature of 113K ([24]). Evidently this is somewhat contradictory and odd.

So, with increasing Silicon content the high temperature deformation regimes extend to lower temperatures, which are in fact much lower than the corresponding critical temperature. The main reason for this behaviour seems to be the decrease in mobility of non-screw dislocations after addition of Silicon to Iron, resulting from interactions of the dislocations with solute atoms. So as temperatures decrease there is a reduction (due to the alloying) of the mobility of non-screw dislocations and This reduction approaches that experienced by screw dislocations (whose mobility is already inherently relatively small in bcc metals - see section 1.7) as Silicon content increases.

This can be explained qualitatively if one considers the ability of an edge dislocation, unlike a screw, to interact with a pure dilatational strain field. Complete

pinning of an edge dislocation by a solute atom (i.e. decoration) will not occur as Iron-Silicon is a substitutional alloy and diffusion would have to be possible for such decoration to occur (this only occurs at high temperatures in Iron). However, the interaction of an edge dislocation with such a strain field may be enough to make non screw mobility keep track with screw mobility as temperatures decrease.

Measurements made by Stein and Low [26], of the velocity of edge dislocations in Fe 3.25 wt % Si single crystals using an etch pitting technique, seem to indicate that the mobility of edge dislocations in the alloy is not very much greater than that of screw dislocations. It was shown that over the temperature range 78K to 373K the yield stress changes with temperature in a similar way as the stress to produce a constant velocity of edge dislocation motion. As pointed out by Bowen [27], the two curves should have the same slope at a given temperature if they have the same temperature dependence. Hence a translation perpendicular to the temperature axis should bring the two curves into coincidence. Stein and Low's published curves do not obey this definition, but the deviation is probably within the experimental error. Since it is now accepted that screw dislocations are the rate controllers of deformation in bcc metals, this implies that there is no remarkable difference between edge and screw mobility, and that the low temperature regime does not develop.

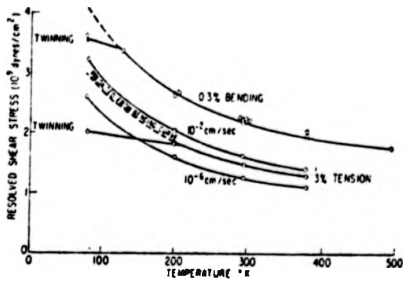

Fig. 6 Comparison of the temperature dependence of the 0.3% offset yield strength in bending and in tension with the temperature dependence of the stress to produce a constant dislocation velocity for two different constant velocity levels (10^{-6} and 10^{-2} cm sec^{-1}) (after [26])

1.3 Slip Line Morphology

1.3.1 Pure Iron

Slip line morphology investigations in pure Iron, were made by Novak and Sestak [28], at a series of temperatures. At 113K slip traces were only observed after deformation to a shear strain of $\varepsilon \simeq 0.1$. Slip traces were diffuse, and slip was described as being very fine and homogeneously distributed in the specimen. The contrast of slip traces increased with strain, till the necking of specimens. Evaluation of the Nomarski contrast indicated local changes in slope of the surface relief of approximately ten minutes of arc at $\varepsilon = 0.3$. This corresponds to local variations of shear strain $\Delta\varepsilon \simeq 0.006$. Crystals were oriented in the centre of the unit triangle and traces consistent with $(\bar{1}01)(111)$ and $(101)[\bar{1}11]$ slip systems were observed around the whole circumference of specimens. Traces of slip in the two remaining <111> directions were observed only on a part of the specimen surface and this made slip plane determination difficult.

At 295 and 403K Iron exhibits Three Stage Hardening curves (as already mentioned in Section 1.2.1).

In Stage I Iron showed distinct traces of extensive cross-slip of primary screw dislocations. In Stage III (Stage II being a point of inflexion) slip became very inhomogeneous, as indicated by coarse slip bands observed on the surface. These bands were approximately consistent with primary slip on planes of the [111] zone, which are situated in the vicinity of the $(\bar{1}01)$ plane.

1.3.2 Alloys of Silicon in Iron

Observation of slip line morphology in a series of alloys of Silicon in Iron were also made by Novak and coworkers [28].

At 113K Fe 0.5 wt % Si showed similar behaviour to that already described for pure Iron at this temperature.

For Fe 1 wt % Si single crystals at 113°K coarse slip bands mostly corresponding to the primary $(\bar{1}01)[111]$ and the conjugate $(101)[\bar{1}11]$ systems were observed. Inside the bands slip was very fine and relatively homogeneous. A shear strain of $\varepsilon \approx 0.15$ was concentrated in the primary slip bands whilst between the bands $\varepsilon = 0$. With increasing deformation the slip bands broadened up to constant strain and new bands were nucleated.

In Fe 3 wt % Si at 113K only primary slip bands with a shear strain of $\varepsilon = 0.22$ were observed. At a

particular specimen shear strain $\varepsilon = \varepsilon_s$, these bands were seen to fill up the whole specimen surface and as this value of shear strain is exceeded, a relatively homogeneous slip occurs till necking of the specimen ([24],[29]). The same slip morphology was observed on Fe 3 wt % Si single crystals after deformation at all the investigated temperatures, but with the value of ε_s decreasing with increasing temperature ([30]).

At 201, 295 and 403K Fe 0.5 wt % Si and Fe 1 wt % Si exhibited Three Stage Work Hardening curves and the observed slip markings were qualitatively similar in the two alloys. At the beginning of Stage I, and up to a particular value of shear strain which shall be called ε_p, slip was concentrated into primary slip bands separated by undeformed regions of crystal. Values of ε_p become smaller when the Silicon content is decreased and when the temperature is increased. After the specimen surface is covered by bands, slip becomes relatively homogeneous till the end of Stage I. Quantitative evaluation of the Nomarski contrast indicated variations of $\Delta\varepsilon \sim 0.01$ of the shear strain until the end of Stage I.

In Stage I, the observed variation of the shear strain concentrated in glide bands suggests that mobile screw dislocations are situated at the periphery of glide bands with a local density, ρ, which is determined by the elastic interaction between screw dislocations of the same sign forming groups.

Primary slip approximately consistent with ($\bar{1}01$) traces was observed. In Stage III slip became very inhomogeneous again as indicated by the presence of coarse slip bands on the surface. These slip bands were approximately consistent with the primary slip on planes of the [111] zone, which are situated in the vicinity of the ($\bar{1}01$) plane. Inside the bands slip was fine and relatively homogeneous. These bands were much more wavy and branched than the slip bands formed in Stage I.

1.3.3 Interpretation

Firstly an explanation will be given of the behaviour of the metals (pure and alloys) at temperatures at which Three Stage Hardening is observed. This will lead to an attempted explanation for the observed behaviour of for example Iron at low temperatures (113K).

From the macroscopic point of view, two kinds of slip distribution were observed in single crystals of Iron and its dilute alloys with Silicon, namely homogeneous slip and inhomogeneous slip, the latter manifesting itself by well-defined slip bands.

There is also a quantitative difference between the two types of observed slip bands; in Stage I the deformation proceeds by the broadening of the existing bands and nucleation of new ones, whilst the shear strain, ε_p, concentrated in the bands remains approximately constant at a constant strain rate.

The relationship between ε_F and the applied shear stress τ may be expressed as [24]

$$\varepsilon_F = K\tau^2 - B$$

where K and B are constants dependent on crystal orientation and strain rate (not temperature).

Thus ε_F appears to be strongly temperature dependent. According to a simple model, the glide bands are formed by glide, through the undeformed crystal, of screw dislocations with a local density ρ.

The shear strain (in the band) produced is [24]

$$\varepsilon_F = FbA\rho + \text{const}$$

where b is the magnitude of the Burgers vector, $F << 1$ is a numerical factor, and A = 1cm is the constant slip distance [30].

On the other hand, in Stage III, the strain concentrated in the band increases with deformation and reaches $\varepsilon \sim 1$ at the end of the stage, whereas their average spacing B, remains approximately constant.

Typical values of B obtained at 295K are 2.4μm for Iron and 1.2μm for Fe 1wt % Si ([28]). Very faint secondary slip traces were also observed in Stage III.

1.3.4 Glide Band Velocity

Studies of glide band velocity in Fe 3 wt % Si were made by Sestak and Arnold ([31]) from Nomarski observation of slip band growth. They concluded that glide bands are surrounded by a significantly long range stress field

which depends on the applied stress and crystal orientation. The component of this field in the primary slip system acts, in the vicinity of the large bands, against the applied stress and varies approximately inversely with the distance measured from the large band (measured perpendicular to the slip plane). Results obtained by Miltat and Bowen [32], who found a non linear distance - time behaviour under constant stress, when comparing slip bands, confirm that result.

1.3.5 Glide Band Formation

The formation of glide bands observed at the beginning of Stage I in the alloys may be understood as a result of two processes:-

(a) During deformation in the high temperature regime, highly curved dislocation loops develop and extensive multiplication occurs at jogs in the screw segments (see Fig. 7).

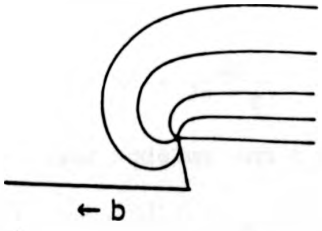

Fig. 7 Multiplication at a jog in a segment of screw dislocation

Rows of parallel screw dislocations several hundred to several ten thousands of Angstroms apart were observed

in the front and in the periphery regions of glide bands in Fe 3 wt % Si single crystals in the electron microscope (for example [6]; see Section 1-4).

(b) A group of parallel dislocations is unstable by itself [33]. However in Iron Silicon alloys (and in other bcc substitutional alloys) such groups are stabilized by a large relatively temperature independent stress component of the Critical Resolved Shear Stress, τ_{Si} (also known as friction stress). This corresponds to the plateau region in the Critical Resolved Shear Stress versus Temperature Plot (see Figs. 4,5).

τ_{Si} makes cross-slip more difficult than in pure Iron. As a result narrow slip bands are formed approximately along the Maximum Resolved Shear Stress plane. This athermal component of the flow stress makes it difficult for the dislocations to move out of the original slip plane by cross-slip, i.e. in effect it causes them to end up closer together, the minimum distance for stability being [31]

$$Xo = \frac{Gb}{2\pi \tau_{Si}}$$

where G is the shear modulus and b the magnitude of the Burgers Vector.

There is a large local density of moving dislocations in these bands, which is sufficient to accommodate the plastic deformation at an applied strain rate.

At low enough temperatures condition (a) is not

fulfilled and consequently slip bands are not formed. The transition between the two regimes is observed in Fe 1 wt % Si at 113K. At this temperature condition (a) is only partially fulfilled. As a result of the decrease in non-screw mobility as well as that of the screw, various slip directions are active. Absolute values of the dislocation mobility are small however, and the flow stress for a given strain rate is high. The criterion for necking ($\frac{d\tau}{d\varepsilon} = 0$, the so called Considère criterion [34]) may then be fulfilled at quite an early stage in the deformation.

1.4 Electron Microscopy

1.4.1 Pure Iron

Two types of dislocation structures have been observed in the two temperature regimes [20][35][36][37].

At relatively high temperatures ($T>T_t$) structures similar to those observed in Fcc metals are observed;- isolated clusters of primary edge dipoles in Stage I, and complex tangles of primary and secondary dislocations linking up into a loose cellular structure in Stage III.

Observations made by Libovicky [35] showed that the ratio of primary to secondary dislocation in Stage I is 100:1, whilst in Stage III it is 1:1.

In contrast, one observes uniform distributions of long screw dislocations at lower temperatures, which often contain many jogs and are accompanied by an appreciable

density of small loop debris.

Dislocation flexibility near obstacles is also very different in the two regimes, with screw dislocations moving as rigid strings at low temperatures and highly curved dislocation loops forming at high temperatures.

1.4.2 Iron Silicon Alloys

Predominantly screw configurations, with screws containing many jogs and the presence of much loop debris, have been observed in Fe 3 wt % Si at Room Temperature ([5],[6],[7],[8],[38]). The structure resembles that obtained at temperatures in the low temperature regime in Iron.

However, typical high temperature regime structures were found in Fe 0.9 wt % Si crystals by (for example) Libovicky [35] at 295K. He showed that in Stage I dense bundles of primary edge dipoles and multipoles were found situated parallel to the primary slip plane. The density of dislocations in the bundles increases till the end of Stage I. Dislocations are aligned in layers parallel to the trace of the primary slip plane. The density of secondary dislocations is much less (two orders of magnitude lower) than that of primaries and does not increase substantially during Stage I.

The transition from Stage I to Stage III is characterized by a substantially increased activity of secondary dislocation sources. As a result, dislocation sheets composed of both primary and secondary dislocations

start to form.

In Stage III the dislocation arrangement is composed predominantly of dislocation sheets, consisting of both primary and secondary dislocations. The density of secondary dislocations between neighbouring sheets alternates successively between high and low value. The primary dislocations can freely glide in areas between these sheets where the density of secondary dislocations is low. In these places, distinct slip bands are formed on the surface.

It was found that the spacing between slip bands remained constant (see Section 1.2) during Stage III. The lattice rotation alternated by successive crossing of the sheets. This was understood as being due to the excess of dislocations of one or other sign in the even or odd sheets.

1.4.3 Interpretation

In pure Iron the separation between T_t and T_c is around 100K (see section 1.2.3). The corresponding temperature gap in Iron Silicon alloys increases with Silicon content, so that an extension of the transition range between the high and low temperature regimes is anticipated. For example at room temperature in Fe 3 wt % Si one is in the region between T_t and T_c (Fe 3 wt % Si T_c = 550K, T_t = 113K). From the observations described above it appears that this temperature is low enough for the dislocation configuration characteristic

of the low temperature regime in Iron to exist. Evidently this is in direct contradiction of the stress-strain curve results (Section 1.2).

The behaviour of screw dislocations under stress was treated by Louchet and coworkers [39] in Niobium, Molybdenum and α-Iron in both temperature regimes. A summary of this approach will now be presented.

Obstacles likely to be encountered by dislocations would include forest dislocations, jogs and superjogs.

1.4.4 Low Temperature

When a moving dislocation meets a forest tree it can either

(i) Cut through it via a partially thermally activated process in the following way;- the screw becomes progressively more bent in the region close to the obstacle. The remaining screw segment still moves on rigidly between the obstacles. The obstacle is overcome before the equilibrium curved shape is attained, when the screw dislocation has passed a certain critical distance X_c beyond the obstacle. Local interaction of dislocations with localized obstacles which do not stop them, means that the local curvature near the obstacle can be attributed to an accumulation of double links.

or (ii) interact with it to form a junction dislocation (an example of such an interaction is shown in schematic form in Fig. 9).

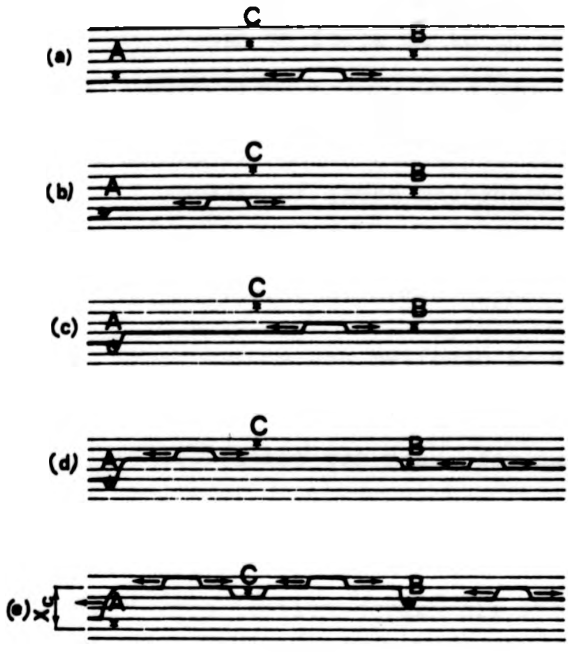

Fig. 8 Advance of a screw dislocation via the creation of double kinks which accumulate on localized obstacles (A, B, C). The obstacle A is overcome at (e), when the dislocation has advanced by Xc (after Louchet [40])

Fig. 9 An example of a reaction between two screw dislocations of Burgers vectors $\frac{a}{2}$ [111] and $\frac{a}{2}$ [$\bar{1}$11], resulting in this case in the formation of a segment of screw dislocation with Burgers vector [011]; (after Louchet [40])

On the other hand, if the dislocation meets an obstacle strong enough to force it to go round it, then multiplication mechanisms occur, when cross-slip of screw segments is involved. Alternatively an Orowan loop is left behind. A summary of these mechanisms was reported by Humphreys and Martin [41], in their electron microscope study of plastically deformed Copper crystals.

Similar observations can be found in a later publication [42](see also [43]). The Orowan mechanism, [44] whereby a dislocation can pass, for example, a precipitate, without shearing it is shown in Fig. 10(a). The alternative mechanisms, originally proposed by Hirsch [45], whereby multiplication occurs are shown schematically in Figs. 10(b), (c) and (d). The dislocation is considered

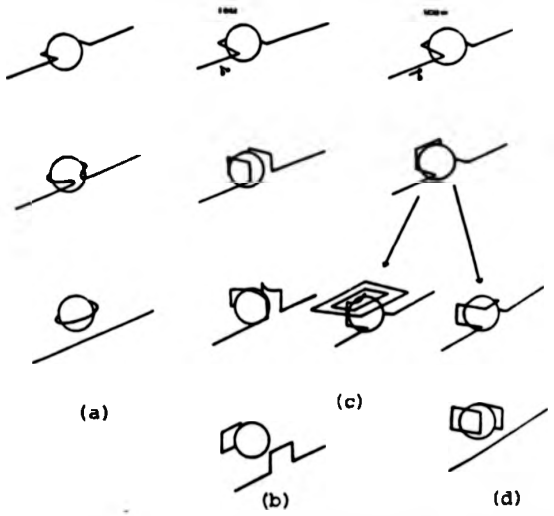

Fig. 10 Interaction of a dislocation with (for example) a precipitate (a) after Orowan ([43]), (b), (c), (d) after Hirsch ([44])

to cross-slip at the pinning point (for example a precipitate), which, in the case of an edge dislocation (10(b)), leaves a prismatic loop, whilst screw dislocations may or may not leave prismatic loops (10(c) and (d)).

Further interaction of edge dislocations with the prismatic loops formed in this way can lead to the formation of further loops [41] (see Fig. 11).

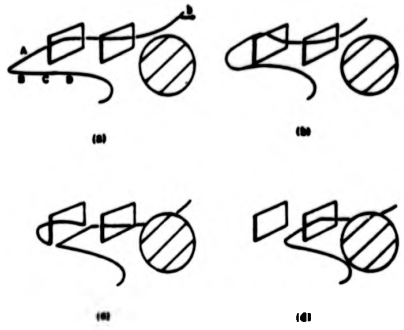

Fig. 11 Propagation of the loop forming mechanism (after [41])

An insight into the interaction to be expected between the screw BCD and the loop may be obtained from the calculation of F. Kroupa ([46]). He considered the case of a screw dislocation approaching an infinitesimal circular loop. It was calculated [41] that the force on an element of the screw at C is zero, whereas at B and D there are forces of opposite sign acting in directions tangential to the loop. Furthermore, it was shown that the force at C remains zero as the dislocation approaches the loop more closely, and the elements BC and CD of the loop bow out in the slip plane as shown in Fig 11(b). The gliding dislocation unites with part of the loop

(as shown schematically in Figs. 11(c) and (d)), with the net result that the gliding dislocation is moved forward through one loop with no change in dislocation structure. This process is then repeated until the dislocation is at the pinning point, when it cross-slips as in Fig. 10(b) leaving a new prismatic loop.

The cross-slip mechanism, produces large jogs in the vicinity of the pinning point. These jogs will in general take up low energy configurations on the $(1\bar{1}1)$ cross glide plane, and will be glissile [47]. These jogs can then further interact with other moving dislocations, leading to the formation of dipoles [41] (see Fig. 12).

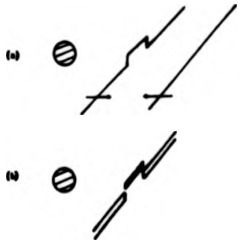

Fig. 12 Interaction of a jogged dislocation with a moving dislocation, (after [41])

Furthermore an edge dislocation can interact with a prismatic loop [48](see Fig. 13).

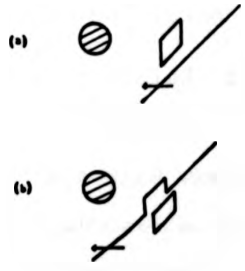

Fig. 13 Interaction of an edge dislocation with a prismatic loop (after [48])

Similar interaction of a screw dislocation with a row of prismatic loops can lead to the formation of a helical dislocation (this has also been reported in reverse in an Al-Cu-Mg alloy [49]), see Fig. 14.

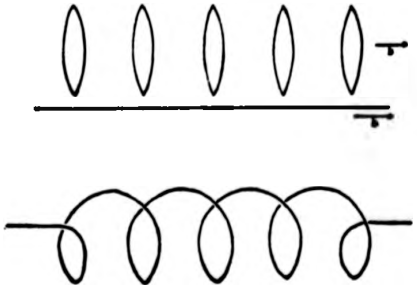

Fig. 14 Interaction of a screw dislocation with a row of prismatic loops (after [41])

In the case of bcc metals at low temperatures, pinning which is strong enough to evoke multiplication mechanisms, can be provided by junction dislocations and superjogs (formed in some cases by cross-slip during cutting). For these two types of obstacles there are two different types of associated dislocation sources. Those associated with superjogs can be called 'wandering sources', as the pinning point can glide along the dislocation. Those associated with junction dislocations can be called 'fixed sources'.

The so called 'fixed sources' can be either slow or rapid. Fig. 15 shows schematically the functioning of a slow source where the anchorage is provided by a forest dislocation. Figure 16 shows the functioning of a rapid fixed source. Fixed sources have been observed in Iron (75K) and Molybdenum (300K) [40].

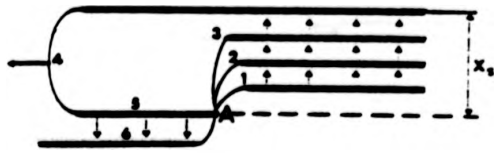

Fig. 15 Slow, fixed source mechanism, (after Louchet [40])

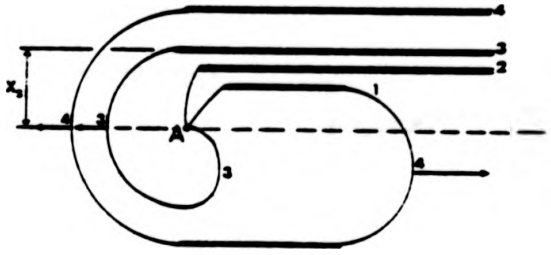

Fig. 16 Rapid, fixed source mechanism, (after Louchet [40])

In the case of the wandering source, whilst the superjog itself can move along the screw dislocation, the dislocation can continue to move on both sides of the superjog, via the nucleation and propagation of double kinks. Following Louchet ([40] pp54), if the superjog moves towards the right, it will be followed by kinks approaching from the left, and will encounter kinks created on the right hand side travelling in the opposite sense (see Fig. 17). The accumulation of these kinks on the superjog will produce, what is in effect a configuration which is glissile on its slip cylinder, but which will experience a resultant force which decreases

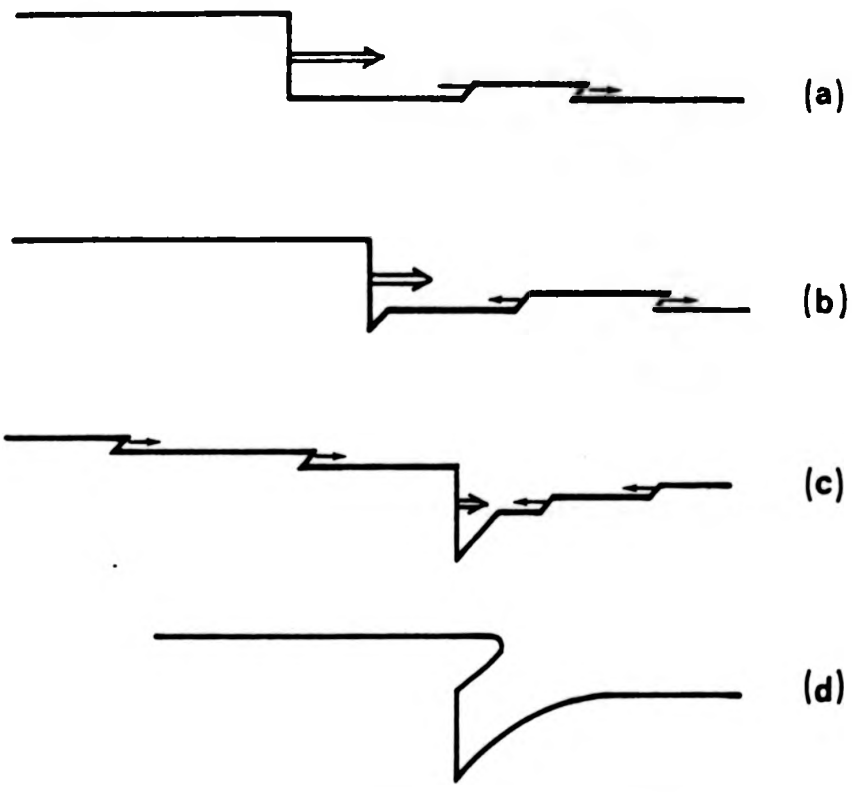

Fig. 17 Stabilization of a superjog by kink accumulation (the movement of the superjog is indicated by the double arrow), after [40]

with increasing kink accumulation. The configuration will eventually become anchored. The anchoring point will encounter jogs coming from both sides, so that the dislocation advances on both sides of the superjog.

When the critical distance X_c is attained, an open loop will be formed. This process can then be repeated. The anchoring point will move in a <111> direction between each such operation. Wandering sources have

been observed by Louchet [40] in Niobium between 100 and 300K, and in Iron irradiated at 77K. They have also been observed at room temperature in Iron 3 wt % Silicon by Furubayashi ([7]).

A slightly different mechanism was also observed in Niobium by Louchet, whereby recombination of the two dislocation segments after formation of the open loop, creates a closed loop.

In all these cases, the limiting factor in the deformation is the lattice friction stress of a screw dislocation.

1.4.5 High Temperatures

With increasing temperature X_c increases. At high temperatures, the bowing out of a mixed segment of dislocation, due to the accumulation of kinks reduces the length of the screw part to zero (the radius of curvature of the mixed segment depends on stress i.e. on temperature, as $R \sim \frac{Gb}{\tau(T)}$). This actually means that the velocities of screw and non screw dislocations coincide, i.e. the lattice friction stress of dislocations of all directions is small, very much like in close packed metals. Dislocations generally become more flexible and shapes at unpinning are close to the equilibrium curved shape. The deformation becomes very heterogeneous on the scale of High Voltage Electron Microscopy (HVEM). [18]

Under these conditions, the plastic deformation is

controlled by the interaction of dislocations with localized obstacles.

1.4.6 Transition Region

At low temperatures, the yield stress depends strongly on temperature varying from about 10^{-2} G (where G is the shear modulus) at 0°K to about 10^{-4} G above the transition temperature. The transition can be associated with the observed change in dislocation flexibility which is obviously related to the relative screw and non-screw dislocation mobilities.

One can be said to enter into the high temperature regime when the length of the screw part of the dislocation just before unpinning is reduced to zero. This is actually achieved when the frictional stress on screw dislocations is as low as that on mixed dislocations.

In the low temperature regime, the screw dislocations move continuously between obstacles without stopping. In the high temperature regime, the lengths of screw dislocation segments reduce to zero before unpinning, and the dislocation segments may stop between the obstacles. These localized obstacles are then the controlling factor in the deformation, as for example in Fcc metals.

This argument implies that the transition temperature should decrease when the density and strength of obstacles increases or when the friction stress on non-screw dislocations increases relative to that on screw dislocations.

1.5 Slip Geometry

It has been well documented (for example [21], [22], [50], [51]) that slip in fcc metals is generally crystallographic. This stems from the fact that the screw dislocation in the fcc lattice is dissociated, making cross-slip difficult. In pure bcc metals however, slip is generally found to be non crystallographic (approximately along the maximum resolved shear stress (MRSS) planes), due to the relative ease of cross-slip, except at very low temperatures.

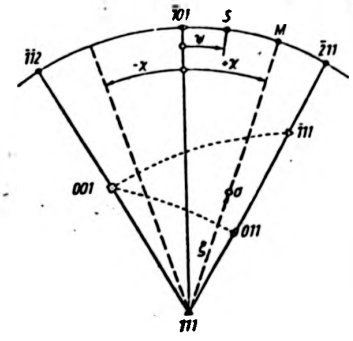

Fig. 18 [111] stereographic projection; the active Burgers vector is situated in the centre of the projection; σ direction of principal stress (longitudinal axis of specimen); M pole of plane with MRSS; S pole of observed slip plane. The angles χ and Ψ are positive in the right half, and negative in the left half of the plotted region

The orientation dependence of slip in bcc metals is found to be sensitive to solute content, strain rate, temperature, and also whether the deformation is performed in tension or in compression. Slip tends to become crystallographic ([52], [53], [54]) at high solute content, at high strain rate and at low temperature.

Experimental results on macroscopic slip planes are usually expressed in the form of $\psi - \chi$ curves [55], where

Ψ and χ are illustrated in Fig. 18.

1.5.1 Pure Iron

The ease with which slip occurs in Iron depends on the sense and direction of the applied stress ([57], [58], [59], [60]). These studies have also shown that the CRSS Law (i.e. that slip begins at a critical value of the shear stress on a slip plane) does not appear to be obeyed in Iron, especially at low temperature (also [56]).

Asymmetry of slip in Iron has been observed in various ways. For example, different slip planes may operate in crystals of similar orientation, depending on whether they are deformed in tension or compression [57], [58]. This sort of observation was first made by G.I. Taylor [55], who experimentally found different slip planes on single crystals of β-brass with positive and negative χ angles after deformation by tension and compression. The CRSS for slip on {112}<111> has also been seen to differ in tension and compression [55], in that the CRSS in tension for slip on {112}<111> is smaller if the <111> direction corresponds to a twinning direction. Considerable asymmetry was observed at 143K, and also deviation from the CRSS law by Spitzig [56], in agreement with earlier results [59], [60].

Observations (based on the variation in intensity and waviness of slip traces) of asymmetry by Spitzig ([56]) appear to agree with what would be expected with

a change in the ease of cross-slip. This behaviour could be rationalized qualitatively on the basis of dislocation dissociation and stacking fault energies on {110} and {112} planes in bcc metals ([61], [3], [62], see section 1.7).

It is also possible ([56]) that the orientation dependence of the proportional limit, observed for Iron crystals, may have some of its affect attributable to an orientation dependence of the ease of dislocation multiplication ([36], [64], [65], [66]).

The orientations investigated by Spitzig are shown in Fig. 19.

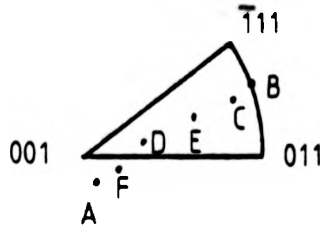

Fig. 19 Orientations investigated by Spitzig ([56])

It was found that for orientations near A, the multiplication rate is one hundred times greater than for orientations near B. Stress strain curve analysis also provides evidence to support the concept of a greater mobile dislocation density for orientations near A, since the intensity of the yield point increased continuously for orientations D to B and was entirely absent for A and F.

The high rate of work hardening observed for

orientations near [001](A,F), is also in accord with a higher rate of mobile dislocation generation for these orientations.

1.5.2 Alloys of Si in Fe

Sestak and Zarubova [67] determined slip planes on specimens of Fe 3 wt % Si and Fe 6.5 wt % Si after slow deformation ($\dot{\varepsilon} \simeq 10^{-6}$ s^{-1}) at room temperature, with the following results. For a silicon content of 3 wt %, slip occurred in specimens with orientations $\chi \sphericalangle$ < 0°, + 30 >, after deformation by compression, along the maximum resolved shear stress (MRSS) planes. The same was observed in specimens with orientations $\chi \sphericalangle$ < -30°, 0° >, after deformation by tension. After deformation by tension of specimens with $\chi \sphericalangle$ < 0°, +30°> and after deformation by compression of specimens with $\chi \sphericalangle$ < -30°, 0° >, deviations of slip planes from the MRSS planes towards the nearest {110} plane were observed.

With a higher silicon content (∿ 6.5 wt %), systematic deviations of the slip planes from the MRSS planes towards the nearest {110} plane are observed after deformation by compression on specimens with positive χ angles, and after deformation by tension on specimens with negative χ angles. On deformation by tension of specimens with $\chi \sphericalangle$ < 0°, +30° >, and by compression of specimens with $\chi \sphericalangle$ < -30°, 0° >, crystallographic slip along {110} planes occurs. It was also found that if the resolved shear stress on a {112} plane acts in the

twinning sense, the CRSS is smaller than would be the case of the resolved shear stress acted in the anti-twinning sense.

As in the case of Iron, the form of the ψ-χ curves may be predicted with fair success by models such as those of Kroupa and Vitek [68] or Duesbery [62] (see section 1-7), the difficulties encountered being as follows. The theories predict the asymmetry about $\chi=0^{\circ}$ for example, but require that this asymmetry is reversed in tension and compression. As pointed out by Sestak et al [69], this condition is satisfied in Fe Si at room temperature but not at 77K. They also suggested that the normal stress may also influence the behaviour (see also [70]). However, as pointed out by Christian [71] and Kroupa and Vitek [72], normal stress considerations cannot explain the shear asymmetry (i.e. the observed slip asymmetry cannot be explained by slip on {110} planes only, but the crystallographic asymmetry of the splitting must be introduced).

The persistence of {110} slip at low temperatures may depend on the core structure at high stresses; it may imply that a dislocation which attains a glissile configuration and moves in one sense on {110} covers a relatively large distance before it is halted again [68], or alternatively that successive short jumps of the dislocation have a high degree of correlation which keeps the dislocation in the same {110} plane.

1.6 Surface Orientation Effects

Many of the results, presented so far, illustrating the various slip geometries (excluding electron microscopy), have been obtained from specimens of cylindrical shape (i.e. bulk specimens), with only the tensile axis changing. As a result of experiments on the deformation of thin foils and of bulk specimens of Mo, Vesely ([10], [73], [74], [75]) observed that the operative slip plane was very dependent on the orientation of the plane of the foil, or the local surface orientation of the bulk specimen. He found that the operative slip plane was always such that the screw component of a dislocation loop could disappear at the surface. This characterizes the most probable slip direction as that <111> direction which makes the largest angle with the local surface normal, and the slip plane as that plane of the slip zone which is perpendicular to the surface, or most nearly perpendicular if the plane is restricted to one of a number of crystallographically possible planes. This may mean that other sources are blocked by the low mobility of the screw dislocations i.e. the mean free path of the edges is a function of the mean free path of the screws. In the initial stages of deformation often only surface sources can act, and when internal sources subsequently operate, the necessity to eliminate screws by mutual annihilation will continue to favour sources on the same systems as the initial surface sources.

Vesely suggests that the activity of a slip system is partially determined by the Schmid Factor (S) and partially by the surface orientation effect which varies as sin β_1, where β_1 is the angle between the Burgers vector and the surface normal. The relative importance of the surface factor changes with the screw mobility and hence decreases with increasing temperature and increasing stress. Thus, the contribution of any particular system to the overall strain rate will be governed by an expression of the form $V = H(T, \tau, \beta_1)\ S\ (\lambda_0, \phi_0)$, where the function H expresses the influence of the screw mobility at high temperatures, or at high strains. At fixed temperature, with increasing strain, the Schmid factor becomes more dominant and slip on a single system is observed. It is anticipated that the surface effect would be much less marked in alloys than in pure metals, as the ratio of screw to edge mobility changes, leading to sharper yielding. Vesely was able to verify his suggestion by making qualitative estimates of the relative strengths of surface slip markings on Mo.

Miltat and Bowen [32] attempted to investigate any effect of surface orientation on slip system selection in Fe 3.5 wt % Si single crystals using X-ray topographic (conventional and white beam synchrotron) techniques. Two types of samples were studied; one where the primary Burgers vector is at a small angle to the surface, and the other where the primary Burgers vector is at a fairly large angle to the surface. The former orientation

is favourable for the easy escape of low mobility screw dislocations; slip systems were, in this case, found tc be as expected from MRSS predictions. However in the second orientation, which is less favourable for the escape of screw segments, the observed slip systems were not so easily identifiable. It was concluded that another Burgers vector may have been brought into play.

1.7 Low Screw Mobility

It is intended in this section to put forward theories explaining the inherently low mobility of screw dislocations in the bcc lattice. Theories designed for pure metals will be discussed and also how these theories can be modified for the case of substitutional alloys.

According to Low and Turkalo ([5]), observations of dislocation configurations in Fe 3 wt % Si single crystals in the electron microscope revealed jogs in screw dislocations in sufficient numbers to account for their lower relative mobility. They assumed these jogs would create a drag on the screw dislocations (due to the additional work which must be expended in creating point defects for very small jogs or in creating the trails of edge dislocations for large jogs). This model, whereby a moving screw dislocation becomes jogged by cross-slip, was proposed by Johnston and Gilman ([76] from an etch pit study of dislocations in Li F crystals).

It is a modification of the double cross-slip mechanism proposed by Koehler [77] and Low and Guard [78]. Depending on their size, the jogs may cause cusps with edge dislocation trails, cusps with no observable trails, or may act as pinning points for single ended sources of new dislocations.

Low and Guard [78] suggested that screw dislocations in Fe 3 wt % Si move in the direction of the maximum shear stress at any point rather than having their motion confined to crystallographic planes. According to Low and Turkalo ([5]), if this conclusion is accepted, then jogging of the screws is to be expected in any deformation in which the plane of the maximum shear stress is not precisely aligned with the crystallographic glide plane. The screw dislocations will, on average, lie in the plane of maximum shear stress, following it by jogging from one close packed plane to the next.

However, Foxall and Statham [79] pointed out that the dislocation structure can also be explained by a simple model based on mutual interaction of glide loops. Neighbouring screws annihilate to leave very long jogs, and the loop shape at higher dislocation densities may then have almost any form.

A number of attempts have been made to explain the lattice friction stress experienced by screw dislocations. The original models of the screw dislocation core in bcc metals were based on a concept originally proposed by Hirsch ([80]) that this defect could be extended in a

non-planar sessile configuration, in contrast to the planar glissile cores expected in close packed lattices. Proposed models based on this concept (the so called extended core or elastic models; [81], [82], [83], [84], [62], [68], [85]) were able, with reasonable success to explain for example the low mobility of screw dislocations, slip geometry and the temperature dependence of the CRSS.

In these extended core (elastic) models, the dislocation core dissociates on three {110} planes or two {112} planes, or in more complex ways. In order that the dislocation may move from one atomic row to the next, it must recombine along a critical length and bow out until it reaches its critical position of instability ([86], see Fig. 20. and Fig. 21).

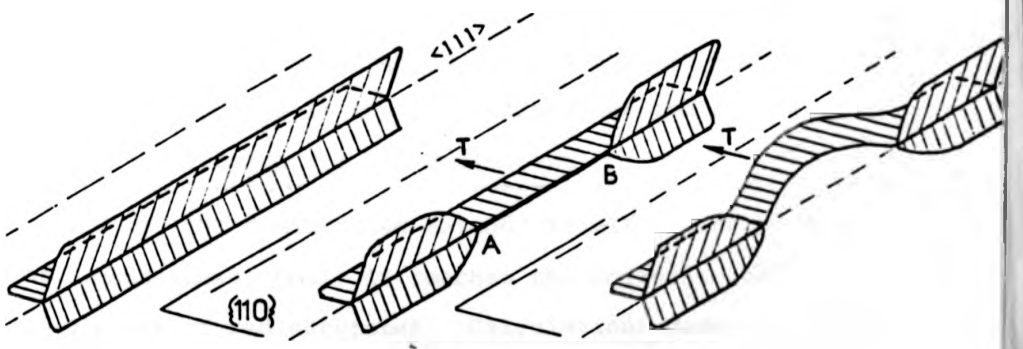

Fig. 20 Model for motion of dislocation dissociated on {110} planes, (after [87])

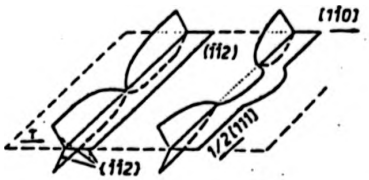

Fig. 21 Similar model for stress assisted, thermally activated glide of screw dislocation dissociated on {112} planes (after [86])

This local change from sessile to glissile configuration can, according to the extended core models, be treated as thermally activated constriction. This stress assisted thermally activated movement of sessile screw dislocations is capable of giving rise to the observed temperature dependence of the yield stress (e.g. [20]). Furthermore, the model illustrated schematically in Fig. 21, suggests that the movements of a sessile screw dislocation under an applied stress for example on the $(\bar{1}\bar{1}2)$ plane in the $[1\bar{1}0]$ direction and in the opposite direction are not equivalent.

Thus, the dislocation extends itself by the propagation of double kinks, until it reaches the adjacent atomic row, where it redissociates. Calculations based on these models, showed that the extent of the dissociated core was of the order of several Burgers vectors ($b = \frac{a}{2}\langle 111\rangle$), with associated fault energies of the order of hundreds of ergs cm^{-2} ([90], [91], [85]).

However, aspects of slip geometry such as anomalous {110} crystallographic slip in Nb ([12]); the presence of slip on multiple systems in the early stages of deformation of Mo ([10], [73]); the very large slip asymmetry and striking temperature dependence of slip geometry in bcc alloys (for example [88], [89]), cannot be conveniently explained within the framework of these theories.

In the extended core models, the assumption of the presence of stable stacking faults in bcc metals, analagous to those in close packed structures was implicit. However, atomistic calculations ([92], [93], [94]) show that such stable stacking faults are unlikely in bcc metals. As pointed out by Duesbery et al ([95], see also [94], [96]), the core theories apply the methods of linear continuum elasticity theory to partial dislocation separations of the order of the lattice parameter (the scale of the dissociation is too small to be able to talk in terms of partial dislocations and associated stacking faults, as defined by linear elasticity theory). The aforementioned assumption, was recognized by the relevant authors as being justified only as an extrapolation.

Observation of wide faults in W, Fe and Mo-Re alloys ([97], [98], [99]) by field ion microscopy (but not by other techniques) can be explained on the basis of the special conditions existing in the field ion microscope, as pointed out by Christian ([1], also [100]).

Treatment of the core which takes into account the discrete nature of the lattice is clearly more appropriate.

Many such calculations have been made ([101], [102], [103], [104], [105], [106], [107]). Of these, Vitek et al ([106]) made calculations of the atomic structure of a screw dislocation using a variety of central force interactions. It was found that there are two metastable configurations, and these correspond to the centre of the dislocation lying along the left and right handed three fold screw axes of symmetry, respectively see Fig. 22 after [1] see also [10].

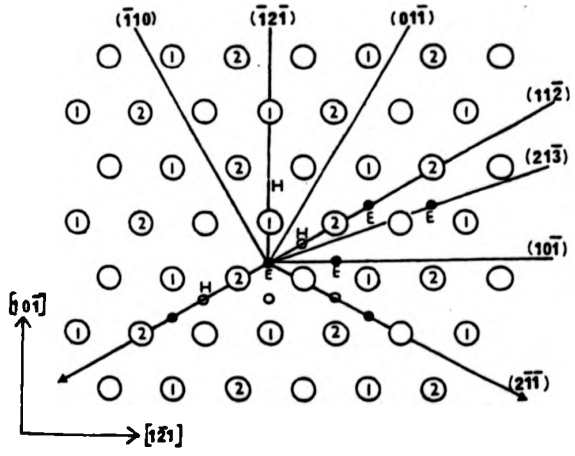

Fig. 22 Projection of bcc structure along [111] (after [1])

The displacements near the centre of the dislocation are mainly concentrated on three {110} planes and are asymmetric, in such a way that for a given {110} plane, there are large displacements on only one side of the core.

Vitek's calculations indicate that the field is made up of large monotonically decreasing displacements on three {110} planes radiating from the centre, plus stacking

faults 1-2b wide on three {211} planes, displaced outwards from the centre. This kind of description provides a link with the older stacking fault models, and confirms that the structure is three dimensional and probably sessile.

Due to its rather unique core structure, the <111>/2 screw dislocations in the bcc lattice experience a high Peierls stress ([95], [106], [109] - Peierls stress is defined as the stress required to lift a dislocation out of its Peierls valley i.e. an intrinsic lattice friction stress due solely to the dislocation core structure).

Evidently an important step is to investigate the behaviour of the dislocation core in the presence of an external stress in order to calculate the Peierls stress and slip geometry.

Values obtained by computer simulations of the dislocation cores under external stress ([110], [111]) show that the Peierls stress of screw dislocations is 6 to 20 times bigger than that of non screw dislocations (depending on the potential used). A difference for the motion of a screw dislocation in the forward and reverse directions on certain planes (for example {211}) was also found.

As a result of the high Peierls stress of screw dislocations, their long range motion at finite temperatures is thermally assisted, via the formation of kink pairs, which transfer the dislocation from one Peierls valley to the next along {110} planes. Neighbouring Peierls

valleys lie on three intersecting {110} planes $\frac{a\sqrt{2}}{3}$ apart, so that the moving screw dislocation may choose, in any of its equilibrium positions between three elementary steps along intersecting {110} planes, according to the local stress distribution. The thermally activated elementary glide steps are in fact cross-slip processes. The ways in which screw dislocations can move in the bcc lattice were considered in more detail by Duesbery et al ([95]).

Calculations made for a model Sodium lattice at OK, by Basinski et al ([109]), [112]), show that the critical shear stress for screw dislocations is much higher in the bcc phase than in close packed structures.

Similarly, Gehlen ([113]) made calculations of the Peierls stress for kink motion along a screw dislocation. This Peierls stress will only be important if one can neglect the energy of formation of kinks. This may be the case for internal friction or microdeformation ([114], [115]) when the grown in kinks move along the screw dislocation, or at high temperatures, when the kinks form very easily.

However, since it has been established experimentally that at low temperatures (below room temperature) edge dislocations have a greater mobility than screw dislocations, it is likely that the same will then apply to kinks of edge character. Kink formation energy therefore, will be dominant for screw dislocation motion. At very low

temperatures (T → OK) the work will have to be done almost entirely by the external stress, and the screw motion will be governed essentially by the Peierls stress for straight dislocations.

To obtain a model for solution hardening in bcc alloys the motion of screw dislocations by the formation of kink pairs and propagation of kinks in the presence of solute atoms have to be considered. Although there is no complete theoretical description of the screw dislocation mobility based on this process, even in the absence of solute atoms, some efforts have been expended in this direction.

In the available theories, one assumed that solute atoms affect; the formation of kink pairs and impede the sidewise motion of kinks ([116]); act as weak obstacles and shorten the effective length of screw segments ([117]); or reduce the activation enthalpy for the nucleation of kink pairs ([118], [119]). A recent theory attributes the Snoek-Koster relaxation to the formation of kink pairs in screw dislocations in the presence of solute atoms ([120]).

Another contribution to the theory of low temperature deformation in bcc metals consists in a combination of the sessile-glissile transformation theory and the pinning effect of interstitial impurities on dislocations ([121]).

1.8 Nucleation

This section is intended to be a brief review of basic

slip nucleation processes in crystals. It should help to bring into context observations of slip nucleation processes reported in this study. Mechanisms relevant to results reported will be discussed.

1.8.1 Nucleation - Theoretical Approach in a Perfect Crystal (after Cottrell [122])

A nucleus of slip is the smallest region of slip that can be made to grow by the action of the applied stress alone. Any region smaller than this will slip back into its original and perfect configuration once the thermal fluctuation that caused the region to slip has passed. The smallest conceivable nucleus is a disc-shaped patch of slip on a slip plane, bounded by a single dislocation. The segments of dislocation on opposite sides of the perimeter are of opposite signs, and so their stress fields will cancel beyond a distance of the order of magnitude of the radius of the disc. Then, the energy per unit length of this dislocation line will be approximately

$$\frac{Gb^2}{4\pi} \log \left(\frac{r}{r_0}\right)$$

where G is the shear modulus, b is the Burgers vector of the dislocation, r = radius of the loop, r_0 = radius of a hole drilled out along the centre of the dislocation - (thus is necessary from the Boundary conditions i.e. the stresses go to infinity as $r \to 0$). The increase in energy when this element of slip takes place i.e. the energy necessary to produce by glide, a loop of radius r,

is

$$U = 2\pi r \left(\frac{Gb^2}{4\pi}\right) \log \left(\frac{r}{r_0}\right) - \pi r^2 \tau b$$

the latter term being the work done by an applied shear stress τ.

This energy has a maximum value

$$U_c = \frac{Gb^2 r_c}{4\pi} \left[\log \left(\frac{r_c}{r_0}\right) - 1\right]$$

when the radius of the disc is

$$r_c = \frac{Gb}{4\pi\sigma} \left[\log \left(\frac{r_c}{r_0}\right) + 1\right]$$

The energy begins to decrease as r increases beyond r_c, which is the critical radius of the disc. If the nucleus is of this size it can then grow by the action of the applied stress above.

Thus U_c is the activation energy for nucleating slip in a perfect lattice.

Assuming $r_0 = 26 \quad b \sim 2.5 \times 10^{-8}$cm $\quad Gb^3 = 1$eV

critical radius r_c (cm)	10^{-6}	10^{-5}	10^{-4}	10^{-3}
applied stress	G/120	G/800	G/6000	G/45000
activation energy(eV)	20	450	6500	90000

TABLE 1

The probability of a thermal fluctuation of energy ε^* taking place is proportional to $\exp(-\varepsilon^*/kT)$. At room temperature $kt \simeq 1/40$ eV so that only those fluctuations for which ε^* is less than 1-2 eV have a reasonable chance of occurring. In view of the energies presented in Table 1

above, this means that slip cannot occur unless the stress exceeds G/100 i.e. approaches the theoretical shear strength ($\sim G/2\pi$), if thermal fluctuations are going to help an applied stress to form a slip nucleus.

So, although the stresses necessary to move a dislocation are small, and thus the values of critical shear stress actually observed in metal crystals for example ($\sim 10^{-4}G$) can be explained, the stresses needed to create a dislocation in a perfect lattice approach the theoretical shear strength.

Adequate explanation of the situation can be achieved if one considers crystals which are not perfect (as is often the case) before deformation. They may for example contain dislocations (which may be residual from the growth process) or precipitates formed by the coalescence of impurity (again possibly formed during the growth process).

Grown in dislocations can become sources of dislocations, if the conditions are correct, i.e. a section of the dislocation may be in an active slip plane, or a segment may cross-slip leaving a jog which could then act as a pinning point for a single or double ended Frank Read source, or the dislocation may be able to rotate around its slip cylinder until conditions become favourable for glide.

One requirement for the operation of the Frank Read mechanism is that the points of emergence should be anchored firmly enough to prevent them from moving under

an applied stress. This condition may be fulfilled if a segment of a dislocation simply does not lie on a close packed plane.

Another possibility arises when the dislocation is prismatic loop. Consider a loop such as EFGH. Apply a shear stress in the slip direction to the top-bottom faces [N.B. the direction of easy motion of an edge dislocation is restricted to the slip direction, so that the slip surface which it generates is cylindrical, with the slip direction for its axis], of the crystal.

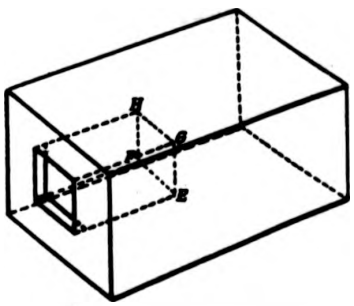

Fig. 23 Schematic diagram of a prismatic dislocation loop in a crystal

Fig. 24 Glide of a prismatic loop under shear stress (after [122])

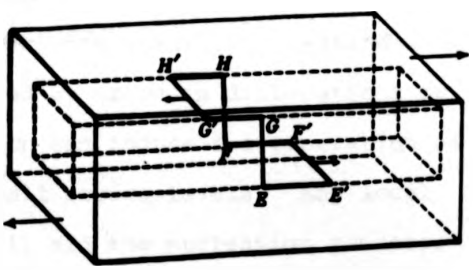

If the dislocation moves as a whole, these faces do not move relative to each other and the shearing forces do not work. Thus the total force on the dislocation is

zero. On the other hand, individual segments must try to move as shown in Figs. 23 and 24. The segment EF is a positive edge and moves towards E'F', while the negative edge along GH moves towards G'H'. The lines EG and HF are not acted on directly by the shear stress and, if these remain fixed, new segments EE', FF', GG' and HH' would be formed. These segments lie along the slip direction and are therefore of a screw type.

This sort of mechanism can provide the type of anchoring required by Frank Read sources.

Another possible mechanism (due to Koehler [77]) can arise from cross-slip of a screw segment from its slip plane. If the segment then cross-slips back (under the action of an applied stress) into the slip plane on a different level, then the cross-slipped segment can act as a pinning point. This is the so-called double cross-slip mechanism.

1.8.2 Effects of Stress Concentration (after [123])

As discussed earlier, the special nucleation sites necessary can be provided by grown in dislocations or other imperfections which can induce the generation of dislocation loops at small stress levels. Any local stress concentration will aid the nucleation process.

It is well known that when an indenter presses strongly enough on the surface of a crystal, it creates an indent by introducing loops of edge dislocations ([124], [125]).

The loops and helices produced are not pinned by impurity clouds or precipitates if produced at low temperatures. If their Peierls-Nabarro force is not too large, they are able to glide. Under a suitable applied stress, any part of such loops or helices can act as a Frank-Read source and multiply into a slip band (see Section 1.8.1) by cross-slipping out of their glide cylinder ([126]). Calculation shows that, Frank-Read sources are slightly more easily nucleated from helices than from prismatic loops (see [127]).

Similar loops and helices are produced inside crystals containing small glass spheres ([128]) or precipitates ([129]), [130], [131], see Fig 25).

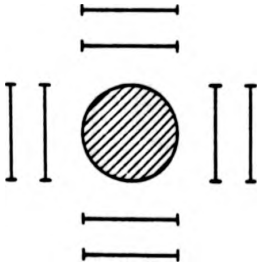

Fig. 25 Volume indentation by a larger precipitate (after [123])

When the rate of growth of a precipitate particle exceeds the rate at which the material of the matrix can be removed from the interface by the condensation of vacant lattice sites, a compressive stress field is established. This can be relaxed by the formation of positive prismatic dislocations which glide away from the interface between the particle and matrix along slip cylinders ([132], [133], [134], [135]).

Loops can also be produced around precipitates in crystals submitted to not very large external stresses, due to a difference in elastic constants. A stress concentration occurs for both softer and harder precipitates but the two cases are somewhat different.

For a precipitate that has higher elastic constants than the matrix, the stress concentration produced when the matrix is under shear is highest at the surface of contact between the precipitate and the matrix. This can be large enough for the precipitate to punch prismatic dislocation loops into the matrix so as to relieve the local stresses, (see Fig. 26).

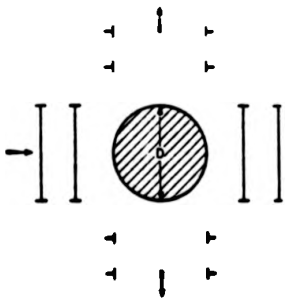

Fig. 26 Volume indentation by a harder precipitate (after [123])

For a suitable precipitate the external stress required for punching is very small. Such a process is common in fairly brittle materials ([136], [137).

No such surface punching occurs around a precipitate with lower elastic constants than the matrix. There is however a more diffuse stress concentration in the volume of the matrix, that is especially strong when the precipitate has fairly sharp edges. At distances of the

order of R of an edge with radius of curvature R, the stress concentration should be at most, about the same as for a Griffith crack with a size equal to the diameter D of the precipitate, and a tip of radius R.

Dislocation loops are much less easily formed by soft than by hard precipitates.

Surface steps and edges provide the same type of stress concentration as cavities ([138]).

CHAPTER 2

Apparatus

APPARATUS

2.1 Precision Laue Camera

Crystal orientation was determined by the back reflection Laue method. For this purpose a precision Laue Camera was designed ([139]). A photograph of the camera is presented in Fig. 27. The camera is totally shielded to satisfy modern radiation safety standards; all the adjustments can be made externally and it sits on a simple optical bench for permanent alignment. The collimator is a hypodermic needle which makes its own hole in the film. The film is covered with black paper on one side only; four 1mm apertures in the cassette backplate are accurately referenced to the hypodermic hole and give small black dots symmetric about the centre of the beam. Joining the dots in pairs gives a cross-centred on the beam and accurately aligned with the goniometer horizontal and vertical. An externally-controlled rod can be lowered to put a small fluorescent screen in the beam for alignment (observed through the PVC or glass side pieces - note that Perspex (plexiglass) does not stop scattered radiation adequately); the rod also carries a needle with a soft fibre tip that can be trimmed at 30mm from the film to set the specimen-film distance. This camera has proved very satisfactory in use and gives a precision of about 0.5° with graphical interpretation and about 0.1° with direct measurement on the film.

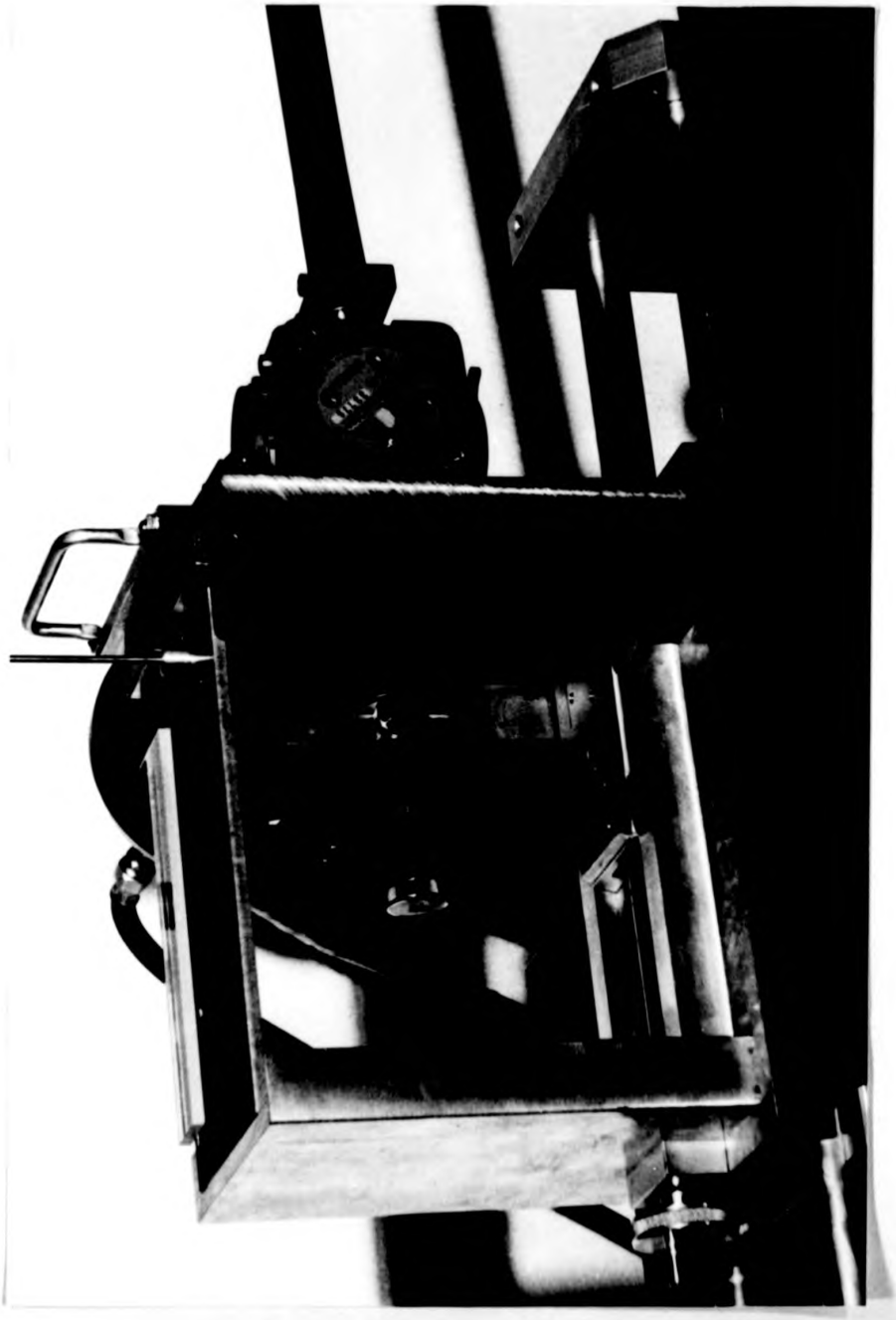

Fig. 27 Purpose built Precision Laue Camera ([139])

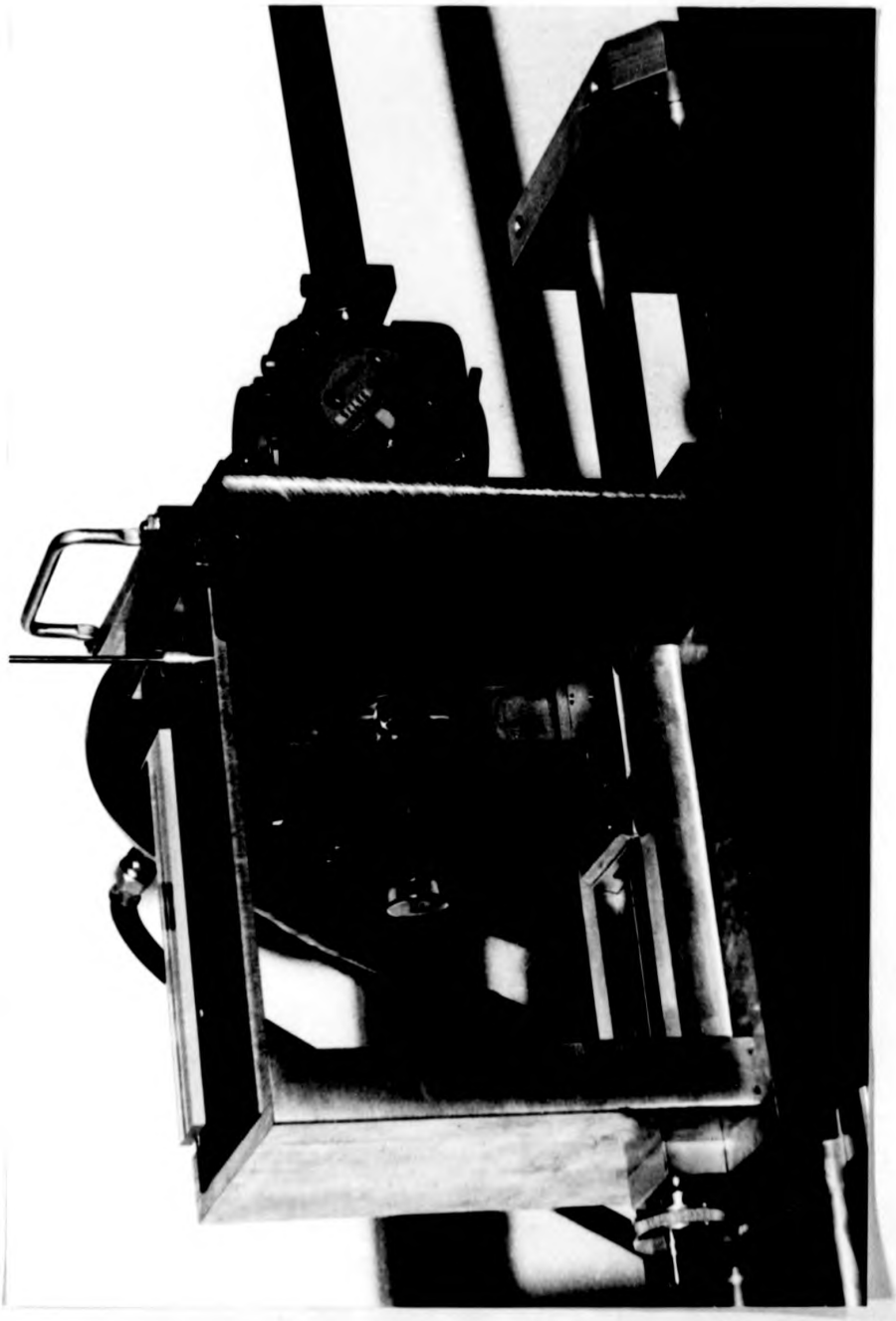

Fig. 27 Purpose built Precision Laue Camera ([139])

2.2 Lang Cameras

Two types of Lang camera were used, a commercially manufactured model from the company C.G.R. in France, under the design of Authier and Rimsky (these cameras were used during the authors stay in Paris), and a model designed by D.K. Bowen and constructed at the University of Warwick workshop.

The author assumes familiarity with the basic technique of Lang topography. Nevertheless a schematic diagram showing all the essential components is presented. See Fig. 28.

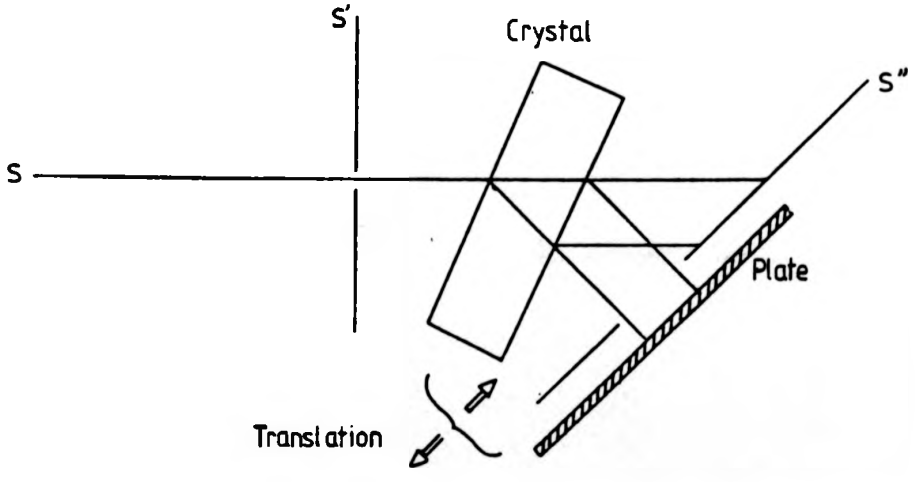

Fig. 28 The essential components of a Lang Camera; the beam from a fine focus source S is collimated by the slits S'. After diffraction from the crystal, the direct beam is stopped by the slits S". The diffracted beam is received on the plate. If the crystal and plate are translated, it is possible to image large areas of crystal.

The French model incorporated a repetitive scanning method, a clutch mechanism being employed to effect the change in direction, so that the motor drive always turned in the same sense. Although the repetitive scanning method is quite effective in 'ironing out' any inhomogeneity in the traverse slide itself, it could become very sensitive in theory, to vibrations, which could cause drift from the exact Bragg angle. Fine and coarse manual controls of both the θ and 2θ axes were easily accessible. In practice these Lang cameras worked extremely well.

On the Warwick Lang camera, (see Fig. 29) both the traverse and θ axis were driven by computer controlled stepper motors (the motors were interfaced to P.E.T. minicomputers via Besselec modules). The traverse axis

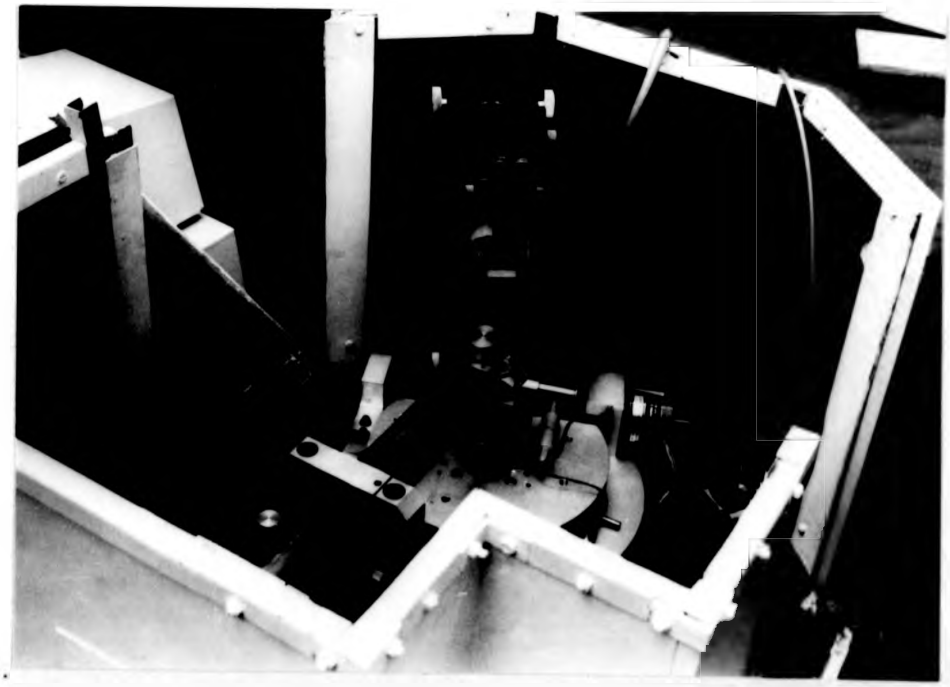

Fig. 29 The Warwick Lang Camera

The French model incorporated a repetitive scanning method, a clutch mechanism being employed to effect the change in direction, so that the motor drive always turned in the same sense. Although the repetitive scanning method is quite effective in 'ironing out' any inhomogeneity in the traverse slide itself, it could become very sensitive in theory, to vibrations, which could cause drift from the exact Bragg angle. Fine and coarse manual controls of both the θ and 2θ axes were easily accessible. In practice these Lang cameras worked extremely well.

On the Warwick Lang camera, (see Fig. 29) both the traverse and θ axis were driven by computer controlled stepper motors (the motors were interfaced to P.E.T. minicomputers via Besselec modules). The traverse axis

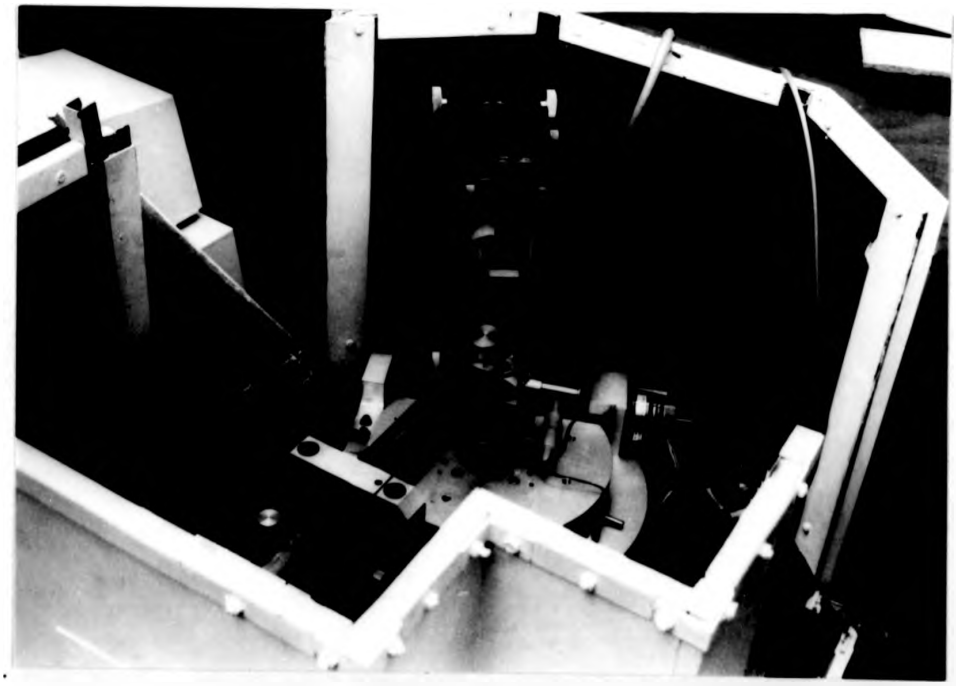

Fig. 29 The Warwick Lang Camera

itself consisted of a Schneeberger linear slide, driven by a high precision 1mm pitch lead screw. A choice between single scan and repetitive scan techniques was available.

The stepper motor driving the θ axis was coupled to a 500-1 gear box and then in turn to a 100-1 gear box connected to the actual drive shaft. This gave the required sensitivity for the finding of Bragg peaks (i.e. seconds of arc).

Large fully motorized Huber goniometers were used. The Warwick Lang camera also worked well in practice.

2.3 X-ray Generators

A variety of generators was used. Initially a Hilger and Watts microfocus set was used, then a series of Tubix, Siemens and Enraf sealed tube sets as well as an Elliot rotating anode generator.

2.4 Tensile Testing Machine

A full description of the tensile machine can be found in the literature ([140]). It is basically a soft tensile machine, which can be mounted on an X-ray camera, ideal for applying a slowly increasing stress. It is suitable for transmission or reflection topography of thin specimens that have a relatively high yield stress (5-500 MPa).

A simple 12v DC motor was used to drive the lead screw which presses on the cantilever spring providing

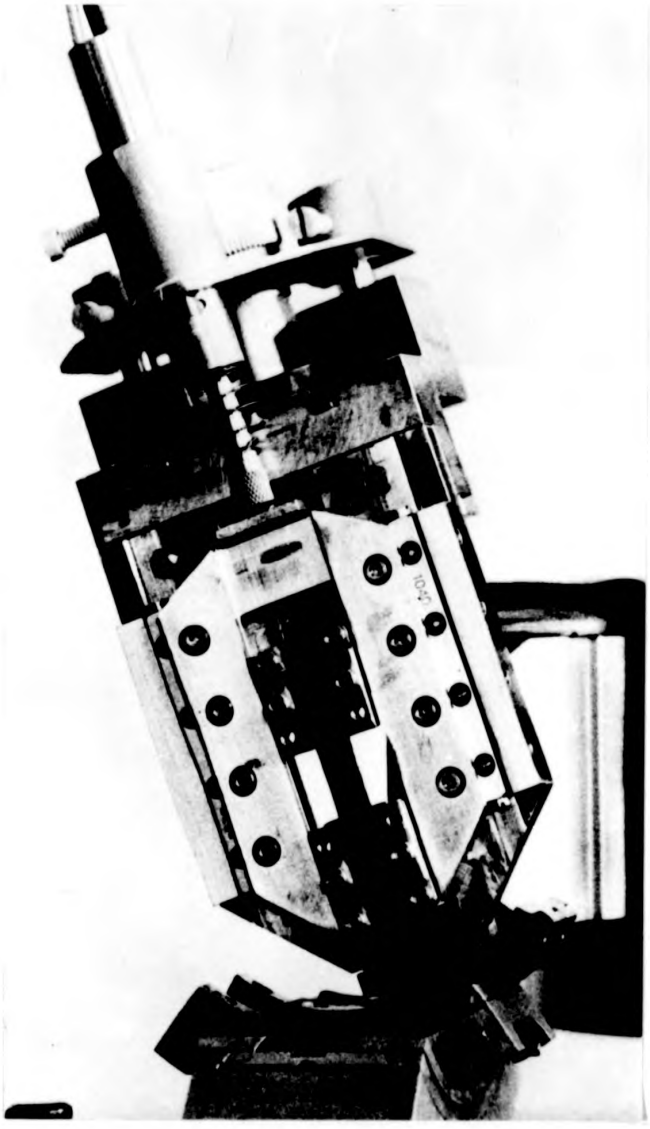

Fig. 30 The Tensile Stage mounted on a Lang Camera (after [140])

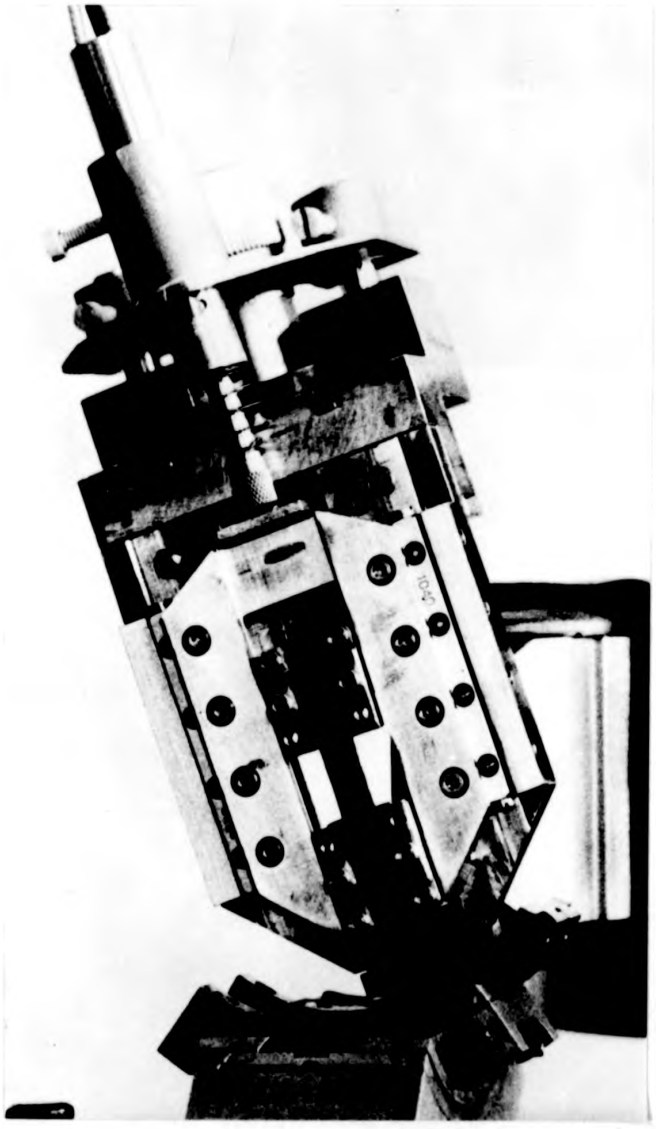

Fig. 30 The Tensile Stage mounted on a Lang Camera (after [140])

the load. Measurement of the deflection of the cantilever by a small capacitance transducer provides a measure of the force. A photograph of the stage mounted on a Lang camera is presented in Fig. 30.

2.5 Synchrotron X-ray Sources (for general reviews see [141], [142], [143])

Charged particles orbiting in circular accelerations emit synchrotron radiation into a small cone in the direction tangential to the particle motion, and symmetric to the orbit plane.

The cone angle (for that wavelength) is given by

$$\nu = \frac{M_0 c^2}{E_e}$$

where M_0 = rest mass of electron, c = velocity of light, E_e = electron energy.

This cone angle narrows with E_e and correspondingly with E.

The total emitted intensity is proportional to ([144]) γ^4 where

$$\gamma = \frac{1}{\nu} = \frac{E_e}{M_0 c^2}$$

It is possible to generate a spectrum of harmonics up to a frequency given by

$$\omega_c = \frac{3c}{2\pi R}\left(\frac{E_e}{M_0 c^2}\right)^3 = \frac{3c}{2\pi R}\gamma^3$$

or in terms of wavelength

$$\lambda_c = \frac{4\pi R}{3}\left(\frac{M_0 c^2}{E_e}\right)^3 = \left(\frac{4\pi R}{3}\right)\gamma^{-3} \cong \frac{5.59R(m)}{E_e{}^3(GeV)}$$

where R is the orbit radius of the electrons.

Since radiation from individual points on the electron path superimpose, the angle distribution of intensity in the cone parallel to the electron orbit plane is in practice essentially isotropic. Only the intensity distribution in the plane perpendicular to the orbit plane ($I(\psi)$) is of interest. This is a function of wavelength (see Fig. 31).

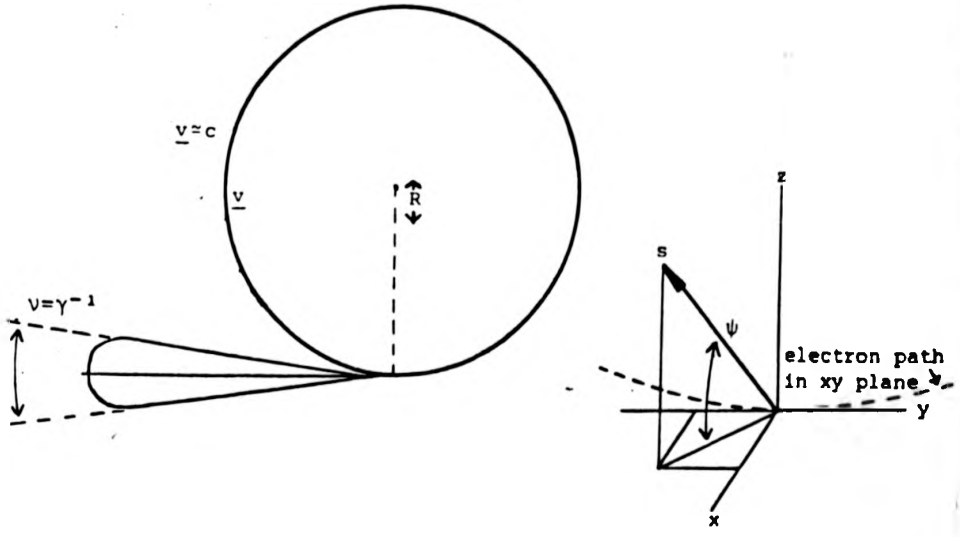

Fig. 31 Angular spread in a Synchrotron (after [143])

Vertical divergence is governed by the vertical source size S_v, the cone angle of emitted radiation classically denoted by γ^{-1}, and the angular distribution (due to trajectory) in the electron bunch characterized by the angle, β_m, between the full width at half maximum gradient lines in the pulse. This can be regarded as the width of the pulse (as β_m increases, δ decreases). However the local

divergence experienced by a point on the sample depends only on the angle δ^* subtended by the source S_v at the sample location, provided δ^* is smaller than β_m or γ^{-1}, which is usually the case (see Fig. 32).

The local horizontal divergence is evaluated in the same way although in some facilities with broad horizontal sources it might be controlled by β_m or γ^{-1}.

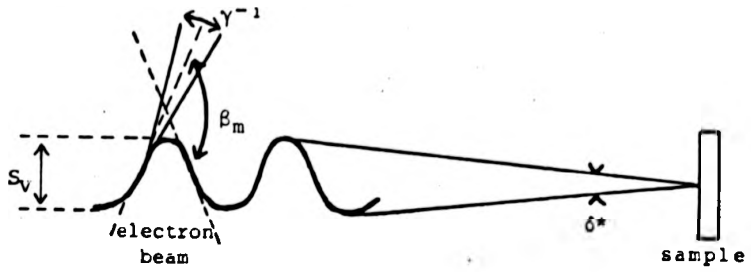

Fig. 32 The three components of vertical divergence (after [143])

In addition, the average incidence angle varies between both ends of the irradiated area, proportionally to the orbit arc intercepted by the sample (see Fig 33).

Fig. 33 The variation, $\Delta\theta_i$, of the average incidence angle along the horizontal dimension of the sample (after [143])

2.5.1 Power

The instantaneous power is given by ([145])

$$\frac{\partial^2 I}{\partial\lambda\,\partial\psi}(\psi, \lambda, E) = \frac{27}{32\pi^3}\frac{e^2 c}{R^2}\left(\frac{\lambda_c}{\lambda}\right)^4 \gamma^8 [1 + (\gamma\psi)^2]^2 \times$$

$$\left[K^2_{2/3}(\zeta) + \frac{(\gamma\psi)^2}{1 + (\gamma\psi)^2} K^2_{\frac{1}{2}}(\zeta)\right]$$

where R = orbit radius.

λ_c is the so-called critical wavelength given by

$$\lambda_c = \frac{4\pi R}{3} \gamma^{-3}$$

$$\lambda_c(\mathring{A}) = 5.59\ R(m)\ Ee^{-3}(Gev) = \frac{12.4}{Ec(Kev)}$$

where $E_c = \frac{\lambda_c}{\lambda}$ and $K_{2/3}$ and $K_{1/3}$ are modified Bessel functions of the second kind, with argument ζ defined by

$$\zeta \equiv \frac{\lambda_c}{2\lambda} (1 + (\gamma\psi)^2)^{3/2}$$

At the critical wavelength, λ_c, the emission is focussed into an angle ν. Below λ_c this angle is smaller, and above λ_c, the intensity is spread over an angle greater than ν. The distribution is symmetrical with ψ.

The terms

$$K_\pi \equiv K^2_{2/3}(\zeta) \text{ and } K_\sigma \equiv \frac{(\gamma\psi)^2}{1 + (\gamma\psi)^2} K_{1/3}(\zeta)$$

correspond to the components which are polarized parallel (π) and perpendicular (σ) to the electron orbit.

Radiation emitted by a nondivergent point source would be 100% plane polarized in the orbit plane but the finite source size and betatron oscillations lead to a smearing of the polarization purity and the beam is around 95% linearly polarized in the horizontal plane.

The polarization is given by

$$C = \frac{(I_\pi - I_\sigma)}{(I_\pi + I_\sigma)} = \frac{(K_\pi - K_\sigma)}{(K_\pi + K_\sigma)}$$

Figure 34 shows the dependence of I_π and I_σ on ψ.

It can be seen that shorter wavelengths are more collimated near $\psi = 0$. There is also a certain amount of circular polarization above and below the orbit plane.

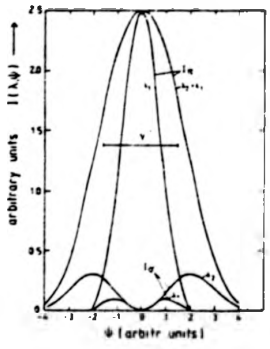

Fig. 34 Dependence of the polarization of synchrotron radiation on the angle ψ against the electron orbit (after [142])

By integrating the instantaneous power over λ, one gets the angular distribution of the radiation ([145]).

$$\frac{\partial I}{\partial \psi}(\psi, E) = \frac{7}{16}\frac{e^2 c}{R^2}\gamma^5[1 + (\psi\gamma)^2]^{-5/2}\left[1 + \frac{5}{7}\frac{(\gamma\psi)^2}{1 + (\gamma\psi)^2}\right]$$

Again the first term in the big bracket corresponds to parallel and the last term to perpendicular polarization. From this equation one calculates that the intensity of the parallel component falls to one half within a cone of $1.13\ \gamma^{-1}$ opening angle. Similarly one finds the perpendicular component to have maximum intensity at $\psi_{\sigma max} \approx \pm\ 0.63\ \gamma^{-1}$.

The spectral distribution (spectral power curve) of synchrotron radiation is obtained by integrating the

instantaneous power equation over ψ ([146])

$$\frac{\partial I}{\partial \lambda}(\lambda, E) = \frac{3^{5/3} e^2 c}{16\pi^2 R^3} \gamma^7 \left(\frac{\lambda_c}{\lambda}\right)^3 \int_{\lambda_c/\lambda}^{\infty} K_{5/3}(\eta) d\eta$$

This spectrum has a maximum at 0.42 λ_c, and below this wavelength intensity falls off very rapidly. It can thus be seen that λ_c is an important parameter. The curves have a full width at half maximum value of 0.84 λ_c.

From the spectral distribution one can obtain the partially integrated intensity N'(λ) for a current i(mA) and an X-ray beam of 1 mrad divergence in the x, y plane (see Fig. 35).

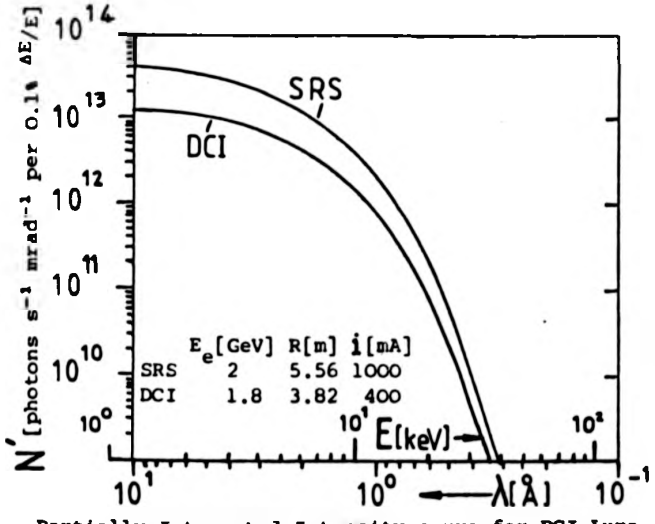

Fig. 35 Partially Integrated Intensity curve for DCI Lure, and SRS DARESBURY (after [142]). NB Idealized current design data displayed.

$$N'(\lambda) = 7.87 \times 10^8 \lambda^2 i \frac{E_e^7}{R^2} \left(\frac{\lambda_c}{\lambda}\right)^3 \int_{\lambda_c/\lambda}^{\infty} K_{5/3}(\eta) d\eta$$

$$[s^{-1}\ mrad^{-1}\ 0.1\%\ \frac{\Delta E}{E}]$$

It is known that $N'(\lambda)$ can be obtained by integrating N (intensity) with respect to ψ, over the range corresponding to σ'_z of vertical divergence, where,

$$\sigma'_z = \frac{0.511}{Ee} \left(\frac{\lambda}{\lambda_c}\right)^{1/3} \qquad \lambda >> \lambda_c$$

$$\sigma'_z = \frac{0.295}{Ee} \left(\frac{\lambda}{\lambda_c}\right)^{1/2} \qquad \lambda >> \lambda_c$$

(where E_e is expressed in Gev) is the angular range outside which the intensity has fallen below e^{-1} of the peak at $\psi = 0$ ([147]).

For DCI LURE $\sigma'_z = 0.096$ mrad which implies that the intensities N' are available within the very small solid angle $\Delta\Omega = \sigma'\sigma'_x < 0.1$ mrad x 1 mrad = 1 mrad^2, so that in the orbit plane of synchrotron sources, N is more than 10 times larger than N'. However, N falls off rapidly above and below this plane.

The total intensity of the synchrotron radiation may be obtained from the angular distribution by integration over ψ, or from the spectral distribution by integration over λ. It can also be obtained from Lienards formula

$$I = \frac{2i\ e^2 c\gamma^4}{3\pi R^2}$$

2.6 Factors affecting resolution

The resolution in all topographic experiments is governed by the size and shape of the source used and its relative position with respect to the crystal and detector. The two cases of a classical X-ray source and a synchrotron

source will be dealt with separately.

2.6.1 Classical X-ray Topography

It is desirable to be able to 'tune in' on the $K\alpha_1$ characteristic line of the particular source spectrum, due to its high intensity compared with the white background and its narrow line width. As this lies in close proximity to the $K\alpha_2$ line, we must be able to resolve the two. This puts an upper limit on the horizontal X-ray divergence that can be tolerated. This beam divergence is governed by the position and size of the source, and the collimator slits.

Vertical resolution is governed by the source height and the position of the specimen with respect to both the source and detector.

The vertical resolution, R_v, can be written

$$R_v = \frac{Vb}{a + b(1 - \frac{V}{c})}$$

however $\frac{V}{c}$ is often negligible for large specimens, hence

$$R_v \simeq \frac{Vb}{a + b}$$

where V, a, b and c are illustrated in Fig. 36.

So for example if the specimen is about equidistant from the source and film, i.e. a = b, the resolution on the plate is about ½ of the diameter of the source i.e. $\frac{V}{2}$.

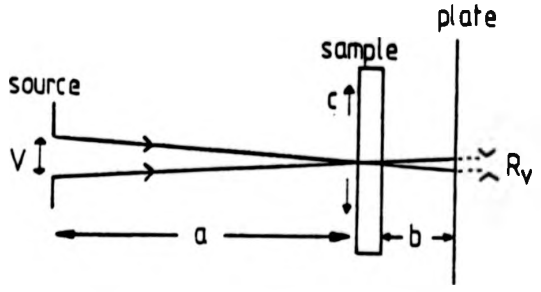

Fig 36 Definition of parameters affecting vertical resolution

2.6.2 Resolution in White Beam Synchrotron Radiation Topography

In an accelerator with no aberrations, so that the electrons move on the arc of a circle, the source size would be extremely small. In practice the source height S_v is between 0.1 and 10 mm, while the projected width S_h of the observable arc of the path near the tangent point is broadened by the betatron oscillations of the beam to lie within the same range.

Unlike conventional X-ray diffraction topography, with characteristic radiation, the whole source contributes to the intensity diffracted by each point in the sample (due to the bigger actual source size at the sample, which means that all the sample is irradiated simultaneously).

The spectral resolution is determined by local divergences and the projected size of the source (see Table II

for a list of parameters of various synchrotrons). So, for a crystal to source distance D and crystal detector distance d,

vertical resolution is given by,

$$R_v = S_v \frac{d}{D} \qquad d << D$$

and horizontal resolution is given by,

$$R_h = S_h \frac{d}{D}$$

provided the detector is perpendicular to the diffracted beam,

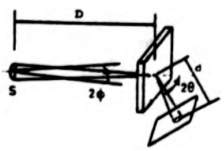

Fig. 37 Definition of experimental parameters contributing to geometrical resolution (after [148])

Both the above relations are valid if $2\phi D$ (beam diameter seen by the specimen from a point in the source) $> S_h$ and S_v respectively, otherwise resolution factors are given by $2\phi D$ ([148] see Fig. 37).

If the diffracted beam is not perpendicular to the detector, then a spreading effect occurs which impairs resolution. As an example consider the case where the detector is perpendicular to the incident beam, then this spreading occurs as a function of 2θ (see Fig. 38)

Synchrotron radiation facility	Horizontal source size S_h (mm)	Vertical source size S_v (mm)	Distance between source and topography beam port D (m)	Angles subtended by source in horizontal and vertical planes		γ^{-1}	Loss of vertical resolution per cm from sample ΔR_v (μm/cm)
				S_h	S_v		
NINA	0.5	0.5	47	10^{-5}	10^{-5}	10^{-4}	0.1
DESY	8	4	40	2×10^{-4}	10^{-4}	$< 10^{-9}$	1
DCI	6	1.5	20	3×10^{-4}	0.7×10^{-4}	3×10^{-4}	0.7
SPEAR	3.2	1.6	17	1.8×10^{-4}	0.9×10^{-4}	1.6×10^{-4}	0.9
VEPP3	1.5	0.2	5	3×10^{-4}	0.4×10^{-4}	2×10^{-4}	0.4

TABLE II after [143]

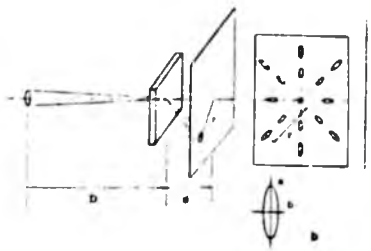

Fig. 38 Behaviour of geometrical resolution as a function of 2θ, when the detector is perpendicular to the impinging beam (after [148])

$$r = d \tan 2\theta$$

The corresponding resolution factors in directions a and b are,

$$R_a = \frac{Sd}{D} \frac{1}{\cos 2\theta} \qquad R_b = S\frac{d}{D}$$

b is perpendicular to the incident plane, and resolution is unaffected along this direction. So, one can get a resolution loss at high θ_B.

As in a Laue pattern, all orders from a particular set of planes are superimposed on the plate. Their relative intensities are determined by the source spectrum, the structure factor, the effect of non ideal Bragg condition, absorption, Polarization factor and Temperature factor.

Each point on the sample reflects X-rays within the angular range $\frac{S'i}{D} = \Delta\theta s$, where S'i is the effective source dimension in the incidence plane (a function of λ).

This corresponds to a spectral pass band

$$\frac{\Delta\lambda}{\lambda} = \cot \theta \, \Delta\theta s$$

Over the whole beam area, the synchrotron radiation has approximately the same divergence, so that different

parts of the image are formed at slightly different wavelengths. Nevertheless, the diffraction topographs are formed with more highly monochromatic radiation than are conventional topographs and this allows for high spatial resolution with large crystal to film distances.

$\Delta\Theta s$ is fixed for a particular synchrotron or storage ring so $\Delta\lambda$ is proportional to $\lambda \cot \Theta$.

Also for each of the harmonics, the crystal is characterized by an angular width of reflection $\delta(\lambda)$ (see for example [149]).

$$\delta(\lambda) = \frac{2C}{\sin 2\Theta} \frac{\gamma_0}{|\gamma_h|} F_h \frac{e^2}{mc^2} \lambda^2 \frac{1}{\pi V}$$

C = polarization factor, V = unit cell volume, F_h = structure factor, $\gamma = \cos \phi_0, \gamma_h = \cos \phi_h$, $\phi_0 = (n,S_0)$; $\phi_h = (n,S_h)$.

To these angles δ and $\Delta\Theta$s corresponds a wavelength spread which can be deduced from the du Mond diagram (see Fig. 39) [N.B. Any wavelength spread in a characteristic K line experiment is fixed by the characteristic line width λ_{ch}]. Due to this wavelength spread, the diffracted intensity for a given harmonic is an integrated intensity.

$$I_h \alpha C\lambda^3 I(\lambda) F_h \frac{1}{\sin^2\Theta} \frac{Si}{D} \left|\frac{\gamma_0}{\gamma_h}\right|$$

(see also [151] and [152]), so I_h is proportional to

$$\frac{C\lambda^3 I(\lambda) F_h}{\sin^2\Theta} \frac{Si}{D}$$

C = 1 for σ polarization ($\perp^r$ to plane of orbit)

$C = \cos 2\theta$ for π polarization.

So for horizontal diffraction at $\theta_B = 45°$, $I_h = 0$ (recently verified by D.K. Bowen and the author on Fe 3.5 wt % Si at Daresbury).

Using this equation for I_h, it is possible to compute the contributions of the various harmonics to a Laue image as well as to compare the integrated diffracted intensities of different Laue images, (see appendix), if one takes into account all the following factors, (1) Absorption; by multiplying I_h by $\exp[-\mu(\lambda)t]$ where $\mu(\lambda)$ is the true absorption coefficient including Borrmann transmission (2) Air absorption; which mostly affects long wavelengths, (3) detector response - photographic emulsions have absorption edges at 0.485 Å and 0.920 Å.

The λ^3 term in I_h determines that almost $\frac{7}{8}$ of the intensity is contained in the lowest order Bragg reflection corresponding to a Laue spot.

The $C\frac{Si'}{D}$ term depends very much on geometry, especially if the source is markedly elliptic.

For a vertical plane of incidence $C = 1$ but the effective source size is small. For a horizontal plane of incidence $C = \cos 2\theta$ but the effective source size is large, which may compensate for the polarization losses (but at the expense of resolution).

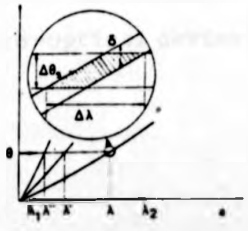

Fig. 39 The Du Mond Diagram for White Beam Topography (after [148])

2.7 Direct Viewing of X-ray Topographs

There are basically two approaches to this problem, which can be called the single stage and multiple stage techniques. In the single stage imaging method, an X-ray sensitive vidicon tube directly converts the X-ray topograph into an electronic charge pattern as follows. The X-ray image is transmitted through a Beryllium faceplate directly to a photoconductive PbO target (or other, for example Se As Te) layer on its inner surface. The inner surface of the target is scanned repetitively by a low velocity electron beam emitted from a cathode (like a normal TV system). The faceplate is maintained positively charged with respect to the cathode, by an external voltage. If the target is made photoconducting by X-rays, the charge is conducted to the faceplate, and then replenished by the external field. Capacitive coupling between target surface and faceplate produces a voltage drop across an external load resistor, and this on amplification becomes the video signal. This technique has so far been limited to achieving a spatial resolution of no less than approximately 20 μm ([153], [154], [155], [156]).

The multiple stage technique involves conversion of the X-ray image into a visible light pattern, via a suitable fluorescent screen and subsequent optical coupling either by a lens or fibre optic plate, to the input cathode of a light sensitive electro-optical device ([157]).

The output image is then displayed on a TV monitor. This method is inherently capable of a resolution of $\sim$ 10 μm and was the method adopted for the TV system used in the present experiments, which was developed by Thomson-CSF for LURE laboratories. A schematic diagram of this detector is presented in Fig. 40.

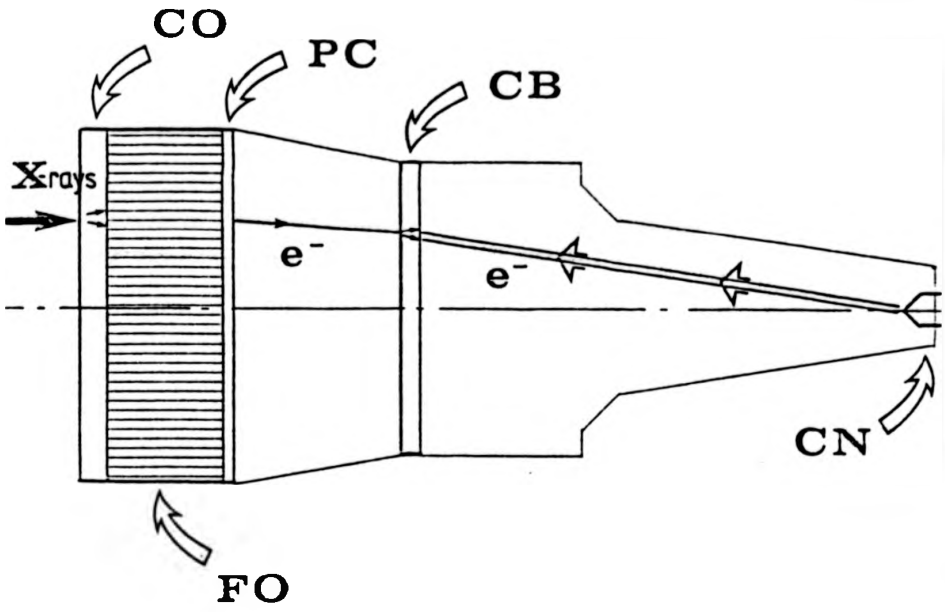

Fig. 40 Schematic diagram of TV System: CO is converter screen, PC is photocathode, FO is fibre optic plate, CB is target, CN is electron gun

The X-rays are converted to light by the 5 μm thick $Gd_2O_2S:Tb$ fluorescent screen. This screen is coupled to a photocathode by a thin plate of optical fibres. The photocathode then converts the light into electrons, which are then accelerated under a potential of 9 Kv to the target. Each emitted electron is capable of creating 1500 to 2000 pairs of 'holes' in the target which consists of a mosaic array of diodes. The target

behaves like a capacitor, the charge in which depends on the number of electrons received. The charge distribution is replenished by the electron gun. Any charge re-distribution leads to an intensity modulation in the scanning electron beam. This modulation constitutes the primary video signal which is then amplified.

Resolution limiting effects of photon noise assume great significance in direct viewing of X-ray topographs. One can obtain some sort of feel for the criteria needed for a 'defect' to be visible by adopting the approach used by Lang ([158]). This is presented below.

Divide the diffracted beam into picture elements of linear size h (Pixels), and consider the criteria necessary for perception of a difference in intensity between picture elements (1) and (2). At (1) the diffracted X-ray flux is X_1 and at (2), X_2 photons cm^{-2} sec^{-1}. Let Q be the quantum efficiency of the detector system (percentage conversion of incident photons into visible flashes on the screen).

The signal can be defined as the difference in the number of flashes n_1-n_2, which build up in the system integrating time τ' in the Pixels (1) and (2), the signal is

$$n_1-n_2 = h^2 \, Q \, \tau' (X_1-X_2)$$

Statistical fluctuation in the brightness of this pair of pixels, taken together has the r.m.s. value

$$(n_1+n_2)^{\frac{1}{2}} = h\{Q\tau'(X_1+X_2)\}^{\frac{1}{2}}$$

From this one can obtain the signal to noise ratio

$$\frac{S}{N} = (X_1 - X_2)\, h(Q\tau')^{\frac{1}{2}}\, (X_1 + X_2)^{-\frac{1}{2}}$$

or in terms of contrast, defined as $c_o = (n_1 - n_2)/(n_1 + n_2)$

$$2c_o^2 h^2\, \bar{X}\, \tau' Q = \left(\frac{S}{N}\right)^2$$

$X_1 + X_2$ is replaced by $2\bar{X}$ which is mean flux into pixels (1) and (2).

It is usually considered that $\frac{S}{N}$ should approach a value of 3 for possible detection. This means that $c_o^2 h^2\, \bar{X}\, \tau' Q \sim \frac{9}{2}$. c_o is determined by the nature of the image, h is determined by the resolution demanded. Maximum τ is determined by the speed of movement in the image, $\bar{X}$ depends on general intensity, Q depends on the detector system.

It is believed that the system used achieves a resolution of 15 μm. Magnetic domains are resolved, clusters of dislocations and slip bands, and precipitates.

Similar results were obtained by Bowen and Hall ([159]) using a slightly different approach, who employed a very useful graphical presentation of the number of photons per square micron required in order to resolve features of a given size at various contrast levels (see Fig. 41 after [159]).

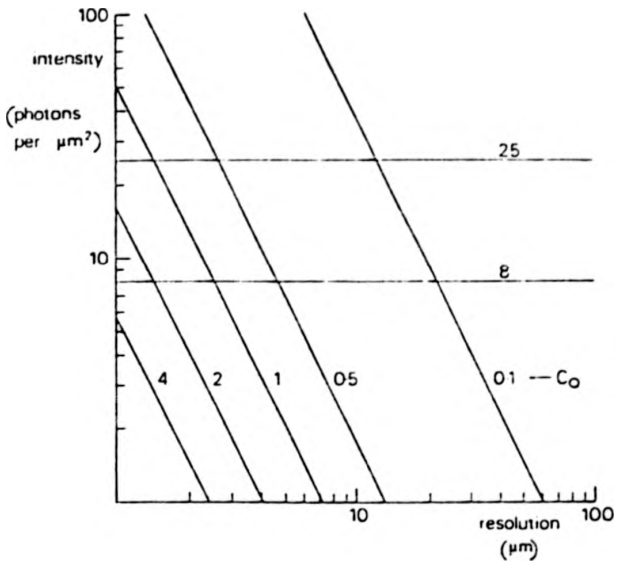

Fig 41 The number of photons per square micron required in order to resolve features of a given size at contrast levels from 0.1 to 4. The lines at 8 and 25 photons per square micron are the maximum intensities that can be recorded on nuclear emulsions with MoKα and CuKα respectively (after [159])

CHAPTER 3

Experimental Techniques

3.1 Materials

Single crystals of Iron 3.5 wt % Si grown by the Bridgeman technique were purchased from 'Cristal Tec', Grenoble, in the form of discs 2 cm in diameter and 0.5 mm thick. It was not possible to get a manufacturers analysis.

Crystal orientation was accurately determined using the precision Laue camera already described.

3.2 Crystal Preparation

3.2.1 Shaping

Crystals were cut by spark machining into conventional I shaped sheet tensile specimens with gauge dimensions 8 x 4 mm. It is believed that damage introduced by the spark machining is minimal. The orientations used are shown in the stereographic projections in Figs. 42 a and b, and the relationship between the two chosen orientations is shown in the schematic in Fig. 42c.

3.2.2 Mechanical Polishing

Crystals were glued (using a low melting point wax) to an adjustable lapping block. This block consisted of a central threaded shaft made from brass, to which the crystal is glued, and a stainless steel shoulder (also threaded to fit the brass shaft), the height of which can be adjusted, which protects the crystal to a certain extent, and ensures an even polish.

The thickness of the crystals was then reduced to

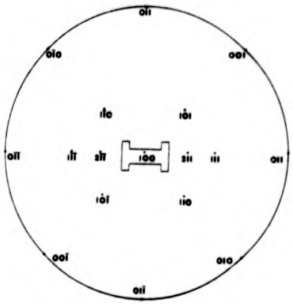

(a) Stereographic projection illustrating the orientation of specimen C1, C2, C4

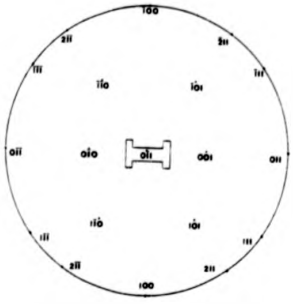

(b) Orientation of specimen C3

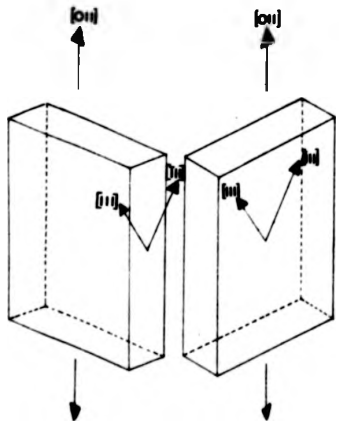

(c) Schematic diagram showing the relationship between the two orientations

FIG. 42

about 200μm by polishing on a series of fine grain emery papers, ranging from 320 grade down to 600. The crystal and block were thoroughly cleansed in acetone in an ultrasonic bath between each stage.

A similar technique was then adopted for a much finer mechanical polish using a series of diamond lapping compounds, ranging from 14μm grain size down to $^{1}/_{4}$μm.

3.2.3 Chemical Polish

Finally specimens were chemically polished using a solution made up of 5% HF and 95% H_2O_2, to remove surface damage introduced by the mechanical polishing. Specimens were simply held by a long thin strip of magnetic material and agitated vigorously in the solution for several minutes.

After this specimens were considered fit for X-ray topographic examination.

3.2.4 Anneal

Specimens were annealed in H_2 to reduce the dislocation density. Initially the specimens were annealed at 900°C for 40 hours (the furnace was typically brought up to this temperature at a rate of 300°C/hr, and after the anneal cooled at a rate of 75°C/hr); however in the case of specimen C1 this did not seem enough to adequately reduce the dislocation density. A similar technique was tried for specimen C2, but on topographic investigation the dislocation density was still considered too high, so

a second anneal was carried out at 1000°C. This further reduced the dislocation density, but even after this second anneal, the crystal still had a dislocation density in excess of 10^4 cm^{-2}. Time restrictions made it impossible to consider a third anneal before deformation (similarly a second anneal was impossible for C1). Figs. 43 a,b,c show Lang topographs of crystal C2 after one and two anneals. Modification of the dislocation structure and even sub-grain shape is evident.

In the case of the last two specimens, C3 and C4, the technique of the anneal at slightly higher temperatures was adhered to. The quality of C3 and C4 was much higher, in terms of dislocation density, than that of C1 and C2. It is considered that this is simply due to the 'luck of the draw' when buying crystals commercially.

3.2.5 Etch Pitting

The technique of Bradler ([161]) in Prague was used. This consists simply of immersion in a 3% solution of HNO_3 in pure alcohol for about 30 seconds. This technique is only useful for specimens of (100) surface, it does not work for specimens of (110) surface (for crystallographic reasons).

3.2.6 Mounting of Specimens

Low melting point wax (applied at only 1 point on the specimen) was used to glue the specimens onto goniometers for simple topographic analysis.

Crystals were glued onto the tensile stage using

(a) g = $0\bar{1}1$ AgKα (b) g = $0\bar{1}1$ MoKα

1mm ← g

Fig 43 Lang topographs taken of C2 after first anneal (a) g = $0\bar{1}1$ AgKα radiation (b) g = $0\bar{1}1$ MoKα radiation

(c) $g \approx 01\bar{1}$ MoKα

$\overrightarrow{g}$

Fig 43c Lang topograph taken of C2 after 2nd anneal; Sub grain structure has slightly changed from Fig 43a, b and dislocations bow out towards the edges of the crystal, and form into clusters in the central region

(c) $g = 01\bar{1}$ MoKα

$\overrightarrow{g}$

Fig 43c Lang topograph taken of C2 after 2nd anneal; Sub grain structure has slightly changed from Fig 43a, b and dislocations bow out towards the edges of the crystal, and form into clusters in the central region

ordinary araldite heated to about 60°C to increase fluidity and improve curing following the original technique of Bowen and Miltat ([140]). The flat surface of the specimen was placed in direct contact with the reference flat of the chuck and the glue applied to the other side of the specimen, with a short piece of metal transmitting the stress, affixed to both the chuck and this glued face. This method was designed to avoid any detrimental effects due to the presence of any rotation components arising from a specimen misaligned with respect to the intended tensile axis.

3.3 X-ray Topography

Four specimens (C1, C2, C3 and C4) were deformed in tension, in situ, on the double axis spectrometer at LURE DCI, Orsay. A photograph of the spectrometer and a schematic diagram illustrating its main components are presented in Fig. 44. All the tests reported here were performed at room temperature, and in the case of specimens C2 to C4 the experiments were performed in an inert atmosphere to prevent rusting (see [32]).

In all specimens the orientation of the tensile axis was [011]. This means that the Schmid factor is zero for two of the <111> vectors and thus the specimens are oriented for double slip. The face orientation of samples C1, C2 and C4 was (100) and that of C3 was $(0\bar{1}1)$ (see Fig. 42).

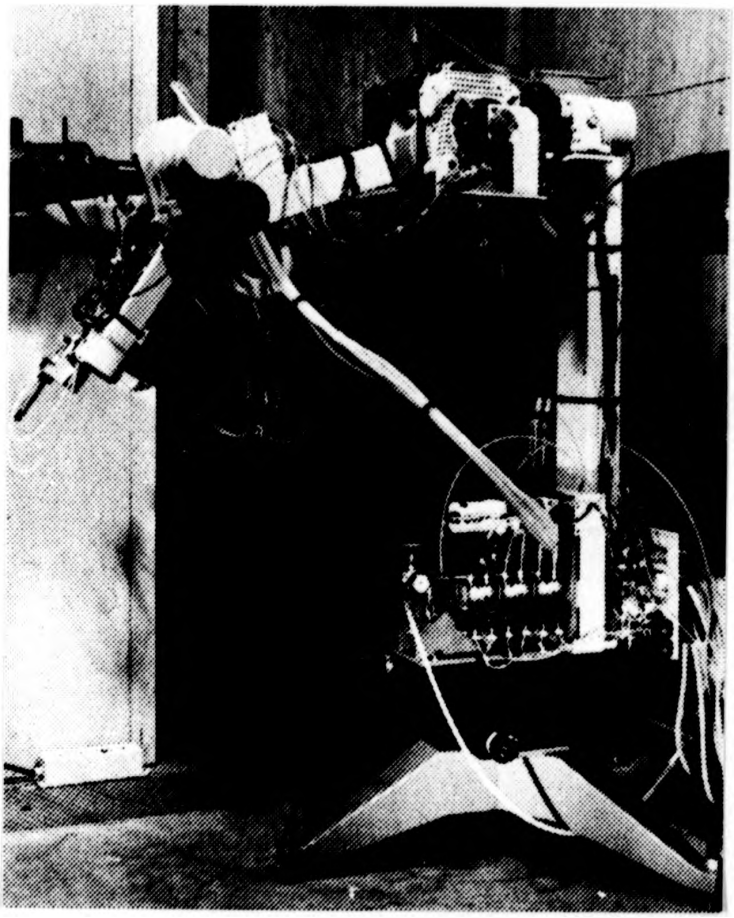

Fig. 44a Photograph of the double axis spectrometer at LURE, DCI, Orsay (after [143])

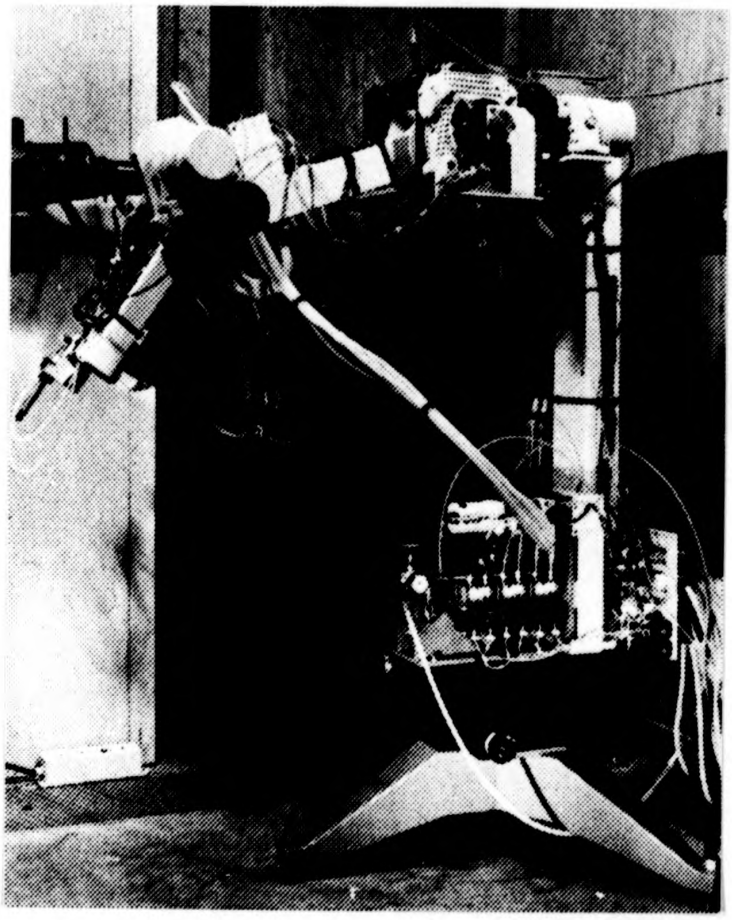

Fig. 44a Photograph of the double axis spectrometer at LURE, DCI, Orsay (after [143])

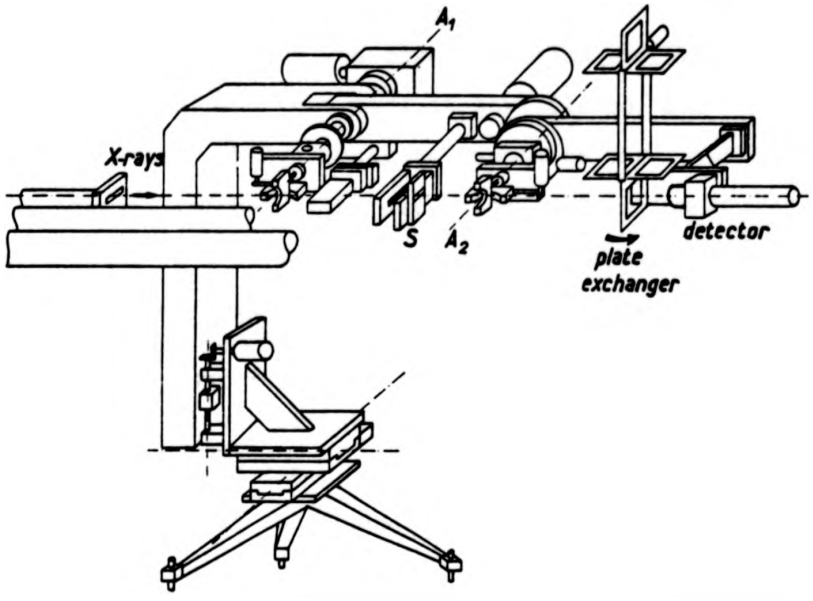

Fig 44b Schematic diagram illustrating the main components of the double axis spectrometer (after [143])

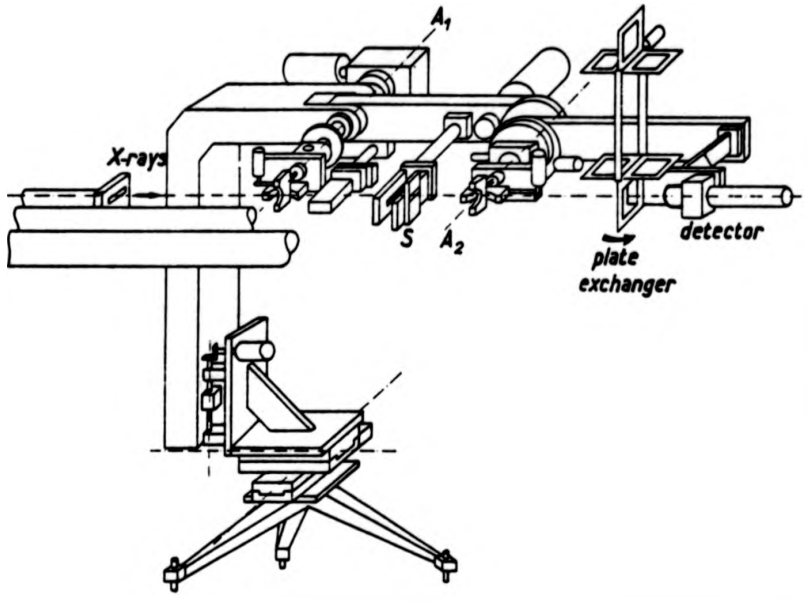

Fig 44b Schematic diagram illustrating the main components of the double axis spectrometer (after [143])

3.3.1 White Beam Techniques

The white beam synchrotron radiation topography technique ([148]) was used to investigate, in situ, the plastic deformation behaviour of the crystals. Television monitoring of all tests was conducted (and videotape recordings made) and this made it possible to 'see' when interesting things began to happen to the crystal under stress, so that high resolution nuclear (L4 50μm) plates could be inserted at appropriate stages in the experiment i.e. when the television image showed substantial change.

Specimen C1 was oriented so that planes perpendicular to the tensile axis i.e. (011) planes, picked out a wavelength close to the K absorption edge for iron and the detector (TV camera, film, plate, counter) was placed normal to the diffracted beam corresponding to this reflection. This will be called the $0\bar{1}\bar{1}$ main spot geometry - by main spot the author refers to that spot which was formed by a diffracted beam hitting the detector normally. This convention will be used throughout. As well as this main spot, various other reflections are present, which will be geometrically distorted due to non-normal incidence on the detector. This distortion can be predicted using the calculation presented in appendix II. The TV camera is always focussed on the main spot throughout these experiments.

This diffraction geometry was chosen for the number of useful high structure factor reflections that could be

obtained with comparable intensity on the same plate. The same principle should always be used when choosing a diffraction geometry. Spatial restriction can sometimes hinder the choice of diffraction geometry. The reflections obtained, as seen on the plate, are shown in Fig. 45.

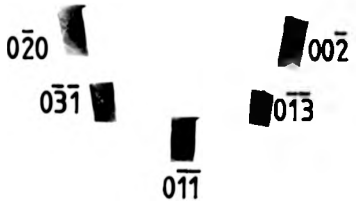

Fig 45 Reproduction of a plate taken of C1 in the $0\bar{1}\bar{1}$ main spot geometry (1x)

Whilst in this orientation specimen C1 was then tested to failure in the beam.

Specimen C2 was oriented for an $00\bar{2}$ main spot diffraction geometry. See Fig. 46 for the appearance of a plate.

Whilst in this orientation, the specimen was first tested dynamically to study the effect of an elastic

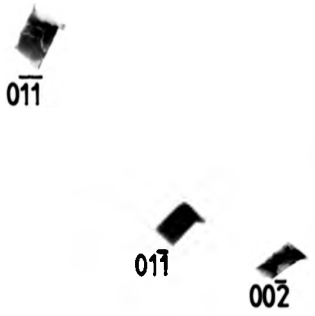

Fig 46 Reproduction of a plate taken of C2 in the $00\bar{2}$ main spot geometry (1 x)

stress on the magnetic domain configuration - these results will be discussed separately (see appendix I). Both C3 and C4 were also initially tested under elastic stress.

After deforming C2 up to a stress just above the elastic limit for Silicon Iron ($\sim$ 200M Pa), as soon as slip became visible on the television image, the stress was relaxed and then the operative slip systems were studied using several different diffraction geometries. The $(0\bar{1}1)$ and $(0\bar{1}\bar{1})$ main spot geometries were set up. The appearance of a plate taken in the $0\bar{1}1$ main spot geometry is shown in Fig. 47.

Fig 47 Reproduction of a plate taken of C2 in the $0\bar{1}1$ main spot geometry (1 x)

Crystal C2 was later imaged in the synchrotron beam using a double crystal technique (see section 3.3.2). It was also imaged on a conventional Lang camera.

The surface was also studied optically, both before and after post-deformation etch pitting.

Sample C3 was oriented in the $0\bar{1}\bar{1}$ main spot geometry, Fig 48 shows the appearance of such a topograph.

After deformation the crystal was studied on a conventional Lang camera, and later in various geometries on the synchrotron, SRS Daresbury.

Sample C4 was oriented for a $00\bar{2}$ main spot geometry and tested in the beam.

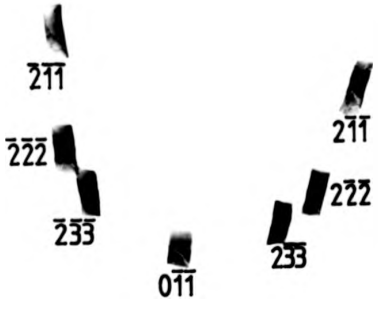

Fig 48 Reproduction of a plate taken of C3 in the $0\bar{1}\bar{1}$ main spot geometry (1x)

3.3.2 Double Crystal Techniques

A Ge 220 reflection was used as a monochromator. This was adjusted to choose a wavelength of 0.85Å (a wavelength on the lower side of the absorption edge was chosen as more flux is available in this region). μt is 5.8.

It is worth noting here that even under these conditions one is still in the realm of spherical wave topography (see section 4.1) and only if one uses a multi reflection 'double crystal' system does one enter the realm of plane wave topography (see [160]). The experimental conditions are illustrated in the Du Mond diagram presented in Fig. 49 (after [160]).

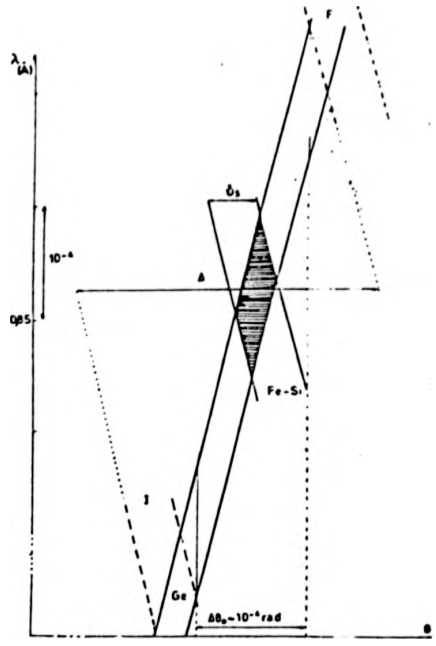

Fig 49 Du Mond diagram for double crystal topography; monochromator Ge reflexion 220. Sample Fe -3.5% Si, reflection 110, $\lambda \approx 0.85$Å. Δ: angular range ($2.7\ 10^{-4}$ rad) between the initial position I and the final position F of the sample for which an overlap region exists.
δ_s: sample reflection width : 4.6×10^{-5} rad

CHAPTER 4

Contrast Theory

CONTRAST THEORY

This section is intended to be a brief review of contrast theory in X-ray topography. A detailed discussion of dynamical theory of X-ray diffraction in perfect crystals (see [162]) will not be entered into, but a brief outline of how to approach a contrast problem in topography, with specific reference to dislocation images, will be given. Theories dealing with mildly distorted crystals, and how these theories fall down under conditions of considerable lattice distortion, will be briefly described. This will lead to a description of concepts such as interbranch scattering.

The way in which these basic concepts can be applied to X-ray topographic interpretation will be described in Chapter 5.

This section will ease the understanding of some of the ideas regarding the contrast from slip bands presented in the discussion. It will also be of help in understanding the sometimes very complex contrast from magnetic domains.

The author assumes familiarity with basic concepts such as the excitement of wavefields and the dispersion surface.

4.1 Conditions Usually met in Lang and Synchrotron White Beam Topography

The dynamical theory of the diffraction of X-rays by perfect crystals has been studied in detail by, for example, Batterman and Cole ([163]). The approach is

usually based on the diffraction of a plane wave by a perfect crystal lattice. Now one of the conditions for a plane wave approximation to be valid is that the angular width of a coherent incident wave at the entrance surface, must be smaller than the angular width of the reflection. These sort of conditions are rarely met in X-ray topography, which led Kato ([164]) to suggest that one can assume the incident wave to be a spherical wave.

Kato showed that the true incident beam can be represented as a superposition of plane waves each of which produces a set of waves in the crystal. These plane waves superpose to create wave bundles in the crystal.

The finite divergence of the incident beam in Lang and White Beam Topography (even in double crystal topography unless one is working under extremely special conditions) means that the whole of the dispersion surface is illuminated simultaneously. A range of incident angles of a few seconds of arc produces an angular spread of 2θ within the crystal.

This can result in a slight modification of the processes giving rise to Pendellosung phenomena. However in Lang topography or White Beam Synchrotron topography, one is concerned with integrated intensities, and here the spherical wave theory gives results essentially identical to those calculated from the plane wave theory.

As soon as the lattice becomes distorted, one has to make new assumptions in order to solve Maxwells

equations. In the next section a brief outline of one of the theories of wave propagation in mildly distorted crystals will be given.

4.2 Kato's Eikonal Theory ([165], [166], [167], [168])

This theory is analogous to that formulated for classical optics theory. If a plane wave is incident upon a homogeneous medium, a refracted plane wave results. If the medium becomes inhomogeneous, one can describe the wave which propagates therein in the form

$$d(\underline{r}) \exp(-2\pi i \, . \, S(\underline{r}))$$

where S(r) is a so-called Eikonal function.

This description is only valid if the variation of the refractive index is feeble over a distance of the order of the wavelength $1/k$.

A similar approach to the solutions of the propagation equation for X-rays traversing a perfect crystal (these solutions must be Blochwaves) leads to modified Bloch-wave solutions of the form

$$\underline{D} = \underline{D}_0 (\underline{r}) \exp(-2\pi i \underline{k} S_o(\underline{r}) + \underline{D}_h (\underline{r}) \exp(-2\pi i k S_h(\underline{r}))$$

This is analogous to the wavefield or Blochwave description in the perfect crystal ([163]) but with k_0 replacing kS_h and K_h replacing kS_h.

Similarly one obtains a modified expression for the susceptibility of the crystal, incorporating the vector displacement in the distorted lattice $\underline{u}$

$$X' = \Sigma X_h \exp(-2\pi i \underline{h} . \underline{r}) \exp(2\pi i \underline{h} . \underline{u})$$

Now the Eikonal functions must satisfy

$$S_h(\underline{r}) = S_o(\underline{r}) + H(\underline{r})$$

where $$H(\underline{r}) = \underline{h}(\underline{r}-\underline{u})$$

again this takes into account the lattice distortion.

The local wave vectors

$$\underline{K}_o(\underline{r}) = k \text{ grad } S_o(\underline{r})$$

$$\underline{K}_h(r) = k \text{ grad } S_h(\underline{r})$$

are thus related by

$$\underline{K}_h(\underline{r}) = \underline{K}_o(\underline{r}) + k \text{ grad } H(\underline{r})$$

$$= \underline{K}_o(\underline{r}) + \underline{h}'(\underline{r})$$

This is equivalent to the Bragg relation $\underline{K}_h = \underline{K}_o + \underline{h}$ in the perfect crystal.

Insertion of the modified Blochwaves into the propagation equation leads essentially to the following fundamental results:

1. One can consider the presence of a local dispersion surface with the same equation as that associated with the perfect crystal case.
2. The existence of an amplitude ratio identical to that in the perfect crystal.
3. The knowledge that the Poynting vector associated with the wavefields is normal to the local dispersion surface.

It is also possible to calculate the trajectories of these modified Blochwaves using the Variational principle, and also amplitudes and intensities can be determined

after calculating the phase differences along the trajectory.

In the relatively simple case of a constant deformation gradient, (G = const. see appendix III) the trajectory equation can be calculated analytically. These trajectories turn out to be the branches of hyperbolae ([169]).

The curvature of wavefields associated with branch 1 of the dispersion surface are of opposite sign to those associated with branch 2. This means that if both sets of wavefields reach the exit surface the resultant intensity will not be very different to that corresponding to a perfect crystal. However if, as is the case as absorption increases, wavefields from one of the branches of the dispersion surface are damped out, contrast will result.

Under intermediate absorption conditions, and for a constant deformation gradient, when G is positive wavefields associated with branch 1 of the dispersion surface are curved in the same sense as the reflecting planes. The inverse is true for negative G.

A change in sign of G can be achieved by a change in sign of diffraction vector or vector displacement in the lattice. This means that Friedel's law is no longer satisfied (this is only valid in perfect crystals or non absorbing distorted crystals).

Fig. 50 shows the range of absorption conditions over which this can occur ([170]).

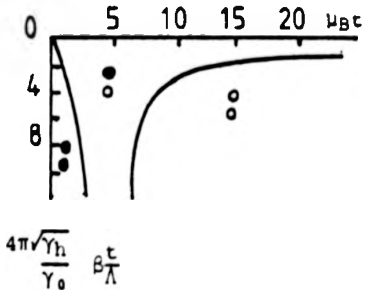

Fig 50 Illustration of the zones of black and white contrast as a function of deformation gradient and absorption (after [170]). The upper and lower circles refer to positive and negative G values respectively

The kind of lattice deformation for the geometrical optics assumption to be valid was considered by Authier and Balibar ([171]).

Essentially $G << \frac{\delta}{\Lambda}$, where δ = rocking curve width, Λ = Pendellosung length, G = deformation gradient, or defining β as $G = \beta \frac{\delta}{\Lambda}$, $\beta << 1$.

These inequalities mean that the variation of the effective misorientation $\delta(\Delta\theta)$ must be inferior to δ over a Pendellosung length. They can also be expressed in terms of lattice curvature ρ_L

$$\rho_L >> \Lambda$$

Kato and Katagawa proved that the Eikonal theory is valid for β values less than 1 (of the order of a few tenths).

4.3 Essential Phenomena

4.3.1 Anomalous Transmission - Borrmann Effect ([172], [173]).

This is a consequence of the nature of the wavefields

or Blochwaves propagating in a crystal. Each Blochwave is made up of a superposition of incident and diffracted components, E_o and E_M respectively. Now for a particular wavefield the E_o and E_M components add together to give a travelling wave moving along the direction of the normal to the corresponding tie point on the dispersion surface (for the symmetric Laue case this is the bisector of K_o and K_h), and a standing wave at right angles to this.

Anomalous transmission arises due to some of the wavefields having antinodes in between the atomic planes. Photoelectric absorption of an atom is proportional to the electric intensity there. This phenomenon is radically altered due to the presence of the standing waves so that those wavefields with antinodes in between the atomic planes will suffer less than normal absorption, and those with antinodes at the atomic planes suffer greater than normal absorption.

For Iron, a centrosymmetric crystal, the coefficient of Borrmann absorption in low order reflections only differs from unity by the Debye Waller factor (see appendix III). A strong Borrmann effect can develop in these low order reflections, with wavefields from branch 1 of the dispersion surface experiencing absorption less than the normal photoelectric absorption.

4.3.2 Interbranch Scattering or Creation of New Wavefields

This describes the transfer of energy which can

occur from a wavefield associated with one branch of the dispersion surface into another created wavefield which is associated with the other branch of the dispersion surface. This can occur when a wavefield encounters a planar fault, or when it encounters highly distorted areas around, for example, a dislocation ([174], [175], [176]).

Although the Eikonal theory, can explain interference phenomena in mildly distorted regions, it cannot predict this creation of new wavefields.

4.3.3 Pendellosung Phenomena ([163])

Wavefields associated with branches 1 and 2 of the dispersion surface, whether they are defined from a plane or spherical wave viewpoint, interfere.

This interference can be described in terms of the Poynting vector of the energy flow within a crystal. For 1 reciprocal lattice point and two consequent tie points on the dispersion surface, the Poynting vector can be expressed as follows:

$$S_T = [\mu_0/\epsilon_0]^{\frac{1}{2}} \langle\langle S \rangle\rangle = S_1 + S_2 + S_{12}$$

This can be regarded as the vector sum of the effective Poynting's vectors of 3 wavefields in the crystal. S_1 and S_2 are the effective energy flows each with its own absorption, associated with a tie point on the branches 1 and 2 of the dispersion surface, respectively. S_{12} represents a coupling term between the two, which is constant in planes parallel to the crystal surface, varying sinuisoidally

with depth with period $P = (\frac{1}{\kappa'_{O1} - \kappa'_{O2}})$. The vector S_{i2} is parallel to the crystal surface and does not contribute to energy flow through the crystal (see Fig. 51).

Energy swaps back and forth between the S_O and S_H directions, as a function of depth, extinguishing completely in the S_H direction and very nearly in the S_O direction, with a period P.

For traverse topographs, Pendellosung fringes should only be observed in wedge shaped crystals; where the exit surface intersects the fronts of similar integrated intensity.

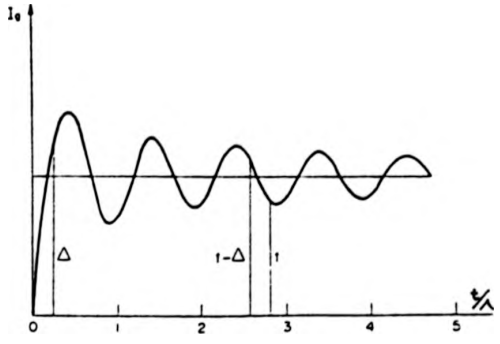

Fig 51 Integrated plane wave intensity as a function of thickness in the Laue case

They can also be observed at sub-grain boundaries which are not perpendicular to the surface (see Chapter 6), or even from magnetic domain walls at an angle to the surface ([177]).

4.4 Dislocation Images

The strain field around a dislocation can be separated into two parts; one in which the geometric optics approximation is valid, and a more distorted region which gives rise to the creation of new wavefields.

Those areas around a dislocation where the geometric optics approximation is valid give rise to the so-called dynamical image, whereas the more distorted regions mentioned give rise to the so-called intermediary image.

Apart from these, if the incident beam divergence is larger than the rocking curve width, highly distorted zones (close to the dislocation core) can diffract X-rays which do not participate in the diffraction from perfect regions of crystal. This gives rise to the Direct image. ([174]).

These three types of image will be considered separately.

4.4.1 Dynamical Image

This arises from regions around the dislocation for which the geometric optics, approximation is valid i.e. regions further from the dislocation than that defined by the curve $G = \frac{\delta}{\Lambda}$ (β=1). As stated earlier wavefields from branches 1 and 2 of the dispersion surface experience a curvature of opposite sign. So neglecting absorption, the contrast expected from wavefield curvature (for a dislocation in the centre of the crystal) would be little different from that expected from a perfect crystal. However, in for example Fe, often only wavefields associated with branch 1 of the dispersion surface have appreciable intensity at the exit surface (of course this is dependent on the crystal thickness and wavelength used) and a net contrast, i.e. a dynamical image, is expected.

However equi G-contours of a dislocation in an

incidence plane can be very complex, resulting in curvature of a wavefield in opposite senses around a dislocation, and this again would lead to a reduction in overall contrast.

One can say ([178]) that the image will be black (white) when the reflection is taken from the concave (convex) side of the reflecting planes .

The sign of the Burgers vector of a dislocation can be determined from consideration of the dynamical image ([179], [180]).

4.4.2 Intermediate Image

The creation of new wavefields in zones of large deformation gradient, similar to that which occurs at a planar fault ([181], [182]), leads to

1. A reduction in intensity in regions close to the direct beam, due to transfer of energy into the $\underline{S}_h$ direction. The dislocation is said to cast a shadow. This is the mechanism of dislocation visibility in Borrmann topography ($\mu t > 10$).
2. The formation of fringes due to the overlap and interference of wavefields which originate from the same spherical wave. These are, in effect, Pendellosung fringes.

The fringes may be averaged out in integrated topographs, but they will usually result in an overall darkening on the dislocation image.

The intermediate image is insensitive to the sign of the diffraction vector. However the lateral width of the image is very sensitive to the distance of the dislocation from the exit surface.

The intermediate image is formed from regions inside the curves defining the limit of the geometric optics approximation i.e. within the curves defining $G = \frac{\delta}{\Lambda}$.

4.4.3 Direct Image

X-rays reflected by zones of strong misorientation close to the dislocation, intercepting the direct beam, only experience normal photoelectric absorption. The direct image of a dislocation will therefore be of strong intensity under low absorption conditions. It will gradually disappear as absorption increases.

The contrast is independent of the sign of g.

The width of direct images can be calculated from an essentially geometric point of view ([183], [174]).

The direct image width is determined by the width of the region around the defect for which

$$| \delta (\Delta\Theta) | > \alpha \delta$$

where $\alpha = 1$ or 2 and $\delta(\Delta\Theta)$ is the misorientation (see appendix III).

However Miltat and Bowen ([184]) in a detailed study of direct dislocation images in Si, found that α was dependent upon the type of reflection used, in a different way than δ. So here the model was found to partially fail.

However, they concluded that the correlation was reasonable considering the approximate nature of the model.

These basic concepts will now be used in a chapter designed to ease the interpretation of topographs presented here; for example it should act as an aid in identifying slip bands.

CHAPTER 5

X-Ray Topographic Interpretation

X-RAY TOPOGRAPHIC INTERPRETATION

It is essential in dynamic experiments to be able to distinguish between contrast observed before the application of any constraint, and any new contrast observed after constraint. It is also vital to be able to recognize and classify these various types of contrast, and, if possible, introduce some quantitative data such as image width, image symmetry, and any effect of the proximity of a defect to the X-ray exit surface. It is also possible in White Beam Topography to be able to detect any lattice rotation and this can be correlated with the defect structure.

The following types of contrast are typically observed on topographs of undeformed Fe 3.5 wt % Si.

1. Magnetic domain contrast.
2. Dislocation contrast (grown in).
3. Precipitate contrast.
4. Sub-grain boundary contrast.

On mechanically deforming Fe 3.5 wt % Si one expects to initiate slip processes in the lattice. This is understood to occur via the propagation of dislocation sources under stress, and these dislocations then form into slip bands.

So after deformation one observes, in addition to the contrast observed prior to deformation (which may have been modified by the constraints),

5. Slip band contrast.

6. Image distortion due to lattice rotation.
7. At high strain, 'Luder's band' contrast, and rotation boundary contrast.

Each of these categories will be considered separately in order to facilitate interpretation of the X-ray topographs presented later.

An additional type of contrast is sometimes observed along the edge of White Beam Synchrotron topographs. This contrast consists of a narrow band of dark contrast. It is believed that this band of contrast is due to X-rays falling on the edge of the specimen, undergoing Bragg type diffraction and possibly Laue-Bragg diffraction. As the reflection curve for the Bragg case is larger than that of the Laue case, an enhancement of intensity is expected. It is also possible that the lateral width of the diffracted beam is larger than that of the incident beam in the Bragg case ([163]) so a rather broader image of the edge of the specimen than might be expected is not too surprising. This will be discussed in more detail later.(see section 7.2.8).

5.1 Contrast from Ferro Magnetic Domains in (100) Surface Fe 3.5 wt % Si Single Crystals

The author assumes familiarity with concepts such as magnetostriction (from which magnetic domain contrast originates in Fe 3.5 wt % Si). A detailed study of the strain fields associated with this magnetostriction and their effect on the propagation of X-ray wavefields can be found in the literature (for review see [185], [186])

and will not be undertaken here. Rather, the actual experimentally observed contrast effects will be described, and the general approach used to interpret such contrast will be outlined.

5.1.1 180° {001} walls

The magnetostrictive deformation is the same in the two regions separated by a 180° wall (assuming it to be of zero thickness) and so no contrast is expected. Even if one considers the internal structure of the wall still no contrast is to be expected ([187]). However, if one considers the effects due to the presence of free surfaces (i.e. relaxation), non zero overall displacements result ([188]) which can give rise to some contrast ([189]). It is often found that 180° walls are more visible when decorated with fir-tree patterns.

5.1.2 90° {110} walls

Extinction

Polcarova and Kaczer ([190]) have shown that {110} 90° walls are visible in reflections such that $\underline{g}.\Delta\underline{M} = 0$ (where $\underline{g}$ is the diffraction vector and $\Delta\underline{M}$ is the vector $\underline{M}_2 - \underline{M}_1$, where $\underline{M}_1$ and $\underline{M}_2$ are the magnetization vectors in domains I and II respectively - $\underline{M}_1$ is taken to be followed by $\underline{M}_2$ along the magnetic flux).

5.1.3 Contrast in Reflections such that $\underline{g}.\Delta\underline{M} \neq 0$

Only symmetric Laue reflections will be considered.

1. 110 reflections

Translation topographs (these are related to a mapping

of the integrated diffracted intensity - as in White Beam Synchrotron topographs also).

If the specimen surface normal belongs to the incidence plane, {110} 90° walls are seen through a narrow contrast line which is usually whiter than the background ([191]). If the specimen is tilted around g the wall appears as a band of width t sin α (t is specimen thickness; α = angle of tilt), this band is black (white) if g.ΔM is positive (negative) ([189], [191], [192]).

2. 200 reflections

In 200 reflections, 90° {110} walls usually appear, under intermediate absorption conditions, as relatively narrow, predominantly black or white contrast lines, bounded by a faint line of opposite contrast. The contrast is predominantly white (black) when g.ΔM is positive (negative).

The sort of contrast arising from {110} 90° walls can be qualitatively (and in some cases semi-quantitatively) explained by treating the wall (assuming it is non decomposed) as a sort of planar fault, where the reciprocal lattice vectors in the two regions separated by the wall have a relative rotation.

The thickness of the wall ($\sim$ 1000Å) is always much smaller than the Pendellosung length. Many authors have treated 90° {110} walls as coherent twin boundaries ([193], [194], [189], [190], [191], [192]).

Consider the wall to separate regions I and II of the

crystal (see fig.52). Dispersion surface considerations as one traverses the domain wall result in the formation of caustics in region II (caustics correspond to the envelope of ray trajectories in region II, where wavefields do not focus at any one point, but perhaps along a series of points [195]).

Fringes observed on 110 reflections (see fig. 104) are not those expected from the dispersion surface construction, similar to those expected from a stacking fault or a twin boundary. The striped contrast observed (e.g. fig. 104) is due to the fact that 90° (110) walls are decomposed.

It is worth noting that magnetic domain walls are rarely as simple as a planar fault, but are often characterized by long range strain fields. Detailed interpretation could only be achieved using a general contrast theory valid for deformed crystals.

5.1.4 Junctions of Domains

Contrast from junctions of domain walls are often evident on topographs presented here (e.g. see fig.104). Consideration of the displacement field asscciated with for example, a junction of 2 {110} 90° walls and an {010} 180° wall (a so called Y Junction) leads tc the assumption that Y junctions can be treated as wedge disclinations ([196].

The shape of the image is closely similar to equi-G contours in the plane of the specimen surface, the so-called butterfly black and white contrast with a line

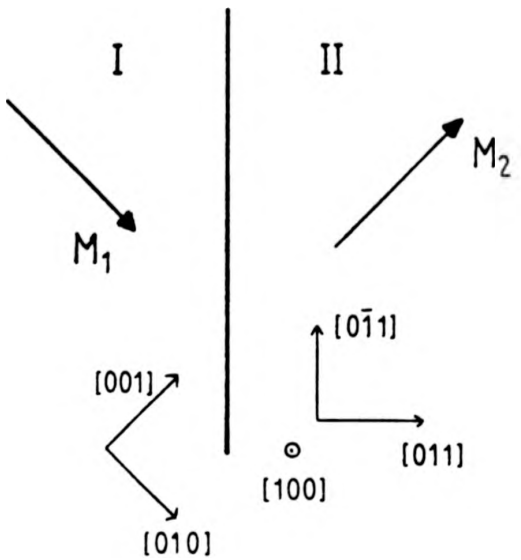

Fig 52 Geometry of {110} 90° wall

of no contrast perpendicular to g. There is a total contrast reversal when g switches to -g.

The contrast can be understood using the Eikonal theory of Kato under the condition of a constant deformation gradient. As mentioned in section (4.2), this theory predicts that under the conditions of a positive deformation gradient, the curvature of the wavefields associated with branch 1 of the dispersion surface undergo curvature of the same sign as that of the reflecting planes. Conversely, under similar conditions, the curvature of wavefields associated with branch 2 of the dispersion surface is in the opposite sense to that of the reflecting planes. These results are inverted for a negative deformation gradient.

The major part of the image of such a junction can be treated as dynamical ([185]).

5.2 Contrast from Magnetic Domains in (0$\bar{1}$1) Surface Fe Si Single Crystals

The rather complex domain configuration observed in such Fe 3.5 wt % Si single crystals was investigated in detail by Schlenker ([177]). Basically the same mechanisms of contrast formation occur as in the case of (100) surface crystals, but the images can be much more complicated. Initially (under zero strain) a relatively simple domain configuration is observed (see fig. 77) consisting of domains magnetized along ±[100] and separated by 180° walls which intersect the surface linearly and along

[100]. However rather complicated closure domains are observed at the edges of the specimen, which are similar to those observed by Schlenker [177] (these are shown in fig.111). The visibility of defects is affected by the domain structure, an effect which was also observed by Schlenker ([177]). This will be explained in detail in the discussion.

Rather special domain configurations are induced in specimens of this orientation, when subjected to elastic stresses. These structures are known as Dijkstra and Martius ([197]) type I and II. The results obtained will be presented in appendix I.

5.3 Dislocation Contrast

The relatively high absorption of Fe Si coupled with the thickness of samples studied (< 200μm) would lead one to expect mainly dynamical contrast from dislocations. Dynamical images of dislocations are usually predominantly white in character (this is not always the case, a fact which is useful in determining the signs of the Burgers vectors of dislocations ([179]). At high values of μt one expects wavefields associated with branch 2 of the dispersion surface to be damped out and only those wavefields associated with Branch 1 of the dispersion surface to emerge at the exit surface. This implies that direct image effects, and intermediary image effects should diminish whilst dynamical effects should predominate.

Predeformation grown in dislocation images observed

on the White Beam Synchrotron topographs presented here are mainly dynamical (white) in character, but some intermediary effects are observed on some conventional Lang topographs (e.g. fig. 77).

5.4 Precipitate Contrast

The physical explanation for the contrast observed around precipitates will be considered in more detail in the discussion. It is useful here simply to point out the nature of the contrast. This is found to consist of two lobes of opposite contrast. Following the empirical rule formulated by Meiran and Blech ([198]), if the X-ray intensity is enhanced on the side of positive diffraction vector, the lattice is under compression, if reduced it is under tension.

5.5 Grain Boundary Contrast

On the conventional Lang topographs presented, often not all of the crystal contributes to Bragg reflection simultaneously. This is due to the misorientation between subgrains being greater than the beam divergence. On White Beam topographs all the subgrains contribute as each subgrain is able to select its appropriate wavelength for Bragg reflection. Misorientation between subgrains can either cause image overlap, which would lead to a relative darkening on the plate or image 'underlap', which would show as a 'gap' between subgrains on the plate. One can obtain quantitative information about the misorientation between subgrains provided three non coplanar

reflections are used.

5.6 Slip Band Contrast

Several types of contrast are observed, depending on the surface orientation of the specimen [N.B. the detailed physical interpretation of the contrast effects will be postponed until the discussion].

Slip planes in a specimen will project onto a two dimensional plate in a way directly related to the orientation of the plane to the surface and the diffraction conditions. The two hypothetical situations shown schematically in Fig 53 indicate the sensitivity of this effect to diffraction and specimen geometry.

It is useful to be able to talk in terms of the projected width of slip bands, and also their projected directions. From the diagrams one can see that part of the slip band image will correspond to the intersection of the band with the exit surface, and part will correspond to its intersection with the entrance surface. The line on the image which corresponds to the intersection of the slip band with the exit (or entrance) surface, will be called its projected direction.

Slip band images also terminate along specific directions. Knowledge of these directions can be very useful. The projected width of a slip band can also be very useful in analysing slip systems.

In short, knowledge of the projective properties of a slip band (an essentially two dimensional object in

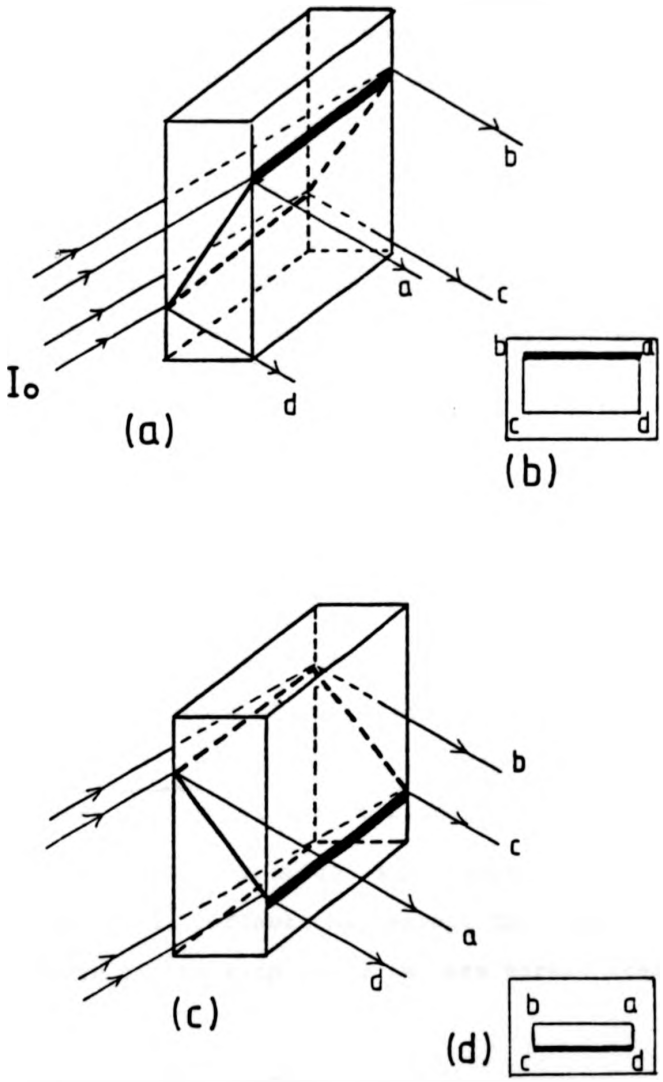

Fig 53 Schematic diagram illustrating the sensitivity of the projection of a slip plane to diffraction geometry. (a) one extreme (b) the corresponding projection (c) the other extreme and (d) its corresponding projection

a three dimensional lattice) onto a two dimensional plate is vital in order to be able to understand slip geometry. A calculation has been made (see appendix II) enabling one to (a) compute the positions of the spots on the detector, and the operative wavelengths, (b) define the trace on the detector plane of the plane of incidence of a given reflection, (c) find the trace on the detector of a given crystallographic direction in the sample for a given spot, and the magnification ratio along that direction, (d) define the trace on the detector of a given crystallographic plane for a given spot, as well as the projected width of that plane.

5.6.1 Specimens of (100) surface

In specimens of (100) surface orientation, slip bands appear on $0\bar{1}\bar{1}$ reflections as small rectangular 'slip cells' which are predominantly white in character, with an associated dark thin line on those parts of the cell which correspond to regions of slip band closest to the exit surface, and a diffuse pale area corresponding to the region closest to the entrance surface.

On 002 reflections, the images are essentially similar to those on $0\bar{1}\bar{1}$ reflections, except that the rectangular nature of the slip cells is less marked (see discussion).

5.6.2 Specimens of $(0\bar{1}1)$ surface

Here, slip bands form into long thin areas predominantly dark or light on the plate, with an associated

line of opposite contrast, depending on the reflection.

5.7 Image Distortion due to Lattice Rotation Effects

It is known that after plastic deformation, lattice rotation effects try to compensate for slip that has occurred in the manner illustrated below. The image distortion due to this effect depends on the orientation of the incidence plane with respect to the rotation axis.

It is worth noting here that if the specimen is constrained by grips, the effect of lattice rotation (which is usually considered as a migration of the tensile axis towards the slip direction) will be opposed. This can lead to rotation boundary contrast (see discussion), which appears as a coarse dark band.

5.8 Luders Band Contrast

This arises due to the difference in diffracting ability between a highly deformed volume of material, and a not so deformed volume of material. In the case observed here, rotation boundary contrast is superposed on this Luders band contrast (see discussion).

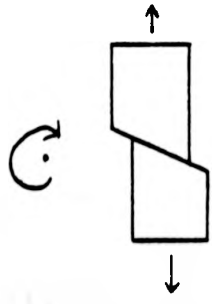

Fig 54 Schematic diagram of lattice rotation induced in order to compensate for slip

CHAPTER 6

Results

EXPERIMENTAL RESULTS

6.1 Crystal C1 (T = [011], N = [100] where T is Orientation of Tensile Axis, and N is Orientation of Surface Normal)

A series of White Beam $0\bar{1}\bar{1}$ main spot topographs taken at various increasing levels of stress on crystal C1 is shown in Fig. 55. For this reflection $\lambda = 1.8\text{Å}$, $\mu t \approx 9$. A predeformation Lang topograph is shown in Fig. 56 (this topograph is a composite made from separate topographs taken from different subgrains).

Fig. 57 shows a series of still photographs taken from the videotape recording of the deformation of C1.

In Fig. 55b,c,d one can see a homogeneous nucleation of small slip cells. Many of these slip cells nucleate side by side and form into slip bands. On this reflection, the slip band intersections with the crystal surfaces project perpendicular to the projection of the tensile axis. Fig. 58 shows the deformation history of C1.

Fig. 59 shows two 002 reflections taken from the same diffraction geometry.

6.1.1 Projected Geometry

Fig. 60 shows a sketch of useful projected directions on the various reflections in the $0\bar{1}\bar{1}$ main spot geometry, and also the predicted image shapes (see also Fig. 45).

For a crystal of this orientation, the maximum resolved shear stress systems are $(\bar{2}11)[111]$ and

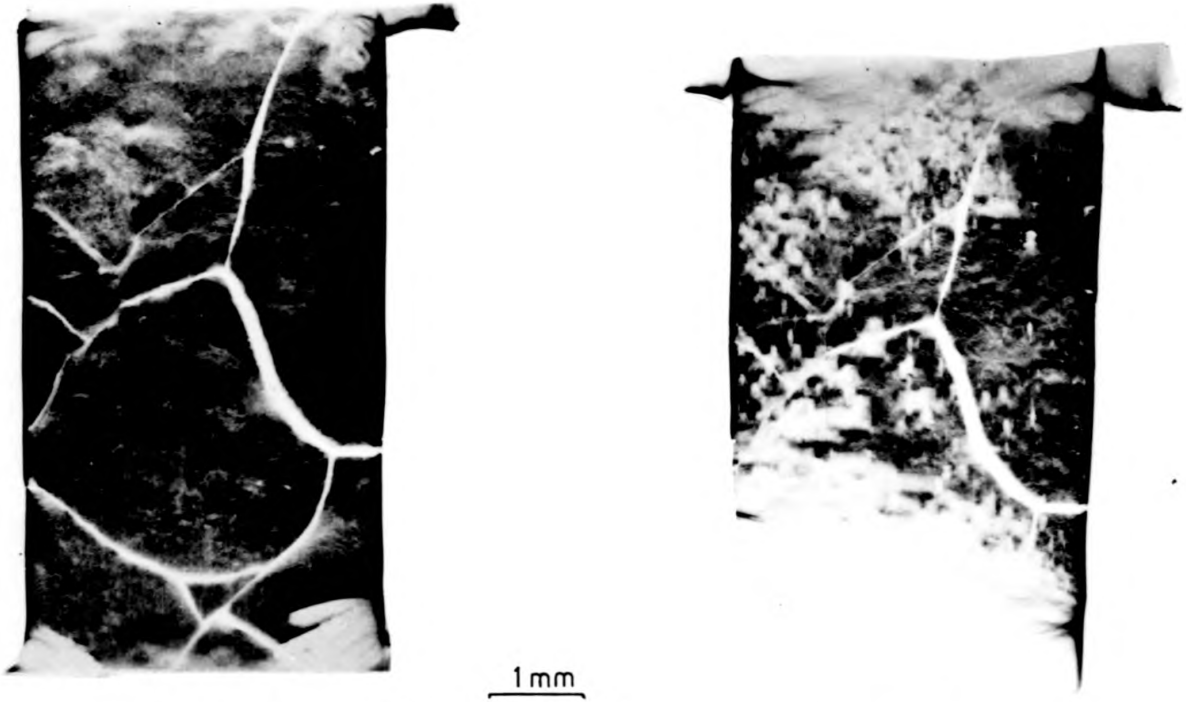

(a) 0 stress

(b) 200.3 MPa

Fig 55

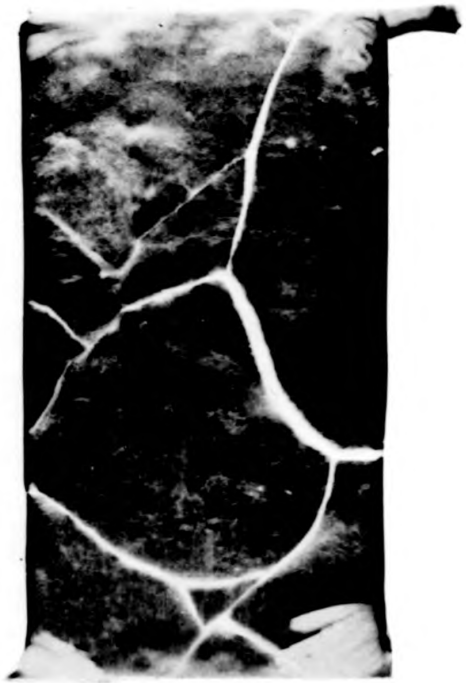

1 mm

(a) 0 stress g↓

(b) 200.3 MPa

Fig 55

(c) 291.1 MPa

Fig 55

(d) 293.8 MPa

A series of white beam main spot topographs taken of crystal C1 at (a) 0 stress, (b) 200.3 MPa, (c) 291.1 MPa, (d) 293.8 MPa ($g = 0\bar{1}\bar{1}$, $\lambda = 1.8\text{Å}$)

Fig 56 Lang Topograph of Cl, Mo Kα radiation
Taken before deformation (g = $0\bar{1}1$)

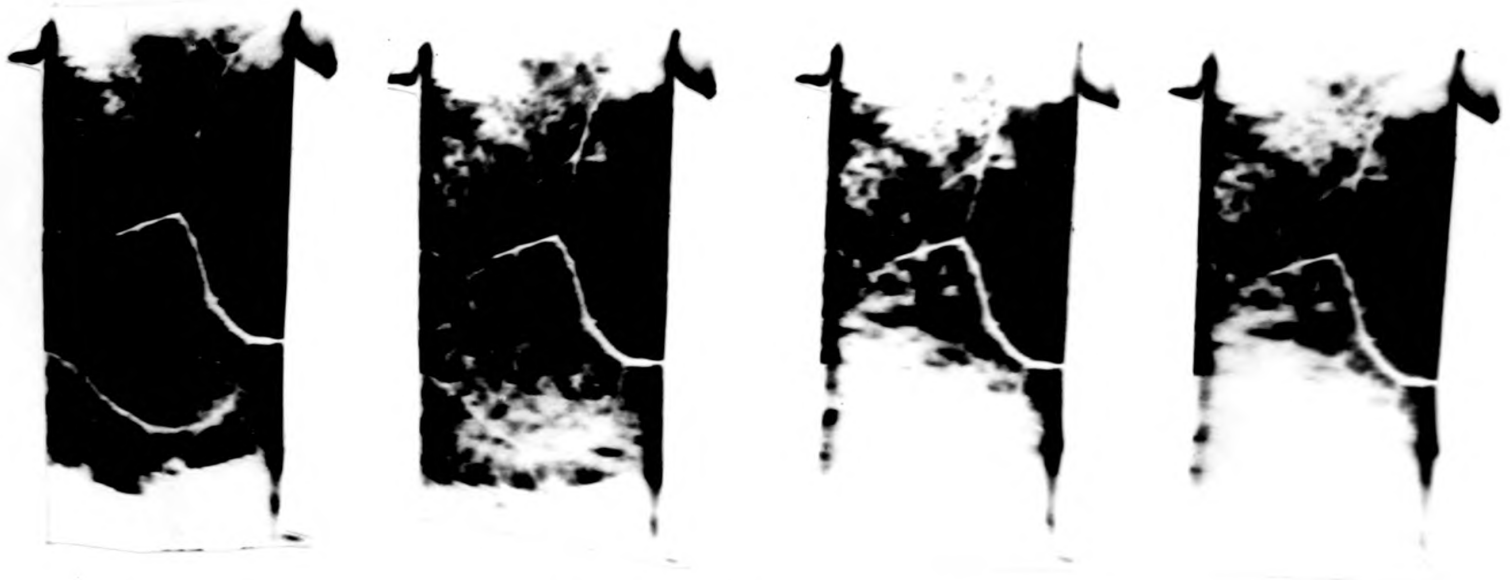

(a) 208 MPa (b) 219 MPa (c) 224.3 MPa (d) 235 MPa

Fig 57

(e) 235 MPa (f) 235.1 MPa (g) 235.5 MPa (h) 236 MPa

Fig 57

A series of still photographs taken from the videotape recording of the $O\bar{1}\bar{1}$ main spot during deformation at (a) 208 MPa (b) 219 MPa (c) 224.3 MPa (d) 235 MPa (e) 235 MPa (f) 235.1 MPa (g) 235.5 MPa (h) 236 MPa

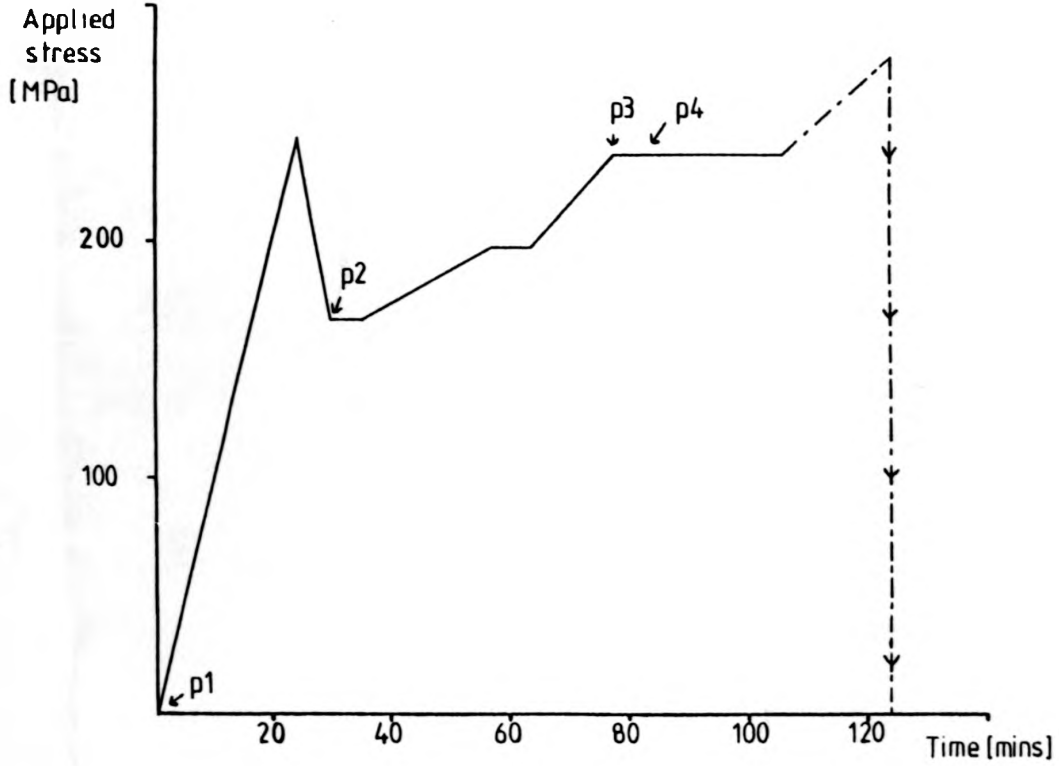

Fig 58 Deformation history of C1. p1-4 indicate where plates were taken

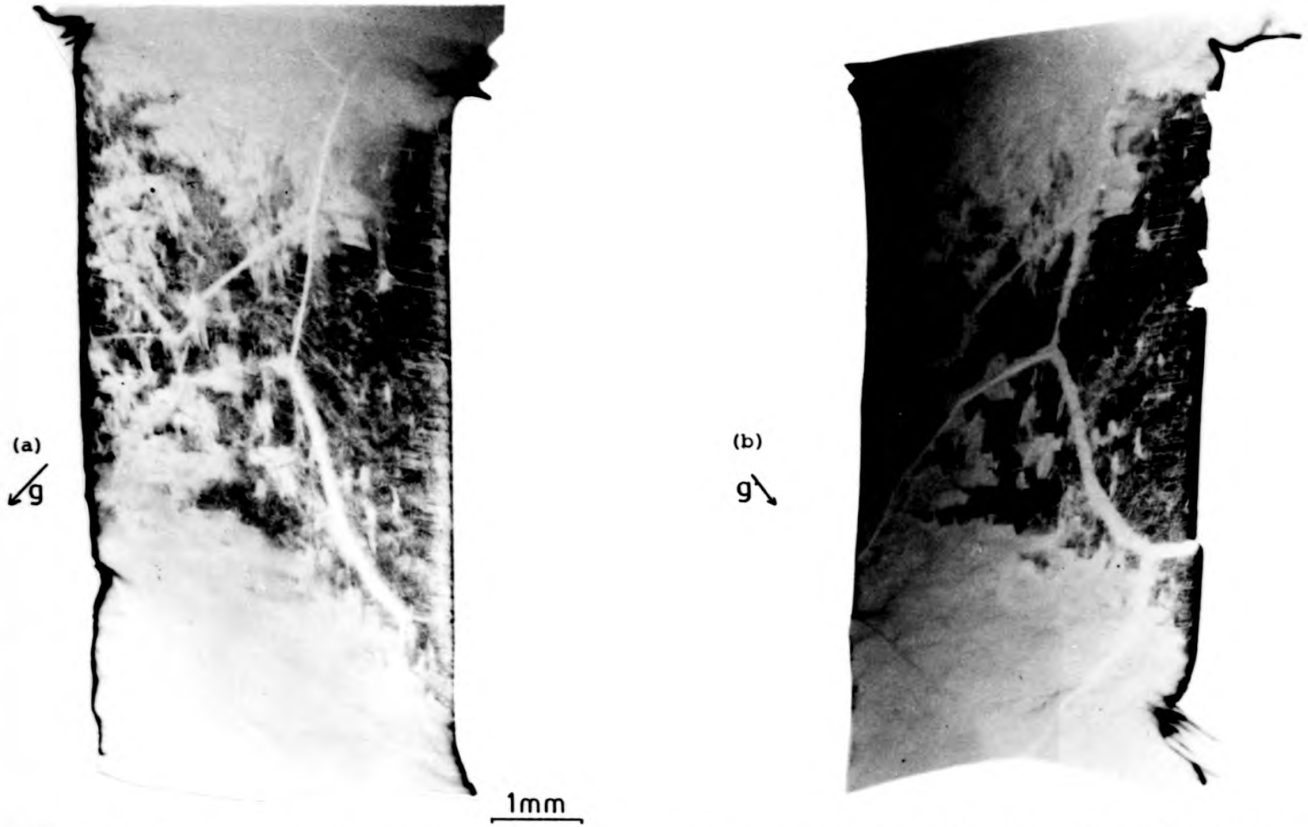

Fig. 59 White beam synchrotron topographs taken from the same plate as Fig. 55b, illustrating the difference in projected direction for the [111] and [$\bar{1}$11] Burgers vectors (a) g = 0$\bar{2}$0 (b) g = 00$\bar{2}$ (λ = 0.9Å)

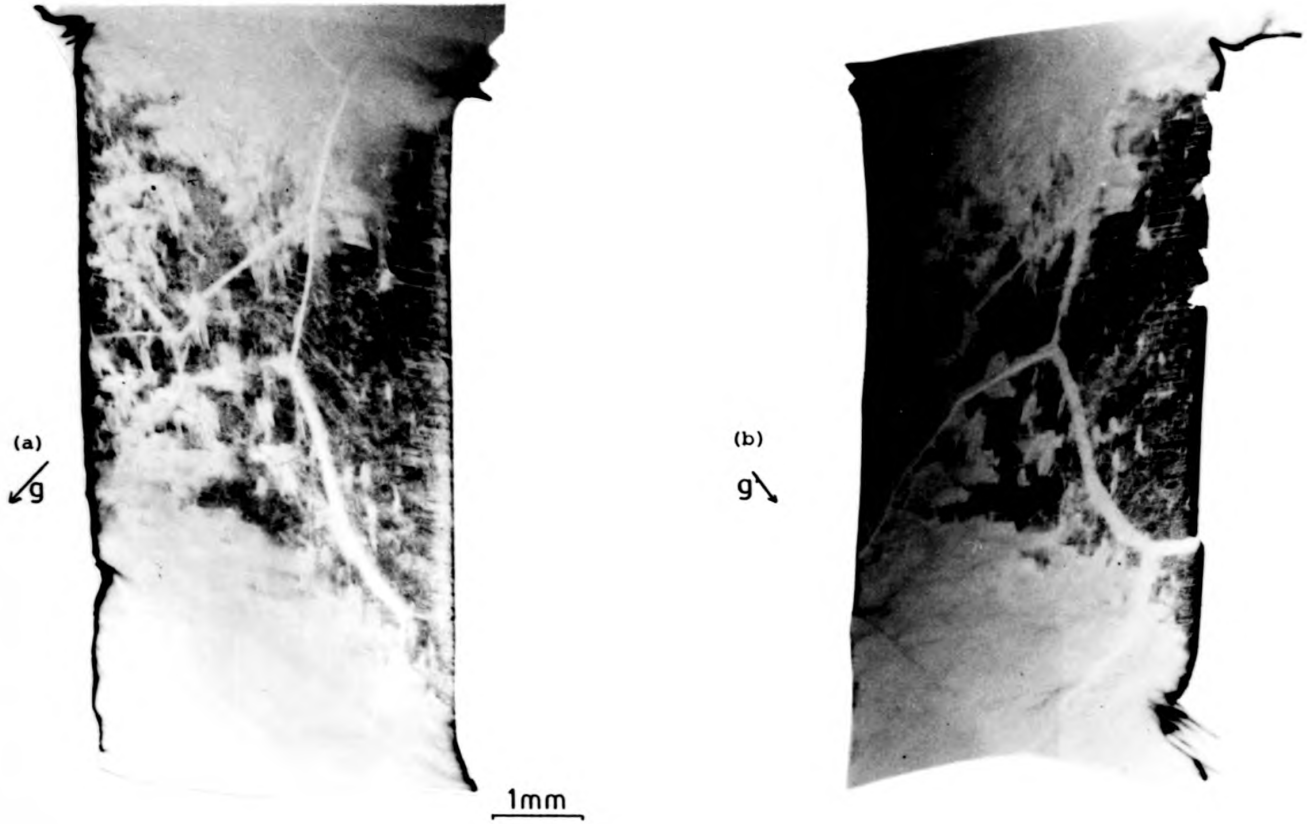

Fig. 59 White beam synchrotron topographs taken from the same plate as Fig. 55b, illustrating the difference in projected direction for the [111] and [$\bar{1}$11] Burgers vectors (a) g = 0$\bar{2}$0 (b) g = 00$\bar{2}$ (λ = 0.9Å)

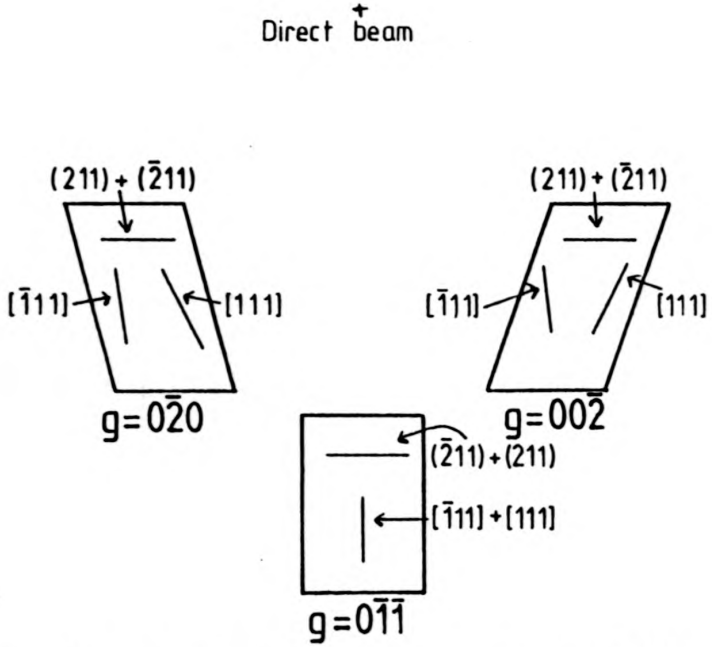

Fig 60 Sketch of the projection on various reflections of the {211} plane intersections with the surfaces, and the <111> Burgers vectors, superimposed on the predicted image shapes, for crystal C1 in the 011 main spot geometry

$(211)[\bar{1}11]$ both having Schmid factors of 0.47. On the $0\bar{1}\bar{1}$ spot the traces of the $(\bar{2}11)$ and (211) planes on the specimen surface are seen to project perpendicular to the tensile axis, and the corresponding Burgers vectors project parallel to the tensile axis. On the 200 spots the two {211} plane intersections with the surface project along the same direction (note geometric distortion), but there is a difference in projected direction for the two Burgers vectors, on both the $00\bar{2}$ and $0\bar{2}0$ reflections. This is readily observed on Fig. 59. In general results obtained on the plates agree well with the predicted projective geometry for $(\bar{2}11)[111]$ and $(211)[\bar{1}11]$ slip systems.

6.1.2 Projected Thicknesses

Table III shows a list of projected thicknesses (measured parallel to the projection of the tensile axis) for the slip planes projecting in the directions observed above i.e. $(\bar{2}11)$ and (211).

Reflection	Slip Plane Projected Thicknesses (μm)	
	(211)	$(\bar{2}11)$
002	316	316
$0\bar{1}\bar{1}$	342	163.8
$0\bar{2}0$	316	316

Table III

It is often difficult to measure absolute values of projected thicknesses of slip bands, due to contrast effects making it difficult to see the point of intersection

with the entrance surface (see discussion) and also at higher stresses due to slip band overlap. It is usually more informative to talk in terms of the relative projected thicknesses of slip bands. For example it is seen that the projected thickness of (211) planes is twice as great as that of $(\bar{2}11)$ planes in the $0\bar{1}\bar{1}$ reflection. It is possible to find a reasonable correlation between these predictions and the observed results.

It is useful to compare the 200 reflections to the $0\bar{1}\bar{1}$ reflection in order to see which planes are the (211) and which are the $(\bar{2}11)$ planes.

6.1.3 Exit Surface Effects

The small slip cells observed are often bounded by a fine dark line at one or other of the intersections with the specimen surface. This thin dark line can help in distinguishing between the two slip systems. Fig. 61 shows how a knowledge of the geometry of these intersections and the diffraction geometry can help in this way.

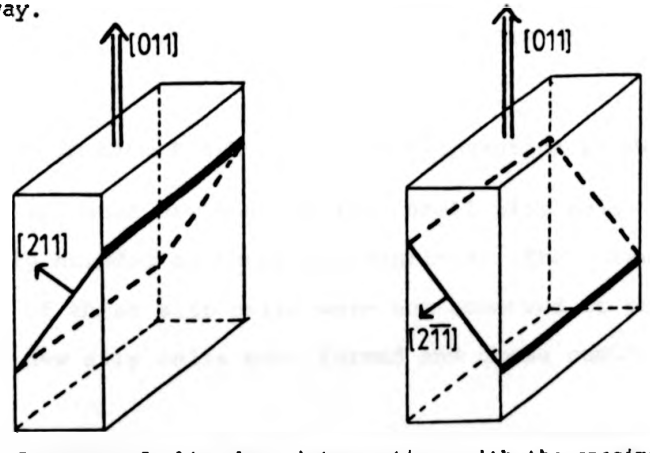

Fig 61 Geometry of slip plane intersections with the specimen surfaces in C1

In X-ray topography, contrast of a defect is very sensitive to its position with respect to the exit surface (see discussion). Due to propagation of wave-fields within the Borrmann fan, a smearing of contrast from a defect far from the exit surface is expected, and finer and clearer contrast is expected the closer the defect to the X-ray exit surface.

In the case of the (211) slip plane better contrast is expected from the upper part of the slip plane as projected on the plate, whilst the converse is true for $(\bar{2}11)$ slip.

It is possible to correlate data on the projected direction of the Burgers vector of a particular slip cell (expecially on 200 reflections in the $0\bar{1}\bar{1}$ main spot geometry) with the contrast observed in the slip cell and the sensitivity of this contrast to the position of the cell with respect to the exit surface. This sort of correlation can be seen in Figs. 55 and 59.

This contrast effect due to the proximity of sections of a slip cell to the exit surface is also clearly seen on the series of video stills shown in Fig. 57.

6.1.4 Slip Line Morphology, and Propagation Evidence

Slip bands are made up from small slip cells probably bounded by screw dislocations. The screw fronts of these slip cells were not observed to propagate, rather new slip cells were formed and these cumulated

side by side. Propagation of screw dislocations is thought to be hindered by the inherent low mobility of screw dislocations in the bcc lattice (see discussion). Propagation of the edge fronts of slip bands on the other hand, was readily observed. These observations have been frozen onto the still photographs presented.

6.1.5 Lattice Rotation

Both on the series of video stills, and the White Radiation topographs, there is a considerable lattice rotation observed. This rotation tends to reduce the Bragg angle for the $0\bar{1}\bar{1}$ spot. This rotation is hindered (and opposed) by the presence of the grips. The image of the bulk of the crystal is seen to fold back onto the image of the crystal near the grips.

If this rotation is homogeneous throughout the crystal, an orientation of slip direction with respect to the incident beam such as shown in Fig. 62 would be required in order to give the correct sense of rotation.

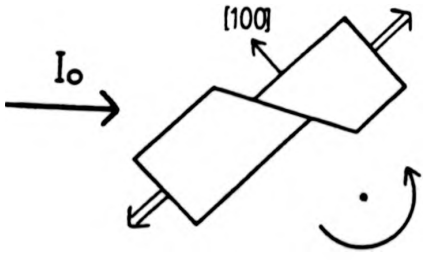

Fig 62 Orientation of slip direction with respect to the incident beam I_o, required for observed lattice rotation

However it is conceivable that due to the presence of two slip systems, this rotation will not be homogeneous. This will be entered into in detail in the discussion.

6.1.6 Luders Band Observations and Rotation Boundary Contrast

Fig. 55 shows a dark line which is seen to progress across the crystal as deformation increases. This dark line separates a region of considerable deformation and a region of lesser deformation. The origin of the contrast effect observed will be discussed later. It is worth noting that this boundary moves away from the end of the crystal where fracture eventually occurred, i.e. the end where slip was most extensive.

6.1.7 Nucleation Evidence

It is worth mentioning here, the generally bad quality of the crystal. Dislocation density remained relatively high, even after the anneal. Also, the deformation experiment on C1 was not performed in an inert atmosphere. This means that the surface of the specimen corroded after exposure to the beam. This will tend to degrade the topographic image quality to a certain extent. This made it difficult to pinpoint precise sites for the initiation of slip. One can say, however, that nucleation was homogeneous throughout the specimen and almost catastrophic, as soon as the elastic limit was surpassed.

6.2 Crystal C2 (T = [011], N = [100]

Fig. 43 shows conventional Lang topographs of crystal C2 taken before deformation, after one and two anneals, respectively. Although change in dislocation density is apparent, it still remains relatively high ($> 10^2$ cm^{-2}).

Fig. 63 shows Synchrotron White Radiation topographs taken before deformation, using the $00\bar{2}$ main spot geometry, and Fig. 64 shows White Radiation topographs from the same geometry taken after deformation.

Fig. 65 shows a series of video stills taken of crystal C2 at various levels of stress, using the $00\bar{2}$ reflection from the $00\bar{2}$ main spot geometry.

Fig. 66 shows White Radiation topographs taken after deformation in the $0\bar{1}1$ main spot geometry.

Fig. 67 shows some reflections from the $0\bar{1}\bar{1}$ main spot geometry, also taken after deformation.

Fig. 68 shows double crystal Synchrotron Radiation topographs taken after deformation. A Ge 220 reflection acted as the monochromator. These reflections used were chosen in order to test the validity of the extinction criterion for dislocations in the slip bands.

Fig. 69 shows a Lang topograph taken of crystal C2 after deformation. Fig. 70 shows the deformation history of C2.

Topographs taken under different conditions will be

Fig 63 White beam synchrotron topographs taken of C2 before deformation (a) $g = 00\bar{2}$, $\lambda = 1.8$Å (b) $g = 0\bar{1}1$, $\lambda = 1.95$Å ($00\bar{2}$ main spot geometry)

Fig 63 White beam synchrotron topographs taken of C2 before deformation (a) $g = \bar{0}0\bar{2}$, $\lambda = 1.8$Å (b) $g = 0\bar{1}\bar{1}$, $\lambda = 1.95$Å ($00\bar{2}$ main spot geometry)

Fig 64 White beam synchrotron topographs taken of C2 after deformation (a) $g = 00\bar{2}$, $\lambda = 1.8$Å (b) $g = 0\bar{1}1$, $\lambda = 1.95$Å ($00\bar{2}$ main spot geometry)

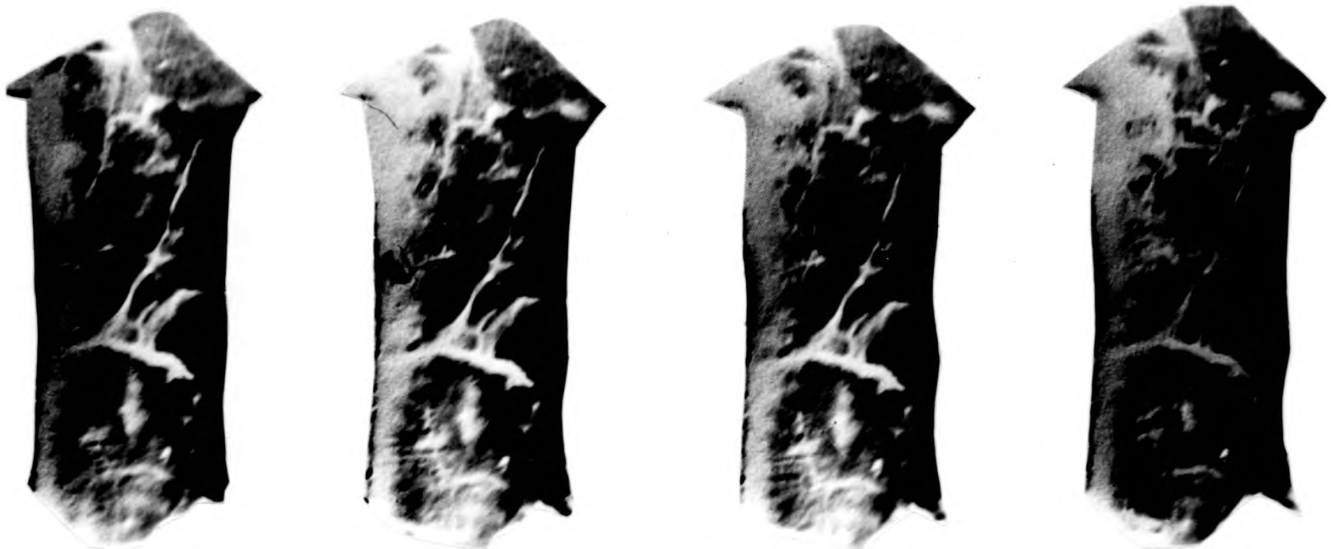

Fig 65

(e) 252.7 MPa (f) 236.8 MPa (g) 230.88 MPa

Fig 65 Still photographs taken from the videotape recording of the $00\bar{2}$ spot, from crystal C2 under deformation at (a) 276.8 MPa (b) 269.4 MPa (c) 261.9 MPa (d) 254.6MPa (e) 252.7 MPa (f) 236.8 MPa (g) 230.88MPa

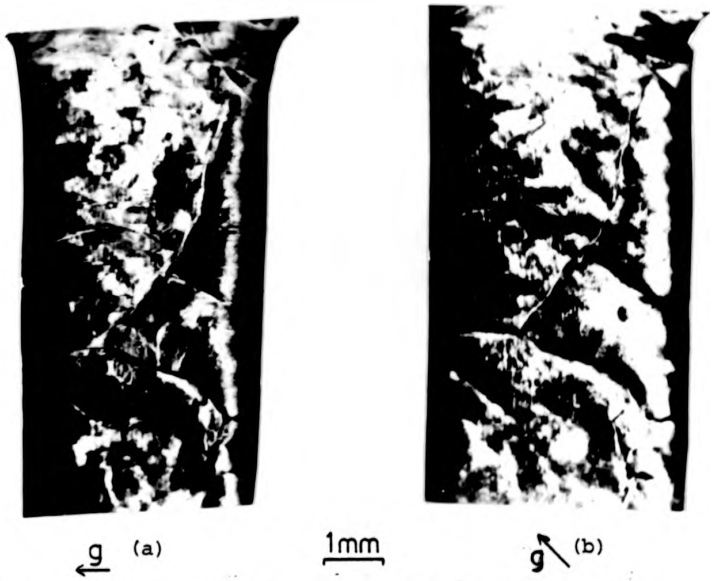

Fig 66 White beam topographs taken in the $0\bar{1}1$ main spot geometry (a) $g = 0\bar{1}1$ $\lambda = 1\text{Å}$ (b) $g = 002$ $\lambda = 0.5\text{Å}$

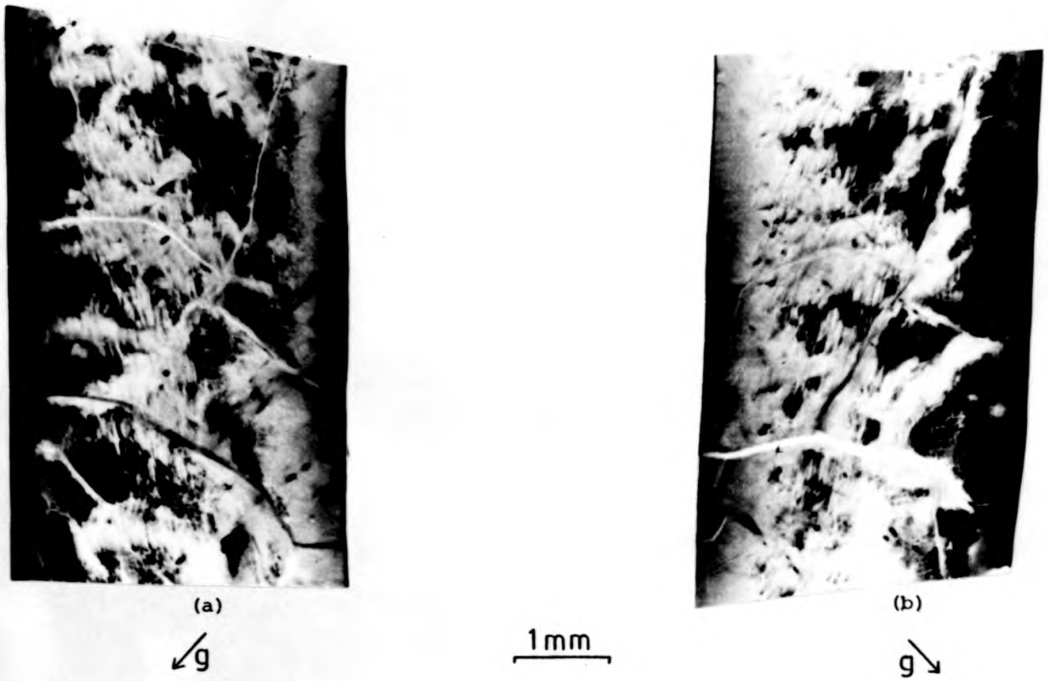

Fig 67 Some reflections taken from the $\bar{O}11$ main spot geometry (post deformation)
(a) $g = 0\bar{2}0$ $\lambda = 0.9\text{Å}$ (b) $g = 00\bar{2}$ $\lambda = 0.9\text{Å}$

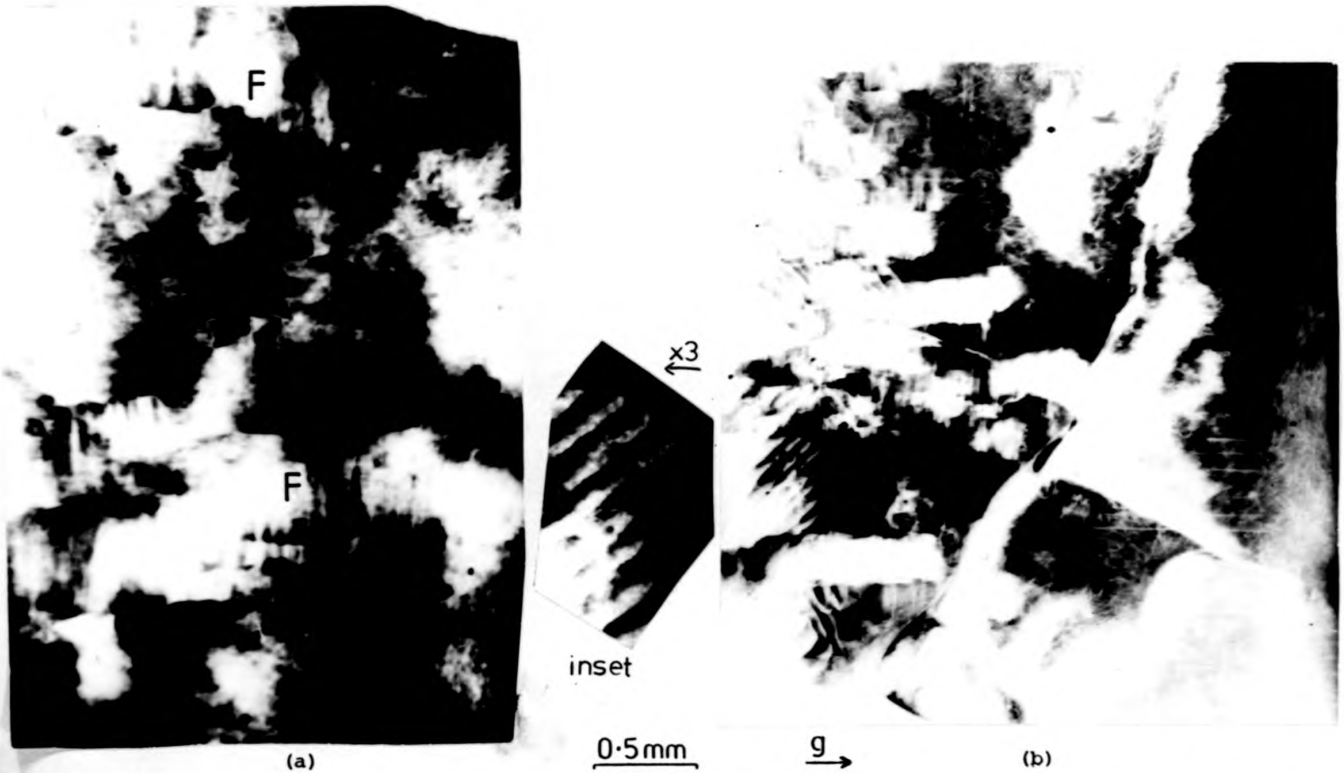

Fig 68 Details from $01\bar{1}$ double crystal topographs taken of C2. (a) Lower grain (illustrating fine slip structure, fringes observed at F are magnetic domain configurations) (b) Upper grains. Residual magnetic domain configurations are seen at M (see inset)

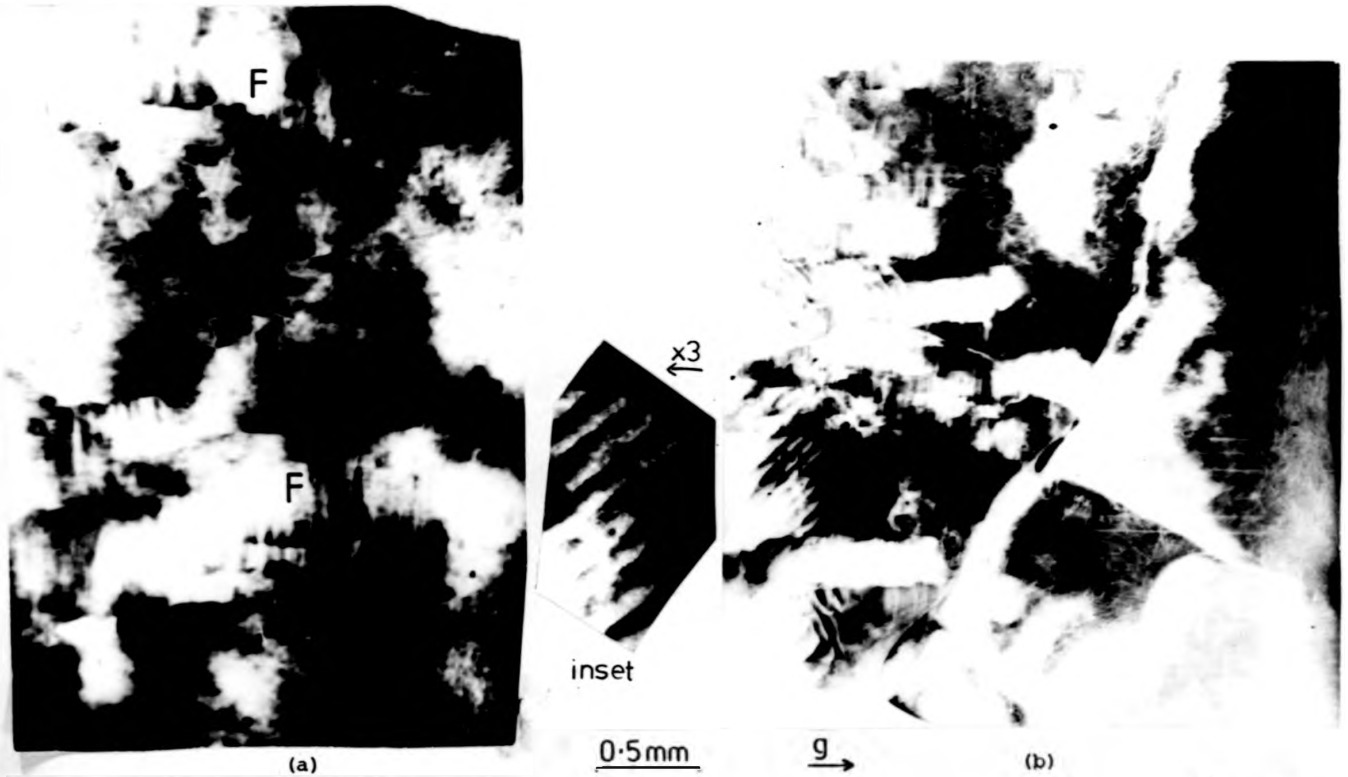

Fig 68 Details from $01\bar{1}$ double crystal topographs taken of C2. (a) Lower grain (illustrating fine slip structure, fringes observed at F are magnetic domain configurations) (b) Upper grains. Residual magnetic domain configurations are seen at M (see inset)

Fig 69 Detail from a Lang topograph taken of C2 after deformation, g ≈ $\overline{222}$ Ag Kα radiation

Fig 69 Detail from a Lang topograph taken of C2 after deformation, g = $\overline{222}$ Ag Kα radiation

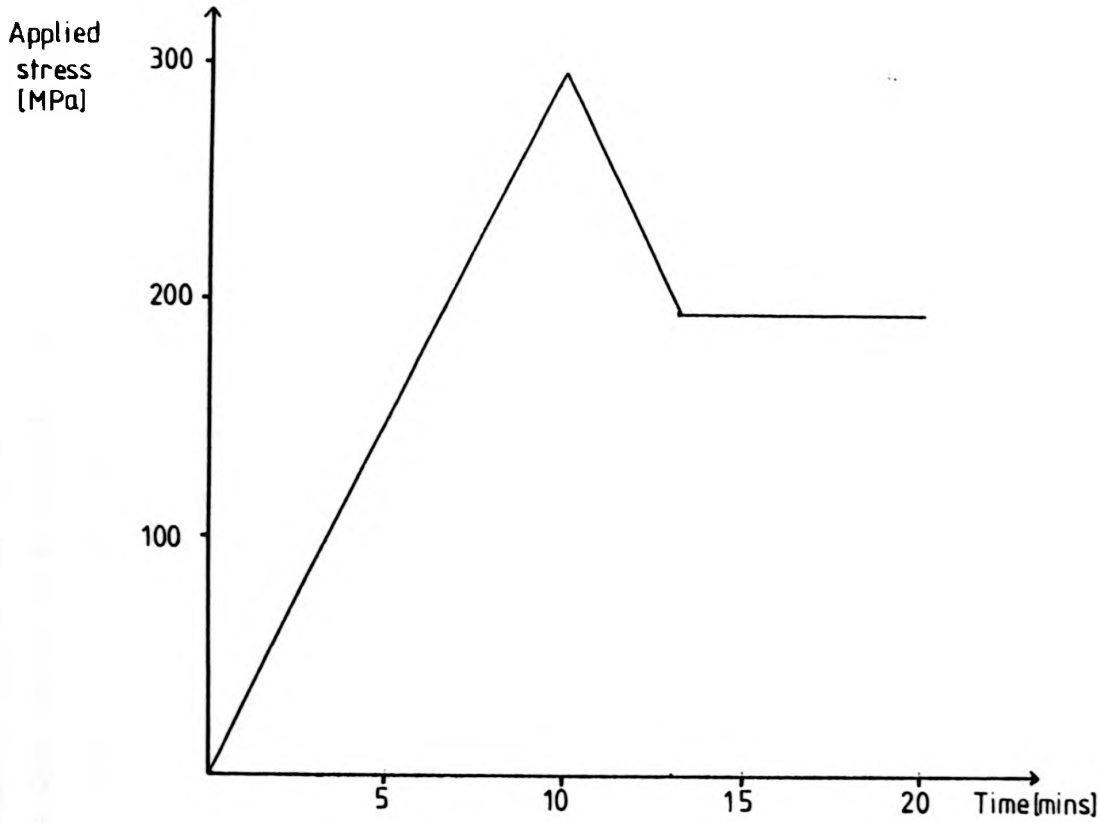

Fig 70 The deformation history of C2

dealt with separately.

6.2.1 $00\bar{2}$ Main Spot Geometry

6.2.1a Projective properties

Fig. 71 shows the predicted projected directions for the highest Schmid factor systems superimposed on the predicted image shapes. Intersections of the two {211} planes of interest are seen to project along the same direction on the $00\bar{2}$ spot and also on the $0\bar{1}\bar{1}$ spot. However the two possible Burgers vectors do not project along the same direction on either of these reflections. Table IV shows the projected thickness of the (211) and $(\bar{2}11)$ slip planes on both the $00\bar{2}$ and $0\bar{1}\bar{1}$ reflections.

Reflection	Slip Plane Projected Thicknesses (μm)	
	(211)	$(\bar{2}11)$
$00\bar{2}$	198	92
$0\bar{1}\bar{1}$	199	78

Table IV

Examination of Fig. 46 confirms the predictions for spot shapes. Examination of Fig. 66 agrees with predictions for the projected directions of the slip band intersections with the surfaces, and also of the projected directions of the operative Burgers vectors.

Again, a reasonable correlation can be made of the predicted and observed projective thickness, especially when using relative values for the two slip systems.

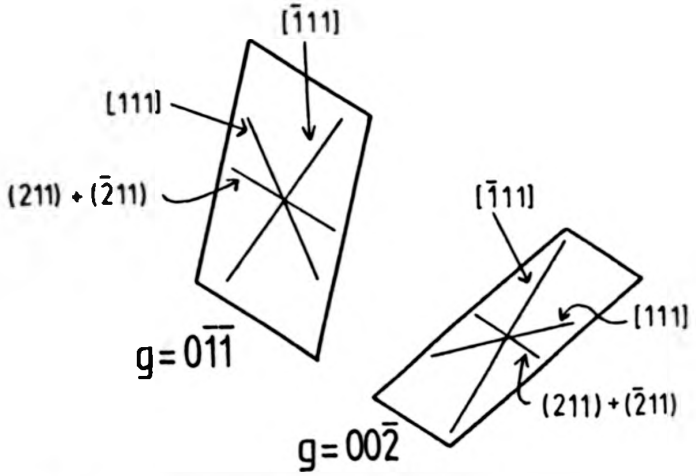

Fig 71 Reconstructed image shapes, projected directions of Burgers vectors and projected directions of slip plane intersections with the surfaces in C2 (00$\bar{2}$ main spot geometry), for the 00$\bar{2}$ and 0$\bar{1}\bar{1}$ reflections. The separation of the spots is arbitrary

As however in C1, contrast effects causing an apparent blurring of the image, and also slip band overlap render the use of absolute projected thicknesses of slip bands rather dubious.

6.2.1b Exit surface effects

The small white slip cells observed in Fig. 66 again show a contrast variation as a function of proximity to the exit surface. This is believed to be a similar effect to that observed in C1 (see discussion).

6.2.1c Slip line morphology and evidence for propagation

As in C1, slip bands are made up from small slip cells, probably bounded by screw dislocations. These slip cells are shown in Fig. 72. It is evident that the slip cells observed on the $00\bar{2}$ reflection are less rectangular than those on the $0\bar{1}\bar{1}$ spot.

This is believed to be due to an effect of the relative sizes of the Borrmann fan in the two reflections, and possibly due to the mode of propagation of the dislocation sources coupled with image forces (active in the anneal) due to the presence of the crystal surfaces. This will be fully investigated in the discussion.

The presence of the two Burgers vectors can be readily seen from these enlargements (Fig. 72).

As in C1 the screw fronts of the slip cells are not seen to propagate, rather, more small slip cells nucleate and accummulate side by side.

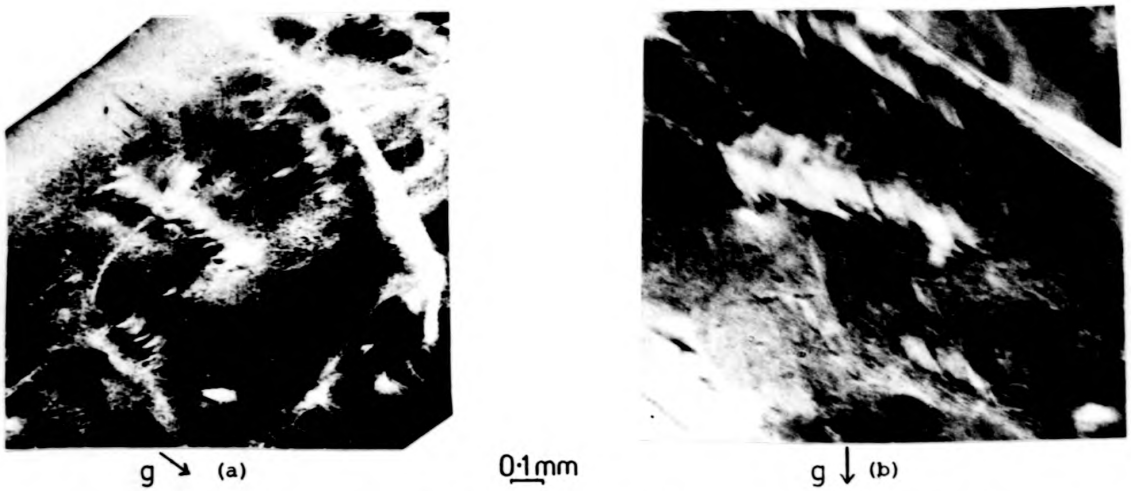

Fig 72 Details from Fig 64, illustrating the morphology of slip cells in C2.
(a) g = 002 (b) g = 011

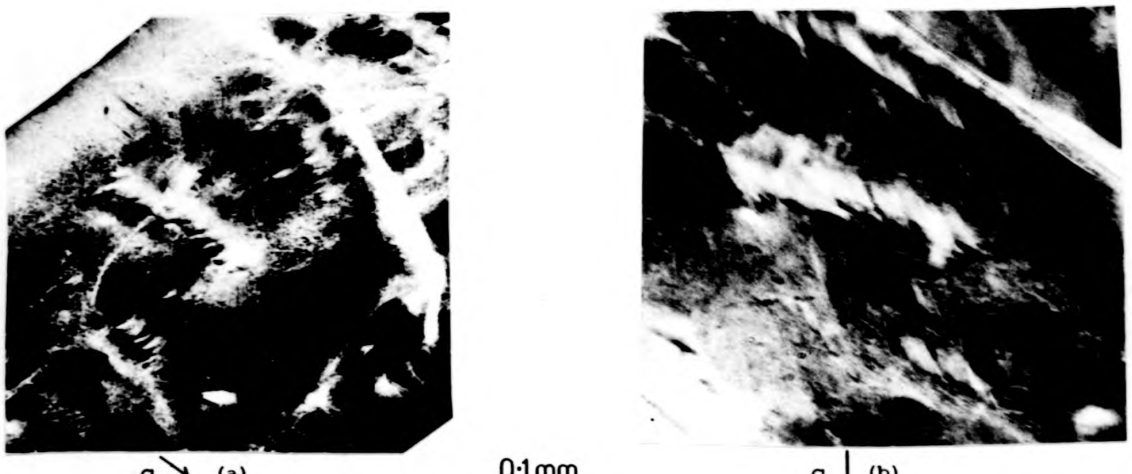

Fig 72 Details from Fig 64, illustrating the morphology of slip cells in C2.
(a) g = 002 (b) g = 011

On investigation of the video stills shown on Fig. 65 , one can see propagation of the edge fronts, through the thickness of the sample. A similar reasoning to that suggested for C1 is postulated, (see discussion).

6.2.1d Nucleation evidence

It is useful here to compare the video stills and the predeformation Lang topograph (Fig. 43) and White Beam Synchrotron topograph Fig. 63. Again it is difficult to get an exact correlation between topographs and video stills due to the relatively high dislocation density present, but unlike C1, C2 was deformed in a Helium atmosphere, so the problem of rusting detericrating the topographic contrast did not arise.

Slip cells are seen to nucleate at what appears tc be a dislocation tangle in the upper central subgrain. Others are seen to start at what appears to be a precipitate in the bottom subgrain. It is, in general, difficult to differentiate between precipitate contrast and the high background density of dislocations. Slip can also be seen nucleating at or close to the subgrain boundary at the bottom of the central top subgrain.

The video stills illustrate the catastrophic nature and homogeneity of slip. The series shown were taken from a section of videotape comprising less than half a minute. A certain amount of creep occurred after the stress was relaxed.

6.2.2 $0\bar{1}1$ Main Spot Geometry

6.2.2a Projective properties

Fig. 73 shows the predicted geometry of projections on the plate. On all the reflections chosen, the two {211} plane surface intersections project along the same line. On various reflections, there is a difference in projected direction between the [111] and $[\bar{1}11]$ directions. This fits in nicely with observations on the plate. Table V shows the list of projected thicknesses of the two slip planes on the various reflections.

Reflections	Slip Plane Projected Thicknesses (μm)	
	(211)	$(\bar{2}11)$
$0\bar{2}0$	193	131
$0\bar{3}1$	187	138
$0\bar{1}1$	162	162
002	131	193

Table V

The relative values of these projected widths agree fairly well with observations on the plate.

6.2.2b Exit surface effects

In general these are not as clear cut as in other geometries, due to slip band overlap. However, similar effects to those observed in other geometries are evident on more isolated slip bands.

6.2.2c Slip line morphology, propagation evidence and nucleation evidence

It is difficult to distinguish between separate slip

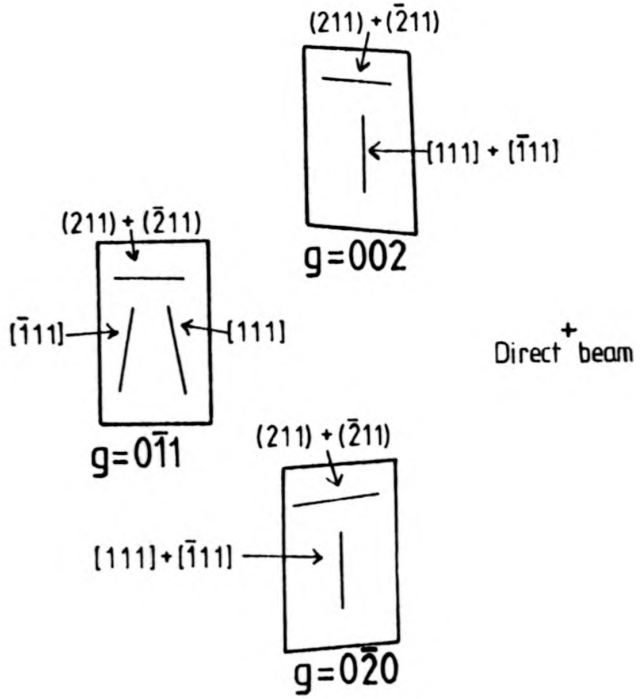

Fig 73 Predicted geometry of projections of slip planes and Burgers vectors in the 011 main spot geometry

cells, due to overlap. In this geometry, diffraction occurs in the horizontal plane and so the resolution will not be as good due to the shape of the source (it will in fact be four times worse for horizontal diffraction than for vertical diffraction). However, even through areas of overlap it is possible to see the screw fronts of the slip cells, stacking side by side.

As plates in this orientation were taken after deformation it was not possible to extract any evidence on propagation or nucleation.

6.2.3 $0\bar{1}\bar{1}$ Main Spot Geometry

The projective properties of this diffraction geometry have already been described for C1. There will however be differences in projected widths of bands due to the different thickness of the crystal, although the ratios of the projected thicknesses of (211) and ($\bar{2}$11) planes will remain the same.

The results obtained in this geometry for C2 are very similar to those for C1. The presence of both Burgers vectors in unequal amounts can again be clearly observed.

6.2.4 Double Crystal Synchrotron Topographs

The reflections used here were chosen in order to test the validity of the extinction rule for the dislocation in the slip bands. Each of the reflections gives a g.b = 0 value for one or other of the operative Burgers vectors. For screw dislocations this should be

the criterion for invisibility. For edge dislocations, the usual criterion is $\underline{g}.\underline{b}\times\underline{u} = 0$ and $\underline{g}.\underline{b} = 0$ (where $\underline{u}$ is the line direction). Reflections obeying this rule are also shown, see Fig. 68.

It is reasonable to conclude that the extinction rule for dislocations does not apply to the dislocations in slip bands in Fe Si.

However, the double crystal topographs do illustrate the fine structure of slip cells present (these topographs will have a higher resolution than the White Beam topographs).

The difference in contrast between those parts of a slip band closest and furthest from the exit surface are still present and is clearly observable even for $\bar{1}11$ Burgers vectors. These conditions, whilst still in the integrated image regime will be more sensitive to long range strain fields.

As the radiation is monochromatic not all the crystal contributes to the image simultaneously, due to the misorientation between subgrains.

One advantage of using the 2° crystal method is that no rusting of the sample due to ozone production on the surface occurs with monochromatic radiation. Another is the low background noise and generally 'clearer images'.

Fig. 74a shows a detail of a Lang topograph taken before deformation, showing clearly the grown in dislocation structure. Fig. 74b shows a detail from a

Fig 74a Lang topograph ($g = 0\bar{1}\bar{1}$, Mo Kα radiation) taken before deformation of the same region of crystal as in Fig. 74b

Fig 74b Detail of double crystal topograph ($g = 01\bar{1}$, $\lambda = 0.85\text{Å}$) taken of C2 after deformation, showing the dislocation structure in a subgrain near the edge of the crystal

Fig 74b Detail of double crystal topograph ($g = 01\bar{1}$, $\lambda = 0.85\text{Å}$) taken of C2 after deformation, showing the dislocation structure in a subgrain near the edge of the crystal

double crystal synchrotron topograph (same reflection) taken after deformation. It is readily seen that the 'grown in' dislocations near the specimen edge, whilst moving under the effect of an anneal (Fig. 43) are not affected by the deformation, or at least this is true for those dislocations situated near the edge of the specimen, where no slip bands formed.

However it is likely that the grown in dislocations are the nucleation points in the body of the crystal.

6.2.5 Lang Topographs

Fig. 69 shows a Lang topograph ($g = \bar{2}22$) taken of C2 after deformation. As is shown on the schematic diagram (Fig. 75), the $(\bar{2}11)$ slip plane should have a very thin projected width under these conditions, whereas the (211) plane should have a relatively large projected width. This can be seen on this topograph. The narrow projected width of the $(\bar{2}11)$ bands makes it possible to resolve small slip cells forming a step pattern, side by side, which merge together on other White Beam topographs already presented .

As this deformation experiment was not taken as far as that with C1, no appreciable effect of lattice rotation is observed.

6.2.6 Summary of Evidence for C1 and C2

Evidence points to mainly $(\bar{2}11)[111]$ slip with a smaller amount of $(211)[\bar{1}11]$ slip.

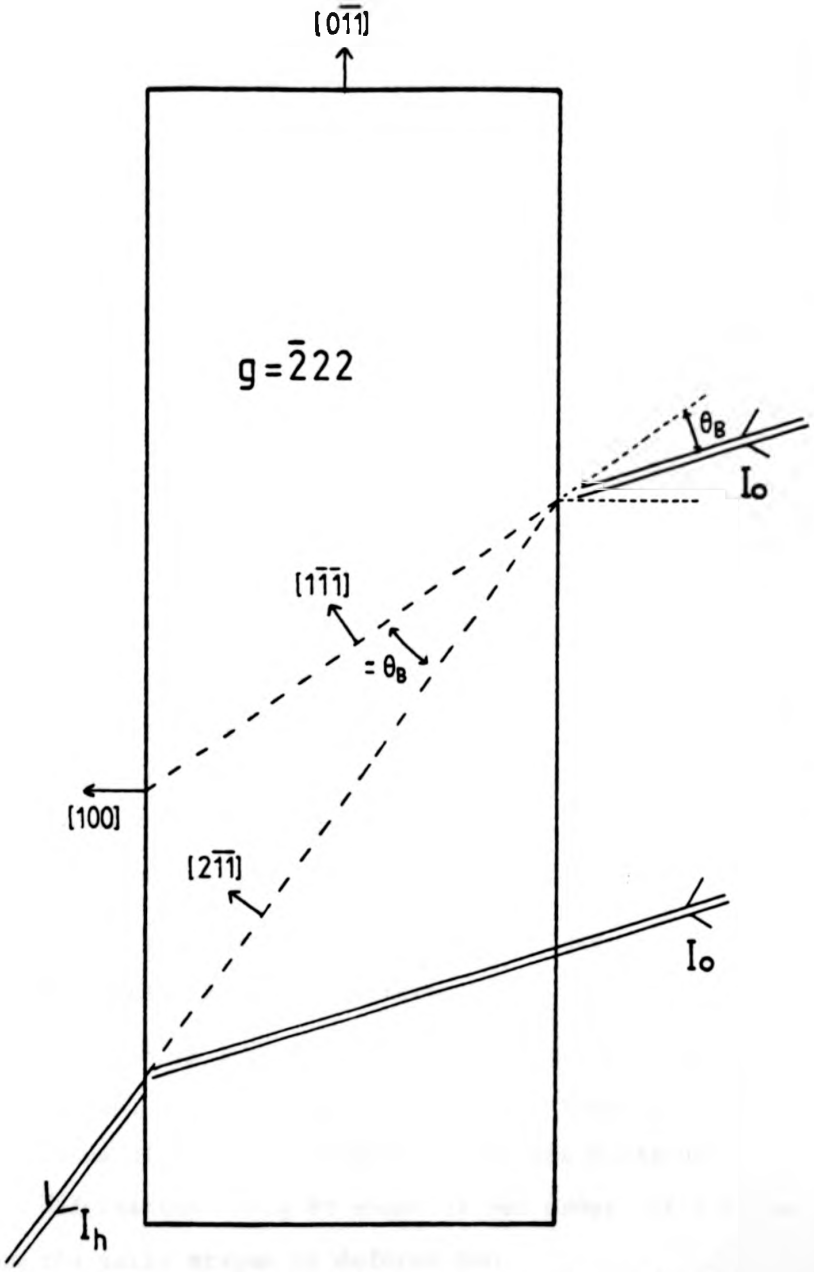

Fig 75 Plan of geometry of $\bar{2}22$ reflection (Ag Kα radiation). The I_h direction is almost coincident with the trace of the ($\bar{2}11$) slip plane

These are the maximum resolved shear stress systems (see discussion).

6.2.7 Etch Pitting

Fig. 76 shows optical micrographs taken of the surface of the crystal after post deformation etch pitting (see section 3.2.5). Slip bands are clearly discernible, and pits from individual dislocations in the slip bands can be resolved. The spacing between dislocations can be measured. This was found to be $\sim$ 10 μm. This will be useful in understanding the contrast arising from slip bands (see section 7.2.4).

6.3 Crystal C3 T = [011], N = [0$\bar{1}$1]

Fig. 77 shows a Lang topograph of crystal C3 taken before deformation. The crystal is generally of better quality than C1 and C2, in that the dislocation density is much lower. Fig. 78 shows a series of Synchrotron White Beam topographs taken at various increasing levels of stress in the 0$\bar{1}\bar{1}$ main spot geometry. Propagation of glide bands is readily observed from one stage to the next. Two slip systems are evident.

Fig. 79 shows a series of video stills taken of C3 at various increasing levels of stress.

Also presented, in Fig. 80 are Lang topographs taken after deformation, and White Beam Synchrotron topographs (Figs. 81, 8 taken in various diffraction geometries (at SRS Daresbury) also after deformation. Fig 83 shows higher order reflections taken from the early stages of deformation.

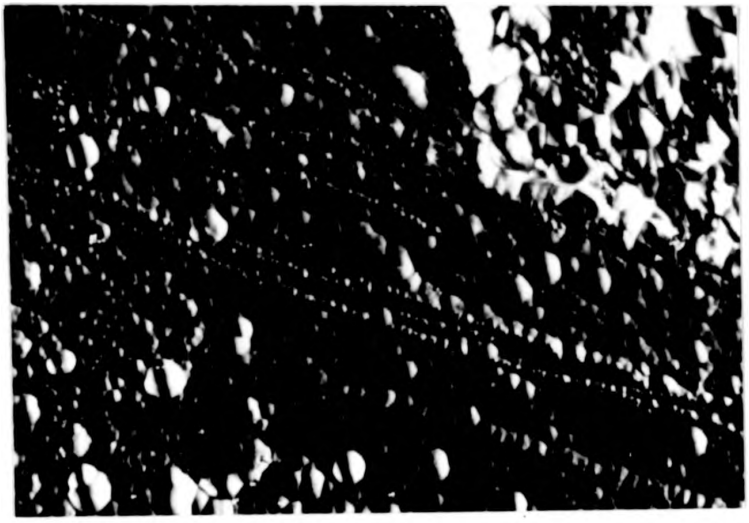

(a)

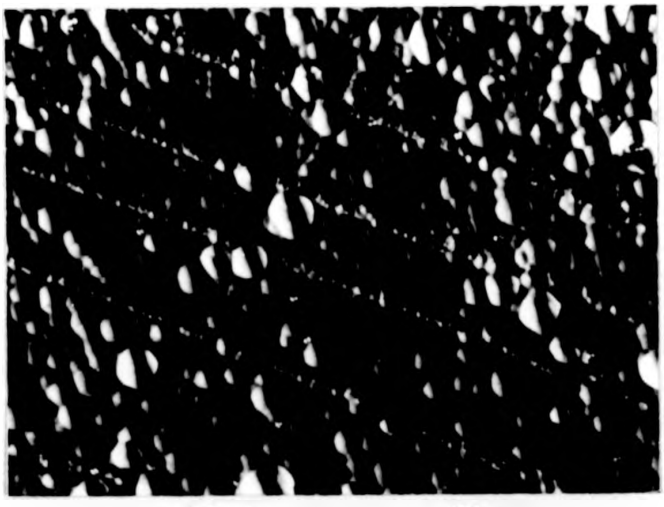

0·1 mm

(b)

Fig 76

(c)

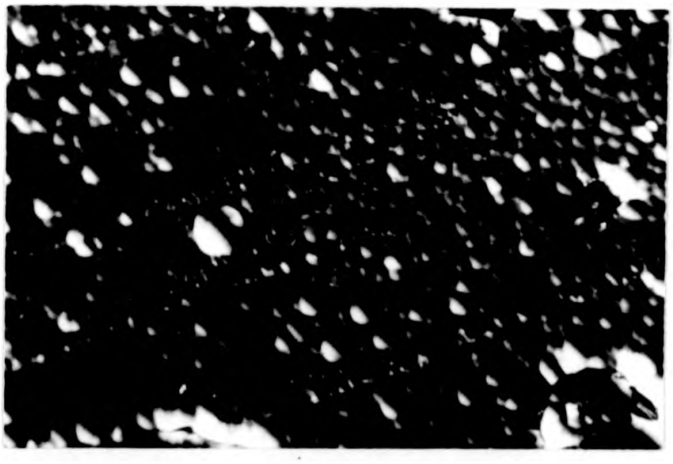

(d)

Fig 76 Details from optical micrographs taken of the surface of C2, after post deformation etch pitting. Approximate dislocation spacings can be determined

Fig 77 Predeformation Lang topograph of C3, g = 200 Mo Kα radiation. S indicates subgrain boundary, P precipitates, D dislocations, M magnetic closure domains.

(a) 0 Stress

↓g

1mm

(b) 251.4 MPa

Fig 78

(c) 251.5 MPa

(d) 226.2 MPa

(e) 100.6 MPa

Fig 78 Series of synchrotron white beam topographs ($g = 0\bar{1}\bar{1}$) taken from the $0\bar{1}\bar{1}$ main spot geometry at (a) 0 Stress (b) 251.4 MPa (c) 251.5 MPa (d) 226.2 MPa (e) 100.6 MPa ($\lambda = 1.96\text{Å}$)

(c) 251.5 MPa

(d) 226.2 MPa

(e) 100.6 MPa

Fig 78 Series of synchrotron white beam topographs ($g = \bar{0}\bar{1}\bar{1}$) taken from the $\bar{0}\bar{1}\bar{1}$ main spot geometry at (a) 0 Stress (b) 251.4 MPa (c) 251.5 MPa (d) 226.2 MPa (e) 100.6 MPa ($\lambda = 1.96\text{Å}$)

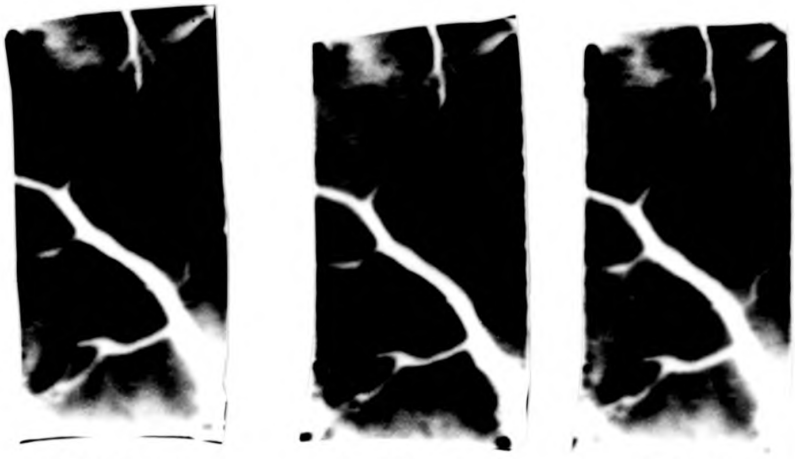

(a) 167 MPa (b) 170 MPa (c) 192.7 MPa

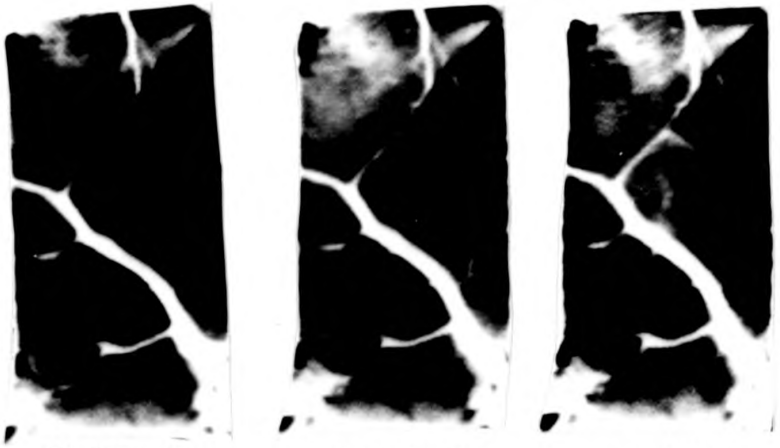

(d) 206.1 MPa (e) 209.4 MPa (f) 232.9 MPa

Fig 79

1mm

g

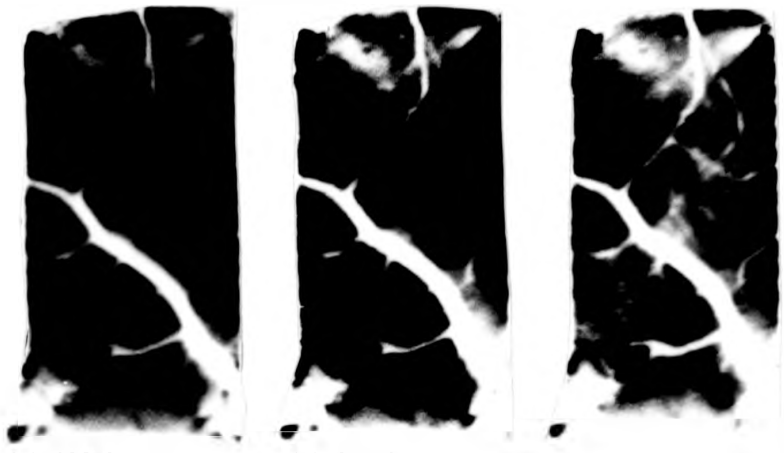

(g) 238.2 MPa (h) 240.9 MPa (i) 243.5 MPa

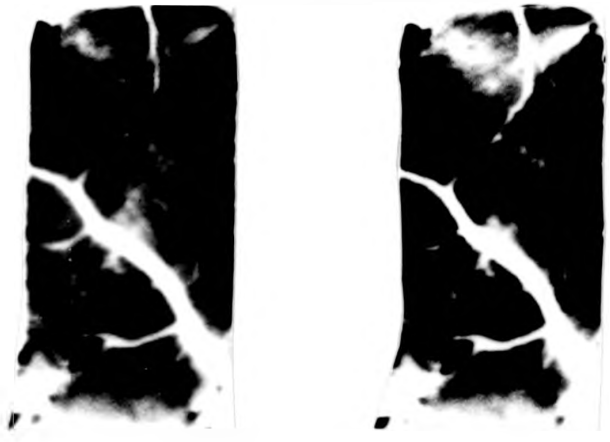

(j) 246.3 MPa (k) 251.4 MPa

Fig 79 Series of still photographs taken from the videotape recording of the 011 reflection (in the 011 main spot geometry) in C3 under deformation at (a) 167 MPa (b) 170 MPa (c) 192.7 MPa (d) 206.1 MPa (e) 209.4 MPa (f) 232.9 MPa (g) 238.2 MPa (h) 240.9 MPa (i) 243.5 MPa (j) 246.3 MPa (k) 251.4 MPa

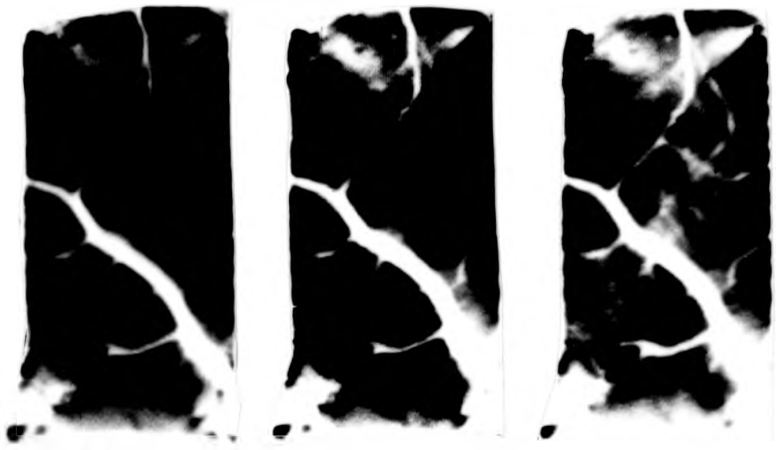

(g) 238.2 MPa (h) 240.9 MPa (i) 243.5 MPa

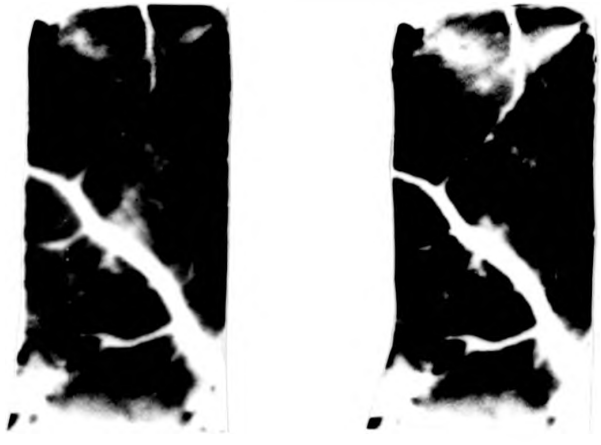

(j) 246.3 MPa (k) 251.4 MPa

Fig 79 Series of still photographs taken from the videotape recording of the O11 reflection (in the O11 main spot geometry) in C3 under deformation at (a) 167 MPa (b) 170 MPa (c) 192.7 MPa (d) 206.1 MPa (e) 209.4 MPa (f) 232.9 MPa (g) 238.2 MPa (h) 240.9 MPa (i) 243.5 MPa (j) 246.3 MPa (k) 251.4 MPa

Fig 80a Detail from Lang topograph of C3, g = $\overline{211}$, MoKα radiation

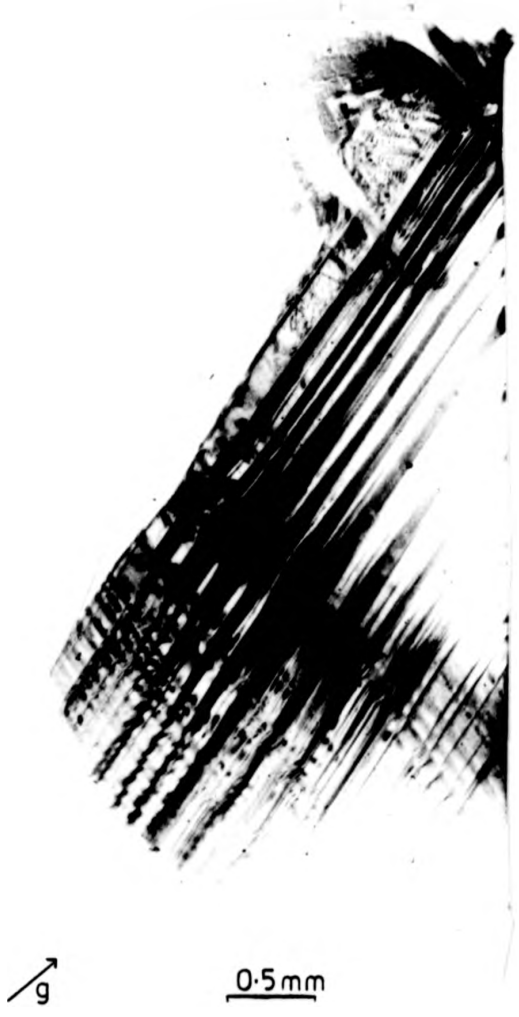

Fig 80b Detail from Lang topograph of C3, g = 211, MoKα radiation. This is the stereo pair topograph of the top right hand section of Fig 80a

Fig 80c Lang topograph of C3, g = $\bar{2}11$, MoKα radiation

Fig 80d Lang topograph of C3, $g = 2\bar{1}\bar{1}$, MoKα radiation. This is the stereo pair to Fig 80c

Fig 81a $\bar{0}11$ reflection taken from Synchrotron white beam topograph (SRS) Daresbury) taken in $\bar{2}22$ main spot geometry. λ = 1.18Å
Note reappearance of Dijkstra and Martius type I magnetic domain structure, with associated fringes at F.

Fig 81b $\overline{222}$ main spot reflection taken at SRS Daresbury.
$\lambda = 0.6\text{Å}$

Fig 81c $\overline{211}$ reflection taken from $\overline{222}$ main spot geometry
$\lambda = 0.8\text{Å}$

Fig 82a $\bar{2}\bar{2}2$ reflection taken in $2\bar{1}\bar{1}$ main spot geometry. λ = 0.57Å

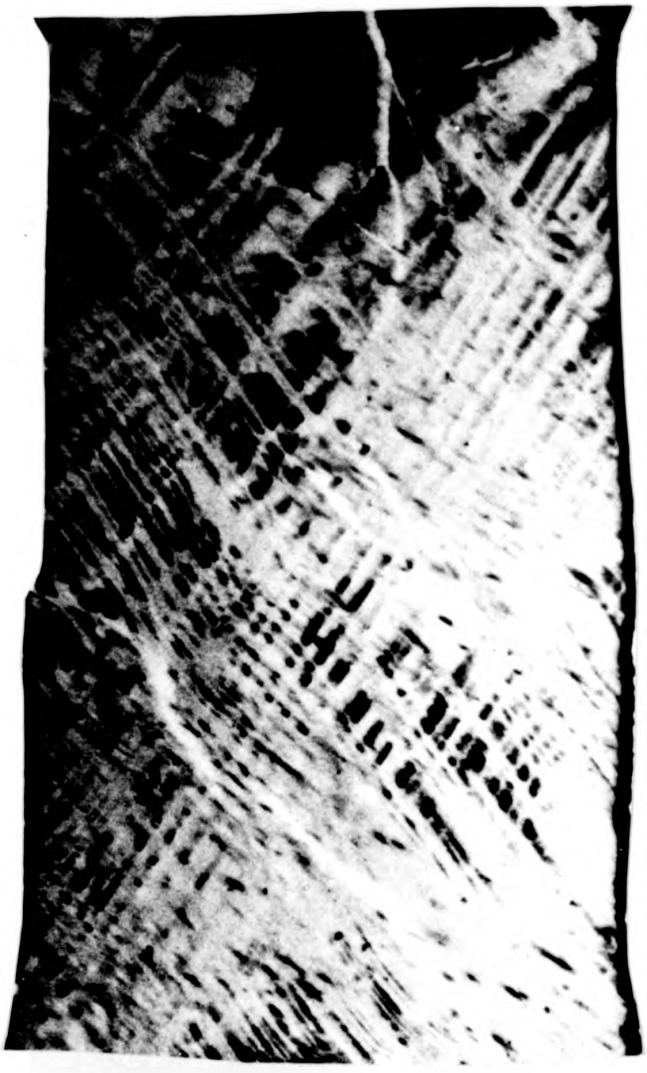

Fig 82b $2\bar{1}\bar{1}$ main reflection. λ = 0.85Å

Fig 82c 200 reflection taken from $2\bar{1}\bar{1}$ main spot geometry
$\lambda = 0.84\text{Å}$

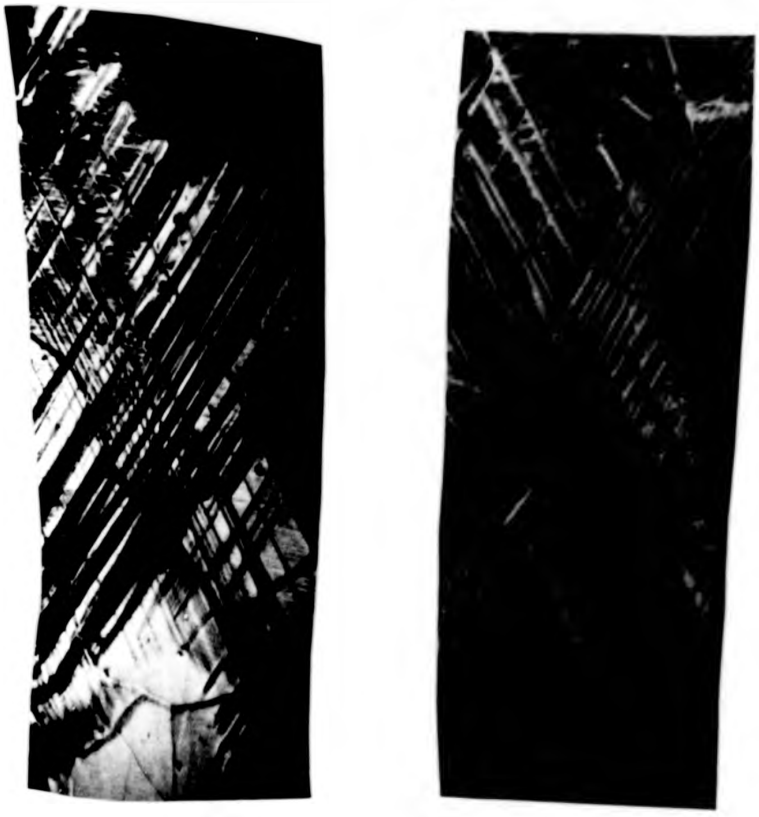

Fig 83 Topographs from $0\overline{11}$ main spot geometry for C3, (a) g = $\overline{211}$ λ = 0.6Å, (b) g = $2\overline{11}$ λ = 0.7Å

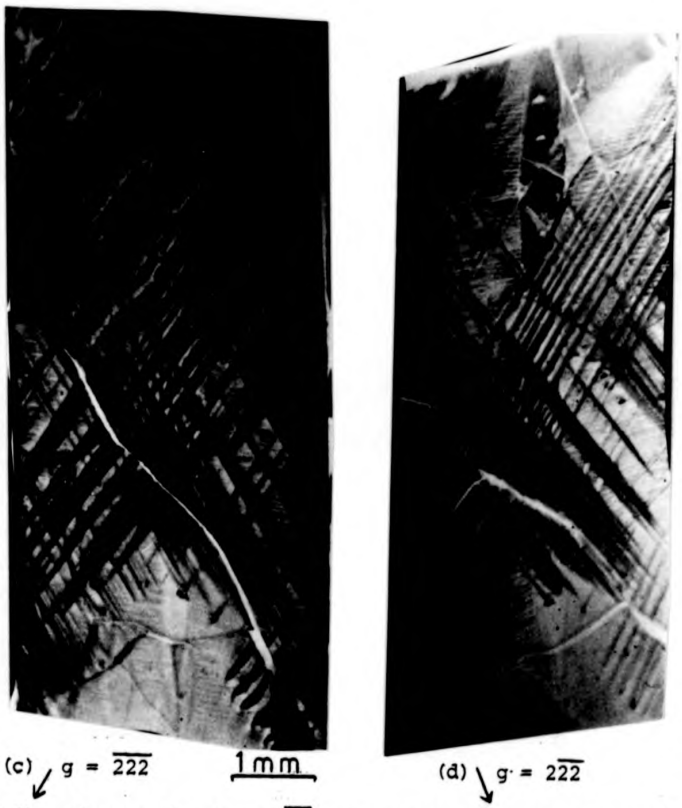

Fig 83 (contd) Topographs from $0\overline{11}$ main spot geometry, (c) g = $\overline{222}$ λ = 0.63Å, (d) g = $2\overline{22}$ λ = 0.68Å

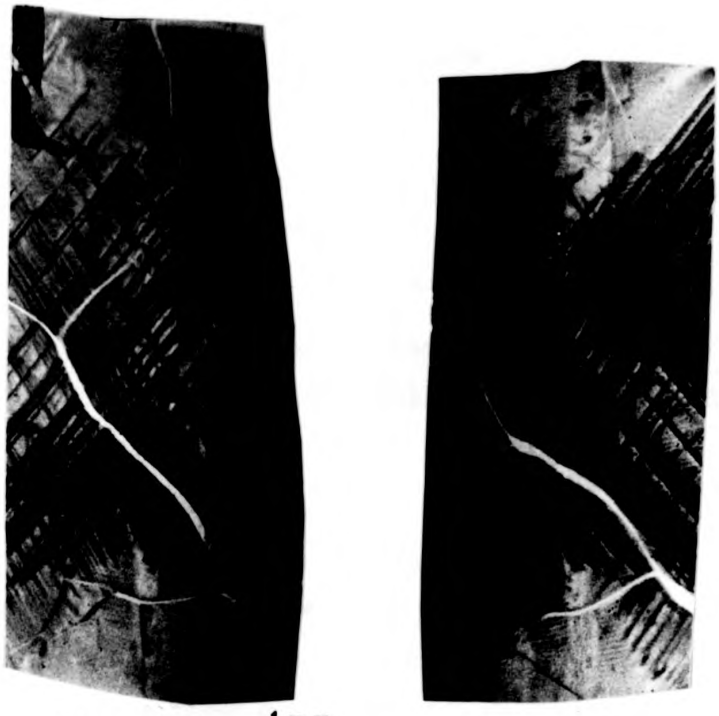

Fig 83 (contd) Topographs from $0\overline{11}$ main spot geometry, (e) g = $\overline{233}$ λ = 0.522Å, (f) g = $2\overline{33}$ λ = 0.55Å

Fig. 84 shows an optical micrograph taken using oblique illumination, of the exit surface of the crystal, taken after deformation.

6.3.1 White Beam Results from DCI, LURE

6.3.1a Projected geometry

Fig. 85 shows a sketch of the predicted image shapes for the $0\bar{1}\bar{1}$ main spot geometry, and also some useful projected directions. This can be compared to Figs. 48,78,83.

As for C1 and C2 the maximum resolved shear stress systems are $(\bar{2}11)[111]$ and $(211)[\bar{1}11]$ both having Schmid factors of 0.47.

The intersections of the (211) and $(\bar{2}11)$ planes with the specimen surface are seen to project in the same directions as the {110} planes in the same zone. The two corresponding {111} Burgers vectors project along the same directions as these planes.

In order to distinguish whether the slip bands are in fact {211} type or {110} type it is necessary to compute the projected widths of these slip bands for various reflections.

6.3.1b Projected widths

The projected widths of possible slip bands are presented in Table VI .

From Fig. 85 it can be seen that on each reflection the $(\bar{2}11)$, $(\bar{1}01)$, $(1\bar{1}0)$ planes project along the same

Fig 84 Optical micrograph taken of the exit surface of C3 after deformation (the sense of the negative was reversed in order to ease comparison with the topographs)

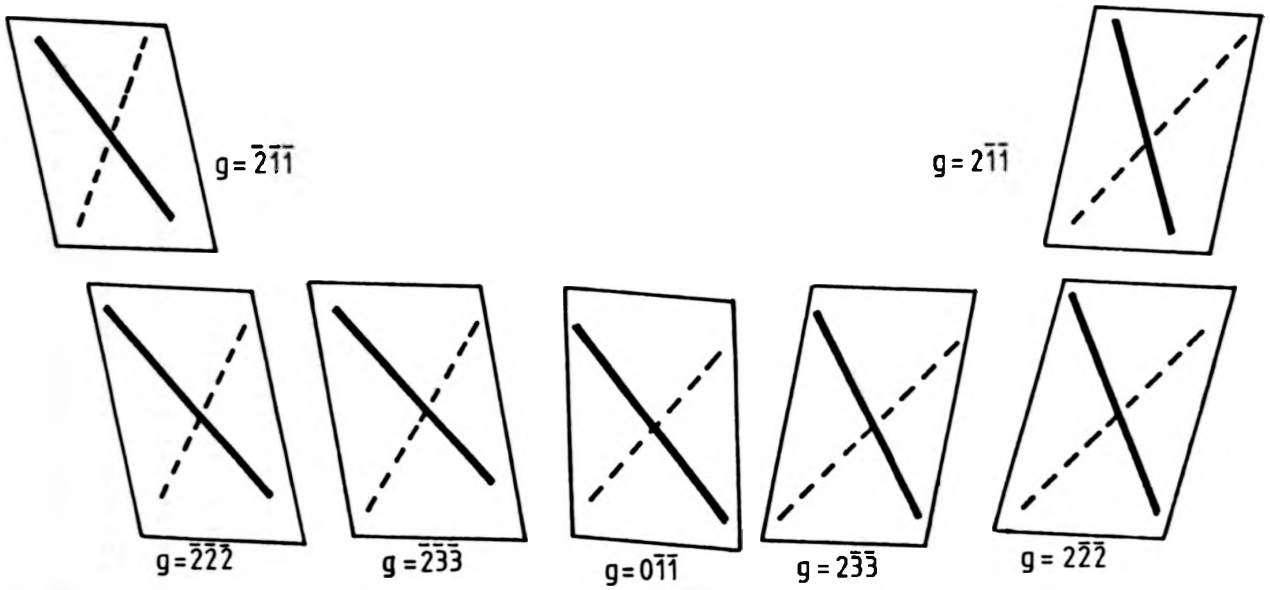

Fig 85 Sketch of predicted image shapes for C3 in the $0\bar{1}\bar{1}$ main spot geometry. ▬▬ represents the projected direction of the intersections of the (211), (101) and $(\bar{1}\bar{1}0)$ planes with the surfaces, and the $[\bar{1}11]$ Burgers vector; - - - represents the projected direction of the $(\bar{2}11)$, $(\bar{1}01)$ and $(1\bar{1}0)$ planes and the [111] Burgers vector. Spot positions are arbitrary.

direction, and the (211), (101) and ($\bar{1}\bar{1}$0) planes project along the same direction.

Reflection	Slip Plane Projected Width (μm)					
	$\bar{2}$11	211	101	$\bar{1}$01	1$\bar{1}$0	$\bar{1}\bar{1}$0
$\bar{2}\bar{1}\bar{1}$	110.3	48.3	181.9	56.3	277.1	84.8
0$\bar{1}\bar{1}$	48.3	55.3	187	181.9	85	76.2
2$\bar{1}\bar{1}$	55.3	102.3	56.9	187	76.2	261.8

Table VI

From Fig. 78 it can be seen that on the 0$\bar{1}\bar{1}$ main spot, there is no appreciable difference in projected width for isolated slip bands. On this spot, bands project at around 50μm thickness. It is believed that in this geometry, it is more reliable to consider absolute projected widths as bands do exist which exhibit a 'measurable' projected width (for instance those situated in the top left hand corner of the topographs).

Useful information can be obtained from comparison of projected widths on 0$\bar{1}\bar{1}$, $\bar{2}\bar{1}\bar{1}$ and 2$\bar{1}\bar{1}$ reflections. As already stated on the 0$\bar{1}$1 spot the two slip systems project with comparable thickness. However, on the 2$\bar{1}\bar{1}$ spot, the (211) planes have a larger projected width than the ($\bar{2}$11) planes, while the converse is true for the $\bar{2}\bar{1}\bar{1}$ spot. From Table VI, this means that slip on (101) and ($\bar{1}$01) planes can be ruled out. This leaves a choice between ($\bar{2}$11) and (1$\bar{1}$0) slip planes and (211) and ($\bar{1}\bar{1}$0) slip planes. (Relative projected thicknesses are illustrated in Fig. 86).

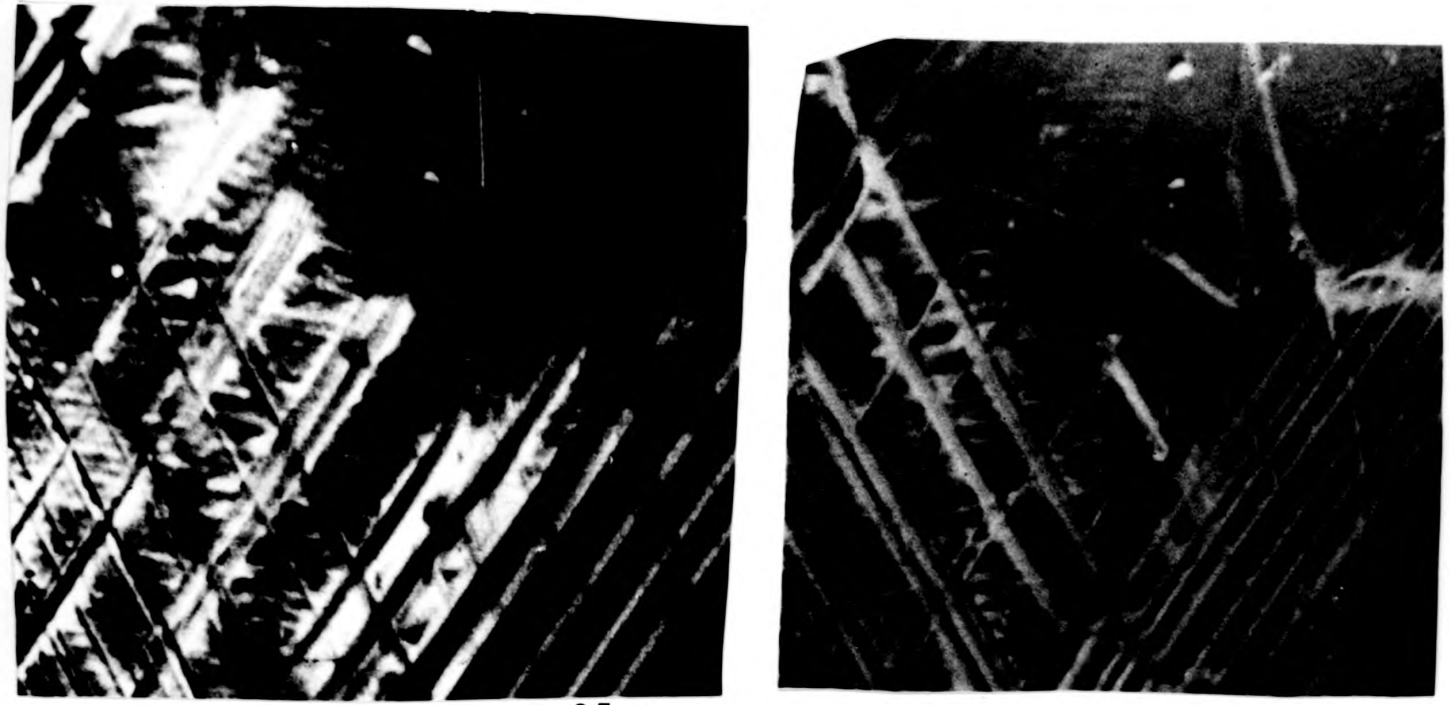

(a) g = $2\bar{1}\bar{1}$ ↙

(b) g = $2\bar{1}\bar{1}$ ↘

Fig 86

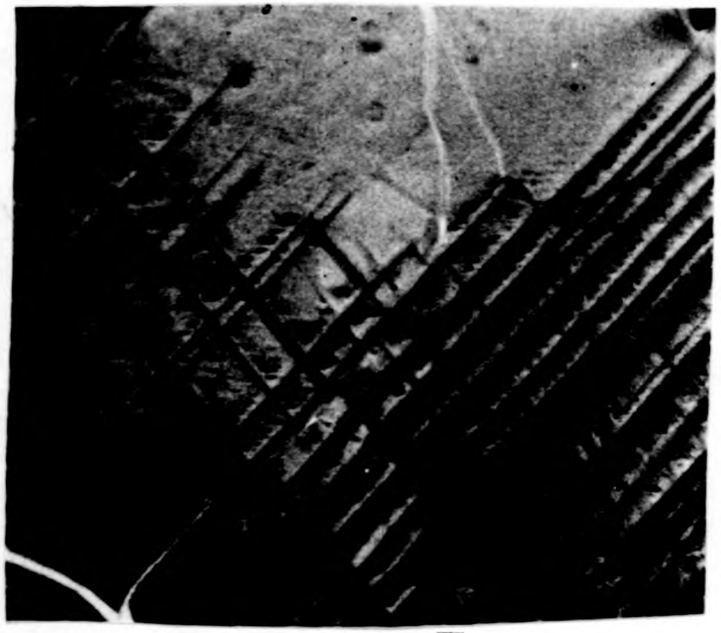

(c) ↓ g = $0\bar{1}\bar{1}$

Fig 86 Enlargements of topographs from the $0\bar{1}\bar{1}$ main spot geometry (at a stress of 251.5 MPa) illustrating the differences in projected widths, (a) g = $2\bar{1}\bar{1}$, $\lambda = 0.6\text{Å}$ (b) g = $2\bar{1}\bar{1}$, $\lambda = 0.7\text{Å}$ (c) g = $0\bar{1}\bar{1}$, $\lambda = 1.96\text{Å}$

Again, from the table, it can be seen that there should be a factor of ≈ 2 difference in projected width for $(\bar{2}11)$ and (211) slip planes on $2\bar{1}\bar{1}$ and $\bar{2}1\bar{1}$ reflections, whereas the corresponding factor is > 3 for $(1\bar{1}0)$ and $(\bar{1}\bar{1}0)$ slip planes. The factor of 2 difference is closest to the observed values.

It is possible to extract additional information regarding projected thicknesses from other higher order reflections on the same plate. Computed projected thicknesses for these reflections are presented in Table VII.

Reflections	Computed Projected Thicknesses (μm)			
	$(\bar{2}11)$	(211)	$(1\bar{1}0)$	$(\bar{1}\bar{1}0)$
$\bar{2}\bar{2}\bar{2}$	67	80.2	226.1	44.7
$\bar{2}\bar{3}\bar{3}$	32.5	83.9	185.3	39.8
$2\bar{3}\bar{3}$	82.9	21.3	40.3	168.9
$2\bar{2}\bar{2}$	81.8	55.6	41.8	209.1

Table VII

If $(1\bar{1}0)$ and $(\bar{1}\bar{1}0)$ slip planes were operative there would be a factor of > 5 difference in projected width between the two slip systems, on both the $\bar{2}\bar{2}\bar{2}$ and $2\bar{2}\bar{2}$ reflections. No such difference is evident on the plate. The calculation also predicts a factor of > 4 difference in projected width in favour of $(1\bar{1}0)$ slip on the $2\bar{3}\bar{3}$ reflection and a factor of > 4 difference in projected width in favour of $(\bar{1}\bar{1}0)$ slip on the $2\bar{3}\bar{3}$ reflection. On the plate, if {110} systems were operative the $(\bar{1}\bar{1}0)$ plane would have the largest projected width

on the $\overline{233}$ reflection, and similarly the $(1\bar{1}0)$ plane would have the largest projected width on the $2\overline{33}$ reflection.

Detailed investigation leads to the conclusion that, in general, much closer correlation between observations and predictions is found for {211} slip than for {110} slip.

The projective properties of the possible slip planes on the White Beam topographs taken in the $0\overline{11}$ main spot geometry, thus provide evidence for $(\bar{2}11)[111]$ slip and $(211)[\bar{1}11]$ slip.

6.3.1c Exit surface effects

From Fig. 87 one can see that on the $0\overline{11}$ main spot, the intersections of the {211} slip planes with the exit surface project onto the upper part of the image of the slip plane. On the topographs (Fig. 78) this can be seen to correspond to a palening on the plate. It is worth noting, that the clearest images of magnetic domains are in the regions associated with these pale sections of slip band, also suggesting that they are close to the exit surface.

The geometry of these intersections depends on the diffraction conditions. On the $2\overline{11}$ spot the intersections with the exit surface project onto the left hand extremities of the slip band images for both systems, while the converse is true for the $\overline{211}$ spot. A gradual transition from the extremes of the 211 reflections and the $0\overline{11}$ reflection

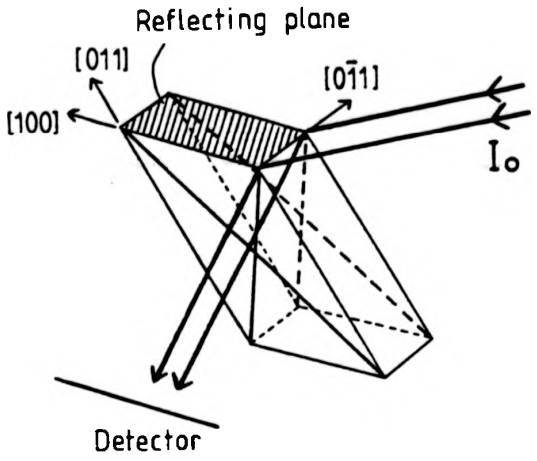

Fig 87 Geometry of the $0\bar{1}\bar{1}$ reflection for C3. The intersection of the slip planes with the exit surface will project onto the upper part of the image of the slip plane.

can be observed on the intermediate, higher order reflections. Detailed discussion of the origins of these contrast effects will be postponed until later (see discussion).

6.3.1d Slip line morphology and propagation evidence

Slip bands are seen to extend long distances through the specimen. Considerable lengthening of slip bands under increasing stress can be seen on Fig. 78 . It is believed that in this orientation, screw dislocations are able to escape through the specimen surfaces, leaving edge dislocations to propagate through the bulk of the sample (see discussion). This is in stark contrast to the behaviour of the slip bands in specimens C1 and C2 where the small 'slip cells' are seen to propagate through the thickness of the specimen, but not through the bulk of the specimen.

The most useful evidence on slip line propagation is found on the video stills. These will be dealt with separately.

6.3.1e Nucleation evidence

Not much evidence on nucleation can be taken from the topographs, as in the time that elapsed between the observation of the initiation of slip and the mounting of a nuclear plate, the sample was considerably deformed. However, the video stills can afford very useful information regarding sites for nucleation of slip.

6.3.1f Intersection of slip systems

The two {211} slip planes intersect along an $[0\bar{1}1]$ direction. At stresses above the elastic limit interaction of the two slip systems is evident on the plate. Small segments of slip band are sheared from their original positions, and end up oriented in small segments which project parallel to the tensile axis. Fig. 88 shows that this can also be a mechanism of slip band broadening.

6.3.1g Lattice rotation effects

These are visible from the early stages of deformation, for example in the lower region of the $0\bar{1}\bar{1}$ reflection (Fig. 78). Lattice rotation manifests itself by a non linear image of the slip bands. This sort of bending is due to a combination of the effect of lattice rotation and the presence of non deformable grips holding the specimen (see discussion).

6.3.2 Video Stills

6.3.2a Projective properties

Other than seeing the direction of projection of the slip bands, little quantitative information can be taken from the projected properties of slip bands on the stills. For instance, due to the lower resolution and general signal to noise ratios (lower than on the plates), it would be very difficult to measure the projected width of a slip band.

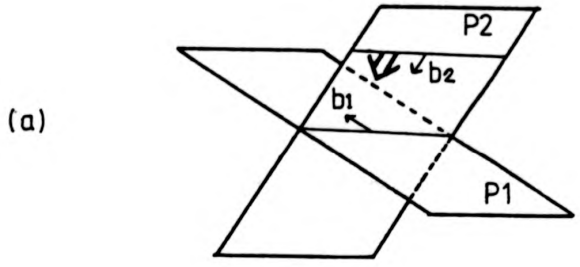

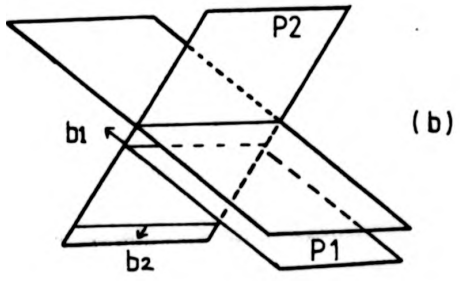

Fig 88a An edge dislocation b_1 in its slip plane P_1, being intersected by a parallel dislocation of different Burgers vector b_2 in its slip plane P_2

Fig 88b This leaves a section of b_1 type dislocation, taken from its glide plane and left still lying in a [011] direction. Evidently this could also be a mechanism of slip band broadening

The most useful aspect is that on the video-tape recording one has an almost real time (25 frames per second) representation of what actually happened. Invaluable information about propagation in the early stages and sites for nucleation of slip can be obtained from looking at the 'frozen' stills.

6.3.2b Exit surface effects

The contrast seen on the television screen is reversed from that seen on the plate (increased X-ray intensity on the television camera leads to increased brightness on the screen, whilst increased X-ray intensity on a plate leads to darkening). To make comparison between plate and video still easier, the contrast on the still was reversed photographically, so that a darkening on the still corresponds to increased X-ray intensity.

After this contrast reversal, one can see that the contrast from magnetic domains, subgrain boundaries and precipitates is similar on the video still and plate (see Figs. 78 and 79). Slip bands appear as pale lines (corresponding to a depletion of X-ray intensity). The darker parts of slip bands visible on the plates are barely visible on the video still. This is probably due to differences in signal to noise ratio between the background intensity and intensity from the darker and lighter parts of slip bands in that there is a bigger contrast between the lighter parts of the band and the

background, than between the darker parts and the background.

As has already been shown, the lighter parts of the slip bands are associated with those sections of band of greatest proximity to the exit surface. Thus, it would appear that slip bands are visible on the television screen mainly through the contrast which arises near the X-ray exit surface.

6.3.2c Evidence for nucleation

For ease of identification of possible sites, subgrains will be classified as shown in Fig. 89 .

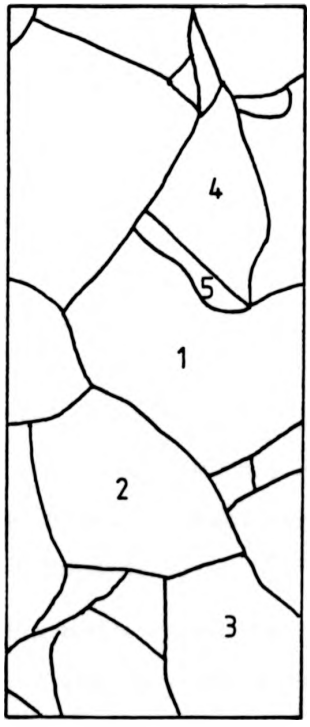

Fig 89 Classification of subgrains in C3

It is also useful to compare the video stills to the Lang topograph (Fig. 77) in order to correlate the positions of, for example, precipitates. It is rather unfortunate that subgrain 2 is out of contrast on the Lang topograph. However, several predeformation White Beam topographs are available which show the defect structure of this grain (Fig. 78).

Slip initiates in both subgrains 1 and 2. Sites coincide with the positions of precipitates seen on predeformation topographs. The contrast around the precipitates in subgrain 1 (see White Beam predeformation topographs, Figs. 78a, 116a-f) is seen to increase as the elastic limit is surpassed, and eventually slip bands are seen to emerge, extending in both directions and from both slip systems. A similar effect is apparent around the precipitates in subgrain 2, although here it is difficult to tell in which direction the slip band propagates, as it is very close to the subgrain boundary. Very similar precipitates to those seen in subgrain 2 are seen in subgrain 3. Again these are very close to a subgrain boundary, but here it is possible to see that slip initiates on one system only at the precipitate and then propagates in both directions (towards and away from the subgrain boundary).

Several slip bands (from one system) are seen to initiate close to the very small subgrain 5. This subgrain has a very high dislocation density, and also contains precipitates.

6.3.2d Evidence for propagation

Only qualitative information can be obtained about propagation rates as stress is increasing, between each video still. Useful quantitative information can only be gathered from creep type experiments (at constant stress).

Propagation of slip systems through the bulk of the sample can clearly be seen. Slip bands are seen to extend in both directions from the point of nucleation, and in some cases both slip systems are seen to nucleate at the same site.

The chronological and stress history of the deformation with respect to when plates and video stills were taken is shown in Fig. 90 . The last video still was taken just before the first plate showing slip was inserted.

Slip bands originating near the precipitates in subgrain 1 seem to start off propagating relatively quickly, but then stagnate. This could be due to the back stress exerted by the piled up groups of dislocations or from interactions with other adjacent slip bands which although below the resolution limit of the television system (see discussion) may still be present, and in fact do become visible at a later stage.

Slip bands which appear to originate in subgrain 5 propagate relatively long distances in a short space of time.

However the slip bands originating near the precipitates

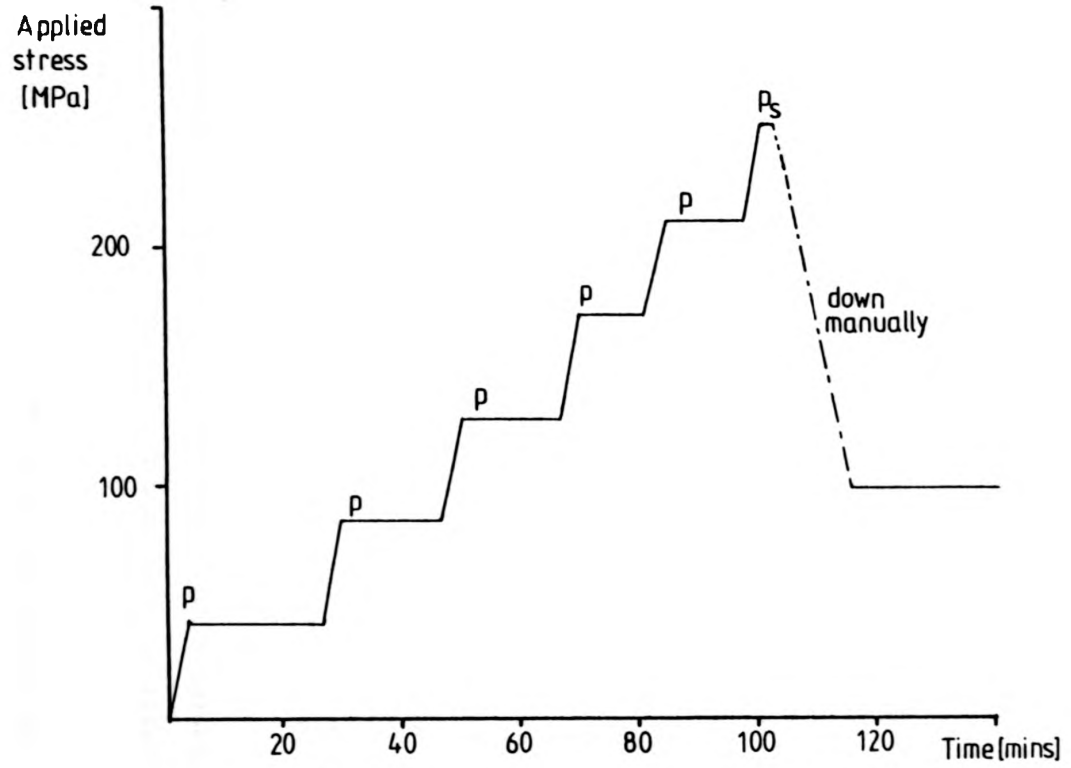

Fig 90 Stress history of C3. P indicates where a plate was taken. Ps is the first plate showing slip

in subgrain 3 seem to be experiencing a large back stress hindering their propagation. Again this could be due to the interaction between the two adjacent slip bands present.

The slip bands which originate close to the precipitates in subgrain 2, propagate in both directions and in the case of the (211) system, propagation occurs across the subgrain boundary in one sense (into subgrain 1) and almost all the way across subgrain 2 in the other sense.

6.3.2e Lattice rotation effects

The gradual increase of the effect of lattice rotation and its interaction with the grips, already pointed out on the White Beam topographs, can be observed on the video stills taken from the later stages of deformation. As already mentioned this manifests itself in a bending of the image of a slip band near the grips (see Fig. 78).

6.3.3 Lang Topographs

Fig. 80a shows a Lang topograph ($g = \overline{2}11$, Mo Kα radiation) of C3, taken in a geometry designed to accentuate the difference in projected widths between (211) and ($\overline{1}\overline{1}0$) slip planes. This geometry is illustrated in Fig. 91 .

The observed projected width corresponds to that for (211) slip as opposed to ($\overline{1}\overline{1}0$). This consolidates earlier claims made in favour of {211} slip.

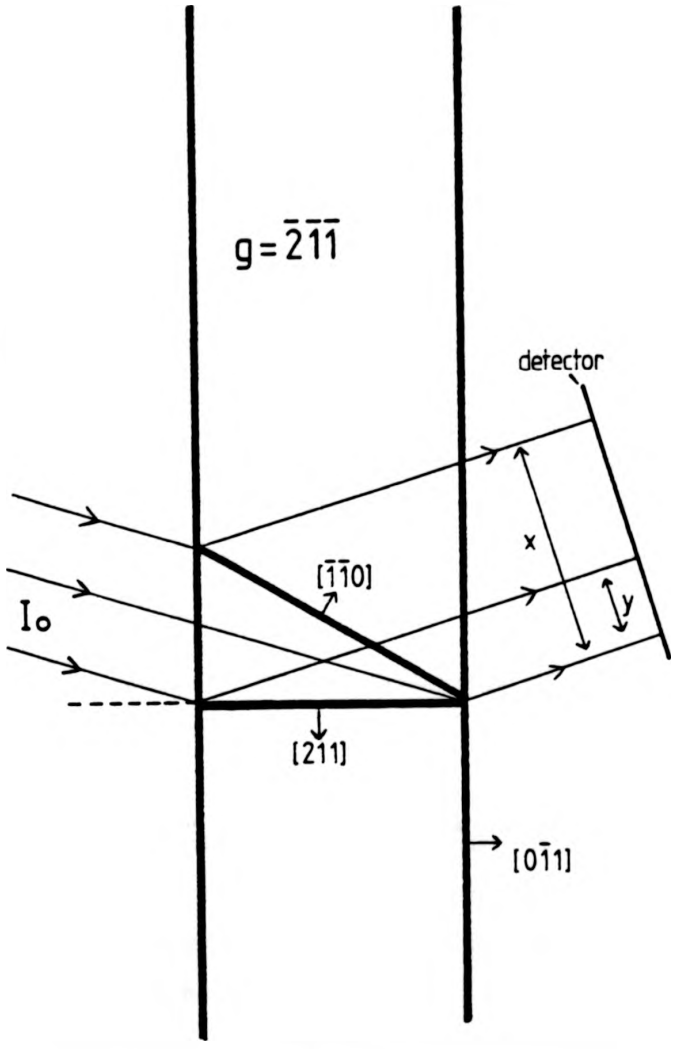

Fig 91 Plan view of geometry of $\bar{2}\bar{1}\bar{1}$ Lang topograph. X indicates projected width of (110) planes, y indicates projected width of (211) planes

As in White Beam topographs, the intersection of the slip plane with the X-ray exit surface gives rise to the paler section of the slip band image. This topograph was taken using a different exit surface in order to investigate this effect.

Also available is a 211 reflection of a single sub-grain, which shows the same projected width for the (211) plane (as expected) and a reversed exit surface effect (also as expected), (see Fig. 80b).

6.3.4 White Beam Topographs taken after Deformation (SRS Daresbury)

Two diffraction geometries were used, the $2\bar{1}\bar{1}$ main spot geometry and the $\bar{2}\bar{2}\bar{2}$ main spot geometry. Fig. 81 shows three reflections from the $2\bar{1}\bar{1}$ main spot geometry.

6.3.4a $2\bar{1}\bar{1}$ main spot geometry

Observations of the projected geometries on the plates agree with calculated predictions for (211) and ($\bar{2}$11) slip.

Again there is a palening effect on part of the image of a slip band which corresponds to that part of the slip band closest to the X-ray exit surface. This is consistent on all of the reflections shown

Those parts of a particular slip band which have been 'left stranded' due to interaction with the conjugate slip system, again project in a direction which would correspond to an actual [0$\bar{1}$1] direction in the crystal

(which, as has already been discussed, corresponds to the line of intersection of the two slip systems). This is consistent for all reflections shown

6.3.4b $\bar{2}\bar{2}\bar{2}$ main spot geometry (see Fig. 82)

All that has been stated for the topographs taken in the $2\bar{1}\bar{1}$ main spot geometry applies for this geometry. Total consistency is found in the results

6.3.5 Optical Micrograph

The angle between the traces of the two slip systems corresponds to the angle between the Burgers vectors ($\sim 70^{\circ}$).

The contrast observed on this micrograph is probably due to preferential rusting due to shearing of the oxide layer on the surface. This contrast (which appears white on a dark background due to oblique illumination) is present only on the X-ray exit surface of the crystal (the entrance surface has too much rust generally for any contrast to be seen). There should be no 'step' present on the surface due to the presence of the slip bands, as the Burgers vectors are in the surface. No Nomarski type contrast was observed.

The micrograph represents a frozen image of the traces of the slip bands on the exit surface, at quite an early stage of deformation. This is probably due to the increase in thickness of the oxide layer as the experiment progressed, actually masking the surface shear due to slip.

CHAPTER 7

Discussion

DISCUSSION

7.1 Factors Influencing Choice of Slip System

Mechanical testing of cylindrical bcc metal single crystals usually leads to a choice of slip system based on Orientation or Schmid Factors (notable exceptions being anomalous slip in Nb ([12]) and the asymmetry of slip with respect to sense of shear often observed in Fe Si alloys ([67]) and Nb ([9]); the latter being a consequence of preference of deformation in the twinning direction as opposed to the anti twinning direction). By definition, the operative slip systems are those experiencing the maximum resolved shear stress, (see Fig. 92)

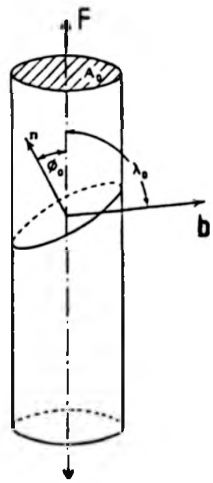

Fig 92 Definition of parameters used in calculating orientation or Schmid Factors. The CRSS is defined as

$$\tau = \frac{F}{A_o} \cos\phi_o \cos\lambda_o$$

The $\cos\phi_o\cos\lambda_o$ term is the so called orientation or Schmid factor.

n is the slip plane normal, b is the slip direction

However, Vesely ([10], [73]) found that when testing Mo single crystals of rectangular cross-section, the orientation of the surface could affect the choice of slip system. For example, when testing crystals of common

tensile axis but with different ratios of the side and front faces, choice of slip system was a sensitive function of this ratio.

Assuming slip is nucleated over a finite area on the active slip plane, then as the slip area (bounded by dislocations) expands it can be seen that those segments of dislocation with edge character can have a slip path which is very different to that corresponding to screw segments, depending on the orientation of the large surface with respect to the slip vector.

In the hypothetical case illustrated below, it is clear that dislocation segments of edge character have a relatively short path through the crystal thickness, whereas the screw segments have a relatively long path through the width of the crystal (see Fig. 93).

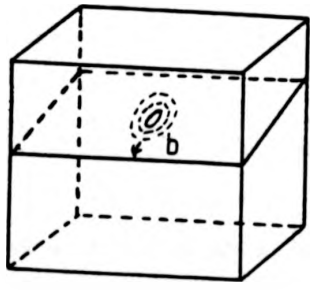

Fig 93 Schematic diagram illustrating the various paths possible for dislocations of different character

As was mentioned in the introduction, screw dislocations in pure bcc metals have a lower mobility than non-screw dislocations. (This effect, based on the core structure of the screw dislocation, is expected to be smaller in the case of substitutional alloys of bcc metals, as explained in section 1.2.3). Screw segments can thus be considered as rate controllers in the slip process, and it is preferable to lose the screw components through the specimen surfaces, to leave the mobile edge segments to propagate freely. Obviously the shortest path available for the screw dislocations is perpendicularly through the specimen thickness.

Vesely found that the low mobility of the screw dislocation (at temperatures of 77°K and 293°K) was such that slip systems were chosen which were not necessarily MRSS systems, but were such that a combination of a relatively high shear stress and a short escape route through the specimen thickness for screw dislocations, rendered them operative.

Vesely's concept can be usefully quantified, by defining what will be called the 'Vesely Factor' (V), which, combined with the Schmid Factor, can give information as to which slip system would be preferred for a given slip vector;

$$V = \cos \Omega$$

where Ω = angle between the intersection of the slip plane with the large surface of the crystal, and the Burgers vector.

7.2 Specimens C1 and C2

For all the specimens tested, the tensile axes were so oriented that two of the <111> possible slip directions, have zero Schmid factor (they are perpendicular to the tensile axis). The tensile axis is located centrally with respect to the remaining two <111> directions, so that samples were ideally oriented for double glide (both possible Burgers vectors equally stressed).

The orientation of C1 and C2 is illustrated in Fig. 42 The two possible slip directions are [111] and [$\bar{1}$11]. The most highly stressed systems under these conditions are ($\bar{2}$11) and (211) slip in the anti-twinning directions i.e. ($\bar{2}$11)[111] and (211)[$\bar{1}$11]. A full list of Schmid factors of possible systems is presented below, along with the corresponding Vesely Factors.

Table VIII

System	Schmid Factor	Vesely Factor
($\bar{2}$11)[111]	0.471	0
(211)[$\bar{1}$11]	0.471	0
(101)[$\bar{1}$11]	0.408	0.58
(110)[$\bar{1}$11]	0.408	0.58
(10$\bar{1}$)[111]	0.408	0.58
(1$\bar{1}$0)[111]	0.408	0.58
(11$\bar{2}$)[$\bar{1}\bar{1}\bar{1}$]	0.236	0.77
(1$\bar{2}$1)[$\bar{1}\bar{1}\bar{1}$]	0.236	0.77
(12$\bar{1}$)[1$\bar{1}\bar{1}$]	0.236	0.77
(1$\bar{1}$2)[1$\bar{1}\bar{1}$]	0.236	0.77

N.B. The slip in the last four systems is in the twinning sense

In C1 and C2 the operative slip systems were $(\bar{2}11)[111]$ in the main, with a lesser amount of $(211)[\bar{1}11]$. These are the systems experiencing the highest resolved shear stress, but they have a zero Vesely factor, and they correspond to slip in the anti-twinning direction. In the corresponding situation in Mo, Vesely showed that the zero Vesely Factor and not the anti-twinning sense of shear, was active in influencing the choice of slip system, such that systems such as $(11\bar{2})[\bar{1}\bar{1}\bar{1}]$ became operative (this works in the twinning sense of shear). As can be seen from table VIII these systems have a much smaller Schmid Factor.

7.2.1 Slip Morphology

In the case of Fe 3.5 wt % Si single crystals a zero Vesely Factor is not enough to induce the nucleation of glide on lower stressed systems, but it may be enough to affect the morphology of slip. (However, there is another possible influence on the slip morphology, see section 7.2.2 on nucleation). As indicated in the results section, slip in C1 is seen to nucleate in the form of small almost rectangular slip cells, which intersect the two large specimen surfaces and terminate along directions which are coincident with the projected directions of the corresponding Burgers vectors. The slip cells are thus considered to be bound by screw dislocation segments. These segments are never seen to propagate across the specimen , rather new slip cells initiate which then run through the specimen thickness (via the

ready propagation of non-screw dislocations).

These small slip cells are seen to accummulate side by side, both in C1 and C2. The rectangular aspect of the slip cells varies from reflection to reflection. This can be sensitive to the projected geometry of the slip cells. However, in C2, the extent of non-rectangularity is quite marked, on the $00\bar{2}$ reflection. Specimen C2 is much thinner than C1 (C1 thickness 200μm, C2 thickness 115μm) and the effect of image forces due to the presence of the crystal surfaces is expected to be more influential. Image forces will tend to attract a dislocation to the surface. This is because as a dislocation approaches a free surface, its strain energy decreases, as the surface can give way easily under the field of the dislocation, for it is not backed up by material on the other side (see section 7.2.5 on exit surface effects). As pointed out by Miltat and Bowen ([32]), the ends of a screw dislocation may be distorted by this image force. This could lead to non-rectangular slip cells.

The effect of image force might also be expected to be smaller in C1 as there was more of an oxide layer present on the surface (C1 was not deformed in an inert atmosphere and the main part of the deformation was performed several months after the chemical polish, due to circumstances beyond the author's control). In some cases the presence of an oxide layer can cause repulsion at the surface ([122]).

The effect of the spreading of wavefields in the

Borrmann Fan will always tend to make the image of a defect situated close to the entrance surface appear wider and more diffuse than that of a defect close to the exit surface. The Bragg angle for the $00\bar{2}$ reflection used ($00\bar{2}$ main spot geometry) for C2, was larger than any used previously in C1 or C2 (see section 7.2.6 on entrance surface effects). This is expected to accentuate the effect of image widening.

If a single or double ended Frank Read source nucleates near the surface of a crystal, then a rather asymmetrically shaped slip cell could possibly result, as illustrated below;-

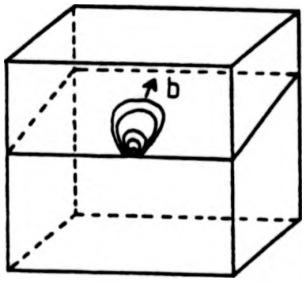

Fig 94 Possible mechanism for formation of asymmetric slip cell

The screw segments would like to be perpendicular to the surface, due to the image forces. This could lead to a teardrop shaped slip cell. This point will arise

again in the nucleation section.

7.2.2 Nucleation

As seen in section 1.8.1 the requirements that must be met for a source to nucleate in a crystal are, either the presence of predeformation dislocations (favourably oriented), or imperfections of other kinds from which dislocations can be created under relatively small stress.

In C1 and C2, it is believed that, due to the high predeformation dislocation densities present in these crystals, the former requirement is met and that grown in dislocations most probably provided the sites for nucleation.

It is worth noting that clear observation of nucleation sites was very difficult in C1 and C2 due to the generally high predeformation dislocation density and general poor quality of these crystals. For C1, topographic image quality was also marred to a certain extent by degradation of the crystal surface (the quality of the exit surface is of greatest importance) due to enhanced corrosion in the synchrotron beam.

However it is clear that nucleation occurred relatively homogeneously at numerous sites simultaneously, rather than slip nucleating at one site and spreading from there. Slip also occurs rather catastrophically, making observation of the early stages of deformation quite difficult.

Despite such difficulties it is possible, in C2 at

least, to find some sort of correlation between the predeformation dislocation configurations and nucleation sites.

Grown in dislocations in the lower subgrain in C2, often exhibit a form which is essentially similar to the ensuing slip cells. This form is probably moulded by the image force field, in the anneal. Slip cells often nucleate in regions containing a high dislocation density, and in some cases it is possible to find a correspondence between particular grown-in dislocations (for example in the central sections of the crystal) and subsequent slip cells (as pointed out in Figs. 63 and 64). Also in C2, nucleation is seen to occur very close to subgrain boundaries (see Fig. 64). Similar nucleation at subgrain boundary intersections was observed by Miltat and Bowen ([32]). Preferential etching occurs along subgrain boundaries, and ridges on the surface can result. Stress concentration can occur at the edges of these ridges which can give rise to nucleation (see section 1.8.2).

It is also possible in C2 to observe dislocations which are unaffected by the plastic deformation (see Fig. 74). These cannot have been favourably oriented.

7.2.3 Propagation

Reference to the video stills of C1 shows that slip appears in some cases to initiate at one of the sample surfaces and then propagate inwards along the slip plane,

most probably via the rapid motion of non-screw dislocations. This process is then repeated, even in regions very close to existing slip cells.

The screw fronts of the slip bands are never seen to propagate across the width of the crystal.

7.2.4 Contrast from slip cells

Absorption is too high to be able to consider direct images of dislocations, in the White Beam topographs presented of C1 and C2. Within the slip bands it is believed that the dislocation densities are so high ($\sim 10^5$ cm^{-2}) as to make the resulting lattice distortion too great for the geometrical optics approximation to be valid. Recall that the dynamical image arises from areas outside the definitive $G = \frac{\delta}{\Lambda}$ curve. As dislocations approach each other the interaction of their deformation gradients would render consideration of wavefield curvature (trajectory), similar to that outlined in the contrast theory section, a very difficult affair.

The transition experienced by wavefields on crossing a slip band is believed to be abrupt enough to promote interbranch scattering.

As μt is relatively high in these samples (see I_h calculations in appendix III) only those wavefields associated with branch 1 of the dispersion surface survive the absorption. This is the case for perfect regions of crystal. Now if the wavefield crosses what would appear to be a very abrupt planar boundary (from post deformation

etch pit studies of slip cells in C2, dislocation spacing was seen to be $\sim$ 10μm, which is considered small enough for the above assumption to be approximately valid), transfer of energy from the original wavefield into one associated with the other branch (2) of the dispersion surface occurs. These branch 2 wavefields will again be damped out on traversing the crystal (except perhaps for sites very close to the exit surface). This resultant reduction in energy flowing along the direction of the original Poynting vector, will lead to a reduction in intensity on the plate. The diffracted (and forward diffracred) beam is depleted in intensity upon crossing the slip band. This would explain the white image of the body of the slip bands in C1 and C2.

The typical width of a slip cell in C1 or C2 is $\sim$ 20μm. Dislocation image widths are between 5 and 15μm wide. As dislocations in slip cells in C2 were observed (via etch pit studies) to be about 10μm apart, this would mean that the dislocation images would overlap. This effect will occur more readily in Fe 3.5 wt % Si than for example in pure iron, as the τ_{Si} term (see section 1.3.5) in the dislocation energy allows the dislocations to pack more closely in the slip bands. In contrast in Si, it is possible to resolve very high densities of dislocations in slip bands before images overlap. Due to the much lower absorption in Si, dislocation images are usually mainly direct.

In C1 and C2 it is possible to see fringe-like detail

within the slip band images. However, as reported by Miltat and Bowen ([32]) it is difficult to know whether these are individual dislocations, dislocation groups (slip cells) or termination lines of different sources (on closely spaced planes) comprising one apparent slip band.

As explained in the results section, in addition to the mainly white character of the slip cell images in C1 and C2, there is a thin line of dark contrast corresponding to slip cell intersections with the exit surface, and a pale diffuse section of the image, associated with the intersection of the slip cell with the entrance surface.

7.2.5 Effects at exit surface

In this slip geometry, assuming that the edge dislocations escape through the surfaces (this process will be helped by the presence of image dislocations), screw dislocations meet the surfaces of the crystal at an oblique angle. Now for a dislocation in such a situation there will be an image dislocation outside the crystal. Relaxing the strain fields associated with the real and image dislocations leads to a resultant stress field.

This additional distortion caused by the intersection of the dislocation with the free surface could be the reason for the line of dark contrast observed, if a curvature of the lattice planes exists such that X-rays are

reflected from the concave side of the planes ([178]).

Another possible explanation is that new wavefields created close to the exit surface, which are associated with branch 2 of the dispersion surface may not have a chance to be damped out, and may cause a darkening on the plate. Such wavefields will only exist at the exit surface, in regions close to the intersection of the slip band with that surface.

7.2.6 Effects at Entrance Surface

As already explained in the contrast theory section under the experimental conditions encountered in Lang and White Beam topography, the whole of the dispersion surface may be illuminated. This means that wavefields fill the Borrmann Fan. This results in a spreading out of the image of any defect (or part thereof) close to the entrance surface due to this divergence of the energy flow. This would explain the diffuse image corresponding to the slip cell intersection with the entrance surface. This effect is expected to gradually decrease as one approaches the exit surface. This is borne out by the slip cell images. As already mentioned, the $00\bar{2}$ main spot reflection has a relatively large Bragg angle and consequently a large Borrmann Fan. The effect of divergence of energy flow is expected to be more evident on this reflection. This is consistent with observations.

7.2.7 Extent of Borrmann Effect

If a very large Borrmann effect were operative, only

those wavefields associated with branch 1 of the dispersion surface which travel parallel to (effectively 'along') the reflecting planes would emerge at the exit surface. Any defect (such as a slip band) encountered by this wavefield would disrupt the Borrmann transmission and result in a depletion of intensity. If such a mechanism were operative, then on the Lang topograph taken of C2 after deformation (see Fig. 69) the slip band image should appear broad and pale. This is clearly not the case. The dark image of the slip band observed on this topograph, would be formed from wavefields with a trajectory corresponding to that which would form a direct image.

However it is believed that a Borrmann effect is present to the extent that most of the branch 2 wavefields are absorbed out, but that branch 1 wavefields fill the Borrmann fan. In other words branch 1 wavefields exist and survive other than those travelling parallel to the reflecting planes.

7.2.8 Effect Due to Diffraction from the Specimen Edge

This only occurs when the incident X-rays can 'see' the crystal edge. This is the case for the $00\bar{2}$ and $0\bar{1}1$ main spot geometries. It is possible in these geometries for X-rays to impinge and emerge from the same crystal surface after diffraction. Asymmetric Bragg reflection occurs. It is known that the intensity reflected in the Bragg case can be greater than that in the Laue

case ([163]). It is also possible in asymmetric Bragg reflection for the cross-section of the diffracted beam to be greater than that of the incident beam. It is also possible that Laue-Bragg diffraction occurs, whereby the X-rays emerge from a surface normal to the one on which they impinged.

Thus different diffraction conditions exist along the edge of the crystal. This could explain the line of dark contrast often observed along one edge of the images, where diffraction from the crystal edge is possible.

7.2.9 Lattice Rotation

As deformation increases the tensile axis rotates relative to the crystal lattice as illustrated below.

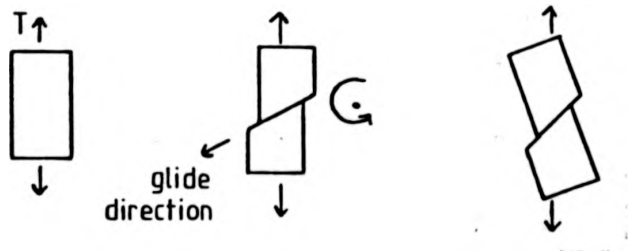

Fig 95 Schematic representation of lattice rotation (or equivalent rotation of the tensile axis, T, with respect to the lattice) induced on tensile deformation

In the case of simple glide the lattice rotation consists of a movement of the longitudinal axis towards the glide direction, during which the longitudinal axis always remains in the plane determined by its original position and the direction of glide.

From the extension formula for double glide ([199]) it is again apparent that, as long as the wire axis remains in the same plane during rotation, the ensuing lattice rotation will follow the same law as applies to simple glide, with the resulting glide direction assuming the role of glide direction. Just as the glide direction is attained by simple glide only after infinite extension, so too, in double glide, the resultant glide direction represents the final position of the wire axis for infinite extension. However, the purely formal nature of this analogy can be seen from the fact that a crystal whose longitudinal axis is parallel to the glide direction cannot be extended in this direction. On the other hand, if the longitudinal axis coincides with the resultant glide direction, it can be extensible by any amount by double glide without change of orientation.

However, any slight misalignment of the intended tensile axis with the crystal axis would lead to non-equal proportion of the two slip systems and a resultant lattice rotation.

7.2.10 Grip Effects

The lattice rotation described above for tensile tests,

cannot take place near the ends of the sample, if, as is generally the case, they are restricted by non-deformable clamps.

The resulting difference in slip can produce a plastic bending of the sample. See Fig. 96.

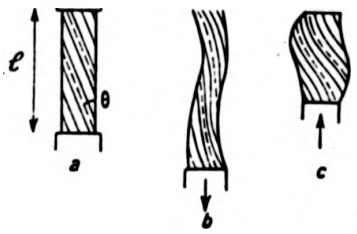

Fig 96 Plastic bending due to the influence of the grips. (a) initial state; (b) tension; (c) compression (after [123])

This can manifest itself in the form of a kink band near the grip, when the continuous bendings are large enough (e.g. in compression, several degrees [200]). Kink bands have been observed near the ends of tensile test specimens of zinc ([201], [202], [203]). analogous bands sometimes observed within these samples have been attributed to heterogeneities of the structure or of the stresses ([204]).

Double kink bands which compensate for lattice rotation are regularly seen in Zn or Cd single crystals

after compression, when the axis makes an angle with the hexagonal axis of less than 25 degrees ([205], [206]). These double kink bands only occur where there is only one possible slip plane.

Deformation bands are a common feature of easy glide in cubic crystals ([207], [208], [209], [210], [211]).

Analogous kink bands are observed in cubic ionic solids under similar conditions ([212]).

A deformation band was observed by Miltat and Bowen after deformation in tension of a Fe 3.5 wt % Si single crystal. This deformation band was seen to absorb the rotation in the lattice.

If the tensile axis is close to the [100] - [111] zone, where a second slip system is equally favoured, the bending stresses can be relieved by the second system, and no deformation or kink bands should occur.

With specimen C1, no deformation or kink band was observed. However, lattice rotation is evident from an early stage of deformation. This desired lattice rotation to relax the bending stresses, is hindered by the grips. The rotation, in effect tries to reduce the Bragg angle for the $0\bar{1}\bar{1}$ spot (i.e. occurs in the plane defined by the tensile axis and slip direction). The result is that the image of the gauge length of the crystal starts to overlap the image of the crystal section near the (upper) grip (see Fig. 55).

As mentioned in the results section, in the case of

double glide it is conceivable that due to the presence of the two slip systems, for which the lattice rotation works in opposite senses, the overall rotation might not be homogeneous throughout the crystal.

If the rotation, as is to be expected, is inconsistent near the grips, where slip is first to initiate and most extensive, a situation such as that shown below may arise.

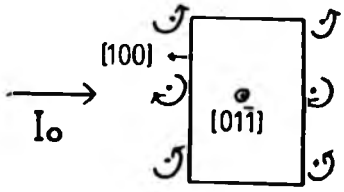

Fig 97 Possible inhomogeneity in lattice rotation

Rotation could thus be in a different sense near the grips, to that present in the bulk. If this is the case, this would lead at one extreme, to dilations of the reflecting planes on the X-ray exit surface, and at the other extreme, compression. The lattice parameter distortion at the boundaries between such volumes of rotation, would lead to contrast; dark where plane

compression occurs and light where plane dilation occurs.

Fig . 55 shows a line of dark contrast, which progresses across the crystal as deformation increases. It is worth noting that this boundary moves away from the end of the crystal where fracture eventually occurred i.e. the end where slip was most extensive.

From the video stills (Fig. 57) one can observe, via the contrast effects already discussed (section 7.2.5) a preponderance of $(\bar{2}11)[111]$ type slip in the central section of the specimen. The first type of slip to occur in the lower section of crystal (near the grip), is seen to be $(211)[\bar{1}11]$ from the contrast effects. This also seems to be the case in the section near the upper grip. The variation in lattice rotation produced by these differences in slip as a function of position in the crystal, could produce the observed contrast.

7.2.11 Luders Band

The contrast due to the rotation band discussed above, is superposed upon the general contrast difference between the upper and lower sections of the crystal. This is due to the difference in diffracting power of a relatively lightly deformed region of crystal, and a heavily deformed region of crystal. Thus it is referred to as Luder's Band contrast.

7.3 Specimen C3

7.3.1 Operative Slip Systems

As in C1 and C2, the operative slip systems were observed to be $(\bar{2}11)[111]$ and $(211)[\bar{1}11]$. The Schmid factors of all the possible slip systems in C3 are the same as in C1 and C2, but the 'Vesely Factors' (V) are different. The Vesely factors are presented below. This orientation is ideal for $(\bar{2}11)$ and (211) slip as screw segments of dislocation can escape easily through the surfaces.

Table IX

System	V Factor
$(\bar{2}11)[111]$	1
$(211)[\bar{1}11]$	1

The most striking difference between deformation in the two orientations investigated was in the slip morphology.

7.3.2 Slip Morphology

The edge fronts of the nucleated slip cells were seen to propagate freely across the specimen, and long slip bands were formed which had run large distances through the crystal. This is very evident from the video stills. The screw dislocation segments are believed to escape through the surfaces of the specimen, thus leaving the edge segments to propagate.

The mechanism of nucleation was rather more clearly

observable in C3 than in C1 and C2. This is helped by the fact that C3 was a crystal of much better quality than either C1 or C2.

7.3.3 Nucleation

As discussed earlier, specific nucleation sites are necessary for slip initiation. These can either be grown in dislocations or other imperfections which can induce the generation of dislocation loops at relatively small levels of stress. Any local stress concentration will aid the nucleation process.

As seen in section 1.8.2 , dislocation loops can be nucleated around precipitates in crystals submitted to relatively small external stresses, due to a difference in elastic constants. Stress concentration occurs for both softer and harder (than the matrix) precipitates. It is probable that the precipitates present in these crystals are nitrides, and also that the case of the harder precipitate is applicable.

Under suitable conditions, any part of loops created by this mechanism, (or for that matter by any other mechanisms), can act as Frank Read sources and multiply into a slip band by cross slipping out of their glide cylinder ([213]). Slip can often start from the neighbourhood of the surface, owing to volume indentation by precipitates ([214]).

7.3.4 Evidence for Precipitates in C3

The contrast due to precipitates observed on topographs of C3, is of the conventional type ([215]) (see Fig. 77). It consists of two lobes, one light and one dark, with the darker lobe on the side of positive g vector. This is characteristic of a precipitate that is close to the exit surface of a thick crystal and that is compressing the surrounding lattice ([198]). The contrast, of a precipitate situated close to the exit surface of a crystal, can be explained in terms of wavefield curvature, (tie point migration) in the regions close to the defect, where the Eikonal theory is still applicable. On all the topographs presented, the darker lobe of contrast is on the side of positive diffraction vector.

Other possibilities that were considered as the origin for this contrast were surface defects such as etch pits (residual from the chemical polish). However, the contrast expected from an etch pit on the exit surface is thought not to be similar to that of a precipitate close to the exit surface. This is because the etch pit (which probably would have occurred from preferential chemical etching of a dislocation outcrop or even a precipitate close to the surface) should be strain free. It should therefore not affect the choice of tie point in the crystal, or cause tie point migration (curvature of wavefields). An etch pit on the entrance surface may affect the choice of wavefield but the contrast from it will be diluted in the Borrmann Fan.

It is possible that small loops may be present around the precipitate before deformation (due to insufficient vacancy migration in the growth process), which are below the resolution limit on the topographs. These may then form dislocation sources, under the action of an applied stress. This corresponds to observations on the video stills, as the contrast from the precipitates enhances considerably at stresses close to the elastic limit. It is important to note that the size of the image of the precipitate is much larger than the precipitate itself, and any loops which may either have been already present, or which are punched in due to the stress concentration close to the precipitate will not be easily discernible.

Given the presence of these small loops at stresses lower than the elastic limit, (in the predeformation region), the problem then arises how these loops can then give rise to multiplication. Recently Di Persio ([216]) did a detailed study of possible mechanisms for the multiplication of prismatic loops (and edge dipoles), based on the propagation mechanism originally proposed by Vesely (see section 1.4.4).

Different modes of multiplication can occur from a prismatic loop extended on its slip cylinder, depending on how many slip planes become active (one or more than one - cross slip being operative in the latter). The schematic diagrams (Figs 98, 99) illustrate the mechanism, which takes into account the annihilation

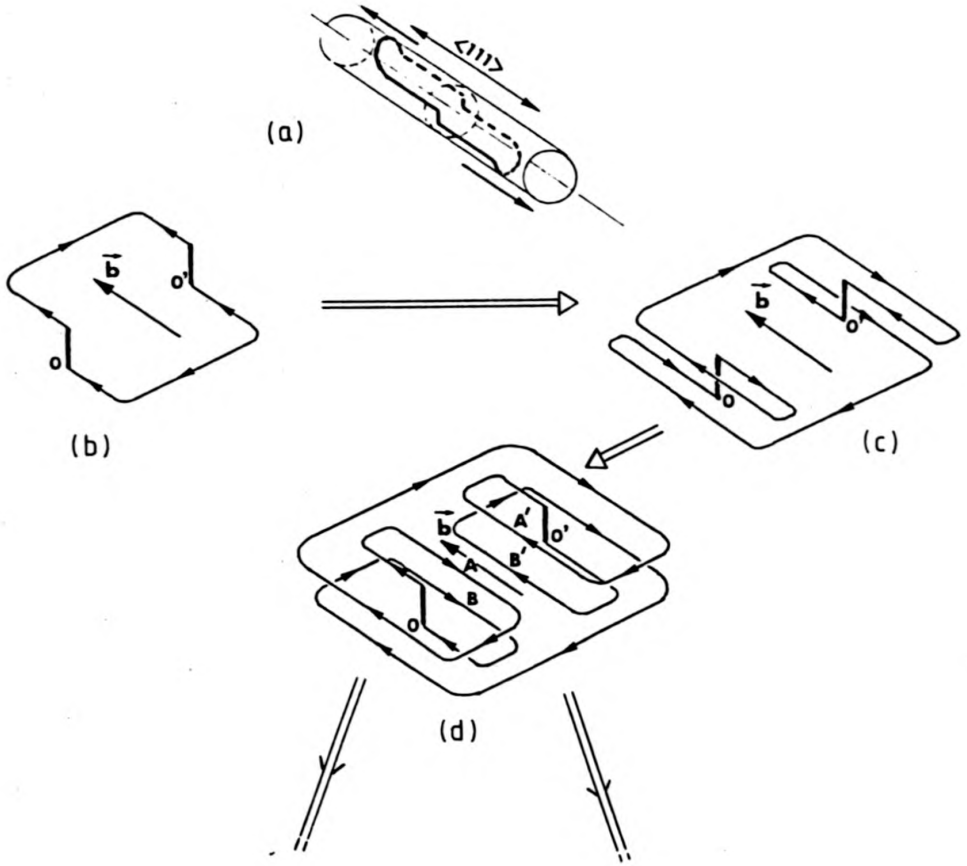
<111>
(a)
b
O'
O
(b)
b
O'
O
(c)
b
A'
O'
B'
A
B
O
(d)

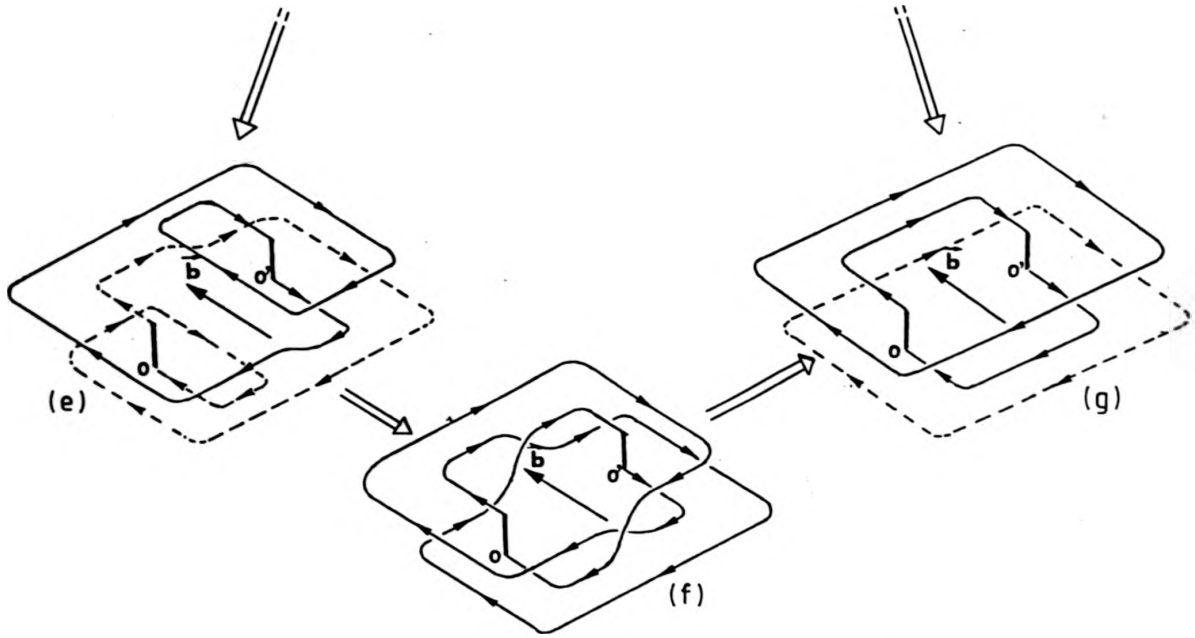

Fig 98 Schematic diagram of the operation of a source when a single slip plane is favoured by the stress. The mechanism is analogous to that of a Frank-Read source (a) rotation of a loop around its slip cylinder, (b)-(c) development of two sources (d)-(e) annihilation between A-B' (opposite sign), (d)-(g) direct annihilation AA' and BB' (e)-(f) annihilation between B-A' (f)-(g) annihilation of intersecting segments (after [216])

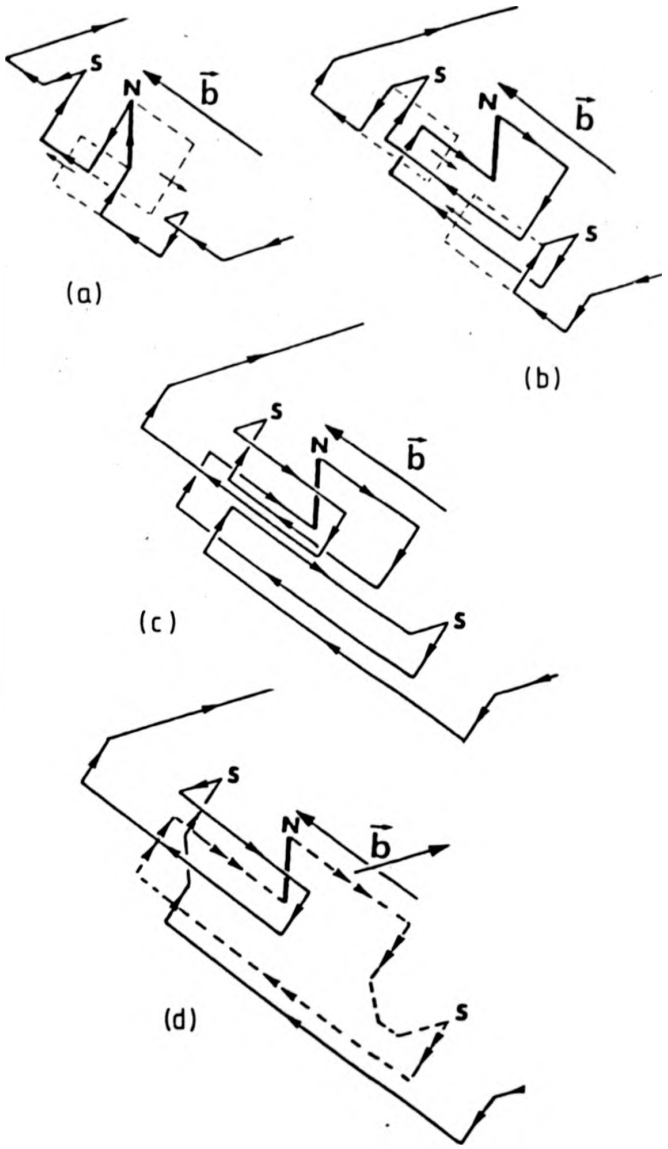

Fig 99 Mechanism of dislocation multiplication when two cross-slip planes operate (S and N indicate dislocation sources, after [218])

of screw segments of opposite sign. These sources are analogous to Frank Read sources but their development is controlled essentially by the mobility of screw segments.

As the schematic diagram shows, if the double kinks initiate on more than one plane at a time, then the situation becomes more complicated, and double sources can be produced.

The effect of surface orientation can be considered in terms of this type of mechanism. The two cases studied are illustrated, one with the operative Burgers vector parallel to the crystal surface, and the other with the Burgers vector at an angle of 35°16' with the crystal surface.

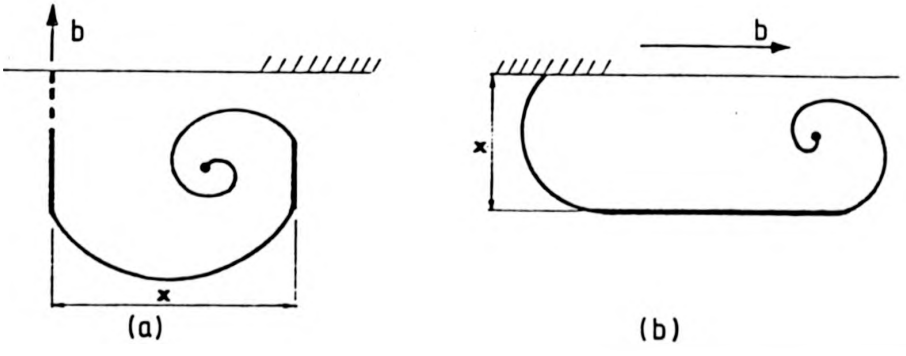

Fig 100 Schematic view (looking down [0$\bar{1}\bar{1}$]) of orientation of Burgers vectors (b) to the crystal surface
(a) Blocked source (b) Active source

7.3.5 Propagation

As pointed out in section 6.3.2d, in order to get useful quantitative data on the rates of propagation of slip bands, it is necessary to perform creep type

experiments. Unfortunately this type of experiment was not performed due to time restriction (several consecutive days of beam time would have been necessary; this was not possible).

However comparison of the video stills of C3 taken at various levels of stress, illustrate that no two slip bands propagate at the same rate. Sestak and Arnold ([31]) found that slip bands (containing parallel screw dislocations) were surrounded by a long range stress field, of which the component in the primary system acts in the vicinity of the large bands, against the applied stress. The velocity measurements made on a slip band are thus very sensitive to its 'slip band environment'. Sestak and Arnold found the same sort of dependence between the applied stress and the glide band velocity for slip bands containing screw dislocations, as for those containing edges. So, it is to be expected that bands made up of parallel edge dislocations, will be surrounded by similar long range stress fields.

In C3, different slip bands, which have been submitted to the same stress increment in between video stills, propagate different distances. This is quite probably due to the presence of other slip bands in the vicinity of the glide path.

7.3.6 Contrast

Slip band images in C3 are characterized by a band of light and a band of dark contrast, the relative proportions

of which can vary, depending on the reflection. The band of dark contrast is always on the side of the image remote from the direct beam.

Defect images on the Lang topograph taken before deformation (Fig. 77) have a certain amount of intermediary character. Pendellosung fringes are clearly seen at subgrain boundaries, and Pendellosung 'beating' can be seen on dislocation images. This topograph was taken with Mo Kα Radiation (0.709Å) and μt was approximately 4.7. This μt value is of the same order of magnitude as the corresponding values for many of the reflections on the White Beam topographs. Therefore, some of the branch 2 wavefields must be assumed to survive the absorption.

Assuming that defect images retain a certain amount of intermediary character, then the line of dark contrast could arise from intermediary effects, arising from inter-branch scattering. This line of dark contrast is on the side remote from the direct beam, which would be expected for an intermediary type of image (see section on contrast theory). The band of pale contrast could arise from a Borrmann shadow type of effect.

So, a small Borrmann effect is assumed. If a strong Borrmann effect was present, only those wavefields belonging to branch 1 of the dispersion surface, which run parallel to the diffracting planes would survive the absorption. If this was the case, for a reflection from the slip plane itself, the slip band would show as a thin white

line (pure Borrmann shadow type of image). This is clearly not the case.

The relative thicknesses of the bands of light and dark contrast are a sensitive function of the diffraction conditions.

In the context of the treatment of contrast in C1 and C2, the band of light contrast corresponds to that part of the slip band closest to the exit surface. The magnitude of the contrast variation (compared with C1 and C2) is believed too large to arise from surface relaxation effects. Confirmation of the fact that the band of light contrast corresponds to regions close to the exit surface is provided by the clear images of magnetic domains attached to it, and the corresponding blurred image at the other edge of the slip band.

7.3.7 Conclusions

1. Choice of slip system in specimens of Fe 3.5 wt % Si deformed at room temperature in tension is unaffected by surface orientation, in contrast to the behaviour of Mo reported by Vesely ([10], [73], [74], [75]).
2. Samples of (100) surface (C1,C2) and $(0\bar{1}1)$ surface (C3) deformed under uniaxial tensile stress in the [011] direction exhibit $(\bar{2}11)[111]$ slip and $(211)[\bar{1}11]$ slip.
3. In specimen C3 evidence for the nucleation of slip at precipitates and subgrain boundaries was obtained. Identification of nucleation sites was more difficult in specimens C1 and C2 as these were more defective prior to deformation. However it is possible in C2 at least, to identify nucleation sites as regions containing high densities of grown in dislocation. Nucleation near to a subgrain boundary was also observed.

   In all specimens slip nucleated at several sites simultaneously and occurred rather catastrophically making the observation of the early stages of deformation quite difficult.
4. In C1 and C2 small slip cells are seen to form via the escape of edge dislocations through the specimen surfaces, leaving behind screw dislocations, which are assumed to propagate a certain distance and then stop. These small slip cells are seen to stack side by side. The screw fronts of the slip bands are never seen to propagate across the width of the crystal.

5. In C3 edge fronts of slip bands are seen to propagate large distances through the width of the crystal. This is possibly due to the escape of the screw segments through the specimen surfaces.

6. Due to slip band morphology it was only possible to consider slip band propagation rates in C3. Lack of creep data (due to synchrotron beam time restriction) prevented quantitative analysis. However, it was possible to make qualitative observations of slip band propagation. It was observed that no two slip bands propagated at the same rate. It is concluded that this is due to the long range stress fields due to the presence of adjacent slip bands.

7. Images of slip bands in C1 and C2 are mainly white in character. This arises due to a Borrmann shadow effect (see section 4.4.2). A thin line of dark contrast is seen to correspond to slip cell intersections with the X-ray exit surface, thought to arise from surface relaxation effects.

Contrast of slip bands in specimen C3 is more complicated. Slip band images are characterized by a band of light and a band of dark contrast, the relative proportions of which depend on the diffraction conditions.

It was shown that due to the spacing of dislocations in the slip bands, they can be considered as a type of planar boundary.

8. In summary, whilst it is clear that at room temperature one is in the region between the critical temperature and the transition temperature, the formation of well-defined slip bands implies that one is in the high temperature regime.

However, in crystals of (100) surface the evolution of small slip cells most probably made up of screw dislocations, and the ready propagation of slip bands most probably made up of edge dislocations in crystals of $(0\bar{1}1)$ surface, indicate a difference in mobility between screw and non screw dislocations, implying a certain amount of low temperature behaviour.

However, the situation is slightly complicated by the fact that in the crystals of (100) surface there was a relatively high dislocation density, which may account for the rather homogeneous nucleation.

The author believes that it is the low relative mobility of screw dislocations that is the most influential factor in the origin of slip morphology in the two types of specimen.

9. White Beam Synchrotron Radiation Topography is an invaluable technique for dynamic investigation of plastic deformation in single crystals Fe 3.5 wt % Si. It has been shown to be possible to identify sites for slip nucleation. The high intensity of the beam and the subsequent possibility of using direct imaging facilities make real-time observation of slip band propagation feasible.

The wide spectral range of the synchrotron beam allows specimens to be imaged up to large strains, without the formation of Bragg contours, characteristic of conventional X-ray topographs of deformed specimens ([32]).

The wide spectral range also allows the whole of Fe 3.5 wt % Si specimens containing subgrains to be imaged. Invaluable information on the lattice rotation that accompanies plastic deformation can also be obtained.

The multiplicity of reflections attainable by the technique can, in a single exposure, yield much information on the operative slip systems in deformed samples.

APPENDIX I

Magnetic Studies

(I) - 1 Basic Domain Physics [217], [185], [186]

This section summarizes some basic concepts in domain physics, which are relevant to studies made on Fe 3.5 wt % Si crystals presented here.

(I) - 1.1 Energy Considerations

Magnetic structure in Ferromagnets is governed by the interaction of all the contributions to the total energy.

The total energy is given by

$$E_{tot} = \int (F_e + F_k + F_{magel})\, dv + F_{mag}$$

where F_e is the Exchange energy, F_k is the magnetocrystalline anisotropy energy, F_{magel} is the magnetoelastic energy, F_{mag} is the magnetostatic energy.

Each of these contributions will be considered in turn :-

(I) - 1.1a Magnetocrystalline anisotropy energy

This results from the presence of preferred directions for atomic moments (a consequence of spin orbit coupling). So called 'easy' directions exist, for example it is much easier to magnetize to saturation an Iron single crystal along <100> than along <110>, and even more <111>.

For cubic crystals, the magnetocrystalline anisotropy energy density has a quadratic form of the type

$$F_k = K_1(\alpha_1^2\alpha_2^2 + \alpha_2^2\alpha_3^2 + \alpha_3^2\alpha_1^2) + K_2(\alpha_1^2\alpha_2^2\alpha_3^2) + \ldots.$$

where α_i are the direction cosines of $\vec{M}$ (the magnetization) with respect to the cubic axes and K_i are the anisotropy

constants.

(I) -1.1b Exchange energy

This is the energy associated with the lack of parallelism of neighbouring atomic moments. If one moment is turned away from an easy direction, neighbouring moments will also rotate due to exchange coupling.

In a cubic crystal the exchange energy density is expressed as

$$F_e = \frac{c}{2} [(\text{grad } \alpha_1)^2 + (\text{grad } \alpha_2)^2 + (\text{grad } \alpha_3)^2]$$

(I) - 1.1c Magnetostatic energy

This arises from contributions to the demagnetizing field, from the presence of magnetic charges on the crystal surface.

The magnetostatic energy is given by the integral form

$$F_{mag} = -\tfrac{1}{2} \int \vec{H}_d \; ; \; Mdv - \int \vec{H}_a \cdot Mdv$$

where H_a and H_d are the applied and demagnetizing fields respectively.

(I) - 1.2 Domain Walls

The energy associated with a domain wall is

$$F_w = F_k + F_e$$

The thickness of a domain wall is determined by the competition between the anisotropy and exchange energies.

(I) - 1.3 Closure Domains

In the hypothetical case illustrated below, where a

crystal consists of one magnetic domain, a lot of magnetic charge is present at the ends of the specimen. This results in a large magnetostatic energy (see Fig. 101a).

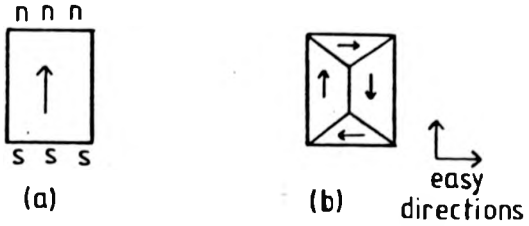

Fig. 101 Minimization of magnetostatic energy by formation of closure domains

F_{mag} can be reduced by splitting the single domain into two, separated by a domain wall. Further improvement is achieved if this process is repeated, (but at the expense of total wall energy), see Fig. 101b.

F_{mag} can be reduced to zero by the formation of flux closure domains.

(I) - 1.4 Magnetostriction

This is the origin of the contrast from magnetic domains in X-ray topography (see sections 5.1, 5.2 and [185]).

As a consequence of the distortion introduced in each separate domain (for example Fig. 102), it becomes evident that the sample could not be reconstructed without introducing internal stresses, the magnetostrictive self stresses σ^{+}_{ij} to which correspond the strains e^{+}_{ij}

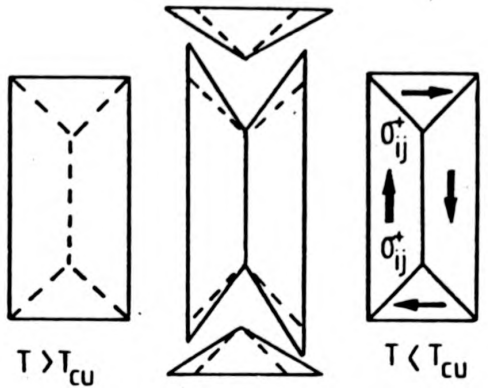

Fig 102 Illustration of the distortion introduced in magnetic domains. Below the paramagnetic-ferromagnetic transition (Curie) temperature, T_{cu}, the bcc Fe lattice changes into a slightly tetragonal lattice

These give rise to an additional energy term, the Magnetoelastic energy.

For cubic crystals, the general form of the magnetoelastic energy density is

$$F_{magel} = \frac{B_1^2}{C_{11}-C_{12}} (\alpha_1^2\alpha_2^2 + \alpha_2^2\alpha_3^2 + \alpha_3^2\alpha_1^2) + \tfrac{1}{2}\sigma_{ij}^{+}e_{ij}^{+} + \tfrac{1}{2}\sigma_{ij}^{A}e_{ij}^{A} + \tfrac{1}{2}\sigma_{ij}^{D}e_{ij}^{D} + \sigma_{ij}^{D}e_{ij}^{+}$$

where C_{11}, C_{12}, C_{44} are elastic constants. D stands for defects, A stands for applied

$B_1 = -\frac{3}{2}(C_{11}-C_{12})\lambda_{100}$, λ_{100} = coefficient of magnetostriction.

The first term is equivalent to an anisotropy term; the following three terms are elastic self energies, the last being an interaction energy. No interaction term of the kind $\sigma_{ij}^{A}e_{ij}^{+}$ is present.

Equilibrium corresponds to the minimization of E_{tot}, so that applied stresses, internal stresses, applied fields, may all influence the magnetic moment configurations.

(I) - 2 Magnetic Domain Configurations in Crystals C2 and C4

(I) - 2.1 Predeformation Magnetic Domain Structures

Figs. 103a, b show details from a Lang topograph taken of crystal C4 (g = $01\bar{1}$ Mo Kα Radiation). This topograph was chosen to illustrate the unstrained magnetic domain structure in crystals of (100) surface, because of the exceptionally good quality of the crystal.

(011) 90° walls appear as thin white lines (see section 5.1.3)

Fig 103a Detail from a Lang topograph taken of C4 ($g = 0\bar{1}1$, MoKα radiation). Precipitates can be seen at P. Wall decomposition can be seen at W. Junction contrast is seen at J. A dislocation is seen at D

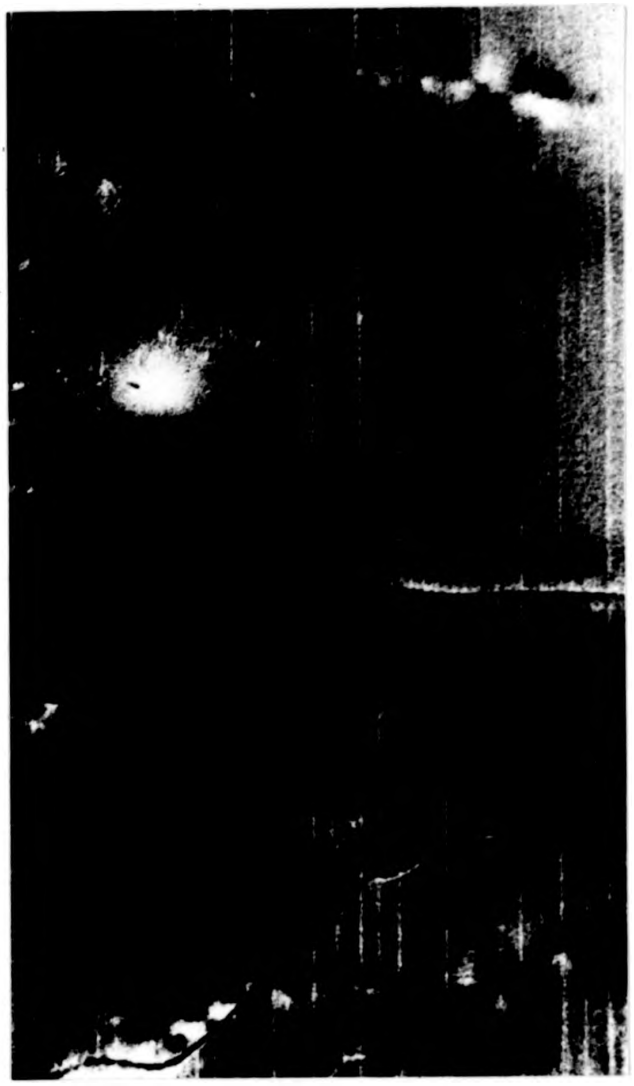

Fig 103b Detail from same Lang topograph as 103a. F represents fir tree patterns, Y junction contrast, D dislocation contrast and W wall decomposition, respectively

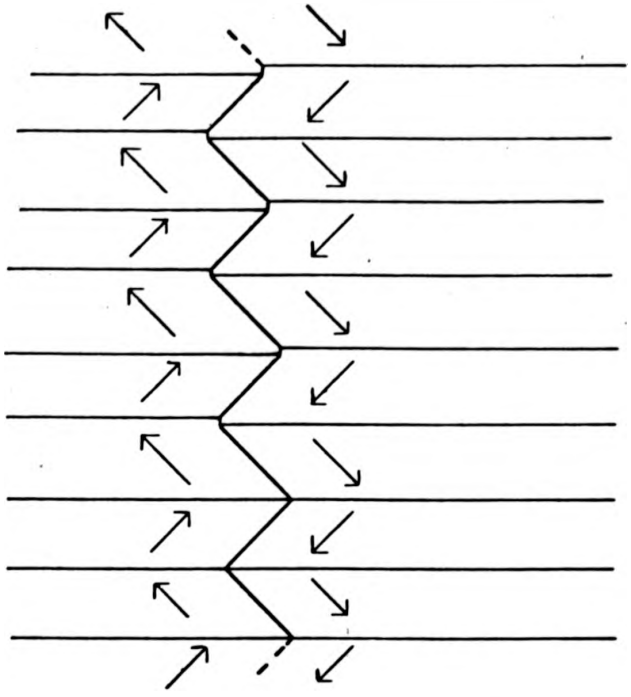

Fig 104 Schematic diagram of domain configurations observed in Fig. 103a

A schematic diagram of the configuration is presented in Fig. 104 . Y junctions of domains, with their associated two lobe wedge disclination type contrast (see section 5.1.4) are clearly visible. Precipitates can also be seen.

'Double Images' of the 90° walls are seen in parts of the topograph. This can arise from a bending of the 90° wall in the bulk of the crystal, in order to improve the distribution of surface magnetic charge ([185]). It can also be considered to be due to decomposition of (011) 90° walls ([218]), into segments of wall making angles of 62° with the surface normal (see Fig. 105).

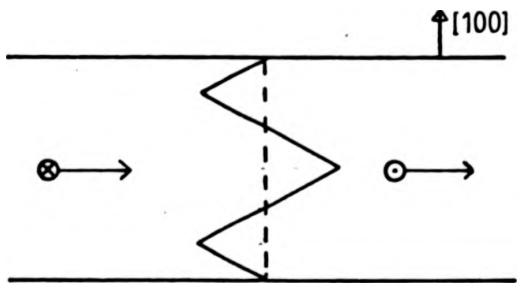

Fig 105 Decomposition of 90° wall into segments making an angle of 62° with the surface normal (after [218])

Residual contrast from 180° walls can be seen. Dislocations appear as white lines.

Synchrotron radiation topographs showing the unstrained magnetic domain configurations in crystals C2 and C4 are presented in Figs. 106,107. Again (011) 90° walls are seen to line up perpendicular to the tensile axis.

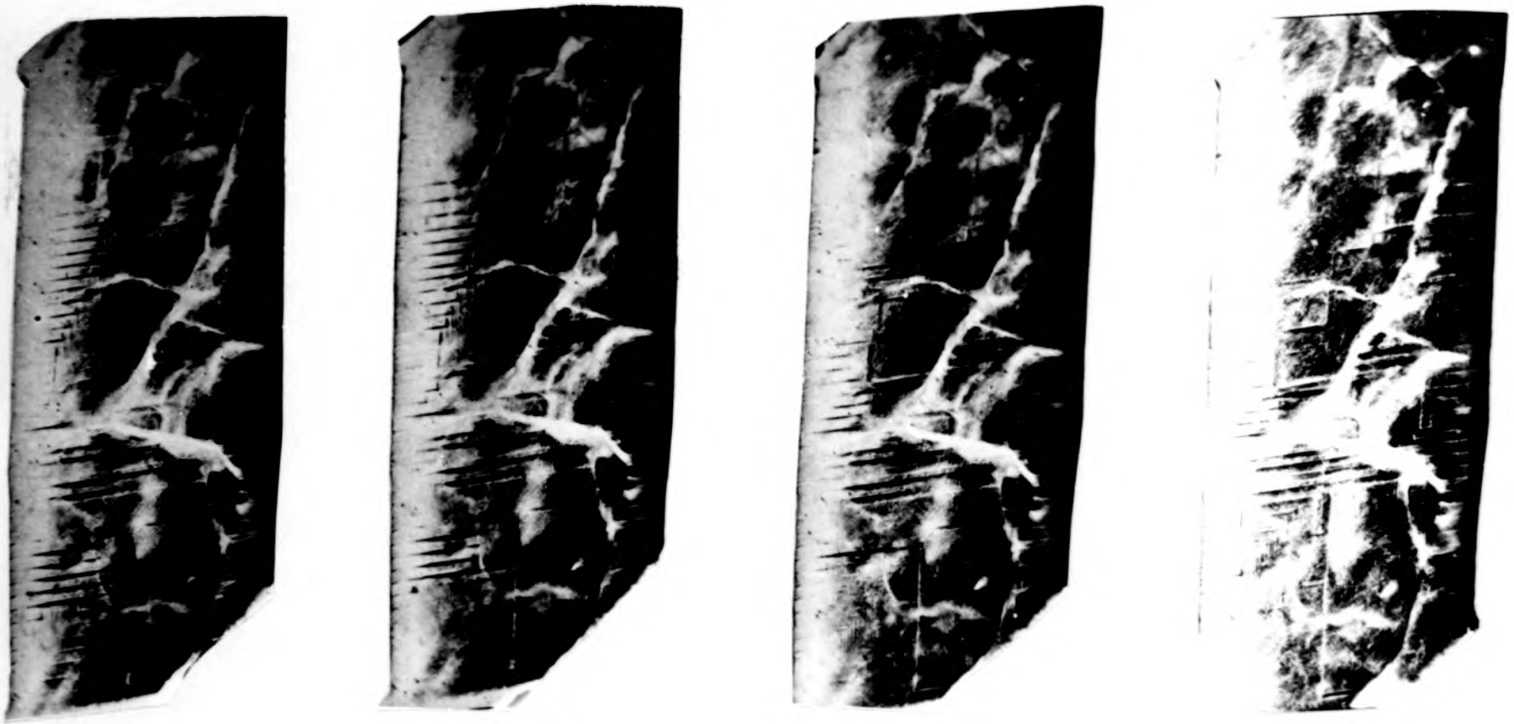

(a) 16MPa (b) 30.7MPa (c) 54.7MPa (d) 86.8MPa

(e) 125.5MPa

(f) 141.5PMa

(g) 176.2MPa

g↘

1mm

Fig 106 Series of white beam topographs (g = $00\bar{2}$ λ = 1.22Å) taken of C2 in the $00\bar{2}$ main spot geometry at (a) 16MPa (b) 30.7MPa (c) 54.7MPa (d) 86.8MPa (e) 125.5MPa (f) 141.5MPa (g) 176.2MPa

Fig 106 Series of white beam topographs ($g = 00\bar{2}$ $\lambda = 1.22\text{Å}$) taken of C2 in the $00\bar{2}$ main spot geometry at (a) 16MPa (b) 30.7MPa (c) 54.7MPa (d) 86.8MPa (e) 125.5MPa (f) 141.5MPa (g) 176.2MPa

(a) Lang topograph $g = 01\bar{1}$
MoKα radiation

(b) 0 stress

(c) 47.5MPa

(d) 95MPa

(a) Lang topograph g = $01\bar{1}$
MoKα radiation

(b) 0 stress

(c) 47.5MPa

(d) 95MPa

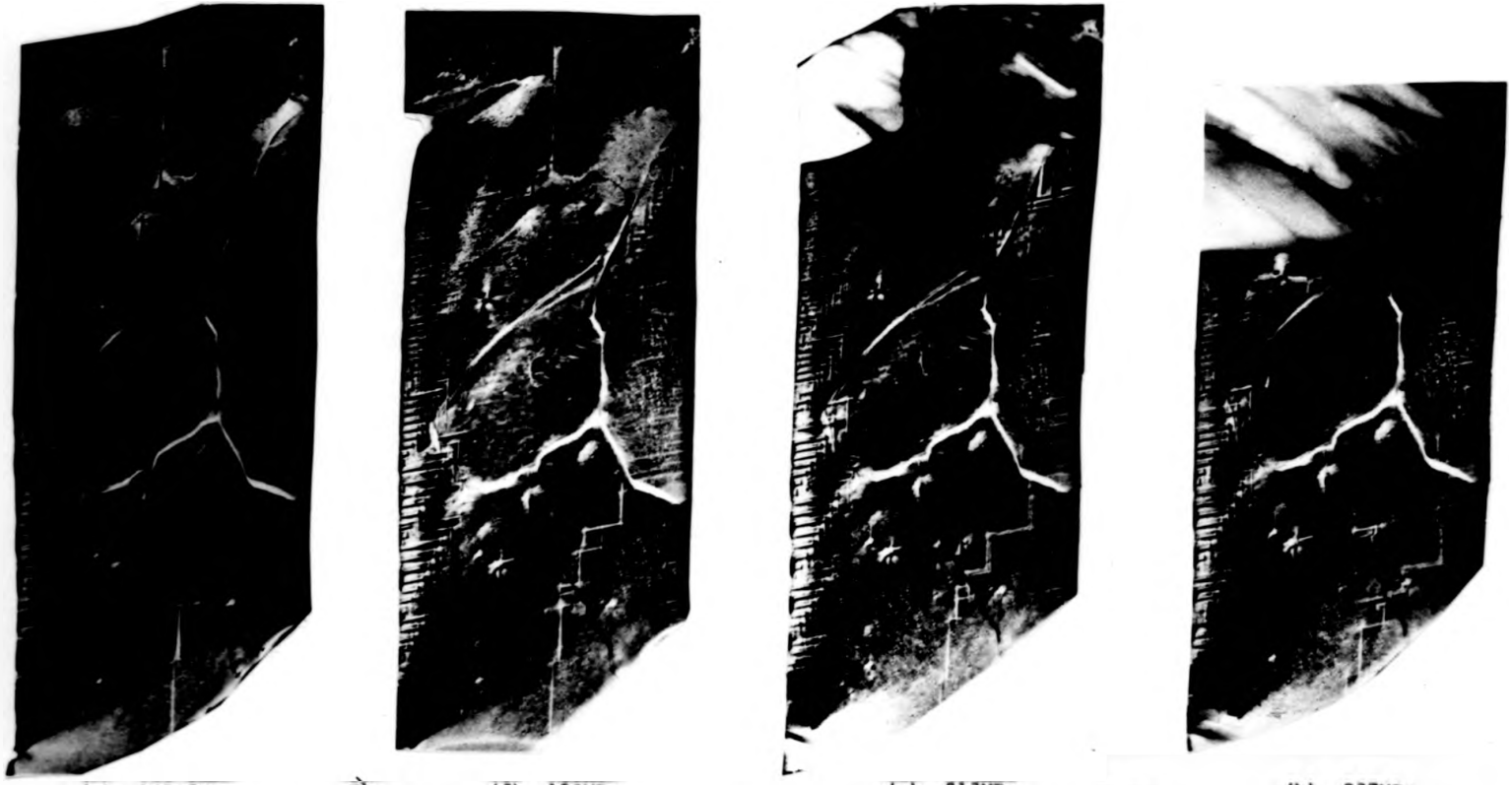

(e) 142.5MPa g (f) 190MPa (g) 213MPa 1 mm (h) 237MPa

Fig 107 Lang topograph (a) and a series of white beam topographs ($g = 00\bar{2}$ $\lambda = 1.79\text{Å}$) taken of C4 in the $00\bar{2}$ main spot geometry at (b) 0 stress (c) 47.5MPa (d) 95MPa (e) 142.5MPa (f) 190MPa (g) 213MPa (h) 237MPa. Crystal C4 necked early in the deformation due to stress concentration caused by uneven crystal thickness

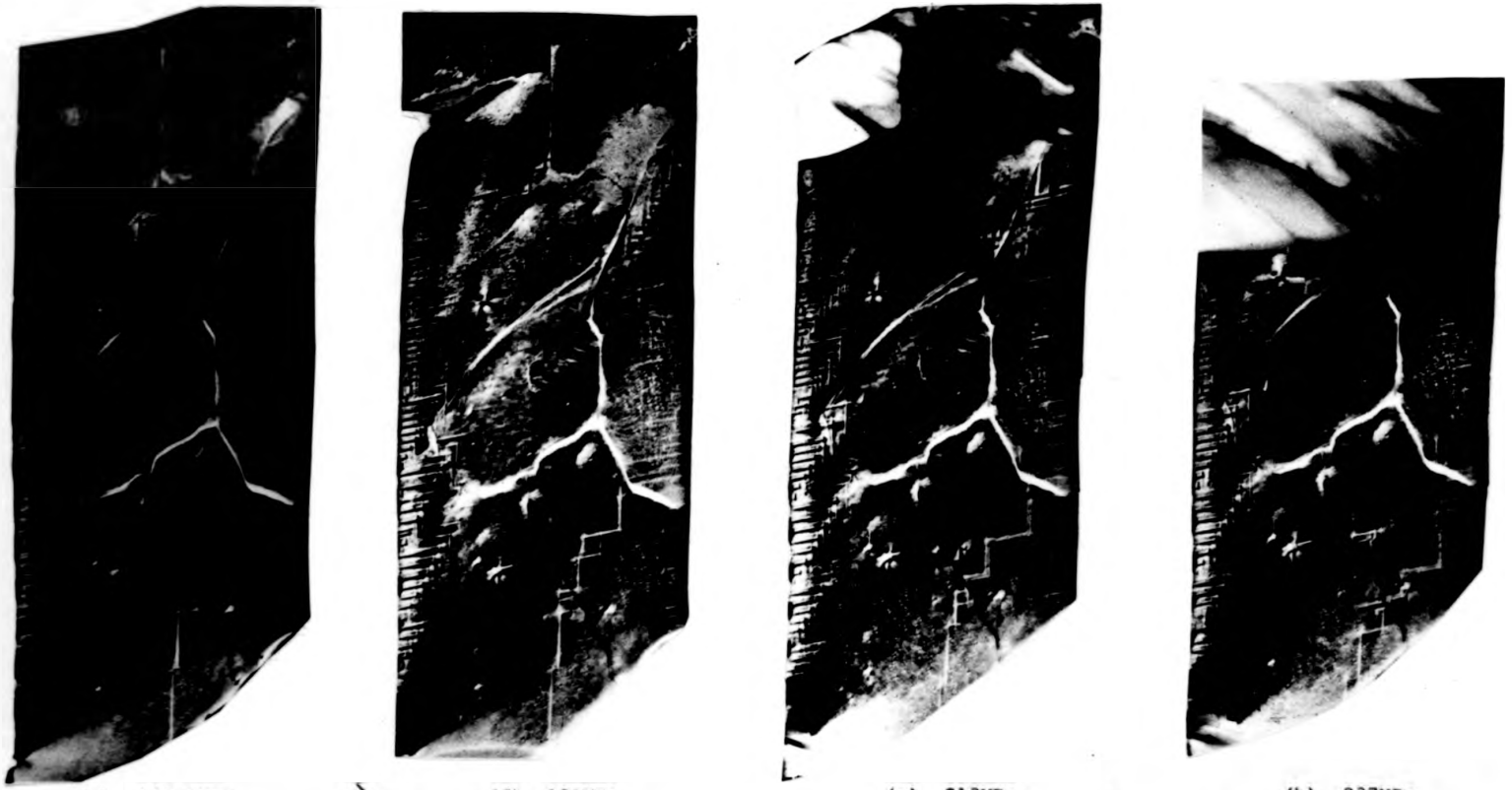

(e) 142.5MPa g (f) 190MPa (g) 213MPa 1 mm (h) 237MPa

Fig 107 Lang topograph (a) and a series of white beam topographs ($g = 00\bar{2}$ $\lambda = 1.79\text{Å}$) taken of C4 in the $00\bar{2}$ main spot geometry at (b) 0 stress (c) 47.5MPa (d) 95MPa (e) 142.5MPa (f) 190MPa (g) 213MPa (h) 237MPa. Crystal C4 necked early in the deformation due to stress concentration caused by uneven crystal thickness

(I) - 2.2 Stress Induced Changes in Magnetic Domain Structure

As is shown in the series of topographs taken under increasing elastic stress (see Figs. 106,107) the unstrained configuration is transformed into one essentially comprising a single ($0\bar{1}1$) 90° wall parallel to the tensile axis, to which (010) 180° walls are attached.

The initial and final configurations are shown schematically in Fig. 108.

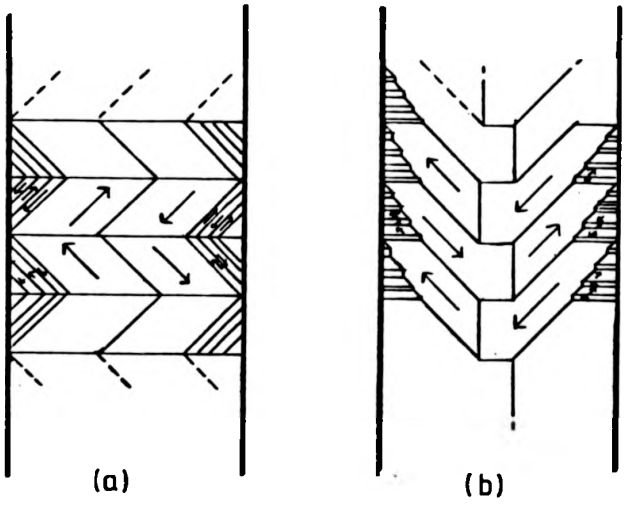

Fig 108 Schematic diagram of Initial (a) and Final (b) magnetic domain configurations in C2 under elastic stress

The two structures are characterized by equal amounts of magnetization along [010] and [001]. This leads to the hypothesis that it is not stress induced anisotropy which

provides the driving force for the transformation.

Detailed calculation ([219]) shows that the energies associated with the two structures (obtained by a summation of wall energy, magnetostatic energy, junction energy and energy associated with the closure domains) are very similar.

The calculation also shows that the density of 90° walls lying perpendicular to the tensile axis is very much smaller in the final configuration than for the initial configuration.

It is therefore possible to assume that the results may indicate a kind of instability of (011) 90° walls under uniaxial tension along [011].

Magnetic domain configurations observed at higher stresses (Fig. 107f) consist mainly of domains separated by 180° walls inclined with respect to the tensile axis.

This could be caused either by the kind of instability already mentioned, leading to a more complete disappearance of (011) 90° walls, or by a small stress induced anisotropy caused by a slight misorientation of the tensile axis with respect to [011].

A finer analysis, with more specific experiments is necessary.

(I) - 2.3 Residual Magnetic Domain Structures in C2

Residual magnetic domain configurations in C2 can be seen in between the slip band images on the post deformation

double crystal synchrotron topographs (see Figs. 68a and b). These are similar to those observed by Labrune and Kleman ([220]) in crystals of Fe 3 wt % Si deformed by bending on Lang topographs taken with the concave side of the bent specimen as the exit surface.

Fringes can be clearly seen parallel to the domain wall images. These fringes are interpreted as being depth contour lines on the closure domain walls in conformity with the results of Labrune, based on an assumption made in a comparable situation by Schlenker and Kleman ([177] ([221]) using Authier's results ([222]).

The observed fringe spacing is 12 μm. The period of the fringes to be expected from a planar boundary at 45° to the surface is given by

$$\frac{\Lambda}{\tan 45^\circ}$$

where Λ is the pendellosung length. Λ for radiation of wavelength 0.7Å is 11.5μm giving a value of 11.5μm for the fringe spacing.

This confirms that the closure domains are of the Landau-Lifschitz type ([223]).

(I) - 3 Magnetic Domain Configurations in C3

(I) - 3.1 Unstressed Configuration

In the absence of any constraint (i.e. before even mounting the specimen on the tensile stage), the magnetic domain structure in the bulk of C3 is quite simple (see Fig. 77). The domains are magnetized along ± [100]

and are separated by 180° walls which intersect the surface linearly along [100]. These domain walls are not visible on the topograph (see section 5.1.1).

A slightly more complicated situation is encountered at the edges of the specimen, where closure domains become necessary to minimize the accummulation of surface magnetic charges.

Observations made by Schlenker ([177]) using the Kerr effect, revealed irregularities in the 180° walls, and also domains which appear in the form of a lance, which exist in order to reduce the magnetostatic energy that could arise from a slight misorientation of the surface from $(0\bar{1}1)$. These domains, which are analogous to the fir tree (chevron) patterns observed in (100) crystals ([185]), are not visible by topographic methods, as they are bounded by 180° walls.

A schematic diagram of these lance type surface domains is presented in Fig. 109 . The flux within

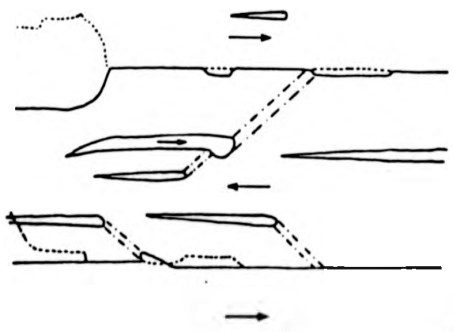

Fig 109 Schematic representation of domains on one surface (-) and the other surface (----) and closure domains in C3 (after [177])

these lance like domains is of the opposite sign to that present in the domains in which they occur. From the magnetostatic point of view, it is preferable to conserve the continuity of magnetic flux in an adjacent domain, in order to avoid the occurrence of magnetic charges on the domain walls.

These domains which are in effect internal flux closure domains should be parallel to a $\langle \bar{1}10 \rangle$ direction to avoid the appearance of further magnetic charges. This is consistent with observations. They should be magnetized along either <010> or <001>. They are also tube shaped, as they are completely immersed in a volume with uniform magnetization. They are usually observed to join an irregularity in a 180° wall and one of the lance like surface closure domains.

The internal closure domains are bound by 90° walls and as such are visible on the topograph (see Fig. 110). Similarly to the observations of Schlenker, a fringe like aspect is evident within the images of these internal flux closure domains. These fringes are again thought to be Pendellosung type thickness fringes associated with the internal 90° wall, inclined to the surface.

The schematic diagram (Fig. 111) approximately shows the structure of these domains (after Schlenker).

These internal closure domains are only present near the edges of the specimen. It is evident that the contrast from these domains is different on opposite edges of the

Fig 110 Enlargement taken from Fig 77, showing closure domains at the edges of the specimen at C, and internal closure domains at I

Fig 110 Enlargement taken from Fig 77, showing closure domains at the edges of the specimen at C, and internal closure domains at I

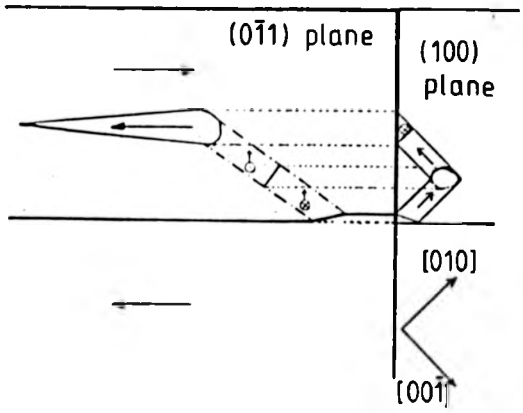

Fig 111 Structure of internal flux closure domains (after [177])

crystal. This is thought to be due to an effect of proximity to the exit surface (see section I.3.3). On the left hand side of the topograph the images of the domains and the fringes associated with them are very sharp, whereas on the right hand side the images are broader and more diffuse. The former closure domains are thought to be associated with lance like domains on the X-ray exit surface, and the latter with lance like domains on the entrance surface. This effect could arise from inhomogeneous mechanical polishing, resulting in a slight asymmetric chamfering at the edges of the crystal, see Fig. 112.

Fig 112 Possible assymetric chamfering (exaggerated) present in C3

Thus lance like surface closure domains would exist on opposite sides of the crystal at the two edges.

The flux closure domains observed at the very edge of the specimen are essentially similar to those observed by Labrune ([224]) in the thin crystal case. This configuration is shown schematically in Fig. 113 .

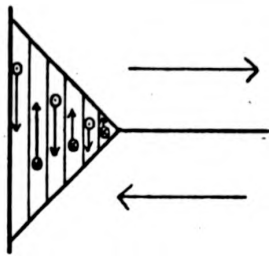

Fig 113 Flux closure domains observed at the edge of thin crystals ([225])

Contributions from the intersections of these closure domains with the entrance surface, do not always coincide exactly with those corresponding to the exit surface, and so multiple images can sometimes result.

A far more detailed investigation of the predeformation magnetic domain structure in C3 is really necessary. This was not possible due to the time restrictions imposed by the LURE shift schedule.

(I) - 3.2 Stress Induced Structures

The small internal stresses that must have been induced on mounting the specimen on the tensile stage, were enough to bring about the characteristic 'Type I' Dijkstra and Martius structure. Schlenker found this structure to be

extremely metastable. He found it could be induced by putting the crystal in a fridge for a few minutes, and that a very small mechanical shock would eradicate the structure.

A model for the magnetic structure based on the Dijkstra and Martius model is shown below in Fig. 114 .

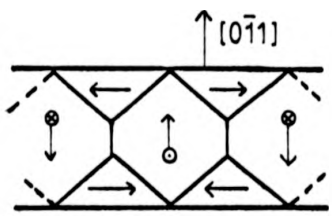

Fig 114 The Dijkstra and Martius model for the stress induced magnetic domain structure in C3

The structure shown in Fig. 115a is essentially similar to that observed by Schlenker, except that no fine Pendellosung fringes are observed in between the main fringes of contrast. Such fringes or equal depth contours are expected if one treats the surface <111> closure domain (see Fig. 114) as a planar boundary (fault plane or twin lamella).

If such fringes were to be observed on this $0\bar{1}\bar{1}$ reflection, a fringe spacing of ∿11μm would be expected. The observed spacing between the fringes is ∿50μm. Polcarova and Gemperlova, using the results of Schlenker and Kleman ([194], [221]) calculated (assuming the wall to be

(a) 0 stress

(b) 41.9 MPa

(c) 83.8 MPa

Fig 115

(a) 0 stress

(b) 41.9 MPa

(c) 83.8 MPa

Fig 115

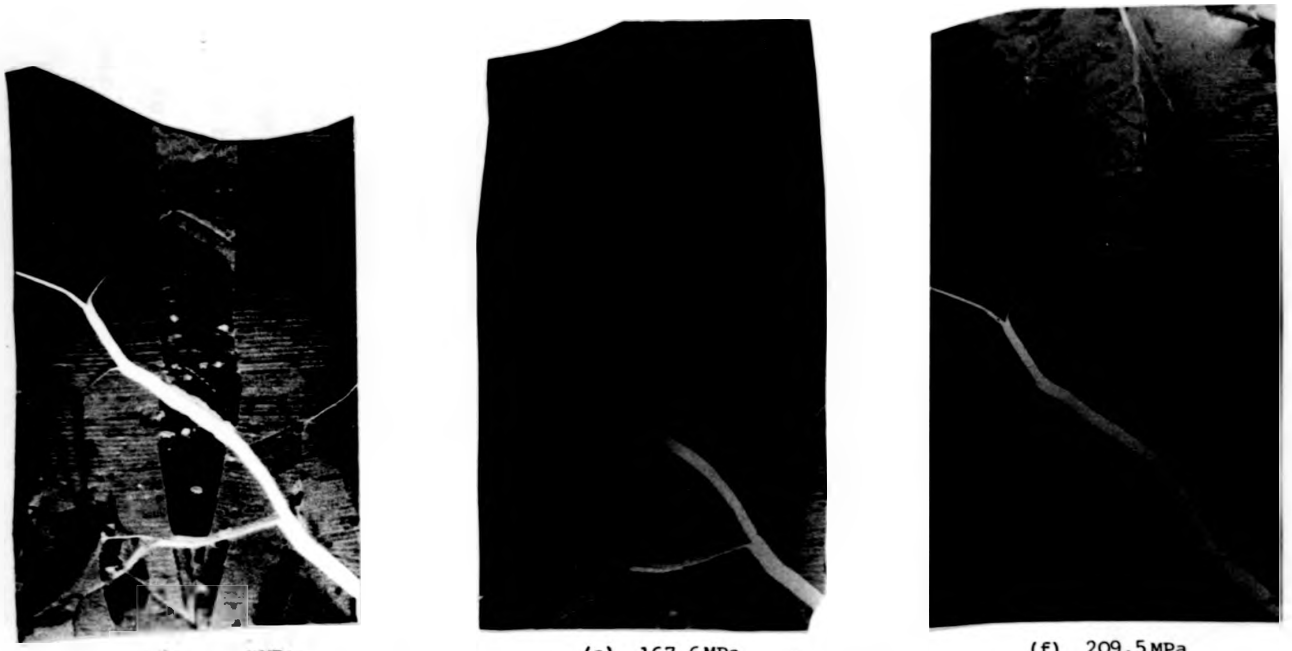

(d) 125.7MPa (e) 167.6MPa (f) 209.5MPa

Fig 115 Series of white beam topographs of C3 taken in the $0\bar{1}\bar{1}$ main spot geometry ($g = 0\bar{1}\bar{1}$, λ = 1.96Å) taken at various levels of stress (a) 0 stress (b) 41.9 MPa (c) 83.8 MPa (d) 125.7MPa (e) 167.6MPa (f) 209.5MPa

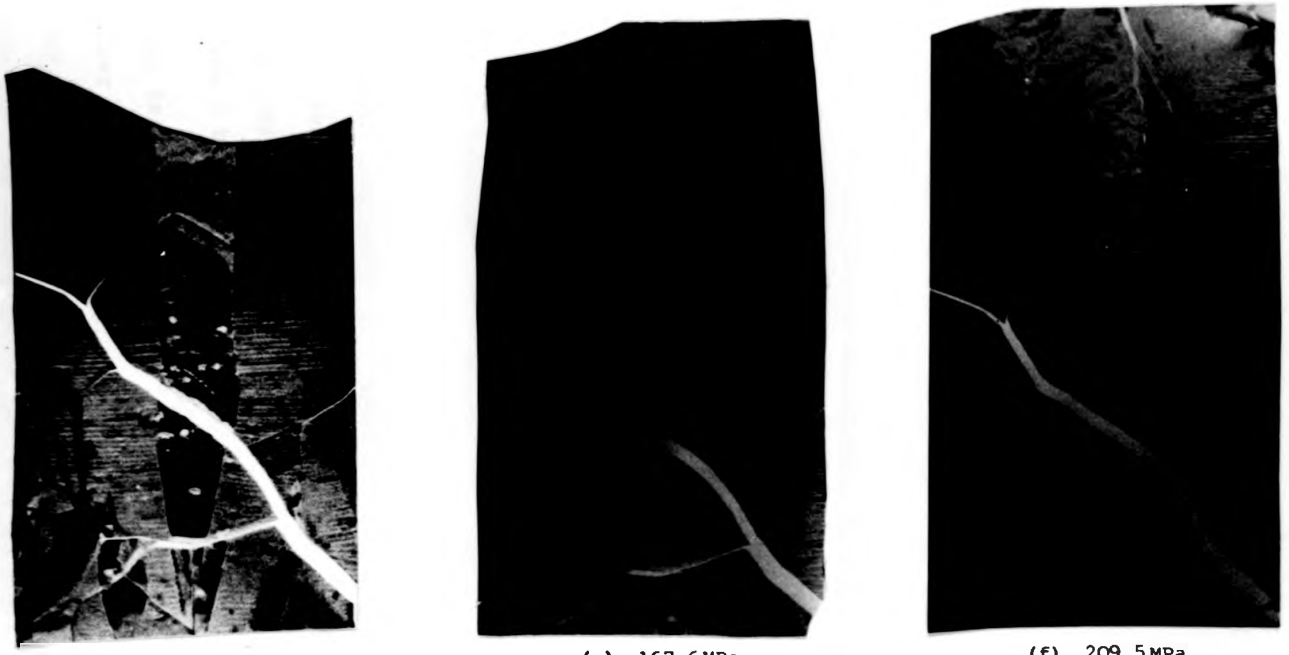

(d) 125.7MPa (e) 167.6MPa (f) 209.5MPa

Fig 115 Series of white beam topographs of C3 taken in the $0\bar{1}\bar{1}$ main spot geometry ($g = 0\bar{1}\bar{1}$, λ = 1.96Å) taken at various levels of stress (a) 0 stress (b) 41.9 MPa (c) 83.8 MPa (d) 125.7MPa (e) 167.6MPa (f) 209.5MPa

infinite and isolated) that the difference in distortion encountered upon crossing a (111) wall between a closure domain magnetized along [100] and a main domain magnetized along [001] or [010] causes the characteristic parameter of a wavefield, the departure from the Bragg angle $\Delta\theta$, to change by $\pm 0.75\lambda_{100}$ i.e. $\sim 2 \times 10^{-5}$ radians. If the relation,

$$\frac{\delta(\Delta\theta)}{\delta}$$

is less than unity where $\delta(\Delta\theta)$ is the effective misorientation associated with the boundary and δ is the rocking curve width, no great deviation of the wavefields occurs at the (111) 90° boundary. Under these conditions, Pendellosung fringes are observed. However if $\frac{\delta(\Delta\theta)}{\delta}$ is greater than unity large wavefield deviations are expected, and a consequent breakdown of phase relationships which may give rise to the Pendellosung type fringes.

For the $0\bar{1}\bar{1}$ topograph presented $\frac{\delta(\Delta\theta)}{\delta} \sim 0.2$, and no fringes would be expected. The absence of fringes is attributed to the resolution on the topograph perhaps not being good enough. Specimen film distance was restricted by the tensile stage. Such fringes are in fact observed on White Beam topographs taken at Daresbury, where the resolution was a bit better (see Fig . 81a).

Parallel Kerr effect studied by Schlenker showed that the clear dark line present on his 011 topographs corresponded to the intersection of the closure domains with the surface (see schematic, Fig. 116).

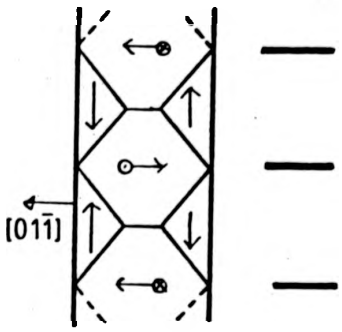

Fig 116 Illustration of the correspondence of dark lines present on 011 topographs to the magnetic structure (after [177])

On 022 topographs Schlenker observed a line of contrast associated with the 180° walls separating the main domains.

The I_h calculations (see Appendix III) showed that ($\sim$ 97.8%) of the intensity on the $0\bar{1}\bar{1}$ main spot is from the $0\bar{1}\bar{1}$ reflection. So this second kind of line characteristic of 022 reflections is not expected. Therefore the line of dark contrast is associated with the complicated closure domain junction at the crystal surface.

As the stress was increased from the nominal zero value, the periodicity of the pattern is reduced, as the domain configuration is compressed. This is attributed to stress induced anisotropy, the surface domains becoming energetically less and less favourable under increasing applied stress.

As the stress reached a value of 41.9MPa, the Dijkstra and Martius type II structure was nucleated, and this grows at the expense of the type I structure, the type I structure being compressed more and more (the same number of vertical fringes is present in the restricted

area in the central portion of Fig. 115b , as was in the whole of Fig. 115a).

The type II structure is characterized by broad horizontal fringes. This type of pattern was interpreted by Dijkstra and Martius as a configuration with basic domain walls parallel to (001) (see Fig. 117), with a complicated surface pattern due to free charges.

One way of evening out the surface charge (reducing F_{mag}) would be as shown in Fig. 118.

In their observations made using the Bitter technique, Dijkstra and Martius noticed upon close examination that what at first appeared as boundaries parallel to [100], were in fact finely divided giving a wavy boundary with its main direction close to <111>.

Within the horizontal wavy boundaries was an extremely complicated closure domain pattern. The fine structure could possibly be made up of {111} domain walls (or $\{21\bar{1}\}$ domain walls).

No fine structure is evident from the LURE White Beam topographs, although the general wavy nature of the major horizontal boundaries is evident.

(I) - 3.3 Contrast of Defects

The contrast of defects is found to be dependent on the presence of the surface closure domains in the type I structure ([177]). This is thought to be related to the redistribution of wavefield energy on crossing the (111) domain wall, on the exit surface.

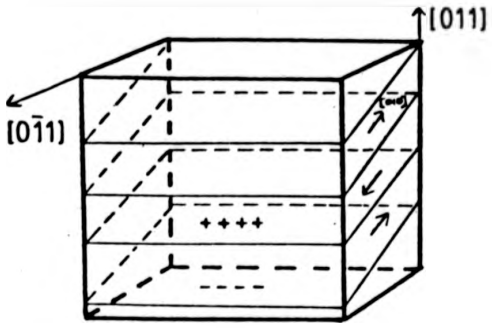

Fig 117 Model for Dijkstra and Martius type II structure

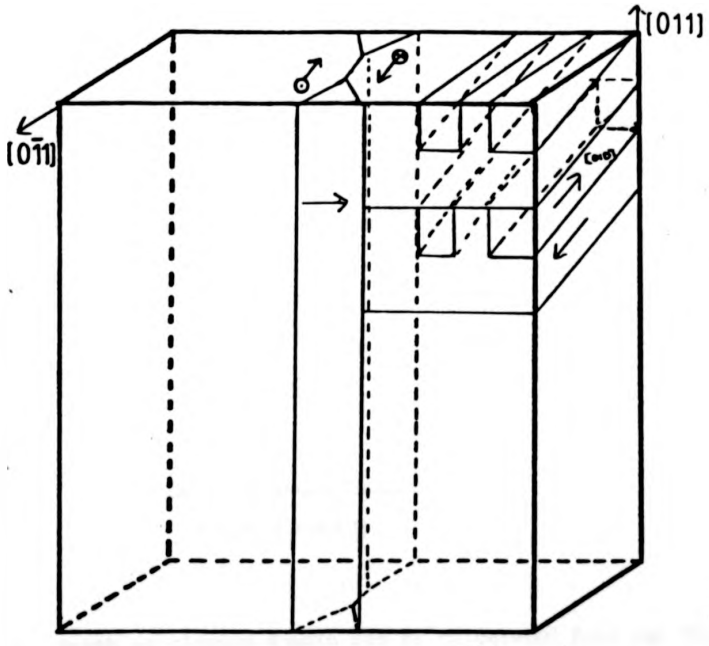

Fig 118 Model for better distribution of surface charge in the Dijkstra and Martius type II structure

If a lot of energy travels in the incident direction, intense images of a defect in the reflected direction can be expected. However, if most of the energy travels in the reflected direction before the defect is encountered, no such intense images can be expected.

If a defect lies between a closure domain and the exit surface, then such a redistribution of wavefields can mean that the image of the defect is 'masked' by the closure domain image.

This effect can be seen to vary as the 'depth' of the closure domain diminishes with increasing stress.

The contrast from precipitates and dislocations is seen to improve as the period of the type I structure diminishes.

The depth of the closure domain can be calculated, and thus an estimate of the distance of the defect from the exit surface can be made (see Fig. 119).

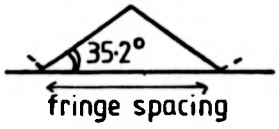

Fig 119 Depth of closure domain can be calculated from the fringe spacing, enabling an estimate to be made of the distance of a defect from the exit surface

The type II structure surface pattern is as effective as the type I structure in 'blurring' the defect images.

APPENDIX II

Projective Properties of Laue Topographs

APPENDIX II PROJECTIVE PROPERTIES OF LAUE TOPOGRAPHS ([225])

(II) - 1 Introduction

This paper presents a simple projective geometry calculation applicable to White Beam X-ray topography such as widely used in conjunction with synchrotron sources.

White Beam topography is basically a transmission Laue experiment ([226], [150]).in which defects or other lattice imperfections may be seen inside the Laue spots due to the small divergence of the beam.

Since usual detectors are photographic plates, which, geometrically, are planes, severe image distortions are observed in the various spots. It is important to know these distortions and more generally to know the projection properties of such an experiment if the ability of the Laue technique of producing several reflections simultaneously is to be fully exploited.

This calculation aims at:

i) computing the position of the spots on the detector and the operative wavelengths,

ii) defining the trace on the detector plane of incidence of a given reflection,

iii) finding the trace on the detector of a given crystallographic direction in the sample for a given spot, and the magnification ratio along that direction,

iv) defining the trace on the detector of a given crystallographic plane for a given spot as well

as the projected width of that plane.

(II) - 2 Reference Axes

The reference axes systems are shown in Fig. 120 .

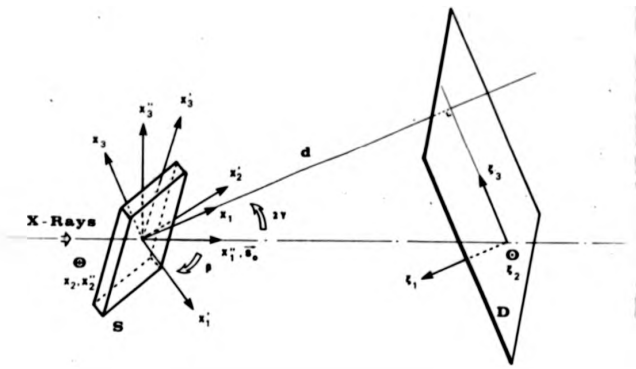

Fig. 120 Sample-detector geometry; the X_1, X_1'', X_3, X_3', X_3'', ξ_1 and ξ_3 axes belong to the plane of the drawing

The $\underline{X}_i''$ system is linked to the incident beam, $\underline{X}_1''$ being the direction of the incident beam $\underline{s}_o$.

The $\underline{X}_i$ system is linked to the detector plane, $\underline{X}_1$ being perpendicular to that plane.

The $\underline{\xi}_i$ set of axes has its origin in the detector plane the equation of which is simply

$$\xi_1 = 0 \qquad (1)$$

which may also be expressed as

$$X_1 = d \qquad (1')$$

Finally, the $\underline{X}'_1$ set of axes is linked to the sample, $\underline{X}'_3$ belonging to the sample's surface and to the $\underline{X}_1$, $\underline{X}_3$ plane, $\underline{X}'_1$ being normal to the sample's surface, $\underline{X}'_2 = X'_3 \wedge X'_1$.

The first step in the calculation consists in transforming any crystallographic direction in the sample into the $\underline{X}'$ set of axes: a unit vector $\underline{v}$ expressed in a set of orthogonal axes $\underline{i}_1$, $\underline{i}_2$, $\underline{i}_3$ linked to the crystal becomes (the $\underline{i}_1$, $\underline{i}_2$, $\underline{i}_3$ set of axes can obviously be the crystal axes for cubic crystals). For non cubic crystals, a proper transformation of the crystal axes into a convenient set of orthogonal axes must first be performed):

$$(V') = (A)\ (\underline{v}) \tag{2}$$

where the matrix (A), which is assumed to be orthogonal, is defined by:

$$(\underline{X}') = (A)\ (\underline{i}). \tag{3}$$

In the following, any quantity appearing with a single (double) prime is assumed to refer to the $\underline{X}'$ ($\underline{X}''$) set of coordinates. When no prime appears it refers to the $\underline{X}$ set of axes. Small letters are used when a quantity is referred to the $\underline{i}$ set of axes.

Other axes transformations read

$$(\underline{X}') = (B)\ (\underline{X}'') \tag{4}$$

where B is assumed to be orthogonal

$$(\underline{X}) = (C)\ (\underline{X}'') \tag{5}$$

$$(C) = \begin{pmatrix} \cos 2\gamma & 0 & \sin 2\gamma \\ 0 & 1 & 1 \\ -\sin 2\gamma & 0 & \cos \gamma \end{pmatrix} \qquad (6)$$

γ is defined in Fig. 120 . It is assumed to be positive according to the usual anticlockwise trigonometric convention.

Finally, one has:

$$\begin{aligned} \xi_1 &= d - X_1 \\ \xi_2 &= -X_2 \\ \xi_3 &= X_3 + \tan 2\gamma \end{aligned} \qquad (7)$$

where d is defined in Fig. 121.

An important practical geometry is met when the detector is perpendicular to the exit beam of a symmetric Laue reflection (Fig. 121). Distortion is, in doing so, minimized for one of the spots, which we shall hereafter call the main spot. Therefore, in addition to general equations, specific results pertaining to this geometry are given in the last section.

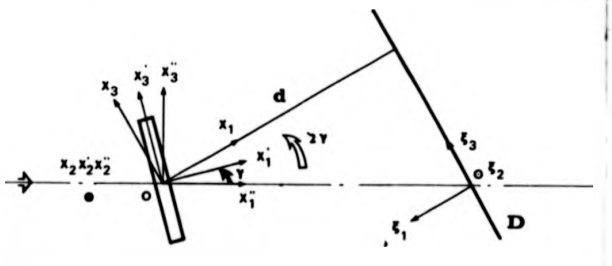

Fig. 121 . Particular sample-detector geometry: the detector is perpendicular to the exit beam of a symmetric Laue reflection. All axes belong to the plane of the drawing except for X_2, X'_2, X''_2 and ξ_2 which are perpendicular to the plane of the diagram.

(II) - 3 Position of the Spots and Operative Wavelength

The reflection is assumed to occur off a plane of normal [h, k, l] expressed in the crystal axes. Let us call $\underline{n}$ a unit vector parallel to the plane normal.

The plane of incidence (Fig. 122) contains, by definition, the incident beam direction $\underline{s}_o$, the reflecting plane normal $\underline{n}$ as well as the reflected direction $\underline{s}_h$. $\underline{s}_o$ and $\underline{s}_h$ are taken as unit vectors.

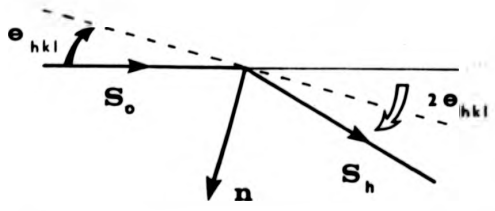

Fig. 122 Definition of $\underline{s}_o$, $\underline{s}_h$ and $\underline{n}$. The dotted line is the trace of the reflecting plane

The position of each spot is determined by the intersection of a straight line parallel to $\underline{s}_h$ and passing through the origin O, with the detector plane. Since the $\underline{s}_h$ direction belongs to the $\underline{s}_o$, $\underline{n}$ plane, one has

$$\underline{s}_h \cdot \underline{s}_o \wedge \underline{n} = 0 \qquad (8)$$

The angle between $\underline{s}_h$ and $\underline{s}_o$ is $2\theta_{hkl}$, θ_{hkl} being the Bragg angle for the h, k, l reflection. Therefore:

$$\underline{s}_h \cdot \underline{s}_o = \cos 2\theta_{hkl} \qquad (9)$$

provided $|\underline{s}_h| = 1$, and

$$\theta_{hkl} = |\text{arc sin } (\underline{s}_o . \underline{n})| \qquad (10)$$

The operative wavelength is deduced from Bragg's law

$$\lambda_{hkl} = 2d_{hkl} \, |\underline{s}_o . \underline{n}| \tag{11}$$

where d_{hkl} is the interplanar spacing.

The calculation of the components of $\underline{s}_h$ is most easily performed in the $\underline{X}_i''$ set of axes. One gets:

$$\underline{S}_o'' = [1, 0, 0] \tag{12}$$

$$(\underline{N}'') = (\tilde{B}) \, (A) \, (\underline{n}) = (\tilde{B}) \, (\underline{N}') \tag{13}$$

$$\underline{S}_h'' \begin{cases} \cos 2\theta_{hkl} \\ \sin 2\theta_{hkl} \; \dfrac{N_2''}{(N_2''^2 + N_3''^2)^{1/2}} \\ \sin 2\theta_{hkl} \; \dfrac{N_2}{(N_2''^2 + N_3''^2)^{1/2}} \end{cases} \tag{14}$$

The equation of a straight line passing through O and parallel to $\underline{S}_h$ is simply given by:

$$\frac{X_1}{S_{h1}} = \frac{X_2}{S_{h2}} = \frac{X_3}{S_{h3}} \tag{15}$$

where

$$(\underline{S}_h) = (C) \, (\underline{S}_h'') \tag{16}$$

or, according to

$$\frac{d - \xi_1}{S_{h1}} = \frac{\xi_2}{S_{h2}} = \frac{\xi_3 - \tan 2\gamma}{S_{h3}}$$

where d is the sample to detector distance (see Fig. 120). It intercepts the detector plane $\xi_1 = 0$ at the point defined by:

$$\xi_2 = - d \frac{S_{h2}}{S_{h1}}$$

$$\xi_3 = d(\tan 2\gamma + (\frac{S_{h3}}{S_{h1}})) \qquad (18)$$

(II) - 4 Trace of the Plane of Incidence

The plane of incidence for the h, k, l reflection contains $\underline{s}_o$ and therefore contains the origin O' in the detector plane and the point on the detector defined by Eq. 18 .

The angle made by the trace, in the detector plane, of the plane of incidence with the ξ_2 axis (Fig. 123) is therefore:

$$\phi = \text{arc tan } (\frac{\xi_3}{\xi_2}) \qquad (19)$$

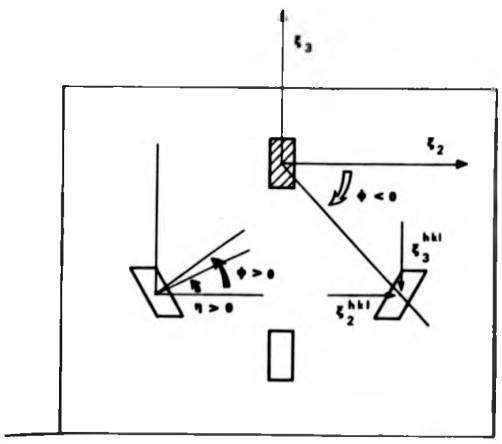

Fig. 123 . Definition of axes and angles in the detector plane. The hatched area represents the direct beam (000 spot). The other geometric figures are Laue spots.

(II) - 5 Projection of a Crystallographic Direction [u, v, w] and Magnification Ratio

Let us call $\underline{u}$ a vector parallel to the [u, v, w] direction expressed in the crystal axes.

The projection of the [u, v, w] direction is determined by the intersection of the detector plane with plane containing $\underline{u}$ and $\underline{S}_h$.

This plane is defined by:

$$\begin{vmatrix} X_1 & X_2 & X_3 \\ S_{h1} & S_{h2} & S_{h3} \\ U_1 & U_2 & U_3 \end{vmatrix} = \text{cst} \qquad (20)$$

where: $\underline{S}_h$ is given by Eq. 16 .

$$(\underline{U}) = (C)\,(B)\,(\underline{U}') \;;\; (\underline{U}') = (A)\,(\underline{u}) \qquad (21)$$

Its intersection with the detector plane satisfies Eq. 20 and Eq. 1' . The angle made by the projection of the [u, v, w] direction and the ξ_2 axis (Fig. 123) is found to be equal to:

$$\psi = \text{arctg}\ \frac{S_{h3}\,U_1 - S_{h1}\,U_3}{S_{h1}\,U_2 - S_{h2}\,U_1} \qquad (22)$$

Let us now consider the unit vector $\underline{u}$ which has its origin at O. The coordinates of the extremity H of this vector are

$$H \begin{cases} U_1 \\ U_2 \\ U_3 \end{cases} \qquad (23)$$

The extremity of this vector projects along $\underline{S}_h$ onto the detector plane. The straight line parallel to $\underline{S}_h$ and passing through that point has the following equation:

$$\frac{X_1 - U_1}{S_{h1}} = \frac{X_2 - U_2}{S_{h2}} = \frac{X_3 - U_3}{S_{h3}}$$

It intercepts the $X_1 = 0$ plane, i.e. a plane parallel to the detector and passing through the origin O, at a point H', the coordinates of which are:

$$H' \begin{cases} X_2 = U_2 - U_1 \dfrac{S_{h2}}{S_{h1}} \\ X_3 = U_3 - U_1 \dfrac{S_{h3}}{S_{h1}} \end{cases}$$

The magnification ratio is simply the ratio of the lengths of the vectors OH' and OH, the latter being by definition equal to 1:

$$M = \left[\left(U_2 - U_1 \frac{S_{h2}}{S_{h1}} \right)^2 + \left(U_3 - U_1 \frac{S_{h3}}{S_{h1}} \right)^2 \right]^{1/2}$$

(II) - 6 Projection of a Crystallographic Plane Other Than the Reflecting Plane; Projected Width

The trace, on the detector, of a crystallographic plane of normal [p, q, r] is determined by the intersection of the detector plane and the plane containing the trace of the (p, q, r) plane on the crystal surface and $\underline{S}_h$.

Let us call $\underline{p}$ a unit vector, parallel to the direction [p, q, r], the plane normal expressed in the crystal axes.

The equation of the (p, q, r) plane, passing through the origin, reads:

$$X_1' P_1' + X_2' P_2' + X_3' P_3' = 0 \qquad (27)$$

where $(\underline{P}') = (A)\ (\underline{p})$. The sample's normal $\underline{\nu}$ is defined by:

$$\underline{\nu} \begin{cases} \nu_1 = 1 \\ \nu_2 = 0 \\ \nu_3 = 0 \end{cases} \qquad (28)$$

The trace of the (p, q, r) plane in the sample's surface is parallel to the vector $\underline{T}$ defined by:

$$\underline{T}' \begin{cases} T_1' = 0 \\ T_2' = -P_3' \\ T_3' = P_2' \end{cases} \qquad (29)$$

As in the former paragraph, the equation of the projection plane is:

$$\begin{vmatrix} X_1 & X_2 & X_3 \\ S_{h1} & S_{h2} & S_{h3} \\ T_1 & T_2 & T_3 \end{vmatrix} = \text{cst} \qquad (30)$$

where $\underline{S}_h$ is given by Eq.

$$\underline{T} = (C)\ (\tilde{B})\ (\underline{T}') \qquad (31)$$

The angle η between the trace of the projection plane in the detector plane and the ξ_2 axis is (Fig. 123):

$$\eta = \arctan\left(\frac{S_{h3}\ T_1 - S_{h1}\ T_3}{S_{h1}\ T_2 - S_{h2}\ T_1}\right) \qquad (32)$$

In order to compute the projected width of the (p, q, r) plane, assuming a parallel sided sample, the constant in

Eq. (30) has to be adjusted in the following way: the (p, q, r) plane (Eq. (27)) intercepts the crystal surfaces $X_1' = \pm t$, 2t being the crystal thickness, along traces defined by:

$$\text{surface a} \quad \begin{cases} X_1' = -t \\ -t P_1' + X_2' P_2' + X_3' P_3' = 0 \end{cases}$$

$$\text{surface b} \quad \begin{cases} X_1' = +t \\ t P_1' + X_2' P_2' + X_3' P_3' = 0 \end{cases} \qquad (33)$$

Now, the constant in Eq. (30) should be adjusted in order that Eq. (30) represents either a plane containing the trace (33a) or the trace (33b). Eq. 30 will do so provided the constant is such that the projection planes contain a point on trace (33a) and a point on trace (33b). The choice of these points is arbitrary provided their coordinates remain finite.

The projection planes corresponding to the traces (33a) and (33b) intersect the detector planes along two straight lines of general equations:

$$\begin{cases} a : \alpha\xi_2 + \beta\xi_3 + \gamma_a = 0 \\ b : \alpha\xi_2 + \beta\xi_3 + \gamma_b = 0 \end{cases} \qquad (34)$$

The distances from the origin O' to those straight lines are:

$$\begin{cases} a : \delta_a = \dfrac{\gamma_a}{(\alpha^2 + \beta^2)^{1/2}} \\ b : \delta_b = \dfrac{\gamma_b}{(\alpha^2 + \beta^2)^{1/2}} \end{cases} \qquad (35)$$

The projected width of the (p, q, r) plane is therefore equal to:

$$\omega = |\delta_a - \delta_b| = \frac{|\gamma_a - \gamma_b|}{(\alpha^2 + \beta^2)^{\frac{1}{2}}} \qquad (36)$$

Finally, for a [u, v, w] direction contained in the (p, q, r) plane (up + vq + wr = 0), ψ, M, η and ω are linked by the relation

$$M \sin | \psi - \eta | = \omega \cos \varepsilon \qquad (37)$$

where ε is the angle between the [u, v, w] direction and the sample's normal. This relation may be used for cross-checking the results.

(II) - 7 Conclusion

The calculations presented in this paper may serve to:

i) characterize the observed spots (operative wavelength, diffraction vector)

ii) provide a graphic representation of the images' distortions

iii) index the observed orientations of unidentified objects contained in the sample.

This last possibility is probably the most interesting as most of the geometrical information which is needed when analysing images is contained in the various spots recorded on a single photographic plate in a White Beam X-ray topography experiment.

(II) - 8 Calculations Pertaining to the Specific Geometry Illustrated in Fig. 121

For this configuration (B) is equal to:

$$(B) = \begin{pmatrix} \cos\gamma & 0 & \sin\gamma \\ 0 & 1 & 0 \\ -\sin\gamma & 0 & \cos\gamma \end{pmatrix}$$

For the sake of brevity, let us write $\theta_{hkl} = \theta$

(II) - 8.1 Position of the Spots

One gets:

$$A1 : \quad \underline{N}'' \begin{cases} N_1'' = \cos\gamma N_1' - \sin\gamma N_3' \\ N_2'' = N_2' \\ N_3'' = \sin\gamma N_1' + \cos\gamma N_3' \end{cases}$$

$$A2 : \quad \underline{S}_h'' \begin{cases} \cos 2\theta \\ \sin 2\theta \ \frac{A}{B} \\ \sin 2\theta \ \frac{C}{B} \end{cases}$$

where $A = N_2'$; $B = (N_2''^2 + N_3''^2)^{1/2}$, $C = N_3''$

$$A3 : \quad \underline{S}_h \begin{cases} \cos 2\gamma \cos 2\theta + \sin 2\gamma \sin 2\theta \ \frac{C}{B} \\ \sin 2\theta \ \frac{A}{B} \\ -\sin 2\gamma \cos 2\theta + \cos 2\gamma \sin 2\theta \ \frac{C}{B} \end{cases}$$

Finally, one has :

$$A4 : \quad \xi_2 = -d \frac{A \sin 2\theta}{B \cos 2\gamma \cos 2\theta + C \sin 2\gamma \sin 2\theta}$$

$$\xi_3 = d \frac{C \sin 2\theta}{\cos 2\gamma \ (B \cos 2\gamma \cos 2\theta + C \sin 2\gamma \sin 2\theta)}$$

For the main spot, one gets ;

$\xi_2 = 0$ since $N_2' = 0$ and $\xi_3 = d\tan 2\theta$ as expected.

(II) - 8.2 Trace of the Plane of Incidence

From Eq. 19 , one gets:

$$A5 : \quad \phi = \arctan\left(-\frac{C}{A\cos 2\gamma}\right)$$

For the main spot, $A = 0$ and $|\phi| = \frac{\pi}{2}$

(II) - 8.3 Projection of a Crystallographic Direction

One gets :

$$A6 : \quad U_1 = U_1' \cos\gamma + U_3' \sin\gamma$$

$$U_2 = U_2'$$

from (21) and $\quad U_3 = -U_1' \sin\gamma + U_3' \cos\gamma$

A7 :

$$\psi = \arctan \frac{U_1'(C\cos\gamma \sin 2\theta - B \sin\gamma \cos 2\theta) - U_3'(C\sin\gamma \sin 2\theta + B\cos\gamma \cos 2\theta)}{U_2'(C \sin 2\gamma \sin 2\theta + B\cos 2\gamma \cos 2\theta) - A\sin 2\theta(U_1'\cos\gamma + U_3' \sin\gamma)}$$

from (22)

Eq. A7 shows, as expected, that the direction satisfying $U_1' = U_3' = 0$ $U_2' = 1$ projects along the ξ_2 axis for any spot. For the main spot, the direction satisfying, $U_1' = U_2' = 0$, $U_3' = 1$ projects along ξ_3, as anticipated, since $U_2' = 0$ and $A = 0$.

The magnification ratio (Eq. (26)) along the [u, v, w] direction, should, for the main spot be equal to 1 for the direction defined by $U_1' = U_3' = 0$, $U_2' = 1$, equal to $\cos\theta$ for the direction defined by $U_1' = U_2' = 0$, $U_3' = 1$. These

results may easily be checked.

(II) - 8.4 Projection of a Crystallographic Plane - Projected Width

Eq. 31 now reads :

$$A8: \quad T_1 = P_2' \sin\gamma$$
$$T_2 = -P_3'$$
$$T_3 = P_2' \cos\gamma$$

Eq. 32 becomes :

$$A9: \quad \eta = \arctan\left(\frac{P_2' (B\cos\gamma \cos 2\theta + C\sin\gamma \sin 2\theta)}{BP_3' \cos 2\gamma \cos 2\theta + \sin 2\theta (AP_2' \sin\gamma + C P_3' \sin 2\gamma)}\right)$$

Eq. A9 shows, as expected, that the trace on the crystal surface of the plane satisfying $P_1' = P_2' = 0$, $P_3' = 1$ projects along the ξ_2 axis since $P_2' = 0$ for any spot. For the main spot, the trace on the crystal surface of the plane satisfying $P_1' = P_3' = 0$, $P_2' = 1$ projects along the ξ_3 axis as anticipated, since P_3' and A are both equal to zero.

Let us finally consider two points, the coordinates of which are:

$$A10: \quad a) \begin{cases} X_1'^a = -t \\ X_2'^a = 0 \\ X_3'^a = t \dfrac{P_1'}{P_3'} \end{cases} \qquad b) \begin{cases} X_1'^b = +t \\ X_2'^b = 0 \\ X_3'^b = -t \dfrac{P_1'}{P_3'} \end{cases}$$

They satisfy Eq. 33a and 33b respectively. This choice is good as long as P_3' is different from 0.

Transformation in the X_i set of coordinates yields:

$$X_1^a = -X_1^b = -\,t\cos\gamma + t\sin\gamma\,\frac{P_1'}{P_3'}$$

A11 :
$$X_2^a = X_2^b = 0$$

$$X_3^a = -\,X_3^b = t\sin\gamma + t\cos\gamma\,\frac{P_1'}{P_3'}$$

Eq. (30)now reads :

A12:
$$\begin{vmatrix} X_1-X_1^a & X_2-X_2^a & X_3-X_3^a \\ S_{h1} & S_{h2} & S_{h3} \\ T_1 & T_2 & T_3 \end{vmatrix} = 0 \text{ for surface (a)}$$

A13 :
$$\begin{vmatrix} X_1-X_1^b & X_2-X_2^b & X_3-X_3^b \\ S_{h1} & S_{h2} & S_{h3} \\ T_1 & T_2 & T_3 \end{vmatrix} = 0 \text{ for surface (b)}$$

Transformation into the ξ_i set of coordinates is straightforward. The planes defined by A12 and A13 intersect the detector plane $\xi_1 = 0$ along two lines. The distance between those straight lines is the (p, q, r) projected plane width.

Let us call:

A14
$$E = S_{h2}\,T_3 - S_{h3}\,T_2$$

$$= -\,P_3'\sin2\gamma\cos2\theta + \left(\frac{A}{B}\,P_2'\cos\gamma + \frac{C}{B}\,P_3'\cos2\gamma\right)\sin2\theta$$

$$F=\alpha=S_{h3}\,T_1-S_{h1}T_3 = -\,P_2'\left(\cos\gamma\cos2\theta + \frac{C}{B}\sin\gamma\sin2\theta\right)$$

$$G=\beta=S_{h1}\,T_2-S_{h2}T_1$$

$$= -\left(P_3'\cos2\gamma\cos2\theta + \left(\frac{A}{B}\,P_2'\sin\gamma + \frac{C}{B}\,P_3'\sin2\gamma\right)\sin2\theta\right)$$

According to Eq. (34)and (36), one gets:

$$\text{A15} \qquad \omega = 2t \left| \frac{E(P_3' \cos\gamma - P_1' \sin\gamma) - G(P_1' \cos\gamma + P_3' \sin\gamma)}{P_3' \ (F^2 + G^2)^{\frac{1}{2}}} \right|$$

For the main spot ($A = 0$, $B = C = \cos\gamma = \cos\theta$) and for the plane satisfying $P_1' = P_2' = 0$, $P_3' = 1$, i.e. the reflecting plane, A15 reduces to:

$$\omega = 2t \sin\theta \qquad \text{as anticipated.}$$

If $P_3' = 0$, another choice of points needs to be made. The nature of the calculation remains however the same.

APPENDIX III

Intensity Calculations

APPENDIX III INTENSITY CALCULATIONS

(III) - 1 Introduction

Due to the wide spectral range of a synchrotron X-ray beam (typically $\sim 0.4\mathring{A} \rightarrow \sim 2.5\mathring{A}$), there is a problem of harmonic contamination. For a given value of θ, in a given g direction, there can be several harmonic wavelengths present, each related by the factor 'n' defined in Bragg's Law

$$n\lambda = 2d \sin\theta$$

This can be conveniently illustrated by the Du Mond diagram corresponding to White Beam X-ray topography (see Fig. 124 , ([195]))

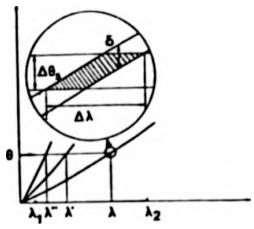

Fig 124 Du Mond diagram for White Beam Topography

It is important to be able to estimate the harmonic content of a particular spot, as contrast effects are a very sensitive function of absorption, which can in turn be a sensitive function of wavelength (as is the case

for example, in Iron, where there is an absorption edge at 1.74Å).

As pointed out in section 2.6.2 , it is possible to calculate the intensity (I_{hkl}) of a given hkℓ reflection.

This is proportional to (for symmetric reflections see section 2.6.2),

$$I_{hkl} \propto \frac{|F_{hkl}|\ P(\lambda)\ \lambda^3\ e^{-\mu_B t}\ S_i}{\sin^2\theta_B}$$

where, $F_{hkl} = \sqrt{F'^2 + F''^2}$ is the structure factor, F' being the real component, F'' the imaginary, $P(\lambda)$ is the intensity of the source at the selected wavelength λ, S_i is the effective source dimension in the incidence plane, μ_B represents the true absorption coefficient taking into account the Borrmann effect.

The former terms can be found in the literature ([227], [228]), but the latter term requires calculation.

(III) - 2 Borrmann Absorption Coefficient

The Borrmann effect arises from an extinguishing of the normal photoelectric absorption that occurs when an X-ray beam traverses a slab of material without diffracting. In such circumstances, which are characteristic of X-ray radiography, one can write the transmitted intensity, I_T, in relation to the incident intensity, I_o, as

$$I_T = I_o \exp(-\mu_o t)$$

where t is the thickness of the slab, and μ_o is the linear absorption coefficient, which is related to the imaginary

part of the average dielectric constant, and hence the imaginary part of the atomic scattering factor, $\Delta F_o''$ (this is the zero order term, which corresponds to hkℓ = 000, i.e. no diffraction), as follows,

$$\mu_o = (\frac{2\pi}{\lambda})\ \Gamma\ \Delta F_o''$$

where $\Gamma = \frac{r_e\ \lambda^2}{\pi V}$, V being the unit cell volume and r_e the classical electron radius.

When diffraction occurs, the Bloch waves or wavefields excited in the crystal actually behave as standing waves. There are two standing waves per polarization state, one with antinodes at the atomic planes, and one with nodes at the atomic planes (similar to, for example, the case in electron microscopy ([159])). The wavefield with antinodes at the atomic sites suffers enhanced absorption and the one with nodes at the atomic sites suffers less than normal photoelectric absorption.

For the symmetric Laue case, the Borrmann absorption coefficient can be written ([163], [229])

$$\mu_B = \mu_o\ [1 \pm |C|\ \varepsilon\ \exp(-M)\ \{1-p^2\}^{\frac{1}{2}}]$$

where C is the polarization factor.

For a centrosymmetric crystal, for a reflection where all the atoms scatter in phase, ε is defined as ([163])

$$\varepsilon = \frac{\Delta F''\ (2\theta_B)}{\Delta F''\ (0)}$$

the ratio of the imaginary part of the atomic scattering factor at diffracting angle $2\theta_B$ to the value for forward scattering.

p is defined as $p = \frac{\tan \Delta}{\tan \theta_B}$, where Δ is the angle between the Poynting vector $\underline{S}$ and the atomic planes, and θ_B is the Bragg angle.

For simplicity the case where energy flow is along the atomic planes will be considered, so that p=0.

Only the absorption for wavefields associated with branch 2 of the dispersion surface will be considered as these are the ones that may experience less than normal photoelectric absorption, so that the expression for μ_B can be written

$$\mu_B = \mu_o \{1-|C| \exp(-M) \{\frac{\Delta F''(2\theta_B)}{\Delta F''(O)}\}]$$

$\Delta F''(O)$ can be calculated from published values of μ ([227]). $\Delta F''(2\theta_B)$ can be interpolated from dispersion corrections published in the literature ([228]).

The Debye Waller factor term was also taken into account in calculating the Borrmann absorption coefficient, but this factor was found to be negligible for Iron at room temperature (it is assumed that the corresponding factor will be very similar for Fe 3.5 wt % Si).

When calculating the relative intensities of the harmonics, it is necessary to take into account absorption by air (if the experiment is not conducted in an inert atmosphere - the case for Cl), which affects mostly long wavelengths ([150], [151]). It is also necessary to take into account the detector response as a function of wavelength ([151]). This is particularly important for

p is defined as $p = \frac{\tan \Delta}{\tan \theta_B}$, where Δ is the angle between the Poynting vector $\underline{S}$ and the atomic planes, and θ_B is the Bragg angle.

For simplicity the case where energy flow is along the atomic planes will be considered, so that p=0.

Only the absorption for wavefields associated with branch 2 of the dispersion surface will be considered as these are the ones that may experience less than normal photoelectric absorption, so that the expression for μ_B can be written

$$\mu_B = \mu_o \{1-|C| \exp(-M) \{\frac{\Delta F''(2\theta_B)}{\Delta F''(0)}\}]$$

$\Delta F''(0)$ can be calculated from published values of μ ([227]). $\Delta F''(2\theta_B)$ can be interpolated from dispersion corrections published in the literature ([228]).

The Debye Waller factor term was also taken into account in calculating the Borrmann absorption coefficient, but this factor was found to be negligible for Iron at room temperature (it is assumed that the corresponding factor will be very similar for Fe 3.5 wt % Si).

When calculating the relative intensities of the harmonics, it is necessary to take into account absorption by air (if the experiment is not conducted in an inert atmosphere - the case for Cl), which affects mostly long wavelengths ([150], [151]). It is also necessary to take into account the detector response as a function of wavelength ([151]). This is particularly important for

photographic emulsions since Ag Br has two absorption edges at 0.484Å and 0.920Å in the spectral range usually employed for topography ([158], [230], [231]).

It is desirable in White Beam topography, to have as many useful reflections as possible, with comparable intensity. This was found to be quite difficult to achieve with crystal C3 in the $0\bar{1}\bar{1}$ main spot geometry. The $0\bar{1}\bar{1}$ reflection was initially much more intense than the other spots of interest. The relative intensities of the spots were adjusted and equalized by inserting an aluminium filter of suitable thickness.

C1 $0\bar{1}\bar{1}$ Main Spot Geometry

Table X

Fundamental	Percentage harmonic intensities in a particular spot
$0\bar{1}\bar{1}$	99.9% $0\bar{1}\bar{1}$ ($\mu_B t$=0.9)
$00\bar{2}$, $0\bar{2}0$	41.8% $00\bar{2}$ ($\mu_B t$=5.8) 58.2% $00\bar{4}$ ($\mu_B t$=1.5)

C2 $00\bar{2}$ Main Spot Geometry

Table XI

Fundamental	Percentage harmonic intensities
$00\bar{2}$	99.9% $00\bar{2}$ ($\mu_B t$=0.4)
$0\bar{1}\bar{1}$	98.4% $0\bar{1}\bar{1}$ ($\mu_B t$=3.4) 1.5% $0\bar{2}\bar{2}$ ($\mu_B t$=4.9)

C2 $0\bar{1}\bar{1}$ Main Spot Geometry

Table XII

Fundamental	Percentage harmonic intensities
$0\bar{1}\bar{1}$	99.9% $0\bar{1}\bar{1}$ ($\mu_B t$=0.5)
$00\bar{2}$	85.5% $00\bar{2}$ ($\mu_B t$=3.7) 14.5% $00\bar{4}$ ($\mu_B t$=0.86)

C2 $0\bar{1}1$ Main Spot Geometry

Table XIII

Fundamental	Percentage harmonic intensities
$0\bar{1}1$	99.2% $0\bar{1}1$ ($\mu_B t$=4.6) 0.8% $0\bar{2}2$ ($\mu_B t$=0.67)
$0\bar{2}0$	99.9% $0\bar{2}0$ ($\mu_B t$=0.6)
$0\bar{3}1$	99.9% $0\bar{3}1$ ($\mu_B t$=0.26)

C3 $0\bar{1}\bar{1}$ Main Spot Geometry

Table XIV

Fundamental	Percentage harmonic intensities
$0\bar{1}\bar{1}$	97.8% $0\bar{1}\bar{1}$ ($\mu_B t$=3.7) 0.8% $0\bar{2}\bar{2}$ ($\mu_B t$=5.5 1.2% $0\bar{3}\bar{3}$ ($\mu_B t$=1.9) 0.2% $0\bar{4}\bar{4}$ ($\mu_B t$=0.5)
$\bar{2}1\bar{1}$, $2\bar{1}\bar{1}$	99.9% $\bar{2}1\bar{1}$, $2\bar{1}\bar{1}$ ($\mu_B t$ ($\bar{2}1\bar{1}$)=2.5, $\mu_B t$ ($2\bar{1}\bar{1}$) = 3.6)
$\bar{2}\bar{2}\bar{2}$, $2\bar{2}\bar{2}$	99.9% $\bar{2}\bar{2}\bar{2}$, $2\bar{2}\bar{2}$ ($\mu_B t$ ($\bar{2}\bar{2}\bar{2}$)=2.8, $\mu_B t$ ($2\bar{2}\bar{2}$) = 3.4
$\bar{2}\bar{4}\bar{4}$, $2\bar{4}\bar{4}$	99.9% $\bar{2}\bar{4}\bar{4}$, $2\bar{4}\bar{4}$ ($\mu_B t$ ($\bar{2}\bar{4}\bar{4}$)=0.7, $\mu_B t$ ($2\bar{4}\bar{4}$) = 0.85)
$\bar{2}\bar{3}\bar{3}$, $2\bar{3}\bar{3}$	99.9% $\bar{2}\bar{3}\bar{3}$, $2\bar{3}\bar{3}$ ($\mu_B t$ ($\bar{2}\bar{3}\bar{3}$)=1.27, $\mu_B t$ ($2\bar{3}\bar{3}$) = 1.5

C2 $0\bar{1}\bar{1}$ Main Spot Geometry

Table XII

Fundamental	Percentage harmonic intensities
$0\bar{1}\bar{1}$	99.9% $0\bar{1}\bar{1}$ ($\mu_B t$=0.5)
$00\bar{2}$	85.5% $00\bar{2}$ ($\mu_B t$=3.7) 14.5% $00\bar{4}$ ($\mu_B t$=0.86)

C2 $0\bar{1}1$ Main Spot Geometry

Table XIII

Fundamental	Percentage harmonic intensities
$0\bar{1}1$	99.2% $0\bar{1}1$ ($\mu_B t$=4.6) 0.8% $0\bar{2}2$ ($\mu_B t$=0.67)
$0\bar{2}0$	99.9% $0\bar{2}0$ ($\mu_B t$=0.6)
$0\bar{3}1$	99.9% $0\bar{3}1$ ($\mu_B t$=0.26)

C3 $0\bar{1}\bar{1}$ Main Spot Geometry

Table XIV

Fundamental	Percentage harmonic intensities
$0\bar{1}\bar{1}$	97.8% $0\bar{1}\bar{1}$ ($\mu_B t$=3.7) 0.8% $0\bar{2}\bar{2}$ ($\mu_B t$=5.5 1.2% $0\bar{3}\bar{3}$ ($\mu_B t$=1.9) 0.2% $0\bar{4}\bar{4}$ ($\mu_B t$=0.5)
$\bar{2}1\bar{1}$, $2\bar{1}\bar{1}$	99.9% $\bar{2}1\bar{1}$, $2\bar{1}\bar{1}$ ($\mu_B t$ ($\bar{2}1\bar{1}$)=2.5, $\mu_B t$ ($2\bar{1}\bar{1}$) = 3.6)
$\bar{2}2\bar{2}$, $2\bar{2}\bar{2}$	99.9% $\bar{2}2\bar{2}$, $2\bar{2}\bar{2}$ ($\mu_B t$ ($\bar{2}2\bar{2}$)=2.8, $\mu_B t$ ($2\bar{2}\bar{2}$) = 3.4
$\bar{2}4\bar{4}$, $2\bar{4}\bar{4}$	99.9% $\bar{2}4\bar{4}$, $2\bar{4}\bar{4}$ ($\mu_B t$ ($\bar{2}4\bar{4}$)=0.7, $\mu_B t$ ($2\bar{4}\bar{4}$) = 0.85)
$\bar{2}3\bar{3}$, $2\bar{3}\bar{3}$	99.9% $\bar{2}3\bar{3}$, $2\bar{3}\bar{3}$ ($\mu_B t$ ($\bar{2}3\bar{3}$)=1.27, $\mu_B t$ ($2\bar{3}\bar{3}$) = 1.5

(III) - 3 Optimization of Choice of Operative Wavelength

In the case of crystal C2 in the $00\bar{2}$ main spot geometry a series of topographs were taken across the K absorption edge for Iron. In this way the choice of operative wavelength was optimized. This series of topographs is presented in Fig. 125 .

(III) - 4 Definition of Effective Misorientation, $\delta(\Delta\theta)$, and Deformation Gradient G

The effective misorientation around a defect is defined as follows ([174],[184]),

$$\delta(\Delta\theta) = \frac{1}{k \sin 2\theta} \frac{\partial(\underline{h}.\underline{u})}{\partial \underline{s}_h} = - \frac{\partial}{\partial x_1} - \tan\theta \frac{\partial}{\partial x_3} (\underline{u}.\underline{e}'_3)$$

where θ is the Bragg angle, k the wave number, $\underline{u}$ is the atomic displacement resulting from the defect (e.g. dislocation), $\underline{h}$ is the reciprocal lattice vector of the reflection, $\underline{e}'_3$ is a unit vector in the direction of $\underline{h}$, and $\frac{\partial}{\partial \underline{s}_h}$ is the partial derivative operator in the reflected direction. The directions x'_1 and x'_3 are coordinates in a system related to the reflecting planes by

$$\underline{e}'_1 = \frac{\underline{s}_o + \underline{s}_h}{2 \cos\theta}, \quad \underline{e}'_3 = \frac{\underline{s}_o - \underline{s}_h}{2 \sin\theta} \quad \text{and} \quad \underline{e}'_2 = \underline{e}'_3 \wedge \underline{e}'_1$$

where $\underline{s}_o$ and $\underline{s}_h$ are unit vectors in the incident and reflected directions respectively (Note that $\underline{e}'_3$ is antiparallel to the $\underline{g}$ vector as normally defined).

The displacements $\underline{u}$ around a dislocation may be given in isotropic elasticity in a coordinate system $\underline{e}_i$ where $\underline{e}_3$ is parallel to the dislocation line, $\underline{e}_1$ parallel to the

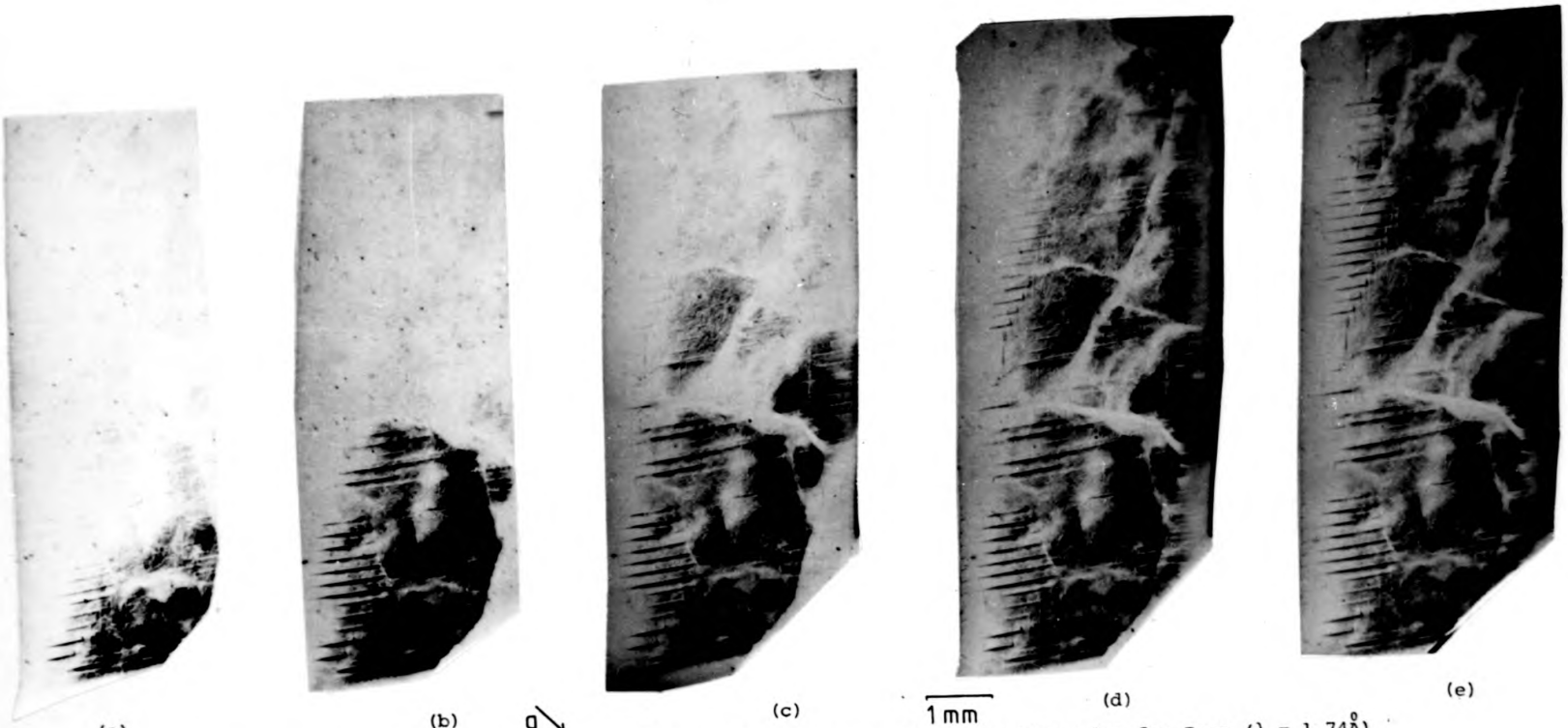

Fig 125 Series of white beam topographs ($g = 00\bar{2}$) of C2 taken across the absorption edge for Iron ($\lambda = 1.74\text{Å}$)

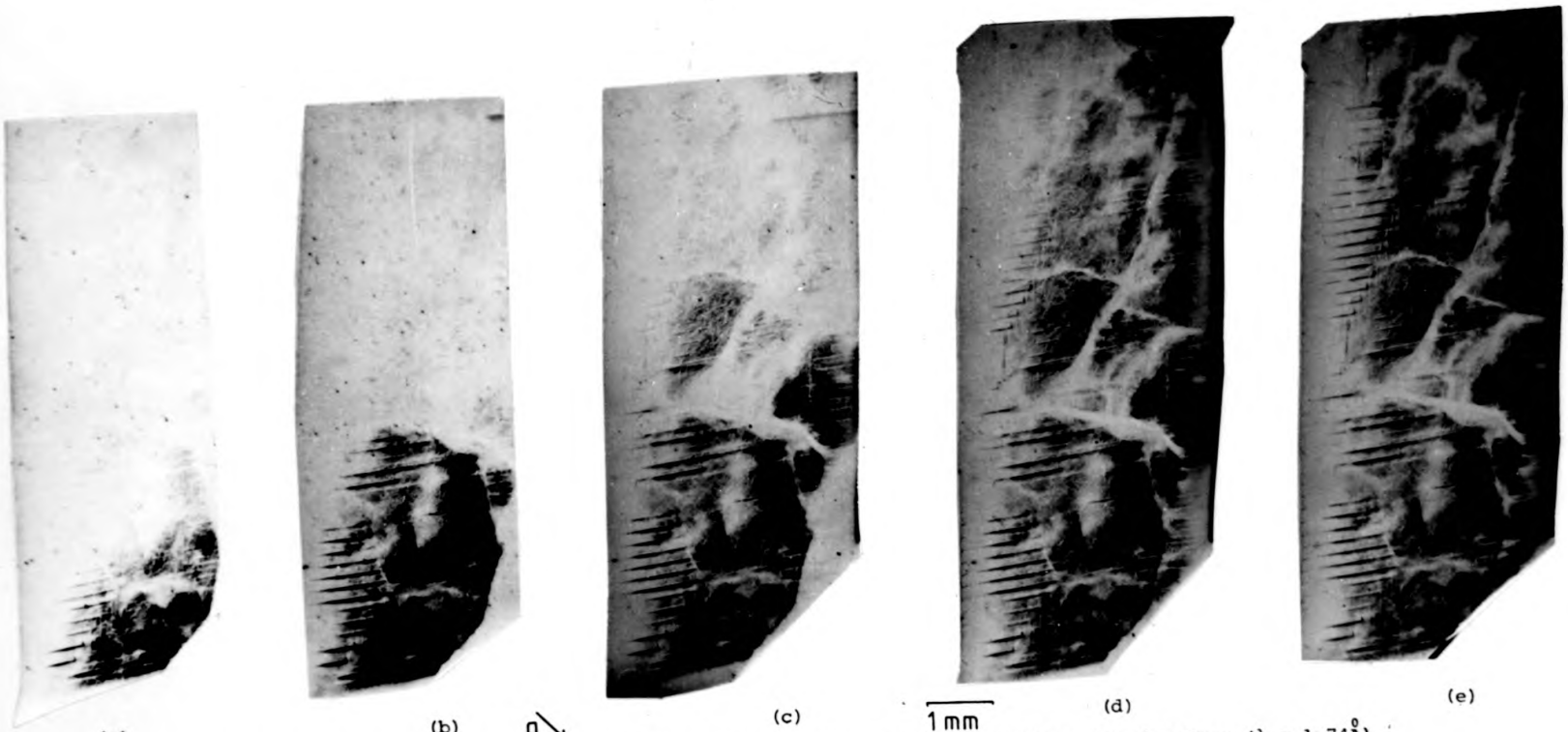

Fig 125 Series of white beam topographs ($g = 00\bar{2}$) of C2 taken across the absorption edge for Iron ($\lambda = 1.74\text{Å}$)

edge component (if any; for a pure screw $\underline{e}_1$ is arbitrary) and $\underline{e}_2=\underline{e}_3\wedge\underline{e}_1$.

If A_{ij} is the matrix relating the two coordinate systems i.e. $A_{ij}=e_j.e'_i$, $\delta(\Delta\theta)$ can be written

$$\delta(\Delta\theta) = -r_i A_{3j} U_{j,i}$$

where $r_i=A_{1i}-\tan\theta A_{3i}$ (the summation convention and the notation $U_{i,j}=\partial U_i/\partial x_j$ are used). For calculation of the deformation gradient we require the partial derivatives of $\delta(\Delta\theta)$ in the direction $\underline{s}_o$ ([171]).

Using the notation

$$\frac{\partial^2 U_i}{\partial x_j \partial x_k} = U_{i,jk}$$

and employing the summation convention and a convention that i+3=i, we find that

$$\frac{\partial}{\partial \underline{s}_o}[\delta(\Delta\theta)] = G = -[r_i a_i A_{3j} U_{j,ii} + (r_i a_{i+1} + r_{i+1} a_i) A_{3j} U_{j,i(i+1)}]$$

where $a_i = A_{1i}\cos\theta + A_{3i}\sin\theta$.

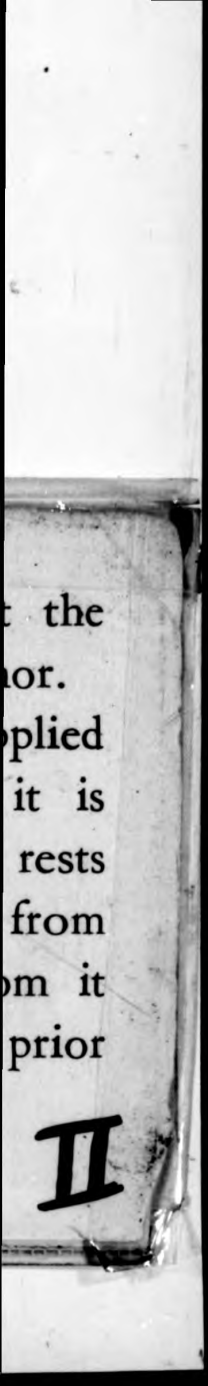
t the
ıor.
plied
it is
rests
from
m it
prior
II